ABSTRACT

Title of Dissertation: ORGANIC ANODES AND SULFUR/SELENIUM CATHODES FOR ADVANCED LI AND NA BATTERIES

Chao Luo, Doctor of Philosophy, 2015

Directed By: Professor Chunsheng Wang
Department of Chemical and Biomolecular Engineering

To address energy crisis and environmental pollution induced by fossil fuels, there is an urgent demand to develop sustainable, renewable, environmental benign, low cost and high capacity energy storage devices to power electric vehicles and enhance clean energy approaches such as solar energy, wind energy and hydroenergy. However, the commercial Li-ion batteries cannot satisfy the critical requirements for next generation rechargeable batteries. The commercial electrode materials (graphite anode and $LiCoO_2$ cathode) are unsustainable, unrenewable and environmental harmful.

Organic materials derived from biomasses are promising candidates for next generation rechargeable battery anodes due to their sustainability, renewability, environmental benignity and low cost. Driven by the high potential of organic materials for next generation batteries, I initiated a new research direction on exploring advanced organic compounds for Li-ion and Na-ion battery anodes. In my work, I employed croconic acid disodium salt and 2,5-Dihydroxy-1,4-

benzoquinone disodium salt as models to investigate the effects of size and carbon coating on electrochemical performance for Li-ion and Na-ion batteries. The results demonstrate that the minimization of organic particle size into nano-scale and wrapping organic materials with graphene oxide can remarkably enhance the rate capability and cycling stability of organic anodes in both Li-ion and Na-ion batteries.

To match with organic anodes, high capacity sulfur and selenium cathodes were also investigated. However, sulfur and selenium cathodes suffer from low electrical conductivity and shuttle reaction, which result in capacity fading and poor lifetime. To circumvent the drawbacks of sulfur and selenium, carbon matrixes such as mesoporous carbon, carbonized polyacrylonitrile and carbonized perylene-3, 4, 9, 10-tetracarboxylic dianhydride are employed to encapsulate sulfur, selenium and selenium sulfide. The resulting composites exhibit exceptional electrochemical performance owing to the high conductivity of carbon and effective restriction of polysulfides and polyselenides in carbon matrix, which avoids shuttle reaction.

ORGANIC ANODES AND SULFUR/SELENIUM CATHODES FOR ADVANCED LI AND NA BATTERIES

By

Chao Luo

Dissertation submitted to the Faculty of the Graduate School of the
University of Maryland, College Park, in partial fulfillment
of the requirements for the degree of
Doctoral of Philosophy
2015

Advisory Committee:
Professor Chunsheng Wang, Committee Chair
Professor James Culver, Dean's Representative
Professor Michael R. Zachariah
Professor Nam Sun Wang
Professor Dongxia Liu

Dedicated to Jingjing Wang, Michelle Luo,

Runzhen Xiong and Honggui Luo,

Love you forever.

Acknowledgements

I would like to acknowledge the support and help from my advisor, Prof. Chunsheng Wang, during my graduate study in his group from 2011 to 2015. Prof. Wang is a diligent, wise and creative researcher, who not only teaches me how to do research in the energy storage field, but also shows me the most important characters for an excellent researcher: diligence, critical thinking and capability of cooperation. Without Prof. Wang's strong support and help, I cannot achieve such a great success in my research area, so nothing is enough to show my great appreciation to him. I wish him every success in life.

I want to thank Dr. Yunhua Xu, who acts as a teacher to me after I join Prof. Wang's group. I wish Dr. Xu to become a successful professor in Tianjin University. I am also grateful to my collaborators, Prof. Huixin He, Dr. Zhonghai Chen, Dr. Guiliang Xu and Mr. Ruiming Huang for the technical support and assistance. I would like to thank my lab mates, Dr. Juchen Guo, Dr. Shiyou Zheng, Dr. Yujie Zhu, Dr. Yanting Luo, Dr. Xiulin Fan, Dr. Liumin Suo, Dr. Jianfeng Mao, Dr. Yang Wen, Dr. Alex Langrock, Dr. Huili Liu, Tao Gao, Fudong Han, Tao Ye, Xiwen Wang, Yihang Liu and Ying Liu, who create a friendly and supportive environment during the four years in lab. I would also like to thank my friends, Dr. Guoqiang Jian, Dr. Kai Zhong, Yujia Liang and Chanyuan Liu.

At last, I want to send my special acknowledgement to my parents, Honggui Luo and Runzhen Xiong, my wife, Jingjing Wang, my daughter, Michelle Luo, and my grandparents, Yingfang Luo and Shiying Wang. Without your love and support in my life, I cannot obtain my Ph. D. in the United States. I know I can never pay back the love that I gain from you. I love you forever. You are always in my heart.

Table of Contents

List of Tables

List of Figures

Chapter 1 Introduction

1.1 Lithium Ion Battery System

Lithium ion batteries (LIB) are widely used as energy storage devices for portable electronics, and are potential to drive electric vehicles. The first commercial LIB was invented by Sony Corporation using $LiCoO_2$ as cathode and graphite as anode in early 1990s [1]. Since then, extensive research interest from academy and industry is invoked to develop advanced cathode and anode materials for high performance rechargeable LIB. In the last two decades, a large variety of cathode and anode materials were investigated, and the energy density of LIB is remarkably improved from 250 $W{\cdot}h\ L^{-1}$ to 650 $W{\cdot}h\ L^{-1}$ [2]. However, current LIB still cannot satisfy the high energy requirement from smart phones and electric vehicles. Therefore, it is of great significance to develop high energy density LIB.

Coin cell, a widely used battery product in the market, is the simplest model for LIB. A typical coin cell consists of cathode, anode, electrolyte, separator, current collectors, two stainless steel spacers, spring and cases. The cathode material is casted on aluminum current collector, while the anode material is casted on copper current collector. Aluminum and copper are used as current collector, because they are highly electro-conductive and highly stable during cycling. Separator, a nonconductive polymer film, is used to separate cathode and anode to avoid the short circuit. Electrolyte, an ionic conductive, but electronic nonconductive liquid, is added between cathode and anode to facilitate the lithium ion transport inside the battery, so during charge/discharge process, lithium ions can transport between cathode and anode through the electrolyte, while the electrons move in the outer circuit of the battery as shown in figure 1.1.

Cathode and anode, which determines the energy density of the battery, are active materials in the coin cell, while the rest components are inactive materials, which lowers the energy density of coin cell. To build the high energy density LIB, it is very critical to find high capacity cathode and anode materials.

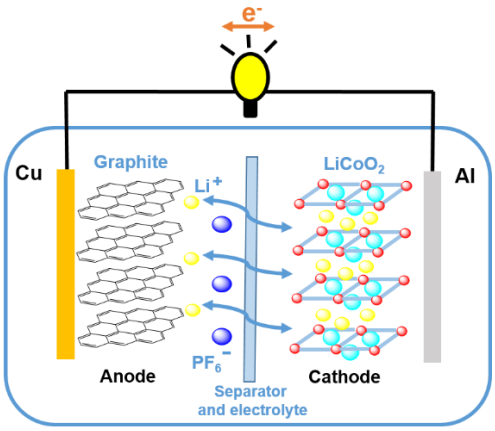

Figure 1.1. A typical LIB.

The energy density of LIB is determined by the total capacity and voltage of the battery. The calculation method of energy density is shown in equation 1.1. Energy density is equal to the product of total capacity and voltage of the battery, which is the voltage difference between cathode and anode. The total capacity of the battery is determined by the capacity of cathode and anode. As shown in equation 1.2, the reciprocal of total capacity is equal to addition of the reciprocal of cathode capacity and the reciprocal of anode capacity, so the total capacity is mainly determined by electrode with lower capacity. In the commercial LIB, $LiCoO_2$ with the specific capacity of ~140 mAh g^{-1} is used as cathode [3], while graphite with the specific capacity of 360 mAh g^{-1} is used as anode [4]. The low capacity of $LiCoO_2$ cathode limits the total capacity of LIB. More importantly, cobalt is a rare, expensive and toxic metal element, which not only enhances the cost of LIB, but also induces serious environmental issues. Thus, considerable

research efforts have been devoted to developing high voltage and high capacity environmental benign cathode materials for LIB, and a large variety of high energy density, low cost and environmental benign cathode materials such as sulfur, selenium, lithium metal phosphates, lithium metal oxides and lithium rich metal oxides are investigated for next generation LIB.

$$E = C_{total} * V \qquad [1.1]$$

E: energy density; C_{total}: total capacity of the battery; V: voltage of the battery.

$$\frac{1}{C_{total}} = \frac{1}{C_{cathode}} + \frac{1}{C_{anode}} \qquad [1.2]$$

C_{total}: total capacity of the battery; $C_{cathode}$: capacity of cathode; C_{anode}: capacity of anode.

Though high voltage and high capacity environmental benign cathodes are desired for next generation rechargeable batteries, sustainable and renewable anodes are also required to match with the cathodes for LIB. The commercial anode is graphite with a maximum theoretical capacity of 372 mAh g^{-1}, calculated based on equation 1.3. It cannot satisfy the requirement for sustainable and renewable anode. In the last two decades, considerable research efforts were devoted to developing advanced anode materials for next generation rechargeable batteries. There are a large number of low cost anode materials such as silicon, tin, metal oxide and metal sulfides with much higher capacity than graphite. They are very promising to replace graphite for the next generation commercial anode. Recently, carbonyl group based organic anodes attracted extensive research interest from battery field due to the low cost, sustainability and renewability of organic materials derived from biomass.

$$C_{theoretical} = \frac{n*F}{M_w} \qquad [1.3]$$

n: number of lithium ions or electrons react with electrode material; F: Faraday constant; M_w: molecular weight of the electrode material.

The great success in the development of advanced cathode and anode materials in the last two decades enables LIB to dominate the market of portable electronics and electric vehicles. LIB are also considered as promising energy storage devices to restore renewable energies such as solar energy, wind energy, hydroenergy and so on. The high electrochemical performance, high stability and high reliability make LIB the most promising energy storage devices in the future market.

1.1.1 Cathode Materials

Since the commercial $LiCoO_2$ cathode suffers from high toxicity and high cost, considerable research efforts have been devoted to developing low cost, high capacity and environmental benign cathode materials. In the last two decades, a large variety of high energy density, low cost and environmental benign cathode materials such as sulfur, selenium, lithium metal phosphates, lithium metal oxides and lithium rich metal oxides were investigated for advanced LIB cathode. Their advantages and disadvantages as cathode materials in LIB are discussed in this section.

Sulfur is considered as one of the most promising cathode materials due to its low cost, abundance and high capacity [5-7]. The theoretical capacity of sulfur is 1672 mAh g^{-1}, calculated based on equation 1.3. Pristine sulfur exists as S_8 molecules, which can reversibly react with 16 lithium ions as shown in equation 1.4. The energy density of lithium sulfur batteries (LSB) is 2600 Wh kg^{-1}, which is three to five times higher than other cathode materials. Though LSB is considered as one of the most promising rechargeable batteries, there are still several challenges,

which impedes its large-scale application. (1) The shuttle reaction due to the dissolution of polysulfide intermediates during lithiation/delithiation process results in low Coulombic efficiency and rapid capacity fading; (2) Low utilization of sulfur induced by the extremely low electronic and ionic conductivity of S and Li_2S reduces the capacity and power density of LSB; (3) The stress/strain induced by the large volume change of 76% between sulfur (2.03 g cm^{-3}) and Li_2S (1.66 g cm^{-3}) during lithiation/delithiation destructs the integrity of sulfur cathode and resulting in fast capacity decline. Significant progress has been made to overcome the three challenges by infusing sulfur into electronic conductive porous carbon matrix such as porous carbon [8], carbon nanotube [9], graphene [10], graphene oxide [11] and carbon nanofiber [12]. The detailed review for sulfur cathode is discussed in section 1.3.1.

$$S_8 + 16\ Li^+ \underset{-\ 16\ e^-}{\overset{+\ 16\ e^-}{\rightleftharpoons}} 8\ Li_2S \qquad [1.4]$$

Selenium was firstly reported as a cathode material for LIB by Dr. Khalil Amine's group in 2012 [13]. As the congener of sulfur, selenium shares similar chemical and physical property as sulfur. As shown in equation 1.5, one Se_8 molecule can reversibly react with 16 lithium ions, corresponding to a theoretical capacity of 678 mAh g^{-1}. Though the gravimetric capacity of selenium is lower than sulfur, the volumetric capacity of selenium (3253 Ah L^{-1} based on 4.82 g cm^{-3}) is comparable to sulfur (3467 Ah L^{-1} based on 2.07 g cm^{-3}). In addition, selenium has 20 orders of magnitude higher electrical conductivity than sulfur. These features make it a promising cathode material for both LIB. However, similar to sulfur, the selenium cathodes also

suffer from shuttle reaction triggered by the dissolution issue of high-order polyselenides in the electrolyte. To circumvent the shuttle reaction, selenium is infused into carbon matrix such as porous carbon [14], carbon nanotube [15], graphene [16], graphene oxide [17] and carbon nanofiber [18]. Analogous to sulfur cathode, carbon/selenium composites show remarkably improved battery performance. The detailed review for selenium cathode is discussed in section 1.3.2.

$$Se_8 + 16\ Li^+ \underset{-\ 16\ e^-}{\overset{+\ 16\ e^-}{\rightleftharpoons}} 8\ Li_2Se \qquad [1.5]$$

Lithium metal phosphates such as lithium iron phosphate, lithium manganese phosphate and lithium vanadium phosphate were investigated as cathode materials for LIB [19-21]. Among them, olivine $LiFePO_4$ is the most promising cathode material due to its low cost, high cycling stability and environmental benignity. However, it suffers from low capacity and poor electronic conductivity. The theoretical capacity of $LiFePO_4$ is 169.6 mAh g^{-1} with charge/discharge plateaus centered at 3.45 V, so the maximum energy density of $LiFePO_4$ is 585 Wh kg^{-1}, which is much lower than sulfur and selenium cathode. To overcome the drawbacks of $LiFePO_4$, various synthetic methods are adopted to prepare $LiFePO_4$ nano-particles with uniform carbon coating. In 2009, Prof. Ceder's group reported nano-size $LiFePO_4$ with particle size less than 50 nm, exhibiting ultrafast charging and discharging [22]. The nano-size $LiFePO_4$ can reach its theoretical capacity at the current density of 2 C, while its reversible capacity can maintain 130 mAh g^{-1} at high current density of 50 C. Recently, graphene coated $LiFePO_4$ cathode reported by Dr. Lain-Jong Li's group delivers a reversible capacity of 208 mAh g^{-1}, which is even higher than its

theoretical capacity, with first cycle Coulombic efficiency of ~100% [23]. Therefore, carbon coated nano-size $LiFePO_4$ cathodes are promising cathode materials for Li-ion batteires.

Despite sulfur, selenium and lithium metal phosphates are promising cathode materials for next generation LIB, the simplest method to design and synthesize cathode materials to substitute for $LiCoO_2$ is to partially or fully replace cobalt in $LiCoO_2$ by other cheap and nontoxic transition metals such as Ni, Mn and Fe. As a result, a large number of lithium metal oxides, such as $LiMnO_2$, $LiMn_{1.5}Ni_{0.5}O_4$, $LiMn_{0.5}Ni_{0.5}O_2$, $LiMn_{1/3}Co_{1/3}Ni_{1/3}O_2$, $LiNi_{0.5}Co_{0.5}O_2$ and so on, are synthesized and investigated as cathodes in LIB. Among them, $LiMn_{1/3}Co_{1/3}Ni_{1/3}O_2$ is very promising to substitute for $LiCoO_2$, because it has similar energy density as $LiCoO_2$, and its cost is much lower than $LiCoO_2$ after partially substitution by nontoxic Ni and Mn [24]. More importantly, the electrochemical performance such rate capability and cycling stability of $LiCoO_2$ is improved after Ni and Mn doping. Another promising cathode material is high voltage $LiMn_{1.5}Ni_{0.5}O_4$ spinel, which has a discharge plateau at 4.7 V [25]. Since $LiMn_{1.5}Ni_{0.5}O_4$ is a cobalt-free cathode material, and it has higher energy density than $LiCoO_2$, there is extensive research interest to synthesize high performance and high voltage $LiMn_{1.5}Ni_{0.5}O_4$ spinel. However, the migration of Mn^{3+} in $LiMn_{1.5}Ni_{0.5}O_4$ spinel induces structure distortion during cycling, resulting in fast capacity fading. Moreover, the commercial electrolyte is not stable at high voltage, which also contributes to the capacity fading. Recent research shows that $LiMn_{1.5}Ni_{0.5}O_4$ spinel with (111) family of surface planes exhibits exceptional battery performance, and fluorinated electrolyte is stable up to 5 V. Therefore, high voltage $LiMn_{1.5}Ni_{0.5}O_4$ spinel is a promising cathode material for LIB.

Another group of promising cathode materials are lithium rich layered oxide cathodes such as $Li_{1.2}Mn_{0.54}Ni_{0.13}Co_{0.13}O_2$ and $Li_{1.2}Ni_{0.2}Mn_{0.6}O_2$ due to their high capacity and low cost [26]. The

lithium rich cathodes can deliver a high reversible capacity of ~250 mAh g^{-1} with a sloping voltage plateau centered at 3.5 V so that their energy density is ~875 Wh kg^{-1}, which is much higher than $LiCoO_2$. The higher capacity and energy density are attributed to the excess lithium, exists in the Li_2MnO_3 phase of lithium rich cathodes. Nevertheless, the lithium rich cathodes suffers from voltage fading and poor long-term cycling stability due to the crystal structure change and Mn^{3+} dissolution during cycling. The phase transformation of lithium and manganese rich cathode from layered structure to defect spinel-like structure and then to disordered rock salt structure has been reported by Jiguang Zhang's group [27]. The voltage fading is related with lithium ion insertion into the octahedral sites in both defect spinel-like and disordered rock-salt structures. Therefore, a lot work needs to be done to improve the structure stability and prevent Mn^{3+} dissolution before the application of lithium rich cathodes in LIB.

1.1.2 Anode Materials

To match with state-of-the-art cathode materials, considerable research efforts have been devoted to developing low cost and high capacity anode materials. Up to date, a large variety of anode materials, such as silicon, tin, metal oxides, metal sulfides, lithium titanium oxide, red phosphorous, lithium metal so forth, are investigated for advanced LIB anode. Compared with the commercial graphite anode, the capacity of the new anodes are much higher. However, the high capacity results in large volume change during lithiation/delithiation process, which causes severe particle pulverization. As a consequence, the particle pulverization is a main reason for the fast capacity fading of anode materials. To circumvent this challenge, numerous synthetic

methods are reported to fabricate nano-structure anode materials, which exhibit superior electrochemical performance.

The lithiation/delithiation process of anode materials undergoes three types of reaction mechanisms: insertion reaction, conversion reaction and alloying reaction [28]. The anodes such as graphite and lithium titanium oxide react with lithium ions via insertion reaction [29]. The volume change during insertion reaction is small compared to conversion reaction and alloying reaction, and the capacity generated from insertion reaction is also smaller than that of conversion reaction and alloying. Red phosphorous, metal oxide and sulfide anodes react with lithium ions via conversion reaction, while silicon and tin anodes react with lithium ions via alloying reaction. These anodes suffer from poor electronic conductivity and large volume change, so fabricating nanomaterial is an effective approach to improve the anode performance.

Silicon is a very promising anode material for LIB due to its low cost and very high capacity [30]. The theoretical capacity of silicon anode is 4200 mAh g^{-1} in that silicon can react with 4.4 lithium ions to form $Li_{4.4}Si$. However, silicon suffers from ~400% volume expansion during lithiation so that large silicon particles pulverize into small pieces, which loss contact with conductive carbon and become electro-inactive. More importantly, the large volume change of Si during cycling can continuously destruct the solid electrolyte interphase (SEI) layer formed on the surface of Si electrode, resulting in large irreversible capacity and low Coulombic efficiency. To overcome the challenge for Si anode, Prof. Yi Cui's group makes significant contribution to prepare nano-Si anodes for high-performance LIB [31]. Their results confirm that minimizing particle size can effectively improve the battery performance of Si anode.

As a congener of Si, tin anode also suffers from large volume change, but the advantage of Sn over Si is its high electro-conductivity. It is not necessary to add a large amount of conductive carbon in the electrode to enhance the conductivity, but carbon coating is required to avoid the Sn agglomeration. A lot of work has been done to prepare carbon coated nano-Sn anodes, which exhibit excellent battery performance [32-35]. Recently, some researchers proposed to use SnM (M = Fe, Co, Ni) as anode material for next generation LIB [36], because SnM anodes with much smaller volume change than Sn and Si have higher reversible capacity than graphite, and the electro-inactive metal can alleviate the Sn agglomeration, so the long-term cycling stability of SnM is exceptional.

Apart from Si and Sn, metal oxides and sulfides, such as Fe_2O_3, CuO, NiO, MoS_2, SnS, SnS_2 and so on, are also investigated as anode materials for LIB due to the low cost and high capacity [37-39]. However, the potential hysteresis of metal oxides and sulfides is over 0.5 V, resulting in low energy efficiency. Though preparing carbon coated nanocomposites can facilitate reaction kinetics and mitigate large volume change of metal oxides and sulfides during lithiation/delithiation process, the low energy efficiency caused by large overpotential hinders its application in advanced LIB.

Lithium metal is the most promising anode material in LIB due to its lowest discharge potential and highest capacity in all the anodes. Lithium metal is the only suitable anode for LSB and lithium air batteries, which show highest energy density in rechargeable batteries. However, the formation of lithium dendrite during cycling can penetrate the electrolyte and separator, and directly contact with cathode material, resulting in short circuit of the battery [40]. The long-term cycling of lithium metal anode not only causes the failure of Li battery, but also leads to the explosion of Li battery due to the large amount of heat generated from short circuit. The safety

issue is a big concern for the application of lithium metal. Recently, Prof. Yi Cui's group synthesized carbon coated lithium metal to avoid the growth of lithium dendrite [41]. They successfully used lithium metal anode to match with $LiFePO_4$ cathode, which is a significant progress for the application of lithium metal anode. Therefore, the lithium metal anode is very promising for the future application in high energy density LSB and lithium air batteries.

Up to date, LIB are the most promising rechargeable batteries in the market due to its high energy density, high cycling stability, high safety and high reliability. A lot of work needs to be done to increase the energy density and decrease the cost of cathode and anode. The high energy density, low cost and environmental benign LIB are demanded in the future market.

1.2 Sodium Ion Battery System

Na-ion batteries (NIB), which share similar chemistry with LIB, attract tremendous research interest from battery field in the last decade due to the abundance and low cost of sodium sources. The chemical and physical properties of sodium versus lithium are summarized in table 1.1 [42]. The cost of sodium carbonate is only 3% of lithium carbonate. More importantly, lithium sources are limited and unevenly distributed in the world, but sodium sources are abundant and everywhere. The large availability and low cost of sodium sources make NIB promising candidates to restore renewable energies such as solar energy, wind energy, hydro-energy and so on. However, the potential of sodium metal is 0.33 V higher than lithium metal and the theoretical capacity of sodium metal is merely ~30% of lithium metal, resulting in lower energy density of NIB than LIB. Moreover, the cation radius of sodium ion is 40% larger than lithium

ion. The larger cation radius causes more severe volume change and complicated reaction mechanism of NIB.

Category	Lithium	Sodium
Atomic Weight (g mol^{-1})	6.9	23
Density (g cm^{-3})	0.534	0.968
Cation Radius (Å)	0.76	1.06
Potential (V) versus SHE	-3.04	-2.71
Cost, Carbonates ($/ton)	5000	150
Theoretical Capacity (mAh g^{-1})	3829	1165

Table 1.1. Sodium versus Lithium characteristics [42].

In the last decade, considerable research efforts have been devoted to developing advanced cathode and anode materials for NIB. Due to the similar chemical and physical property of sodium to lithium, a large number of cathode and anode materials, used in LIB, can also be used in NIB. The promising cathode materials are sulfur, selenium, O3-type and P2-type sodium metal oxides, sodium metal phosphate and sodium metal sulfates, while the promising anode materials are nongraphitic carbonaceous materials, tin, antimony, red phosphorous and metal sulfides. Though significant progress has been made for NIB cathodes and anodes, more efforts are still required to further improve the cycling stability and energy density of NIB.

1.2.1 Cathode Materials

Analogous to LIB, sulfur and selenium can also be used as cathodes in Na batteries [43, 44]. The shuttle reaction caused by the dissolution of polysulfides and polyselenides in the electrolyte also exists in Na sulfur/selenium batteries. Due to the larger ion size of sodium, larger volume change

occurs during sodiation/desodiation process. It is more difficult to stabilize Na sulfur/selenium batteries. Currently, there are few reports related with room temperature Na sulfur/selenium batteries.

Apart from sulfur and selenium, O3-type and P2-type sodium metal oxides are also promising cathode materials in NIB. The crystal structure of O3-type and P2-type sodium metal oxides are shown in figure 1.2a and 1.2b [45]. There are three faces (A, B, C) in O3-type metal oxides, and sodium ions are inserted in the space between two different faces, while there are two faces (A, B) in P2-type metal oxides, and sodium ions are inserted in the space between two same faces. The O3-type metal oxides such as $NaMnO_2$, $NaNiO_2$, $NaFeO_2$ and $NaNi_{0.33}Mn_{0.67}O_2$ contain one sodium ion in the molecular formula, which cannot be fully desodiated, while the P2-type metal oxides such as $Na_{0.5}VO_2$, $Na_{0.5}CoO_2$, $Na_{0.67}MnO_2$, $Na_{0.67}Ni_{0.33}Mn_{0.67}O_2$, and $Na_{0.67}Fe_{0.5}Mn_{0.5}O_2$ contain less than 0.67 sodium ion in the molecular formula, which can be fully desodiated. After first desodiation, one mole of P2-type metal oxides can reversibly react with one mole of sodium ions, resulting in much higher reversible capacity (~200 mAh g^{-1}) than O3-type metal oxides (~120 mAh g^{-1}) [46]. Therefore, P2-type sodium metal oxides are more promising than O3-type sodium metal oxides for NIB cathodes. However, the structure distortion exists in both O3-type and P2-type sodium metal oxides owing to the metal ion migration during sodiation/desodiation process. To improve the cycling stability of O3-type and P2-type sodium metal oxides, a lot of work needs to be done to maintain the crystal structure upon cycling.

Sodium metal phosphate such as $NaFePO_4$ and $NaFePO_4F$, and sodium metal sulfate such as $Na_2Fe_2(SO_4)_3$ are also promising NIB cathodes due to the low cost, abundance and environmental benignity [47-50]. Since NIB are designed to restore renewable energy, its cycle life is the most important factor. Sodium metal phosphate and sulfates show good cycling stability,

which makes them very suitable for NIB. The main drawback of these cathodes is the low capacity, which is less than 120 mAh g^{-1}. Though a number of methods are adopted to synthesize nano-structured sodium metal phosphate, the energy density is much lower than P2-type sodium metal oxides.

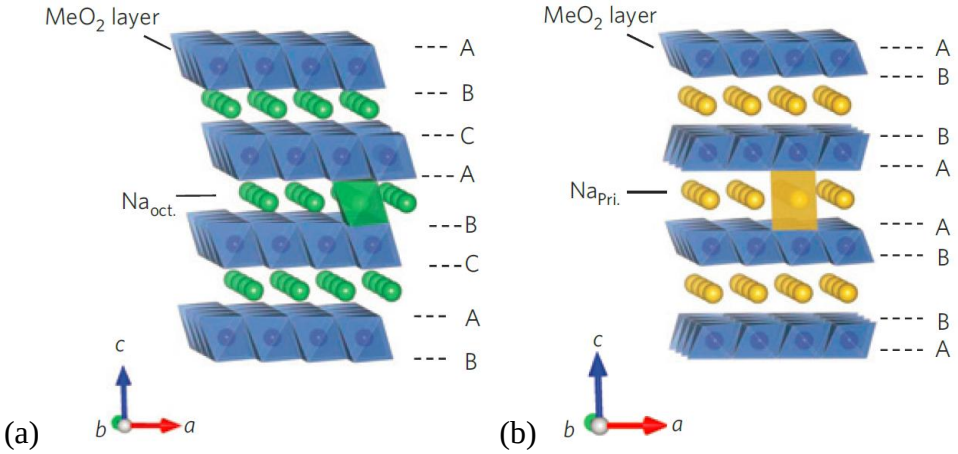

Figure 1.2. Crystal structure of O3 type (a) and P2 type (b) sodium metal oxides [45].

The state-of-the-art cathodes still cannot satisfy the critical requirement for advanced NIB. The cycling stability is the main concern for NIB. However, the cycle life of current cathodes are still far away from the requirement, especially for the cathodes with high reversible capability. Therefore, new cathode materials with high capacity and long cycle life are demanded for advanced NIB.

1.2.2 Anode Materials

Besides cathodes, there are also a lot of anode materials reported for NIB such as nongraphitic carbonaceous materials, tin, antimony, red phosphorous and metal sulfides. The volume change of NIB anodes is even larger than LIB anode due to larger ion size of sodium ion than lithium

ion, so more severe particle pulverization occurs during sodiation/desodiation process, resulting in worse cycle life. Furthermore, the commercial graphite anode and promising Si anode are electro-inactive in NIB. Considerable research efforts have been devoted to developing NIB anodes.

The nongraphitic carbonaceous materials are promising anodes for NIB due to the low cost and high cycling stability. Though nongraphitic carbonaceous materials such as hard carbon [51], graphene [52] and expanded graphite [53] deliver low reversible capacity, which is less than 300 mAh g^{-1}, they exhibit excellent cycling stability. For instance, the expanded graphite anode can deliver a reversible capacity of 284 mAh g^{-1} at 20 mA g^{-1}, and maintain a reversible capacity of 184 mAh g^{-1}, 73.92% of its initial capacity at 100 mA g^{-1} after 2000 cycles [53]. The long cycle life of nongraphitic carbonaceous materials is desired for NIB anode, but more efforts are still required to achieve high capacity and high cycling stability anodes.

To obtain high capacity and high cycling stability anodes, a lot of researchers change their research interest to tin [54], antimony [55], red phosphorous [56] and metal sulfides [57], which undergo either alloying reaction or conversion reaction with sodium ions. The high capacity (600 mAh g^{-1} to 1000 mAh g^{-1}) of these anodes leads to large volume change, resulting in severe particle pulverization. For example, tin anode with high capacity ~800 mAh g^{-1} suffers from 420% volume change during sodiation/desodiation process [54]. The fast capacity decay caused by large volume change can be alleviated by carbon coating and minimizing the particle size. Thus, a lot of work has been done to prepare carbon coated tin nanocomposites to enhance the cycle life of tin anodes. Similar work has also been done to antimony, red phosphorous and metal sulfide anodes. The carbon nanofiber coated antimony anodes show improved cycle life due to accommodation of moderate volume change of nano-size antimony by carbon nanofiber [55]. The

success of carbon coating and minimizing the particle size demonstrates that the high capacity and high cycling stability of NIB anodes can be achieved.

1.3 Review of Previous Work in Sulfur and Selenium Cathodes

LSB is a very promising candidate for the next generation rechargeable battery due to the low cost, abundance and high capacity of sulfur. However, there are three inevitable challenges for sulfur cathode as discussed in section 1.1.1. Firstly, to overcome the insulting property of sulfur, conductive carbon is added into sulfur cathode to increase the electro-conductivity. For the second challenge, a large number of physical and chemical methods are reported to mitigate the shuttle reaction induced by the dissolution of polysulfides [58-60]. As shown in figure 1.3, pristine sulfur exists as S_8 in the nature. During the lithiation, S_8 will gain two lithium ions and two electrons to form Li_2S_8. Then, Li_2S_8 will gain electrons and lithium ions to generate Li_2S_n (n=4-7). $Li_2S_{4\sim8}$ are called lithium polysulfides, which are highly soluble in organic electrolyte. After dissolution, polysulfides can diffuse to the anode side, and react with lithium metal to be further reduced to lithium sulfides such as Li_2S_2 and Li_2S, which are insoluble in the electrolyte and deposit on the surface of anode. After the anode is fully covered, the lithium polysulfides will react with the insoluble lithium sulfides and generate low order lithium polysulfide. When the concentration of low order lithium polysulfide is high enough, it will diffuse back to the cathode side due to the concentration gradient. This whole process is called shuttle reaction. The last challenge is the large volume change of sulfur during lithiation/delithiation process. Professor Yi Cui's group reported hollow structure sulfur/TiO_2 composites, in which the large volume change

of sulfur can be accommodated by hollow TiO_2 shells [61]. The resulting sulfur/TiO_2 composites show excellent electrochemical performance in Li batteries.

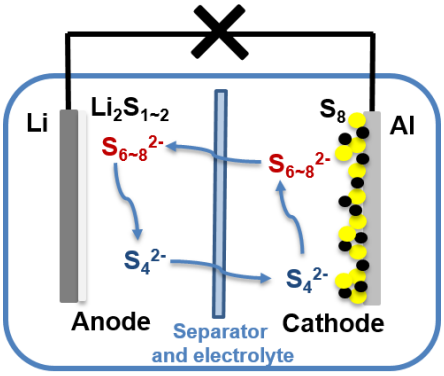

Figure 1.3. The shuttle reaction in LSB.

As a congener of sulfur, selenium also suffers from shuttle reaction and large volume change, so a lot of methods used to stabilize sulfur cathode are useful in selenium cathode. Since the conductivity of selenium is higher than sulfur, and selenium is nonflammable, while sulfur is flammable, selenium is more promising than sulfur to build a safe cathode in Li batteries, which is a very critical concern in industry. The recent progress in sulfur and selenium cathodes are discussed in the following sections.

1.3.1 Sulfur Cathode

Currently, there are several methods to avoid the dissolution of polysulfides in organic electrolyte. Firstly, a variety of physical methods are harnessed to stabilize polysulfides in the cathode electrode. Professor Linda's group fills sulfur into mesoporous carbon matrix by heating the mixture of carbon and sulfur at 155 ^oC [62]. The resulting sulfur and mesoporous carbon composites (SMCC) display good cycling stability and high specific capacity. Since mesoporous

carbon possesses good ionic and electronic conductivity, SMCC overcame the drawback of insulating sulfur material. The good conductivity of SMCC allows lithium ions and electrons to transfer inside the carbon matrix, and the small pores of mesoporous carbon could confine polysulfide in the carbon matrix. Although this material exhibits very good electrochemical performance, the low weight percentage of sulfur in the composite and high cost of mesoporous carbon impede its application in LIB.

Professor Linda's work provided a good concept to stabilize polysulfides in cathode electrode. Afterwards, a lot of other carbon matrixes have been used to trap polysulfides. For example, our group uses disorder carbon nanotubes (DCNTs) to constrain Polysulfides [9]. DCNTs are fabricated by annealing polyacrylonitrile (PAN) in commercial anodic aluminum oxide (AAO) template at 600 ^{o}C. After PAN is carbonized, AAO template is dissolved in the NaOH aqueous solution. The resulting DCNTs are filled with sulfur by annealing in a sealed vacuum glass tube at 500 ^{o}C. Since DCNTs have very good electronic and ionic conductivity, the sulfur impregnated DCNTs material possesses very good conductivity. More importantly, DCNTs are able to constrain polysulfides inside the nanotube, because the pore size of carbon nanotube is too small to allow the diffusion of electrolyte. The polysulfides in DCNTs cannot dissolve into the electrolyte, so the electrochemical performance of this material is very good. Nevertheless, the low content of sulfur in this material and the difficulty to synthesize DCNTs hinder its application in LIB.

Professor Yi Cui's group successfully uses poly (ethylene glycol) (PEG) surfactant and mildly oxidized graphene coating layers to wrap sulfur particles [10]. The amphiphilic PEG surfactant is harnessed to connect hydrophobic sulfur particles and hydrophilic graphene coating layers. Carbon black nanoparticles are decorated on the surface of graphene layers to increase the

conductivity of graphene wrapped sulfur composite, so this material has good electronic and ionic conductivity. More importantly, both PEG layers and graphene layers can trap polysulfide to avoid its dissolution in organic electrolyte. PEG layers can also accommodate the volume change of sulfur particles during the lithiation and delithiation. As a result, this cathode material shows high capacity and long cycle life. However, the graphene-sulfur composites are difficult to fabricate, and the use of graphene enhances the cost of this material. It is unable to use this material for large-scale application.

Professor Yuegang Zhang's group uses graphene oxide sheets (GOS) to immobilize sulfur and lithium Polysulfides [11]. The sulfur nanoparticles are coated on the surface of GOS by simple chemical reaction deposition approach. Then, low temperature thermal treatment allows sulfur to diffuse into small voids of GOS, and removes sulfur particles from the surface of GOS. Since GOS had large surface area and good electronic and ionic conductivity, the electron and lithium ion transfer rate in the resulting sulfur-graphene oxide nanocomposite is very fast. Moreover, the functional groups on the surface of GOS can bind with polysulfides so that it prevents polysulfides from dissolving into the electrolyte. The sulfur-graphene oxide nanocomposites have excellent electrochemical performance in organic electrolyte.

There are some other methods which are also extensively used to reduce the solubility of polysulfides in organic electrolyte. Conductive polymer such as polythiophene (PTH) is used to wrap sulfur particles [63]. The sulfur particles are coated by PTH to form a core/shell structure. Since PTH had good electronic and ionic conductivity, PTH wrapped sulfur composite had good conductivity. PTH also acts as an absorbing agent which could immobilize polysulfides, because of the interaction between polysulfides and sulfur atoms in PTH. The PTH wrapped sulfur composites exhibit high specific capacity and good cycling stability. However, electrolyte could

penetrate porous structure of PTH shell to contact with polysulfides, so the polysulfides would still dissolve into the electrolyte in the long run. In addition, the low content of sulfur in the electrode material also limits the application of this material in LIB.

Besides physical trapping, the other methods are also employed to mitigate the shuttle reaction in LSB. For instance, $LiNO_3$ additive is added into the electrolyte to avoid the dissolution of polysulfides. At low potential, $LiNO_3$ is irreversible reduced and formed a stable passivation film on the surface of lithium anode [64]. It could protect lithium metal from reacting with polysulfides, so the shuttle reaction could be deterred from the anode side. However, the dissolution of polysulfides in the cathode side still takes place. The $LiNO_3$ additive cannot be used to enhance the performance of LSB alone. The synergic effect of $LiNO_3$ additive and carbon wrapping is used in LSB.

Recently, a solvent-in-salt (SIS) electrolyte is used for sulfur cathode [65, 66]. The concentration of LiTFSI in 1, 3-dioxolane (DOL) and dimethoxyethane (DME) (1:1 by volume) is 1 mol L^{-1} in normal electrolyte. However, the concentration of LiTFSI is improved to 5 mol L^{-1} in the SIS electrolyte. The ultrahigh concentration of lithium ions in the electrolyte not only increases mass transfer rate of lithium ion, but also decreases the dissolution of polysulfides. Since the solubility product of lithium polysulfides is a constant, the saturated concentration of polysulfides is very low when the concentration of lithium ion is ultrahigh in the electrolyte. More importantly, the ultrahigh concentration of LiTFSI in electrolyte can increase the viscosity of electrolyte, resulting in a low diffusion rate of polysulfides in electrolyte. As a consequence, the SIS electrolyte can successfully enhance the electrochemical performance of LSB.

Though tremendous work has been done to improve the battery performance of sulfur cathode, LSB are still far from practical application. More work is still needed to synthesize high loading content, high capacity and high cycling stability LSB.

1.3.2 Selenium Cathode

After selenium (Se) and selenium sulfides (SeS_x) were reported by Dr. Amine's group in 2012, Se cathode attracted considerable research interest from battery field due to its higher electrical conductivity than sulfur and similar volumetric capacity to sulfur. In the past three years, a lot of work was done to investigate selenium cathode, and great progress was made in lithium Se batteries.

The lithiation/delithiation mechanism of Se and SeS_x cathodes in ether-based electrolyte is confirmed by Dr. Amine's group [67]. A series of SeS_x (x = 0-7)/carbon composites are synthesized and used as cathodes in Li batteries. During lithiation, Se reacts with lithium ions to generate lithium polyselenides, which is soluble in the electrolyte, and then lithium polyselenides are further reduced to Li_2Se_2 and Li_2Se step by step. During delithiation, Li_2Se is oxidized to Se with the formation of lithium polyselenide intermediates. This result confirms that selenium cathode also suffers from shuttle reaction, and the methods used to stabilize sulfur cathode are also useful for Se cathode.

A lot of efforts have been made to avoid the dissolution of polyselenides in the electrolyte. Prof. Yuguo Guo's group infuses Se into mesoporous carbon to trap polyselenides in the nanopores of carbon matrix, which avoid the contact of polyselenides with electrolyte [14]. In addition, Se exists as cyclic Se_8 molecules, which are converted to chain-structure Se_n molecules in

mesoporous carbon after first cycle. The synergic effect of formation of chain-structure Se_n molecules and confinement of mesoporous carbon remarkably suppresses the shuttle reaction. Therefore, the resulting Se/mesoporous carbon composite exhibits excellent electrochemical performance.

In selenium cathodes, carbon coating and nanomaterial fabrication is used to encapsulate Se, thus circumventing the shuttle reaction. Reduced graphene oxide coated Se [17], nanofibrous Se [68], free standing graphene/Se film [69] and carbonized polyacrylonitrile coated Se [70] are also reported to demonstrate improved electrochemical performance. Up to date, it is confirmed that most of methods used in stabilizing sulfur cathode are also effective to stabilize Se cathode. Therefore, analogous to LSB, More work is still needed to synthesize high loading content, high capacity and high cycling stability lithium Se batteries to fulfill the practical application in the future.

1.4 Review of Previous Work in Organic Electrodes

Energy crisis induced by petroleum exhaustion is a critical issue for the development of world's economy and industry. To circumvent the negative impact of energy crisis, considerable research efforts have been devoted to sustainable and green energy such as solar energy, wind energy and so forth. However, these types of energy are unstable and vary with time and season. To make full use of the renewable energy, it is of great importance to develop an efficient energy storage system. Up to now, the best energy storage devices are LIB, which power most portable electronics [71].

LIB are considered as the most promising energy storage devices for emerging electric vehicles and smart grids due to the high energy density and high power density. Currently, LIB largely rely on inorganic compounds as electrodes such as $LiCoO_2$ and $LiFePO_4$. Most of these compounds are synthesized using non-earth-abundant resources via energy-demanding ceramic processes [72]. Recycling of used batteries further consumes large quantities of energy and chemicals, releasing more CO_2 and SO_2. To satisfy the urgent demand for rechargeable energy storage devices in electric vehicles and smart grids, next generation battery electrodes should be made from renewable or recyclable resources via low energy consumption processes. One possible approach is to use biomass or recyclable organic materials as electrode materials via solution phase routes [73]. In addition, most of organic compounds are degradable in the environment, so the organic electrode materials are environmentally benign.

Recently, carbonyl group based organic materials such as purpurin [74], tribrominated trioxotriangulene [75], perylenetetracarboxylic anhydride [76] and other compounds have been investigated as electrodes for LIB, and some organic materials can also been used for NIB electrodes due to the chemical similarity of sodium to lithium. Two or more carbonyl groups connected by conjugated carbon matrix can react with lithium ions and electrons to induce the electron and charge transfer in the battery. However, due to dissolution of organic compounds in electrolyte and very low electronic conductivity, the electrochemical performance of these sustainable organic electrode materials is much worse than their inorganic counterparts. The solubility of organic compounds could be reduced by enhancing their polarities via salt formation [77]. Among the salts, carbonyl group based organic compounds such as dilithium trans-trans-muconate and dilithium terephthalate have been investigated as electrodes for Li ion batteries [77]. Although use of organic salts can mitigate the dissolution issue [72], the low

electronic conductivity of organic salts and large volume change during lithiation/delithiation still limit the power density and cycling stability of organic electrodes. Due to the very low electrical conductivity of most organic compounds, up to 30 wt% of conductive carbon black is normally mixed into organic electrode to provide electron pathways for the electrochemical reactions and another ~5-10% (by weight) nonconductive polymer binders are also needed to mechanically bind all the components into an electrode. Even adding 30 wt% of carbon black, there is only a portion of active materials contributes to the output power of a battery in organic electrodes due to large size of organic salt particles. A recent work of organic $Li_4C_8H_2O_6$ nanosheets for LIB has demonstrated that nanosheet structure provides short Li ion diffusion pathways and large contact areas for both conductive carbon and electrolyte, leading to high rate capability [78]. Therefore, the fabrication of organic nanomaterials is a new direction for the battery performance improvement of organic electrodes.

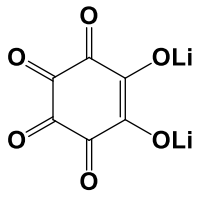

Scheme 1.1. Molecular structure of dilithium rhodizonate.

In 2008, Professor Tarascon's group reported a renewable organic electrode based on dilithium rhodizonate for sustainable LIB [73]. The dilithium rhodizonate derived from biomass is the first small molecular organic salt used in LIB. Its molecular structure is shown in scheme 1.1. The formation of organic salt can remarkably reduce the solubility of organic material in the electrolyte. As a result, this organic salt shows good electrochemical behaviors. As a cathode material, its energy density is over 1000 Wh kg^{-1} at low current density, which is two times

higher than commercial $LiCoO_2$ and $LiFePO_4$ cathodes. This work sheds light on the development of organic electrodes.

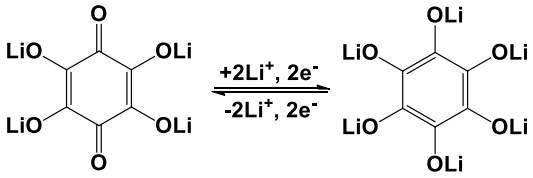

Scheme 1.2. Reaction mechanism of lithium salt of tetrahydroxybenzoquinone in LIB.

Considerable research interest is attracted from battery field after the report of high energy density renewable dilithium rhodizonate cathode. The lithium salt of tetrahydroxybenzoquinone is synthesized by annealing dilithium rhodizonate at 400 ^{o}C [79]. As shown in scheme 1.2, there are two carbonyl groups in the lithium salt, which are redox centers. They can reversibly react with two lithium ions and electrons, and deliver a reversible capacity of ~200 mAh g^{-1} with charge/discharge plateaus centered at 1.8 V. The good electrochemical performance of lithium salt of tetrahydroxybenzoquinone further confirms that sustainable and renewable LIB are very promising solve the environmental issue triggered by current LIB technology.

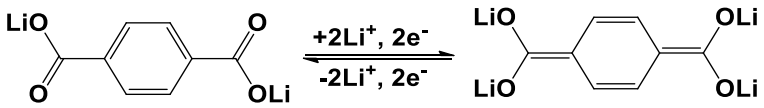

Scheme 1.3. Reaction mechanism of dilithium terephthalate in LIB.

Apart from cathodes, organic salts can also be used as anodes in LIB. The dilithium terephthalate is synthesized by neutralizing terephthalic acids with lithium hydroxide [77]. The two carboxylic groups in dilithium terephthalate can reversibly react with two lithium ions and electrons in scheme 1.3. This organic anode delivers a reversible capacity of 234 mAh g^{-1} with charge/discharge plateaus centered at 0.8 V after 50 cycles. Therefore, this organic anode can

match with previous organic cathode materials to build an organic full cell. To fulfill the large-scale application of sustainable and renewable LIB, the cycling stability of organic cathodes and anodes should be further improved.

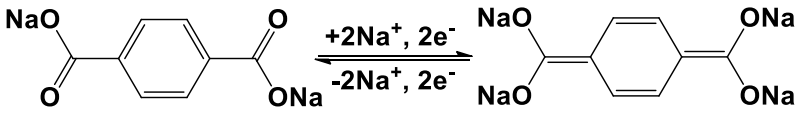

Scheme 1.4. Reaction mechanism of disodium terephthalate in NIB.

Considerable organic materials have been investigated as electrodes for LIB, but only a few orginic materials were explored for NIB. These organic salts which normally contain more than two carbonyl groups, connected by conjugated carbon matrix, are similar as the organic electrodes in LIB. Recently, some sodium salts such as disodium terephthalate, tetrasodium salt of 2,5-dihydroxyterephthalic acid and so forth were reported as organic electrodes in NIB [80]. Similar to lithium salt, disodium terephthalate (scheme 1.4) can also reversibly react with two sodium ions and electrons, but the sodiation/desodiation plateaus are 0.3 V lower than lithiation/delithiation plateaus due to the lower potential of sodium metal than lithium metal. This result confirms that the electro-active organic salts in LIB can also be used in NIB.

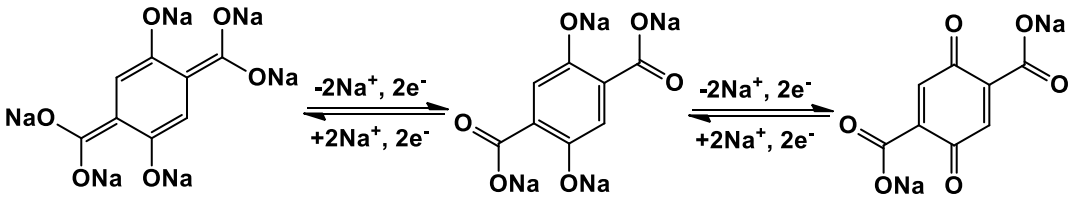

Scheme 1.5. Reaction mechanism of tetrasodium salt of 2,5-dihydroxyterephthalic acid in NIB.

Recently, Professor Jun Chen's group reported the tetrasodium salt of 2,5-dihydroxyterephthalic acid which can be used as both cathode and anode in NIB [81]. There are two types of redox

centers in this organic salt in scheme 1.5. One is the two carbonyl groups in the benzene ring, which can be used as cathode; the other one is the carboxylic group connected with benzene ring, which can be used as anode, so this salt is used to build an all organic NIB with good battery performance. Therefore, organic salts not only can be used to build sustainable and renewable LIB, but also can be used to build sustainable and renewable NIB.

1.5 Motivation and Objective

Sulfur and selenium are promising cathode materials for Li and Na batteries due to their high capacity and high energy density. The application of sulfur and selenium cathodes is desired to satisfy the industrial requirement for high energy rechargeable batteries. However, the severe shuttle reaction caused by the dissolution of polysulfides and polyselenides results in fast capacity decline of sulfur and selenium cathodes, impeding the large-scale application. Though numerous physical and chemical methods are used to trap polysulfides and polyselenides, sulfur and selenium cathodes are still far away from practical application due to the poor battery performance.

My goal is to circumvent the three challenges in sulfur and selenium cathodes, using mesoporous carbon or carbonized organic compounds/polymer. Several different carbon/sulfur or selenium composites are prepared for advanced Li and Na batteries. The conductive carbon matrix cannot only enhance the conductivity of the electrodes, but also mitigate the shuttle reaction and accommodate large volume change of sulfur and selenium cathodes.

To fulfill the large scale application of batteries for renewable energy, the low cost and environmental benignity of electrode materials are pivotal. Since lithium sources are expensive

and limited, the research interest initiates to transfer from LIB to its counterpart, NIB, in recent years. The chemical similarity of sodium to lithium enables most electrode materials in LIB to be used in NIB. The low cost and abundance of sodium sources can satisfy the huge market of energy storage devices for smart grids. Therefore, searching for high capacity and long cycle life cathode and anode materials in NIB is essential for the storage of renewable energy. Besides storage of renewable energy, the trend of energy supply for portable electronics is to develop lightweight, flexible, transparent and green batteries. Organic compounds derived from biomasses are the most promising candidates as future energy supply for portable electronics due to their low density, sustainability, environmental benignity and low cost.

Most reported organic salts experience phase transformation during lithiation/delithiation as evidenced by a flat voltage plateau in charge/discharge profile and structure change in X-ray diffraction (XRD) patterns [77]. The phase transformation is normally accompanied with volume change. The large volume expansion in the first lithiation can even change the crystal structure of organic salts into amorphous structure and retain amorphous structure in the following charge/discharge cycles [77], which is also observed in Si anodes.[33] The structure change of Si from crystal to amorphous structure is attributed to the large volume change (300%) of Si during lithiation [82]. The severe volume change of Si pulverizes the Si particle, resulting in rapid capacity decline during charge/discharge cycles [83]. Therefore, the volume change of organic salts during lithiation/delithiation may be also responsible for the capacity decay.

In principle, the carbonyl group based organic electrode compounds used in LIB can potentially be applied to NIB. However, due to larger ion size of Na^+ than Li^+, only few organic salts are suitable for Na ion batteries. In addition, the larger ion size of Na^+ causes much more severe volume change of organic salts, resulting in fast capacity decay of organic compounds in Na ion

batteries. Therefore, only few organic compounds are explored for NIB. Due to the large volume change, these organic compounds show quick capacity decline during Na insertion/extraction. My goal is to develop low cost, sustainable and green batteries based on high capacity and long cycle life organic electrodes. Several new organic nanomaterials are designed and synthesized to mitigate volume change of organic salts for high performance organic batteries.

1.6 Dissertation Layout

Chapter 2: The poor cyclic stability and low sulfur utilization of sulfur cathodes are significantly improved by forming oxygen stabilized C/S composite where sulfur is bonded with oxygen and uniformly distributed in carbon matrix in nano (or even in molecular) levels through annealing the mixture of sulfur and perylene-3, 4, 9, 10-tetracarboxylic dianhydride (PTCDA) at 600 ^{o}C in a sealed vacuum glass tube. The oxygen stabilized C/S composites are promising cathode materials for Li-sulfur and Na-sulfur batteries. (*Adv. Funct. Mater.* Submitted; C.L., K.X. and C.W. conceived the experiments and wrote the paper; C.L., Y.Z., T.G. and Y.X. conducted the experiments; All authors participated in discussions.)

Chapter 3: Selenium impregnated carbon composites were synthesized by infusing Se into mesoporous carbon at a temperature of 600 ^{o}C under vacuum. Ring-structured Se_8 was produced and confined in the mesoporous carbon, which acts as an electronic conductive matrix. During the electrochemical process in low-cost $LiPF_6$/EC/DEC electrolyte, low-order polyselenide intermediates formed and were stabilized by mesoporous carbon, which avoided the shuttle reaction of polyselenides. Exceptional electrochemical performance of Se/mesoporous carbon composites was demonstrated in both Li-ion and Na-ion batteries. (*ACS Nano* **2013**, *9*, 8003-

8010; C.L. and C.W. conceived the experiments and wrote the paper; C.L., Y.X., Y.Z. and Y.L. conducted the experiments; All authors participated in discussions.)

Chapter 4: Carbon bonded and encapsulated selenium composites have been synthesized by *in situ* carbonizing the mixture of perylene-3, 4, 9, 10-tetracarboxylic dianhydride (PTCDA) and selenium (Se) in a sealed vacuum glass tube. The shuttle reaction of selenium cathode was effectively suppressed by carbon bonding and encapsulation. The C/Se composites exhibit superior cycling stability and rate capability in commercial carbonate based electrolyte. (*J. Mater. Chem. A* **2015**, *3*, 555-561; C.L. and C.W. conceived the experiments and wrote the paper; C.L., J.W., L.S., J.M. and X.F. conducted the experiments; All authors participated in discussions.)

Chapter 5: The SeS_x molecules are confined by N-containing carbon (ring) structures in the carbonized PAN to mitigate the dissolution of polysulfide and polyselenide intermediates in carbonate-based electrolyte. In addition, formation of solid electrolyte interphase (SEI) on the surface of SeS_x/CPAN electrode in the first cycle further prevents polysulfide and polyselenide intermediates from dissolution. The synergic restriction of SeS_x by both CPAN matrix and SEI layer allows SeS_x/CPAN composites to be charged and discharged in a low-cost carbonate-based electrolyte ($LiPF_6$ in EC/DEC) with long cycling stability and high rate capability. (*Adv. Funct. Mater.* **2014**, *24*, 4082-4089; C.L. and C.W. conceived the experiments and wrote the paper; C.L., Y.Z., Y.W. and J.W. conducted the experiments; All authors participated in discussions.)

Chapter 6: Croconic acid disodium salt (CADS) was used as Li-ion battery electrode, and CADS organic wires with different diameters were fabricated through a facile synthetic route using anti-solvent crystallization method to overcome the challenges of low electronic conductivity of CADS and lithiation induced strain. The CADS nanowire exhibits much better electrochemical performance than its crystal bulk material and microwire counterpart. The

theoretical calculation suggested that lithiation of CADS experiences an ion exchange process. The sodium ions in CADS will be gradually replaced by lithium ions during the lithiation and delithiation of CADS electrode, which is confirmed by Inductively Coupled Plasma test. (*Nano Lett.* **2014**, *14*, 1596-1602; C.L., R.H., H.H. and C.W. conceived the experiments and wrote the paper; C.L., R.H., P.K. and M.P. conducted the experiments; All authors participated in discussions.)

Chapter 7: Croconic acid disodium salt (CADS), a renewable or recyclable organic compound, is investigated as sodium ion battery electrodes for the first time. The pristine micro-sized CADS suffers from fast capacity decay during charge/discharge cycles. The detail investigation reveals that the severe capacity loss is mainly attributed to the pulverization of CADS particles induced by the large volume change during sodiation/desodiation rather than the generally believed dissolution of CADS in the organic electrolyte. Minimizing the particle size and Wrapping CADS with graphene oxide can effectively suppress the pulverization, thus improving the cycling stability. (*J. Power Sources* **2014**, *250*, 372-378; C.L. and C.W. conceived the experiments and wrote the paper; C.L., Y.X., Y.Z., Y.L., T.G. and J.W. conducted the experiments; All authors participated in discussions.)

Chapter 8: A new carbonyl group based organic compound, 2,5-Dihydroxy-1,4-benzoquinone disodium salt (DHBQDS), was used as an anode in Na-ion batteries. A unique role-to-role fabrication technology for organic nanorod electrode is reported for the first time. The organic nanorod electrode exhibits superior electrochemical performance in $NaClO_4$-FEC/DMC electrolyte. (*Nano Energy* **2015**, *13*, 537-545; C.L. and C.W. conceived the experiments and wrote the paper; C.L., J.W., X.F., Y.Z., F.H. and L.S. conducted the experiments; All authors participated in discussions.)

Chapter 2 Activation of Oxygen-Stabilized Sulfur for Li and Na Batteries

2.1 Introduction

Li-ion batteries have been widely used to power the portable electronics. However, their penetration into the markets of vehicular electrification and grid-storage has been hindered by their moderate energy densities [2, 71], since the intercalation-type cathode materials in state-of-the-art Li-ion batteries impose an intrinsic limit on device energy density [22, 84]. Even though lithium rich metal oxides have been demonstrated to deliver the highest capacity (~250 mAh/g) [85, 86] among all transition metal oxide materials, their structural stability over the long-term cycling still presents challenges to practical applications, so does their compatibility with the state-of-the-art anode materials such as Si- and Sn-based alloys [87, 88].

At present, the most promising alternative cathode material is sulfur due to its high theoretical capacity (1672 mAh g^{-1}), low cost, high abundance in nature and environmental benignity [89, 90]. However, the rechargeable battery chemistry based on sulfur cathode still faces three intrinsic challenges [91-93]: (1) the formation of intermediate polysulfide products and the parasitic shuttle reaction caused by them during lithiation/delithiation process, resulting in low Coulombic efficiency and rapid capacity fading; (2) the extremely low electronic and ionic conductivities of both starting material S and ending product Li_2S, which are responsible for not only low capacity utilization but also poor power density; and (3) the stress/strain induced by the large volume difference (76%) between sulfur (2.03 g cm^{-3}) and Li_2S (1.66 g cm^{-3}) during a complete lithiation/delithiation cycle, which destroys the physical integrity of sulfur cathode and results in fast capacity loss. Significant efforts have been made to address these challenges, the most

popular of which is to entrap sulfur into electronic conductive hosts of nano-structures, such as microporous carbon, carbon nanotube, graphene, graphene oxide and carbon nanofiber [94-102]; nevertheless, commercialization of sulfur cathode remains remote. In fact, since these three challenges are closely entangled, it is difficult to circumvent all of them with a single strategy. For example, adoption of electrolytes with high solubility for high-order polysulfide effectively relieved the poor conductivity issue and reduced the stress/strain [103], but it also accelerated the parasitic shuttle reaction, while the sulfur–TiO_2 yolk–shell nanoarchitecture with internal void space successfully accommodated the volume expansion of sulfur [61], but the lower electronic conductivity of TiO_2-host further worsened the utilization and reaction kinetics of S-TiO_2. Carbon coating on Li_2S mitigated the stress/strain and the loss of active species due to the physical disintegration of the electrode, but the large particle size (500nm-2μm) of Li_2S reduce the utilization [104].

In this work, oxygen stabilized sulfur in carbon matrix was formed *in situ* by heating sulfur in a sealed vacuum glass tube at 600 ^oC with 3,4,9,10-perylentetracarboxylic dianhydrid (PTCDA), an aromatic compound with the composition of minimum hydrogen, moderate oxygen but rich carbon ($C_{24}H_8O_6$), makes it an ideal precursor for carbon. The carbonization of PTCDA ensures the formation of a carbonaceous matrix that is characterized of oxygen functionalities that might either covalently or Coulombically bonded to sulfur species. The transmission electron microscopy (TEM), X-ray diffraction (XRD), X-ray photoelectron spectroscopy (XPS) and Raman characterizations reveal that sulfur is uniformly immobilized in the carbon host at nano or even in molecular level, which should reduce the parasitic shuttle reactions incurred by unattached sulfur species and their intermediate reduction products. A portion of sulfur is strongly interacted with oxygen-functionalities in the carbon, which is inactive during normal

charge/discharge cycles between 1.0 and 3.0 V, the unbounded sulfur in the carbon provided a reversible capacity of 508 mAh/(g of S) for 2000 cycles with average loss of 0.0045% per cycle in carbonate-based electrolyte, which is lower than the best record by an order of magnitude.

This excellent cycling stability, however, was realized at the expense of capacity utilization, because the 508 mAh/(g of S) only represents a small portion of S accessed by the cell reaction. To liberate electrochemically inactive S species that strongly interacted with oxygen-functionalities, we reduced the lithiation potential down to 0.60 V for several cycles before normal charge/discharge cycling between 1.0 V~3.0 V started, and achieved in the subsequent cycles a remarkably high capacity of 1621 mAh/(g of S), which is close to the theoretical value of sulfur (1672 mAh/g). In the following long-term cycling, an effective capacity of 820 mAh/(g of S) was maintained for 600 cycles between 1.0 V to 3.0 V.

2.2 Experimental Section

Synthesis of C/S composites: All chemicals were purchased from Sigma Aldrich and used as received. Sulfur and perylene-3, 4, 9, 10-tetracarboxylic dianhydride were mixed with a ratio of 1.5:1 by weight and sealed in a glass tube under vacuum. The sealed glass tube was annealed in an oven at 600 °C for 3 h, and it was cooled to room temperature in 24 h. Oxygen-stabilized C/S composites were collected as black powder.

Material Characterizations: Scanning electron microscopy (SEM) images were taken by Hitachi SU-70 analytical ultra-high resolution SEM (Japan); Transmission electron microscopy (TEM) images were taken by JEOL (Japan) 2100F field emission TEM; Thermogravimetric analysis (TGA) was carried out using a thermogravimetric analyzer (TA Instruments, USA) with a

heating rate of 10 °C min^{-1} in argon; X-ray diffraction (XRD) pattern was recorded by Bruker Smart1000 (Bruker AXS Inc., USA) using CuKα radiation; Raman measurements were performed on a Horiba Jobin Yvon Labram Aramis using a 532 nm diode-pumped solid-state laser, attenuated to give ~900 μW power at the sample surface. The X-Ray Photoelectron Spectroscopy (XPS) analysis was performed on a high sensitivity Kratos AXIS 165 X-ray Photoelectron Spectrometer using monochronic Al Kα radiation. The elemental analysis was performed by ALS Environmental Company.

Electrochemical measurements: The oxygen stabilized C/S composites were mixed with carbon black and sodium alginate binder to form a slurry at the weight ratio of 80:10:10. The electrode was prepared by casting the slurry onto aluminum foil using a doctor blade and dried in a vacuum oven at 60 °C overnight. The slurry coated on aluminum foil was punched into circular electrodes with an area mass loading of 1.2 mg cm^{-2}. Coin cells for lithium sulfur batteries were assembled with lithium foil as the counter electrode, 1M $LiPF_6$ in a mixture of ethylene carbonate/diethyl carbonate (EC/DEC, 1:1 by volume) and Celgard®3501 (Celgard, LLC Corp., USA) as the separator. Coin cells for sodium sulfur batteries were assembled with sodium metal as the counter electrode, 1M $NaClO_4$ in a mixture of ethylene carbonate/dimethyl carbonate (EC/DMC, 1:1 by volume) and Celgard®3501 (Celgard, LLC Corp., USA) as the separator. Electrochemical performance was tested using Arbin battery test station (BT2000, Arbin Instruments, USA). Capacity was calculated on the basis of the weight of sulfur in C/S composites. Cyclic voltammograms were recorded using Gamry Reference 3000 Potentiostat/Galvanostat/ZRA with a scan rate of 0.1 mV s^{-1}.

2.3 Results and Discussion

2.3.1 Material Characterization

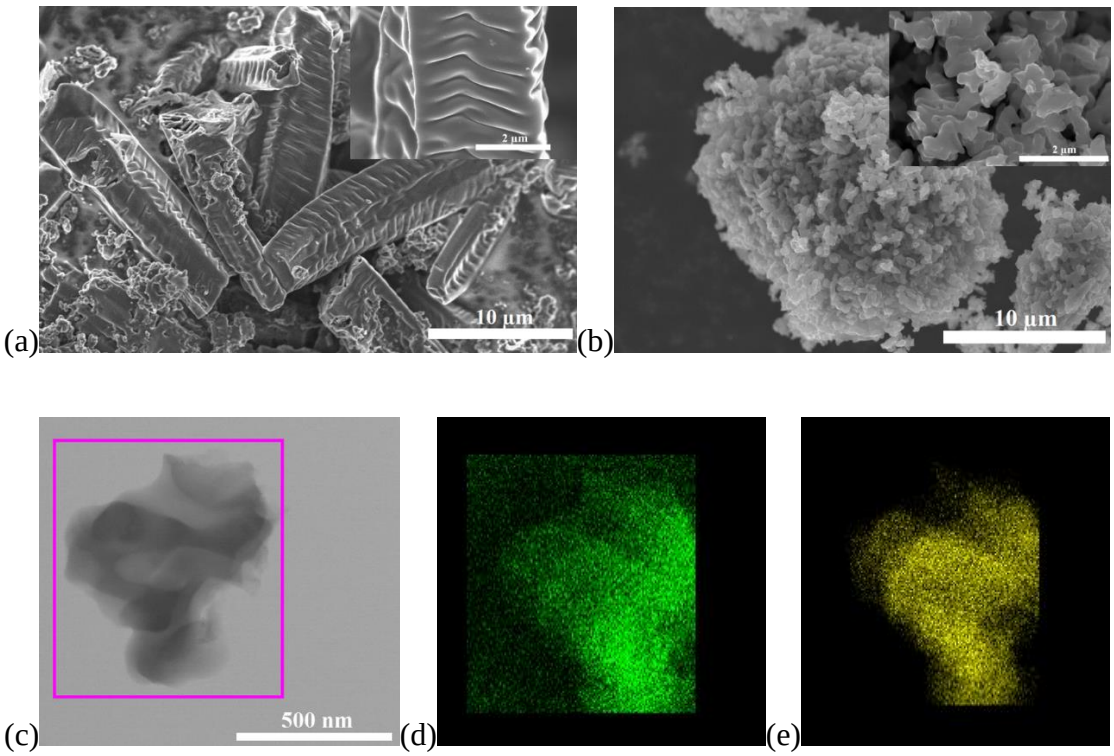

Figure 2.1. SEM images of carbonized PTCDA (a) and oxygen-stabilized C/S composites (b); (c) TEM image of oxygen-stabilized C/S composites: elemental mapping images of the C/S composite: carbon (d) and sulfur (e).

The neat PTCDA carbonized with and without sulfur are characterized by scanning electron microscopy (SEM) and TEM, respectively, as shown in Fig. 2.1. The carbonized PTCDA consists of elongated rectangular plates with a length about 20 µm and a width about 4µm. Uniform wrinkles can be observed on the surface of the plates. However, C/S composites formed by *in situ* annealing the mixture of PTCDA and sulfur are revealed to be porous spheres with diameter around 15-20 µm, which consist of aggregated secondary short plates with diameter of

~500 nm. The drastically different morphology, because of the introduction of sulfur, indicates that possible chemical interactions are formed between carbonized PTCDA host and S guest.

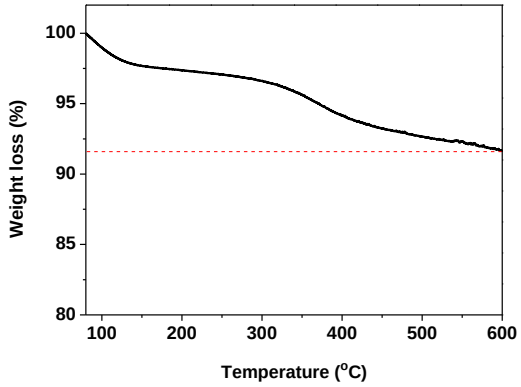

Figure 2.2. TG analysis for oxygen stabilized C/S composite.

The distribution of carbon and sulfur in a secondary C/S particle (Fig. 2.1c) were analyzed using energy dispersive X-ray spectroscopy (EDS), as shown in Fig. 2.1d and 2.1e, in which carbon homogenously overlaps with sulfur, suggesting a uniform distribution of carbon and sulfur throughout the composite. The chemical composition of the composite was determined using the elemental analysis to be 56% of carbon, 38% of sulfur and 5% of oxygen, while thermogravimetric analysis (TGA) was also used to determine sulfur-content, which indicates that there is only 8% weight loss after heating up to 600 ^{o}C as shown in Fig. 2.2, much lower than the sulfur content determined using elemental analysis. Since TGA actually only detects the sulfur species that are simply chemisorbed in micropores and can be evaporated due to heat, the extra sulfur-content as determined by elemental analysis should reflect the fact that a substantial amount of sulfur in the C/S composite may be chemically bonded to the oxygen-functionalities (5%) in carbonaceous host, via either covalent or ionic interactions.

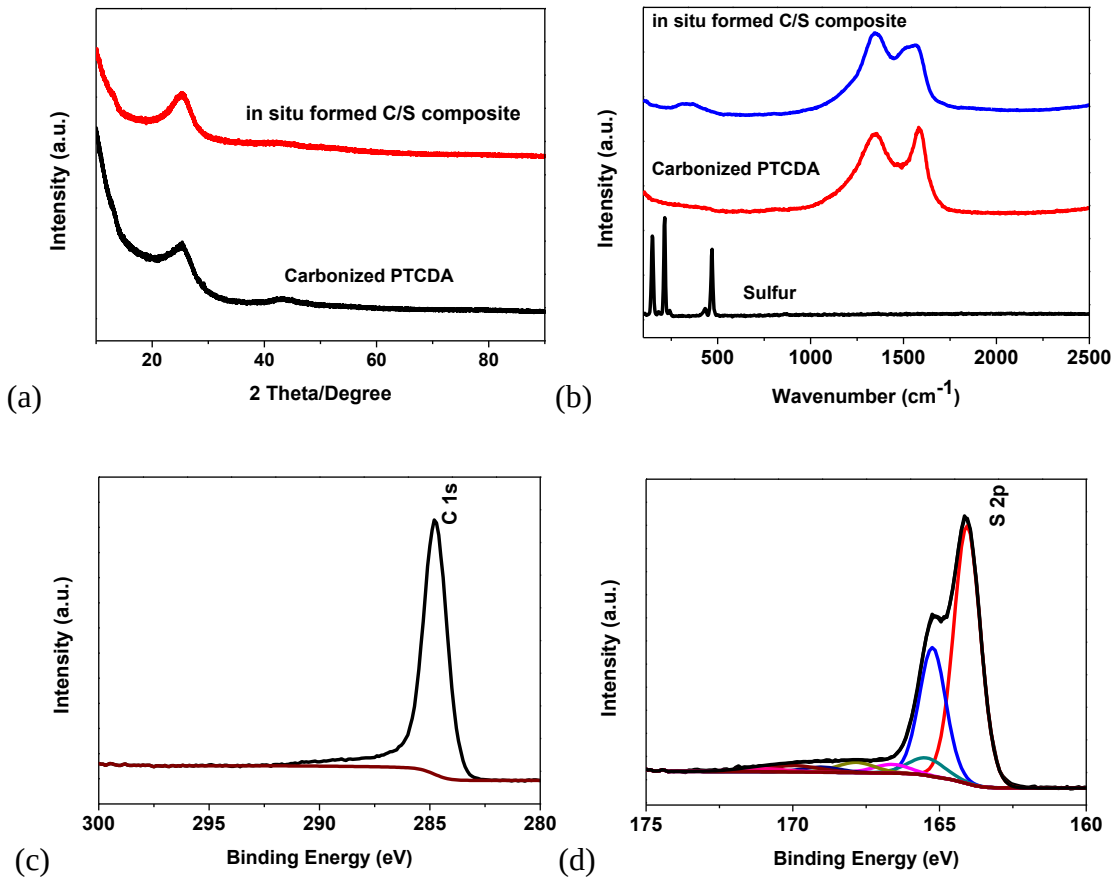

Figure 2.3. XRD patterns (a) and Raman spectra (b) for pristine S, carbonized neat PTCDA and oxygen-stabilized C/S composites; XPS spectra of oxygen stabilized C/S composites: (c) C 1s, (d) S 2p.

The nature of bonding between oxygen and sulfur in C/S composites are further characterized by X-ray diffraction (XRD), Raman spectroscopy and X-ray photoelectron spectroscopy (XPS) (Fig. 2.3). The carbonized neat PTCDA and oxygen-stabilized C/S composites show similar XRD patterns (Fig. 2.3a), where a broad peak at 26 degree indicates the existence of graphitic carbon in both samples. No sulfur peak is observed in C/S composites, suggesting that sulfur species fails to crystallize and remains in amorphous form, perhaps due to the strong interaction with O-functionalities. Raman spectra of carbonized neat PTCDA and oxygen-stabilized C/S composites in Fig. 2.3b show two broad peaks at 1345 cm^{-1} and 1595 cm^{-1}, respectively, confirming the co-

existence of disordered graphite (D band) and crystalline graphite (G band). The valence states of sulfur in the composite could be determined from high resolution XPS, as shown in Fig. 2.3c and 2.3d, where elemental C 1s at 284.8 eV was used as reference binding energy. The asymmetry of C 1s spectra demonstrates the presence of both sp^2 and sp^3 carbon, which are ascribed to graphitic carbon and amorphous carbon in the composite, respectively. A host of peaks corresponding to the S 2p spectra are detected between 164 eV and 170 eV, among which the twin peaks located at 164.0 eV and 165.2 eV should be attributed to the S $2p_{3/2}$ and S $2p_{1/2}$ of sulfur species containing S-S bond, probably arising from short-chain S_x ($x \leq 8$), while a host of small peaks at higher binding energies starting from 165.5 eV should arise from sulfur in strong interaction with oxygen in varying manners (S-O, S=O etc), which were results of the reaction between sulfur and oxygen functionalities in PTCDA. The Brunauer-Emmett-Teller (BET) analysis (Fig. 2.4) revealed that C/S composite thus made has a dense structure with a surface area of 23.4227 m^2 g^{-1}. From the shape of N_2 adsorption/desorption isotherms and pore-size distribution, one can conclude that the composite is not a porous structure, which might suggest that sulfur filled the micropores of carbon host and is tightly bonded to the carbon matrix.

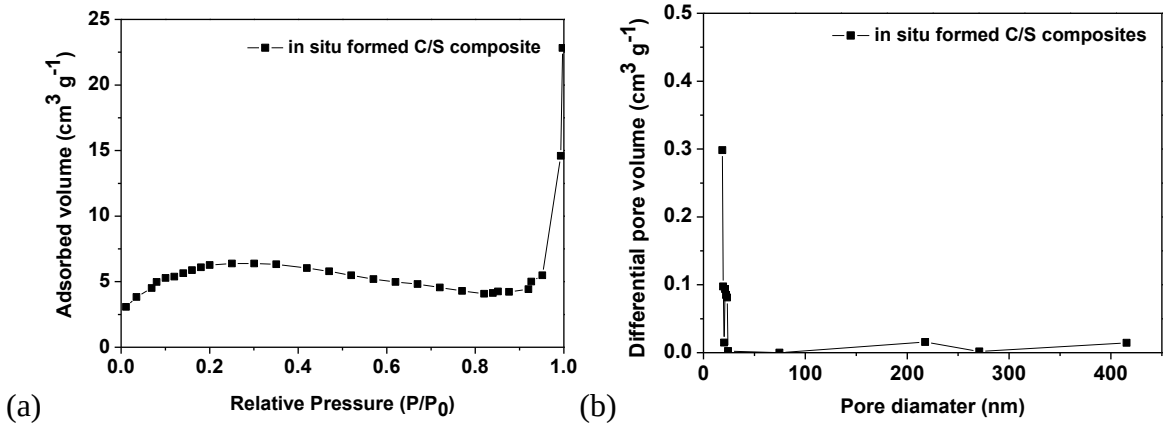

Figure 2.4. N_2 adsorption/desorption isotherms (a) and pore-size distribution curve (b) of oxygen stabilized C/S composite.

2.3.2 Electrochemical Performance

The electrochemical performances of oxygen-stabilized C/S composites are evaluated in coin cells with Li metal as anode. Fig. 2.5a shows their galvanostatic voltage profiles when cycled between 1.0 V ~ 3.0 V. In the first cycle, a short plateau at 2.4 V represents the reduction of S_x to Li_2S_x, followed by a long plateau at 1.6 V corresponding to further reduction of shorter S chains to Li_2S_2/Li_2S. During the delithiation a rather slopping plateau at 2.0 V is observed . In the 2nd cycle, the short plateau at 2.4 V completely disappears, indicating that Li_2S_x is not stable in the electrolyte with carbonate solvents and $LiPF_6$. Zhang et al. have reported that polysulfides can react with $LiPF_6$, resulting in rapid capacity fading of sulfur cathode in carbonate based electrolyte [105]. The long plateau at 1.6 V shifts to a slopping plateau centered at 1.7 V owing to the release of strain/stress in C/S composite in the first cycle. After 100 cycles, the strain/stress of C/S composite is completely absorbed, and the slopping plateau shifts to 1.8 V, which is the intrinsic reaction potential for the lithiation of short-chain sulfur molecules. The corresponding delithiation plateau is centered at 2.2 V after 100 cycles. Cyclic voltammograms in Fig. 2.5b show that there are two cathodic peaks at 2.4 V and 1.2 V and one anodic peak at 2.2 V in the first cycle, which coincide with galvanostatic tests. In the subsequent cycles, the cathodic peak at 2.4 V disappears, and both cathodic peak at 1.2 V and anodic peak at 2.2 V shift to positive values, which is consistent with charge/dicharge behavior in Fig. 2.5a. The oxygen-stabilized C/S composites maintain a reversible capacity of 508 mAh/(g of S) at a current density of 150 mA/g for 2000 cycles with a Coulombic efficiency close to 100% (Fig. 2.5c); however, poor electrochemical performance was demonstrated by the same composite in LiTFSI-DOL/DME, which is more typical electrolyte used in literature (Fig. 2.6). This anomaly is consistent with earlier report that a unique interphase can only be formed in carbonate-based electrolytes [106].

An excellent rate capability is also achieved by the composites as indicated by Fig. 2.5d. When current density increases from 60 mA g^{-1} to 6 A g^{-1}, the reversible capacity remains at 180 mAh/(g of S), which is over 30% of its initial capacity (580 mAh/(g of S)). After current density returns to 60 mA g^{-1}, the reversible capacity recovers its initial level without any kinetic delay.

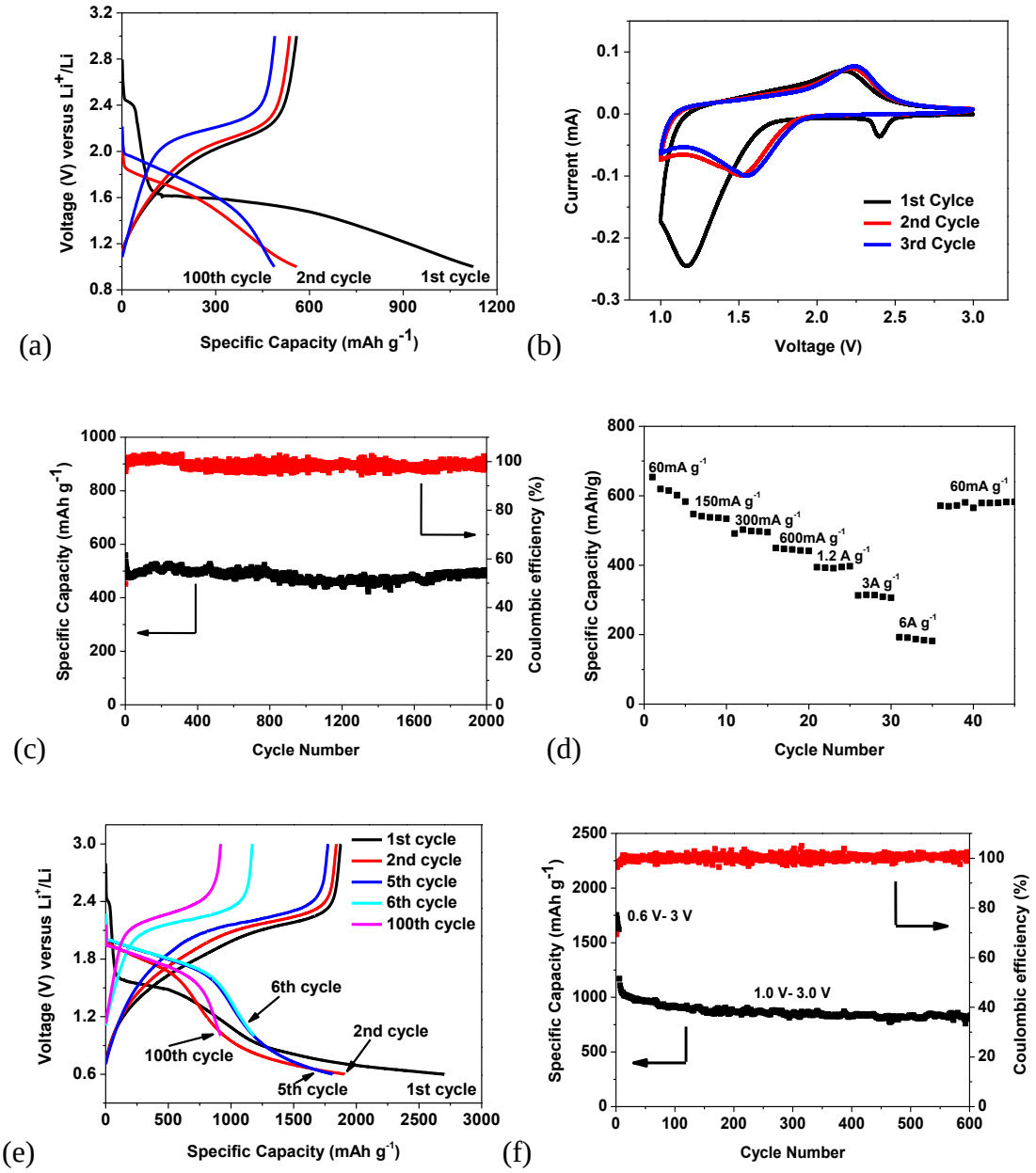

Figure 2.5. Electrochemical performance of oxygen-stabilized C/S composites. (a) The galvanostatic charge–discharge curves between 1.0 V and 3.0 V versus Li/Li^+; (b) Cyclic

voltammograms at 0.1 mV s^{-1} in the potential window from 1.0 V to 3.0 V versus Li/Li^+; (c) Delithiation capacity and coulombic efficiency versus cycle number at the current density of 150 mA g^{-1}; (d) Rate performance at various C-rates; (e) The galvanostatic charge–discharge curves between 0.6 V and 3.0 V in initial 5 cycles and between 1.0 V and 3.0 V after 5 cycles; (f) Delithiation capacity and coulombic efficiency versus cycle number at the current density of 150 mA g^{-1} in the cutoff window from 0.6 V to 3.0 V in initial 5 cycles and from 1.0 V to 3.0 V after 5 cycles.

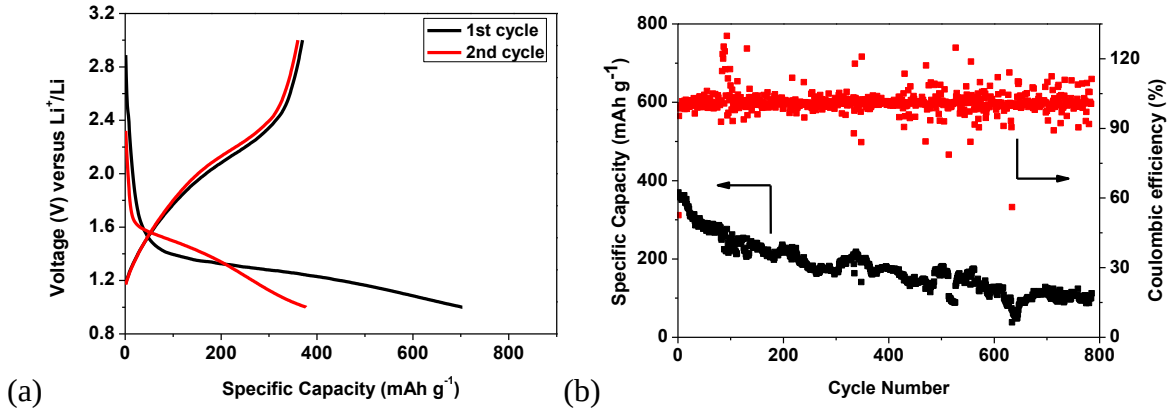

Figure 2.6. Electrochemical performance of oxygen stabilized C/S composite in LiTFSI-DOL/DME electrolyte. (a) The galvanostatic charge–discharge curves between 1.0 V and 3.0 V versus Li/Li^+; (b) Delithiation capacity and coulombic efficiency versus cycle number at the current density of 150 mA g^{-1}.

Despite the excellent cycling stability and rate capability, the low reversible capacity of 508 mAh g^{-1} at a current density of 150 mA g^{-1} suggests that only part of the confined sulfur participates in the cell reaction and hence falls short of the promise of sulfur-based cathode. To liberate more sulfur that are harnessed by oxygen functionalities, we subjected the cathode to a pre-lithaition process down to the potential of 0.6 V, in the hope that electrochemical reduction

could break the strong interaction between sulfur and oxygen. The consequence of this deep lithiation is the release of extra sulfur species that are originally immobilized by oxygen and their subsequent electrochemical activity. As shown in Fig. 2.5e and 2.5f, the first five cycles are conducted between 0.6 V and 3.0 V. There are three plateaus observed at 2.4 V, 1.6 V and 0.7 V during the 1^{st} lithiation, while only one plateau centered at 2.0 V is observed during the delithiation immediate after. In the second cycle, the plateau at 2.4 V disappears, while the plateau at 1.6 V shifts to 1.8 V, and the plateau at 0.7 V becomes shorter. In the fifth cycle, the plateau at 0.7 V almost disappears, while the plateau at 1.8 V shifts to 1.9 V and becomes much longer than that in the second cycle. This dynamic change in the voltage profiles reflects that more and more sulfur is released in each cycle from the oxygen immobilization and then becomes available for the electrochemical reactions. After normal cycling protocol is resumed between 1.0 V and 3.0 V starting at the 6^{th} cycle, the newly-increased capacity remains at 1170 mAh/(g of S), which is much higher than the delithiation capacity in Fig. 2.5a and 2.5c, and this capacity rapidly stabilizes to 820 mAh/(g of S), which is retained for 600 cycles with negligible fadings at a Coulombic efficiency close to 100%. To confirm the origin of such extra capacity incurred by pre-lithiation, a blank test was conducted using carbonized neat PTCDA without sulfur by pre-lithiating it in the range of 0.6 V and 3.0 V (Fig. 2.7), where a reversible capacity of only ~60 mAh g^{-1} was observed, probably contributed by Li^+-intercalation into the graphitic portion of the carbon host as well as the surface non-Faradaic processes. Apparently, the extra capacity of > 1000 mAh/(g of S) is not contributed by the carbon host itself.

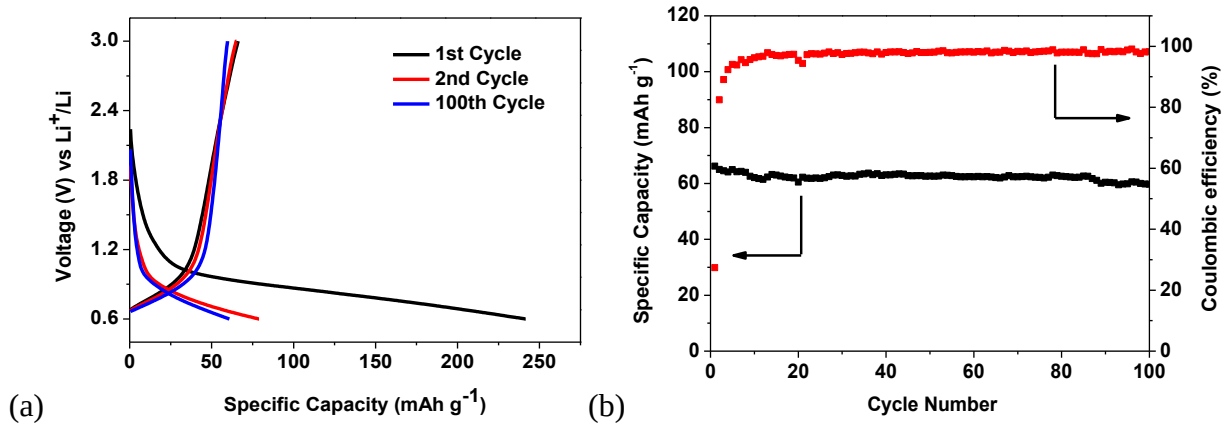

Figure 2.7. Electrochemical performance of carbonized PTCDA. (a) The galvanostatic charge–discharge curves between 0.6 V and 3.0 V versus Li/Li^+; (b) Delithiation capacity and coulombic efficiency versus cycle number at the current density of 150 mA g^{-1}.

2.3.3 Activation Mechanism of Pre-lithiation

To understand the activation mechanism of oxygen-stabilized C/S composites in different potential windows, cyclic voltammetry (CV) and galvanostatic intermittent titration technique (GITT) are carried out. Fig. 2.8a shows the cyclic voltammograms of the composite in different potential windows at a scan rate of 0.5 mV s^{-1}. The cell is initially cycled from 1.0 V to 3.0 V for two cycles, and then the potential window is widened from 0.8 V to 3.0 V for another two cycles, followed by an even wider potential window from 0.5 V to 3.0 V for five cycles with the purpose to fully lithiate S-species in the composite. After that, narrow window from 0.8 V to 3.0 V is resumed for two cycles and then from 1.0 V to 3.0 V for two cycles. Cyclic voltammograms of the last cycle in each potential window are displayed in Fig. 2.8a. With the discharge potential changed from 1.0 V to 0.8 V, and then to 0.5 V, the intensity of redox peaks becomes stronger with each cycle, consistent with the charge/discharge plateaus in Fig. 2.5e that more S is released

from carbon host upon deep discharging. The sharp rise of cathodic peaks at the end of each cathodic scan should be responsible for the formation of SEI layer and the continuous lithiation of sulfur-species immobilized by oxygen in the carbon host. With lower cut-off limit reverts to 0.8 V and 1.0 V, the intensity of redox peaks becomes a little weaker due to the narrowed potential window, but it is much stronger than that of initial scan, indicating that extra sulfur has indeed been liberated from the carbon host during the deep lithiation process. The deeper the discharge, the more sulfur will be released. When the discharge potential maintains at 0.5 V, the released sulfur in each cycle gradually reduce as demonstrated in Fig. 2.9. Fig. 2.9a shows that with a lower cutoff limit of 0.5 V, the sharp CV peak at the end of cathodic scan becomes weaker, while the intensity of redox peaks at 1.7 V and 2.3 V increase from the 1^{st} scan to 30^{th} scan. The voltage profiles in Fig. 2.9b also confirms that the slopping plateau below 1.0 V becomes shorter, but the slopping plateau centered at 1.7 V becomes longer upon cycling, further confirming that deep discharging to 0.5 V can release more sulfur from carbon host. The equilibrium potential during lithiation/delithiation process is evaluated by GITT (Fig. 2.10). The oxygen-stabilized C/S electrode is lithiated/delithiated by a series of constant current pulse of 150 mA/g with an equal duration period of 1 h, and then rested for 12 h to reach the equilibrium potential after each current pulse. The colored symbol lines in Fig. 2.8b represent the equilibrium open circuit potentials (OCP). Upon lithiation/delithiation cycles from 0.5 V to 3.0 V, the equilibrium potential shift upward. The slopping potential line change into a plateau center at 1.7 V at the expense of reducing the slopping plateau below 1.0 V. More importantly, the lithiation/delithiation equilibrium OCP plateaus centered at 2.0 V are extended and shifted to positive values upon cycling, while the equilibrium plateau centered at 0.9 V becomes shorter with each cycle, consistent with the changes of voltage plateaus in Fig. 2.5e. The equilibrium

potential curves of C/S composite change upon cycling, demonstrating that the deep lithiation process has changed the thermodynamics of C/S composite instead of kinetics. This fundamental change is due to the generation of new sulfur species produced by the reaction between Li^+ and oxygen-stabilized sulfur. The reaction resistance of C/S electrode during lithiation/delithiation process is calculated by dividing the overpotential with pulse current amplitude as shown in Fig. 2.8c and 2.8d. Compared to the subsequent charge/discharge cycles, the reaction resistance in the 1st lithiation process is the largest, reflecting the largest strain/stress induced by the strong interaction and physical encapsulation of sulfur with oxygen-rich carbon matrix. The reaction resistance slightly decreases after 50% of lithiation, while the reaction resistance remarkably increases at the end of delithiation. The difference of reaction resistance during lithiation/delithation may be attributed to the electrical contact resistance change caused by the volume expansion/shrinkage during lithiation/delithiation process. Hence, both CV and GITT results confirm that pre-lithiating the composite at low potentials liberates sulfur species by changing their chemical valence states.

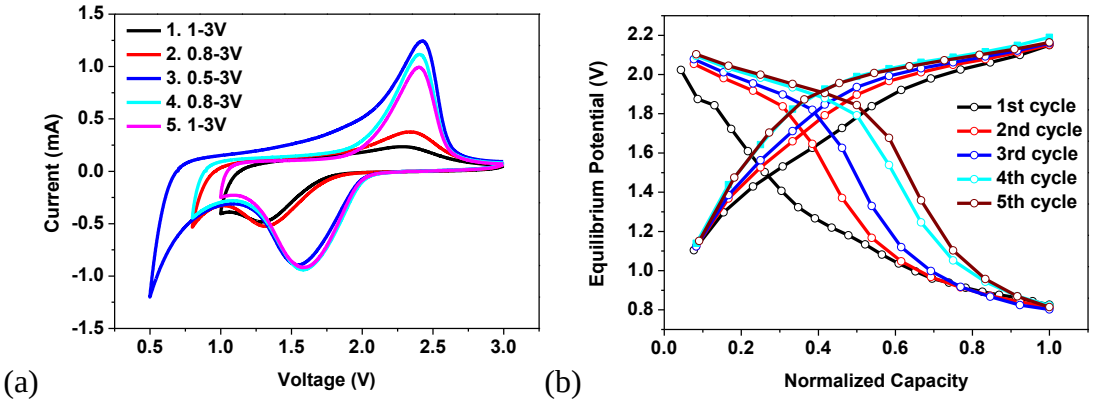

(a) (b)

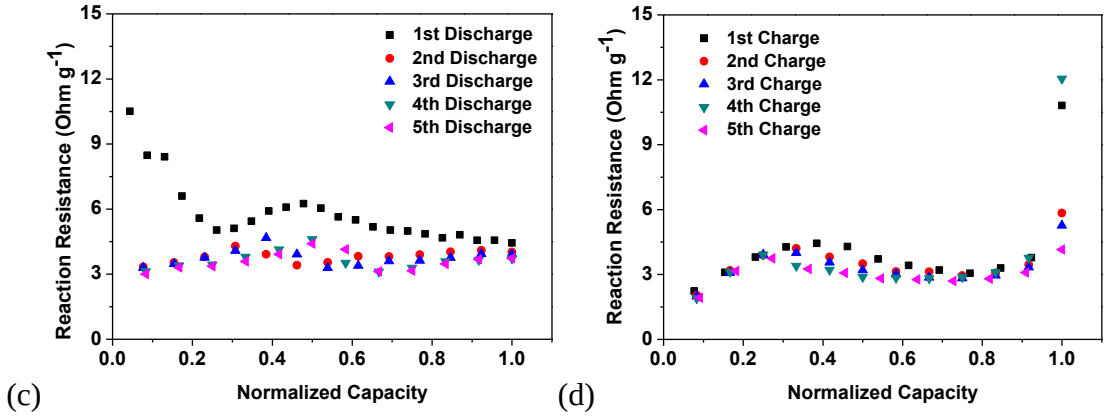

Figure 2.8. (a) Cyclic voltammograms of oxygen-stabilized C/S composites in different potential windows versus Li/Li^+; (b) Equilibrium potential versus normalized capacity during GITT measurement; Reaction resistance of oxygen stabilized C/S composites during GITT measurement from 1^{st} discharge to 5^{th} discharge (c) and from 1^{st} charge to 5^{th} charge (d). Note: Current density was calculated based of the total weight of oxygen stabilized C/S composite; The charge/discharge capacity was normalized by dividing the discharge capacity.

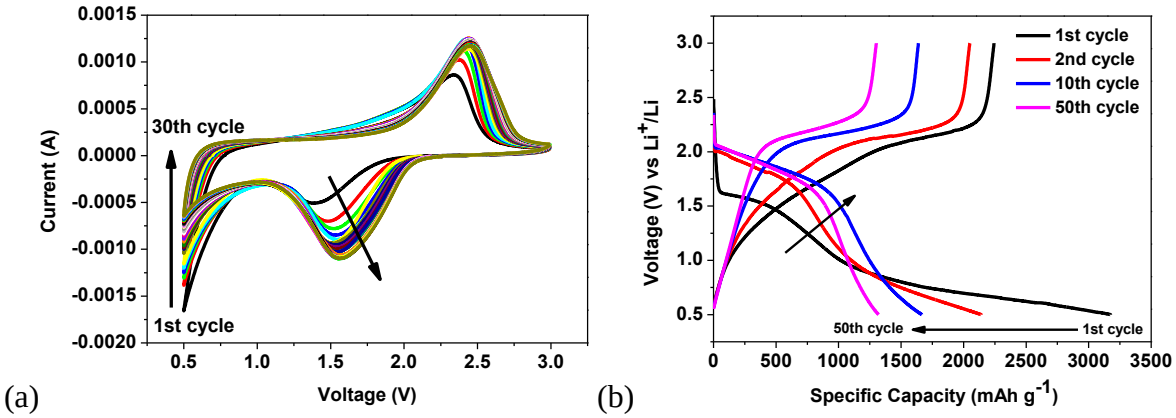

Figure 2.9. (a) Cyclic voltammograms of oxygen stabilized C/S composites in the cutoff window from 0.5 V to 3.0 V versus Li/Li^+; (b) The galvanostatic charge–discharge curves between 0.5 V and 3.0 V versus Li/Li^+.

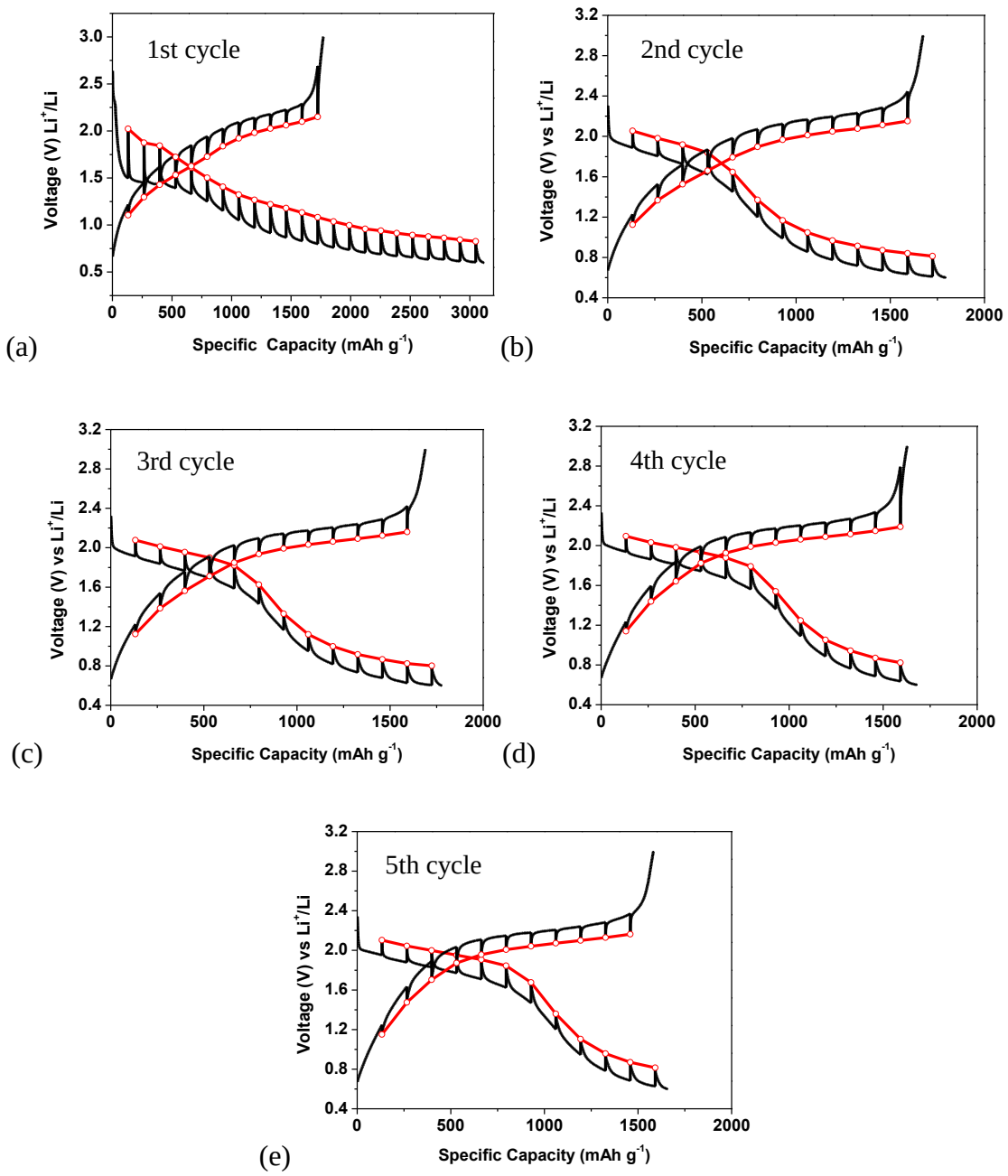

Figure 2.10. Potential response of oxygen stabilized C/S electrodes in the first cycle (a), second cycle (b), third cycle (c), fourth cycle (d) and fifth cycle (e) during GITT measurements.

Electrochemical impedance spectroscopy is also used to monitor the impedance evolution upon cycling. The depressed semi-circle in the high frequency area represents interphasial resistance, including contact resistance of the composite particles, SEI layer and charge transfer resistance,

while the low frequency line stands for ion diffusion resistance in the composite particles. As shown in Fig. 2.11, the interphasial resistances is ~250 ohm for the fresh cell, while it increases to ~700 ohm once discharged to 1.5 V, due to the lithiation of sulfur in the composite. When the discharge lower limit becomes 1.0 V, two depressed semi-circle can be observed, and the interphasial resistance increases to ~900 ohm, owing to the growth of SEI layer and further lithiation of sulfur in the composite. The first semi-circle should represent the sum resistance of SEI layer and particle-to-particle resistance for the composite, while the second semi-circle stands for the charge transfer resistance. When the cell is further discharged to 0.6 V, the interphasial resistance decreases to 720 ohm. Though the resistance of SEI layer increases upon further discharging, contact resistance of the composite particles decreases due to the volume expansion, and more S is released by the lithiation process so that more active sites for sulfur and lithium ions are available, which helps reduce the charge transfer resistance. After the cell is charged to 3.0 V, the original value of ~250 Ohm interphasial resistance was restored, representing an ideal state of both excellent conductivity and good integrity of the electrode. In the following 5 cycles, the interphasial resistance maintains this initial value, ensuring the excellent cycling stability of the sulfur-based cathode.

Besides the cell chemistry coupled with Li anode, the obtained oxygen-stabilized C/S composites is also coupled to Na anode. The electrochemical performance of the composites is measured between 0.8 V and 2.5 V versus Na/Na^+. As shown in Fig. 2.12a, the sodiation and desodiation plateaus are centered at 1.4 V and 1.8 V, respectively, which are 0.4 V lower than the Li counterparts. Cyclic voltammograms in Fig. 2.12b confirm that there is only one pair of redox peaks at 1.15 V and 1.7 V respectively during sodiation/desodiation, revealing that the cell reaction consists of a one step mechanism between sulfur and Na in this composite. The oxygen-

stabilized C/S composites deliver a reversible capacity of 500 mAh/g at the current density of 150 mA/g initially, which reduces to 400 mAh/g after 150 cycles as shown in Fig. 2.12c. The rate capability of the composite is also measured by increasing the current density every five cycles, as shown in Fig. 2.12d, in which the desodiation capacity decreases from 550 mAh/g to 130 mAh/g, when the current density increases by 20 times from 60 mA/g to 1.2 A/g. This combination of decent cycling stability and rate capability makes the electrochemical couple between Na and oxygen-stabilized C/S composite a promising cell chemistry for Na/S batteries.

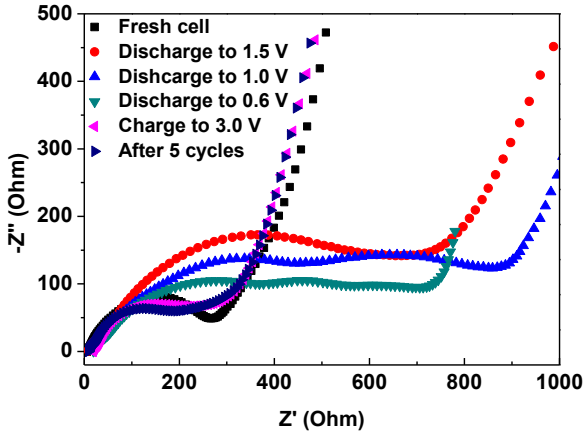

Figure 2.11. Impedance analysis for oxygen stabilized C/S cell before test and during discharge to 0.6 V and charge to 3.0 V.

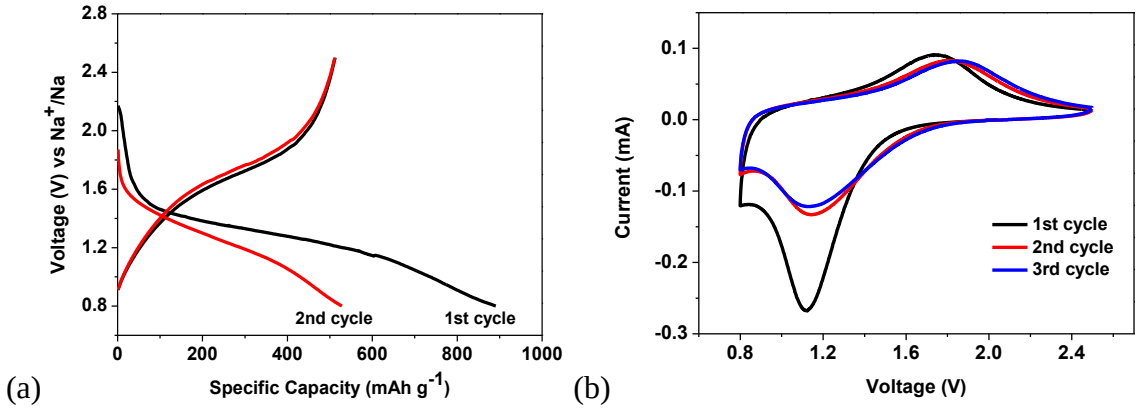

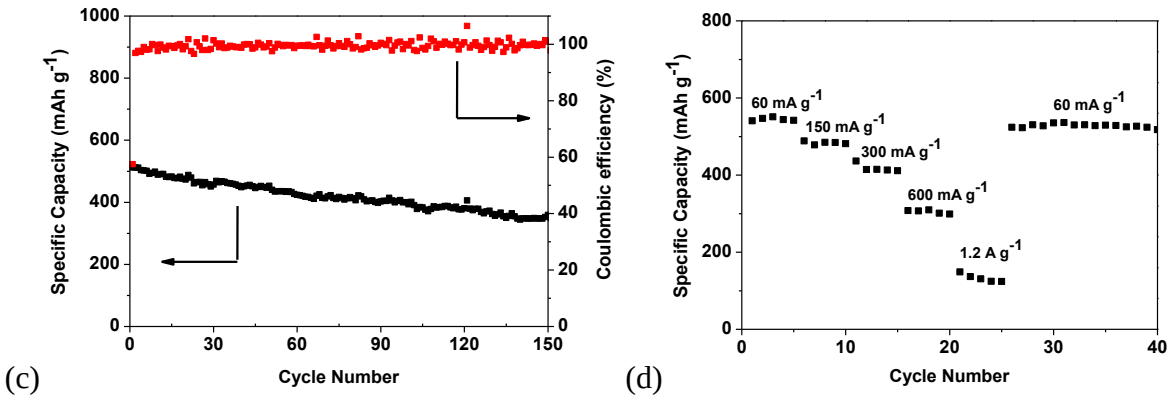

Figure 2.12. Electrochemical performance of oxygen-stabilized C/S composites. (a) The galvanostatic charge–discharge curves between 0.8 V and 2.5 V versus Na/Na^+; (b) Cyclic voltammograms at 0.1 mV s^{-1} in the potential window from 0.8 V to 2.5 V versus Na/Na^+; (c) Desodiation capacity and coulombic efficiency versus cycle number at the current density of 150 mA g^{-1}; (d) Rate performance at various C-rates.

2.4 Conclusion

The oxygen-stabilized C/S composites are synthesized by annealing the mixture of sulfur and perylene-3, 4, 9, 10-tetracarboxylic dianhydride in a sealed vacuum glass tube. The resulting composites exhibit superior electrochemical performance for both Li and Na cells. In the former, a reversible capacity of 508 mAh/g is maintained in carbonate based electrolyte for 2000 cycles when cycled between 1.0 V and 3.0 V. Furthermore, it is discovered that that extra reversible capacity could be obtained if pre-lithaiting the composite at low potentials (0.6 V), as evidenced by the stably delivered 820 mAh/(g of S) for over 600 cycles and a Coulombic efficiency close to 100%. Based on spectroscopic studies, we attributed the extra capacity to the sulfur-species liberated by the pre-lithiation from their strong interaction with oxygen functionalities in the carbon host. Similar excellent electrochemical performance is also achieved when the C/S

composite is coupled with Na anode, where a reversible capacity of 400 mAh g^{-1} is maintained for 150 cycles. Therefore, the oxygen-stabilized C/S composites make promising sulfur-cathode materials for both Li-S and Na-S batteries.

Chapter 3 Selenium@Porous Carbon Composite with Superior Lithium and Sodium Storage Capacity

3.1 Introduction

High-energy lithium ion batteries and low-cost sodium-ion batteries are the most promising candidates for emerging electric vehicles and large-scale renewable energy storage, respectively. In current technology, the energy density of lithium ion batteries is mainly limited by the cathode material [22, 107]. The same problem also impedes the development of sodium-ion batteries [108]. Therefore, development of high energy density cathodes for both Li-ion and Na-ion batteries is critical for the success in electric vehicle and renewable energy storage.

Sulfur is the only cathode material that has comparable capacity with Si anode material for Li-ion batteries. However, sulfur cathodes face three major challenges, which limit its practical applications [9, 10]: (1) sulfur has low electronic conductivity; (2) sulfur undergoes large volume change during lithiation/delithiation; (3) high-order polysulfide intermediates are soluble in carbonate electrolytes. The dissolution of high-order polysulfides is essential for progressive lithiation of S_8 due to the non-conductive nature of elemental S_8 and its reduction products [105]. However, the dissolved high-order polysulfides also cause a shuttle reaction, because dissolved high-order polysulfides in the cathode side can diffuse to and chemically react with Li anode to either form soluble low order polysulfides and then transport back to cathode side, causing a shuttle reaction, or form an insoluble dense sulfides (Li_2S and Li_2S_2) layer on Li anode, increasing the resistance of Li anode. The shuttle reaction and deposition of Li_2S on Li anode significantly reduce Coulombic efficiency and cycle stability of sulfur cathodes for both lithium-

and sodium-sulfur batteries [109, 110]. Most effective ways to alleviate dissolution and shuttle reaction are (1) to physically trap the high-order polysulfides inside host materials (mostly conductive carbon) [111, 112], (2) to directly form insoluble low-order sulfides [102], and (3) to manipulate the solubility of polysulfides by selection of different electrolytes [65, 66]. Our previous work showed that small sulfur molecules obtained at a high temperature (500 ^{o}C) can be infused into carbon nanotubes and stabilized to room-temperature [9]. The small sulfur/carbon nanotubes composite can directly form insoluble low-order polysulfides, thus avoiding the dissolution and shuttle reaction.

As a congener of sulfur, selenium has similar chemical properties, but higher electronic conductivity. Selenium can also react with lithium and sodium ions to generate selenides [13]. Although the gravimetric capacity of selenium cathode (678 mAh g^{-1}) is lower than sulfur (1672 mAh g^{-1}), the volumetric capacity of selenium (3253 Ah L^{-1} based on 4.82 g cm^{-3}) is comparable to sulfur (3467 Ah L^{-1} based on 2.07 g cm^{-3}). In addition, selenium has 20 orders of magnitude higher electrical conductivity than sulfur. These features make it a promising cathode material for both lithium- and sodium-ion batteries. However, similar to sulfur, the selenium cathodes also face the dissolution issue of high-order polyselenides, resulting in fast capacity fading and low Coulombic efficiency.

In this study, using the same strategy of S/C cathode in Li-sulfur batteries, we broke Se_{12} into Se_8 at a high temperature of 600 ^{o}C and impregnated Se_8 into mesoporous carbon to alleviate the dissolution of polyselenides. The Se_8/C cathode in carbonate-based electrolyte demonstrated excellent electrochemical performance in both Li-ion and Na-ion batteries. It can deliver reversible capacity of 480 mAh g^{-1} in lithium-ion batteries, and maintains 1000 cycles without any capacity loss. The capacity of the Se/C composite for sodium ion batteries is as high as 485

mAh g^{-1} in the first cycle, and retains 340 mAh g^{-1} after 380 cycles. The Se_8/mesoporous carbon composites also show excellent rate capability. As the current density increased from 0.1 C to 5 C, the capacity retained about 46% in Li-ion batteries and 34% in Na-ion batteries. The charge/discharge mechanism of Se_8/C was investigated by comparing the electrochemical behavior of Se_8/C with 1M $LiPF_6$ in a mixture of ethylene carbonate/diethyl carbonate (EC/DEC, 1:1 by volume) and 1M LiTFSI in tetraethylene glycol dimethyl ether (TEGDME) electrolytes. The excellent battery performance of Li-Se and Na-Se batteries demonstrates that selenium is a promising alternative to sulfur and currently used cathode materials for large scale and high-energy applications.

3.2 Experimental Section

Synthesis of mesoporous carbon spheres. All chemicals were purchased from Sigma Aldrich and used as received. 0.66 g resorcinol (R), 0.38 g triblock copolymer (Pluronic F127) and 0.66 g HCl aqueous solution were dissolved in a mixture of 4.35 g distilled water and 5.75 g ethanol alcohol, where triblock copolymer and HCl functioned as soft-template and catalyst, respectively. When a clear solution appeared, 0.8 g 37% formaldehyde (F) aqueous solution was added. After 1 hour vigorous stirring, the solution was transferred into a teflon-lined autoclave and sealed. It was heated to 150 °C and maintained for 10 hours. After naturally cooling to room temperature, a light brown power was collected and dried in air for 24 hours, and then followed by further curing in an oven at 100 °C for 24 h in air. Finally, the resulting precursor was carbonized in flowing argon at 600 °C for 5 h, with a heating ramp of 2 °C min^{-1} to achieve mesoporous carbon spheres.

Synthesis of selenium impregnated carbon composite. Selenium and mesoporous carbon were mixed with a ratio of 1:1 by weight and sealed in a glass tube under vacuum. The sealed glass tube is annealed in an oven at 600 °C for 5 h. Selenium impregnated carbon composite was collected as black powder.

Material Characterizations. Scanning electron microscopy (SEM) images were taken by Hitachi SU-70 analytical ultra-high resolution SEM (Japan); Transmission electron microscopy (TEM) images were taken by JEOL (Japan) 2100F field emission TEM; Thermogravimetric analysis (TGA) was carried out using a thermogravimetric analyzer (TA Instruments, USA) with a heating rate of 10 °C min^{-1} in argon; X-ray diffraction (XRD) pattern was recorded by Bruker Smart1000 (Bruker AXS Inc., USA) using CuKα radiation; BET specific surface area and pore size and volume were analyzed using N_2 absorption on Micromeritics ASAP 2020 (Micromeritics Instrument Corp., USA). Raman measurements were performed on a Horiba Jobin Yvon Labram Aramis using a 532 nm diode-pumped solid-state laser, attenuated to give ~900 μW power at the sample surface.

Electrochemical measurements. The selenium impregnated carbon composite was mixed with carbon black and sodium alginate binder to form a slurry at the weight ratio of 80:10:10. The electrode was prepared by casting the slurry onto aluminum foil using a doctor blade and dried in a vacuum oven at 60 °C overnight. The same method is used to fabricate pure selenium electrode material. Coin cells for lithium selenium batteries were assembled with lithium foil as the counter electrode, 1M $LiPF_6$ in a mixture of ethylene carbonate/diethyl carbonate (EC/DEC, 1:1 by volume) or 1M LiTFSI in tetraethylene glycol dimethyl ether (TEGDME) as the electrolyte, and Celgard®3501 (Celgard, LLC Corp., USA) as the separator. Coin cells for sodium selenium batteries were assembled with sodium foil as the counter electrode, 1 M $NaClO_4$ in a mixture of

ethylene carbonate/dimethyl carbonate (EC/DMC, 1:1 by volume) as the electrolyte, and Celgard®3501 (Celgard, LLC Corp., USA) as the separator. Cells with pure selenium electrodes were also fabricated using the same procedure. Electrochemical performance was tested using Arbin battery test station (BT2000, Arbin Instruments, USA). Capacity was calculated on the basis of the mass of selenium in selenium impregnated carbon composite. Cyclic voltammogram was recorded using Solatron 1260/1287 Electrochemical Interface (Solartron Metrology, UK) with a scan rate of 0.1 mV/s.

3.3 Results and Discussion

Figure 3.1a shows the SEM image of the mesoporous carbon. The mesoporous carbon has a spherical morphology with particle size of a couple of micrometers. The Brunauer–Emmett–Teller (BET) analysis shows that mesoporous carbon has high porosity of 0.2 $cm^3 g^{-1}$ and large surface area of 462 $m^2 g^{-1}$. The average pore size in mesoporous carbon is about 1.6 nm.

As revealed in Figure 3.1b, no morphology change is observed after selenium is infused into the mesoporous carbon spheres, suggesting that most of the Se is filled inside the mesoporous carbon. The infusion of Se into mesopores of carbon is confirmed by the drastic decrease in surface area from 462 $m^2 g^{-1}$ for as-prepared samples to 5 $m^2 g^{-1}$ after Se infusion, while the average pore size increases from 1.6 nm to 4.1 nm, indicating that small pores are occupied by Se. The elemental mapping images (Figure 3.1d and 3.1e) reveal that selenium is uniformly distributed in the mesopores of carbon spheres. It is also confirmed by XRD pattern that selenium in mesoporous carbon maintains its crystal structure (JCPDS File NO. 86-2246).

Thermogravimetric analysis (figure 3.2) shows that the porous C/Se composite contains 30% selenium and 70% mesoporous carbon spheres.

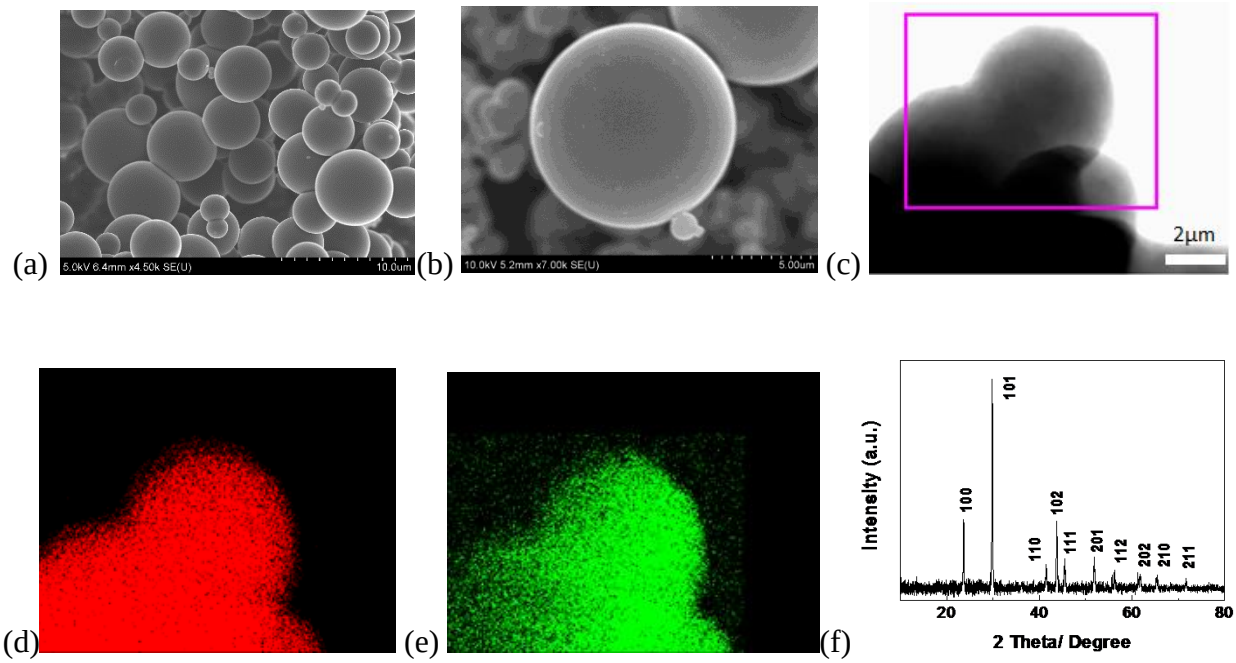

Figure 3.1. SEM images of mesoporous carbon spheres (a) and Se/C composite (b); (c) TEM image of selenium impregnated carbon composite; elemental mapping images of the Se/C composite: Se (d) and Carbon (e); (f) XRD pattern of the Se/C composite.

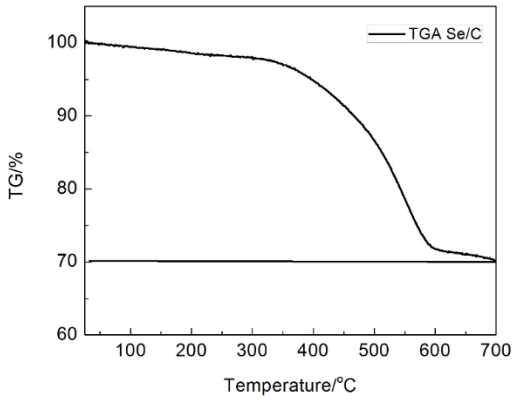

Figure 3.2. Thermogravimetric (TGA) curve of selenium impregnated carbon composite in argon.

The nature of Se in the composite was investigated by Raman spectroscopy. For comparison, porous carbon, pristine Se and 600 ^{o}C-treated Se under the same conditions as those used for Se/C composite were also analyzed (Figure 3.3). The pristine Se displays three peaks at 142 cm^{-1}, 235 cm^{-1} and 458 cm^{-1}, respectively. The peaks at 142 cm^{-1} and 458 cm^{-1} represent Se_{12} with a ring structure [113]; while the 235 cm^{-1} peak is attributed to chain-structured Se [114], indicating the pristine Se is a mixture of Se_{12} ring and chain-structured Se molecules. To examine the effects of the heat-treatment history on the structure of Se, the pristine Se was heat-treated using the same procedure used for the Se/C composite. Compared with the non-treated Se, there is no change in Raman spectra, indicating that the mixture of ring and chain-structured Se is a thermodynamically stable form at room temperature. However, the Se/C composite synthesized at 600 ^{o}C in vacuum doesn't show these three peaks. Instead, a peak at 262 cm^{-1} which is assigned to the ring-structured Se_8 appears [115]. Therefore, the ring-structured Se_8 is stabilized by porous carbon at room temperature. Two strong peaks at 1350 cm^{-1} and 1600 cm^{-1} which represent the D and G bands of mesoporous carbon, respectively, are observed for the composite, showing that the porous carbon is partially graphitized. The Raman spectra reveal that the mesopores of carbon can physically restrict Se in the form of small molecules of Se_8, which is similar to sulfur in S/porous carbon composite [102].

The electrochemical performance of the Se/C composite cathodes was examined for both lithium- and sodium-ion batteries using conventional carbonate-based electrolyte. Figure 3.4 shows cyclic voltammograms (CV) and charge/discharge profiles of Se/C composite cathodes in Li-ion and Na-ion batteries. The CV curves show only one pair of reversible redox peaks for both lithium- and sodium-selenium batteries, indicating that the electrochemical process is a single phase-change reaction. For lithium-selenium batteries, cathodic peak and anodic peak

appear at 1.1 V and 1.8 V, respectively, in the first cycle. After the first cycle, the cathodic peak shifts to a higher voltage of 1.4 V, while the anodic peak remains at 1.8 V. Therefore, there is an electrochemical activation process during the first lithiation. This activation process is associated with the deformation of Se/C composite induced by the volume increase in the first lithiation. Similar phenomena have been reported in high capacity Si, MnO_x and other high-capacity anode materials [116, 117]. The stable anodic and cathodic peaks after the first cycle demonstrate good cycling stability of the Se/C composite. Figure 3.4b shows the CV curves of the Se/C composite in Na-Se batteries measured at a scan rate of 0.1 mV/s between 0.5 – 2.5 V. The Se/C composite in Na-Se batteries also shows similar activation behavior as in Li-Se batteries. The cathodic peak is at 0.7 V in the first cycle and shifts to a higher potential of 1.0 V in subsequent cycles, while the anodic peak at 1.4 V remains constant in all cycles. Therefore, the redox potentials in Na-Se batteries are about 0.4 V lower than those in Li-Se batteries, which is similar to Sn anodes where the potential in Na-ion batteries is also lower than that in Li-ion batteries [33].

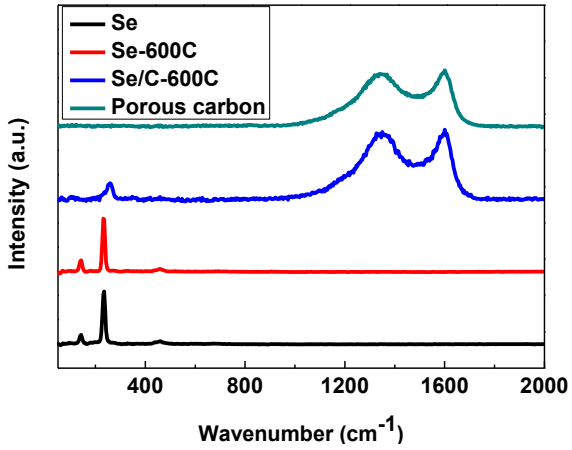

Figure 3.3. Raman spectra of pristine Se, heat-treated Se, Se/C composite and porous carbon.

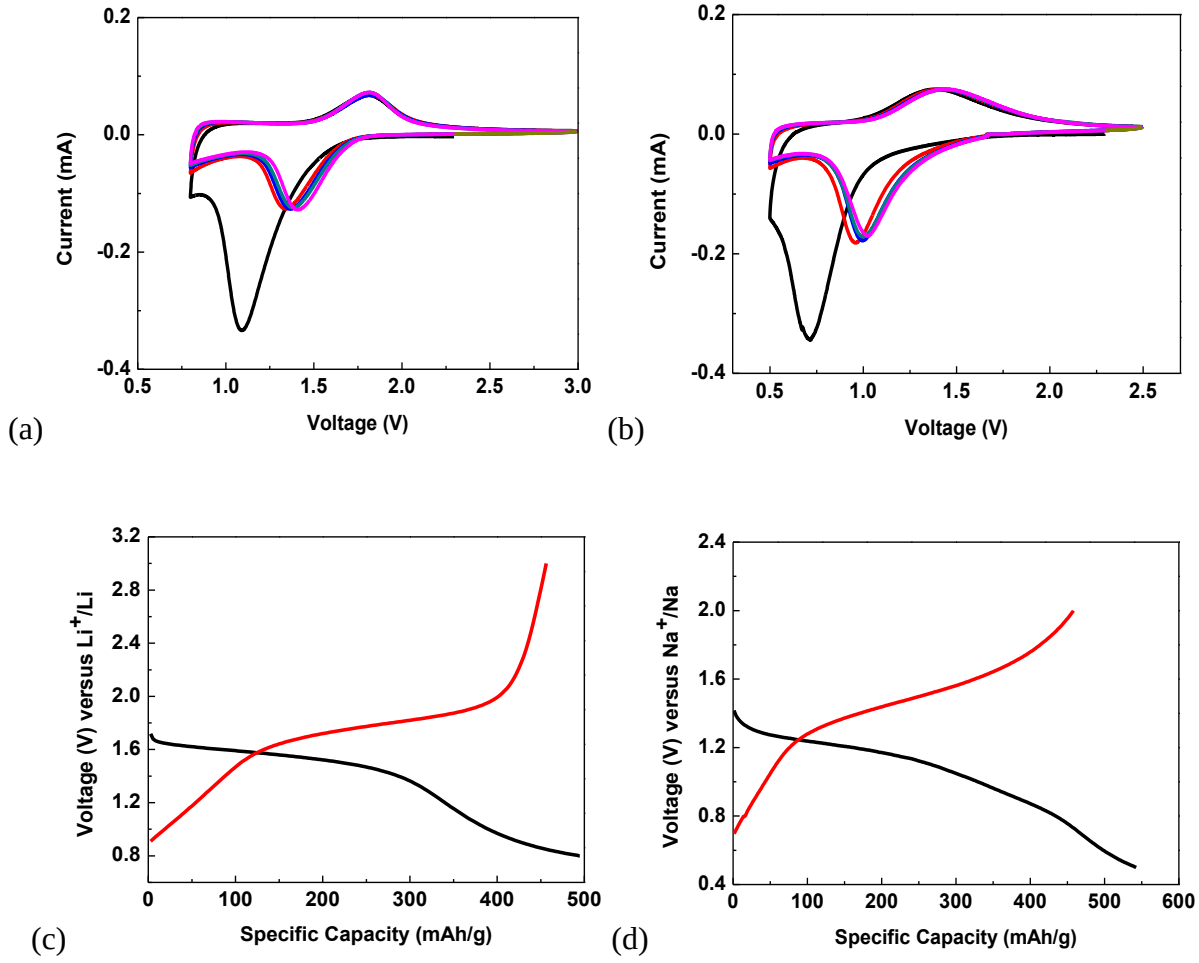

Figure 3.4. Cyclic voltammograms of the Se/C composite in the initial 5 cycles vs Li (a) and Na (b); Charge/Discharge profiles at the 2nd cycle of the Se/C composite in Li-ion (c) and Na-ion batteries (d).

The charge/discharge profiles of Se/C cathodes at a current density of 0.25 C for both Li- and Na-Se batteries are shown in Figure 3.4c and 3.4d, respectively. As demonstrated in CV, ring-structured Se_8 cathodes present only one slope voltage plateau in both Li-ion and Na-ion batteries, which is in agreement with Yang's results using the same electyrolyte [67]. This charge/discharge behavior is different from previous reports on chain-structured Se_{12} cathodes [13, 14], where multiple plateaus were displayed. Therefore, the difference in charge/discharge curves

between Se_{12} (a mixture of ring and chain) and Se_8 indicates different reaction mechanisms in different electrolytes. The charge/discharge potentials are 1.8/1.6 V in Li-Se batteries, which are 0.4 V higher than those in Na-Se batteries (1.4/1.2 V).

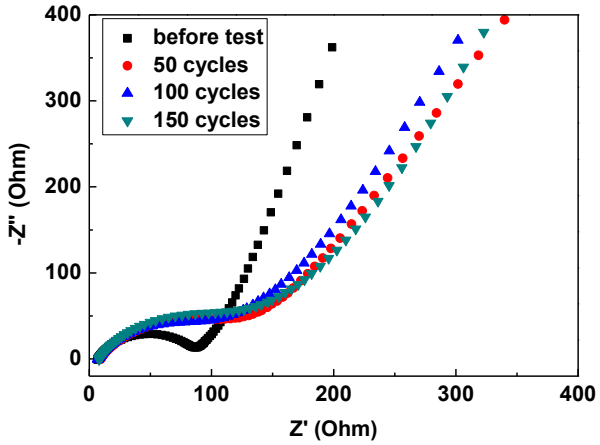

Figure 3.5. Impedance analysis for Se/C cell before test and after cycling.

The (De)lithiation mechanism of Se cathode in ether-based electrolyte has been reported by Cui *etc.*[25] During the lithiation, Se undergoes a two-phase transition process that Se is firstly reduced to soluble high order polyselenide Se_n^{2-} ($n \geqslant 4$), and then the Se_n^{2-} ($n \geqslant 4$) is further reduced to Se_2^{2-} and Se^{2-}. During the delithiation, Li_2Se is firstly oxidized to Se_n^{2-} ($n \geqslant 4$), and then the high order polyselenide is further oxidized to Se. The soluble polyselenides Li_2Se_n ($n \geqslant 4$) in ether-based electrolyte can cause shuttle reaction [13, 14]. In our work, we only observe one plateau of Se/C during lithiation/delithiation in carbonate electrolyte, which is in agreement with Yang's results using the same carbonate electrolyte [67]. Yang *etc.* believed that Se/C in carbonate electrolyte only experience a direct phase change between insoluble chain-structured Se_n to insoluble Li_2Se without formation of soluble lithium polyselenide Li_2Se_n ($n \geqslant 4$) [67]. The difference in lithiation/delithiation mechanism of Se/C between our work and Cui's work is mainly attributed to the use of different electrolyte. The multistep phase transitions of Se/C in

ether-based electrolyte but a single-step reaction in carbonate-based electrolyte was also reported by Amine's group [13, 14]. Although the carbonyl groups of the carbonate electrolyte can react with Se anions, the mesoporous carbon host reduces this side reaction and the stable Se-O layer formed on Li_xSe protects Li_xSe from further reduction (Se-O layer functions as a SEI) as demonstrated by stable interface impedance during charge/discharge cycles (Figure 3.5) and long cycling stability (Figure 3.6).

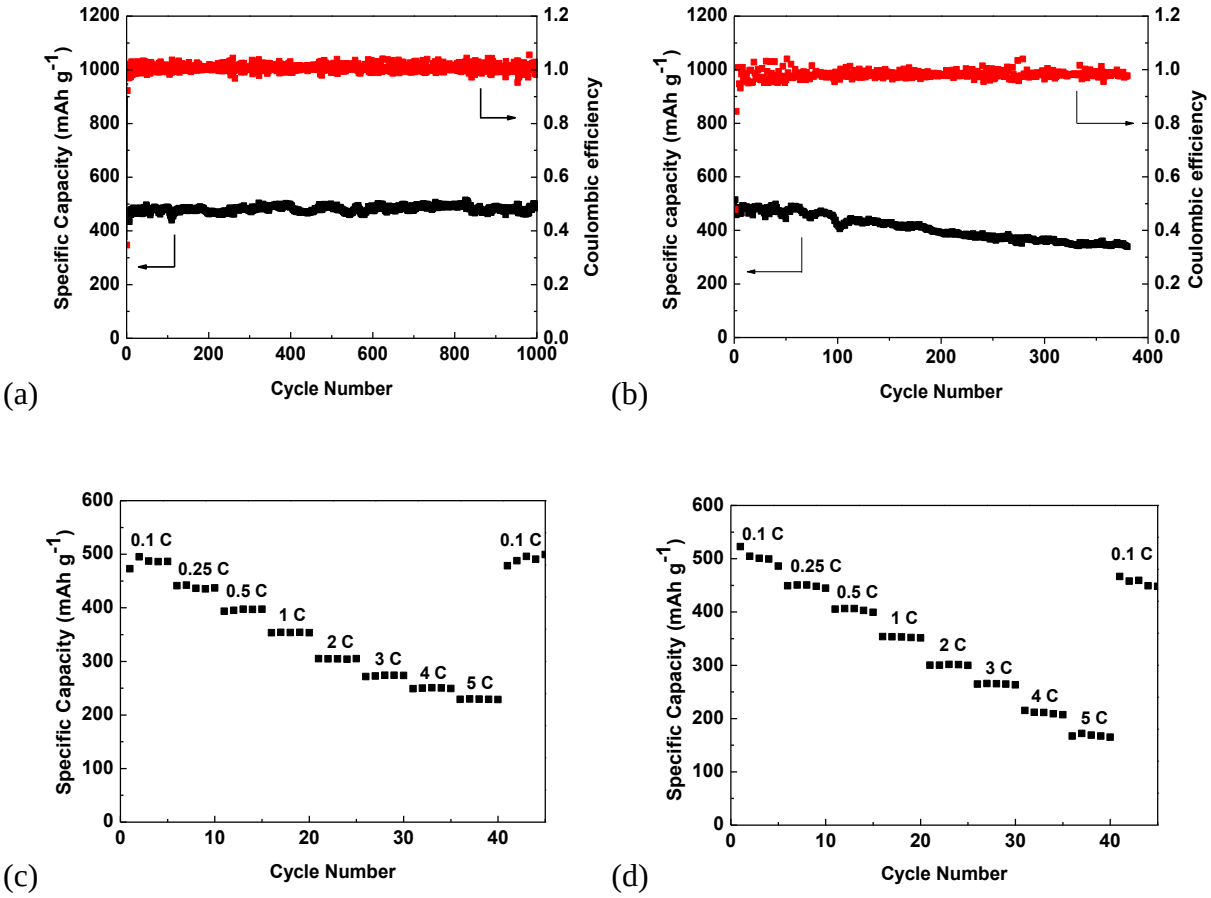

Figure 3.6. Cycling performance of the Se/C composite in Li-ion (a) and Na-ion (b) batteries; Rate capability of the Se/C composite in Li-ion (c) and Na-ion (d) batteries. (1C is defined as 678 mA g^{-1} based on Se)

The cycling stability of the Se/C composite was investigated at a current density of 0.25 C for both Li-Se cells and Na-Se cells (Figure 3.6). The Se/C composite exhibits exceptional cycling stability in both lithium ion and sodium ion batteries. The Li-Se batteries deliver a reversible capacity of 480 mAh g^{-1} in the first cycle and no capacity decline is observed during 1000 cycles, demonstrating superior cycling performance. The Coulombic efficiency of Li-Se batteries is nearly 100%, demonstrating that the shuttle reaction has been effectively suppressed. It is worth noting that good cycling performance is also obtained for Na-Se cells. Normally, electrodes in Na-ion batteries show much worse reaction kinetics, lower capacity and poorer cycling stability than in Li-ion batteries due to the larger diameter of sodium ions compared to lithium ions [42]. In this study, the Se/C composite shows similar reversible capacity (485 mAh g^{-1}) in Na-ion cells to that (480 mAh g^{-1}) in Li-ion cells and retains 340 mAh g^{-1} after 380 cycles which corresponds to 70% of the first cycle.

In addition to the good cycling stability, the Se/C composite also shows high rate capability in both Li-ion and Na-ion batteries. As current density increases from 0.1 C to 5 C, the capacity of Se/C composite in Li-Se batteries only decreases from 500 mAh g^{-1} to 229 mAh g^{-1}, while the capacity of Se/C composite in Na-Se batteries reduces from 500 mAh g^{-1} to 168 mAh g^{-1}. The impedances of Se/C cathodes before cycling, and after 50, 100, 150 cycles are compared in Figure 3.5. All EISs show a depressed semicircle in high frequency region and a slop line in the low frequency region, which is the same to the impedance of Se/C reported by Cui *etc* [67]. The depressed high-frequency semicircle represents interface impedance (including contact impedance of Se/C particles, or SEI impedance, and charge transfer impedance), while the low-frequency line is attributed to ion diffusion in the Se/C particles. The fresh Se/C cell possesses a small interface resistance of ~ 100 Ω and increase to 150 Ω at 50 cycles and stabilize to 150 Ω in

the flowing cycles. The initial increase in interface impedance in the first few cycles may be attributed to volume change of Se/C during charge/discharge cycles and side reaction between polyselenides and carbonate electrolyte [67]. The stable interface impedance during charge/discharge cycles demonstrates that the formation of Se-O layer on polyselenides protects polyselenides from further side reaction. The low and stable interface resistance of Se/C in the charge/discharge cycles demonstrates that Se/C cathodes have fast reaction kinetics, which has been confirmed by the high rate capability (Figure 3.6c), while the stable interface resistance of Se/C during charge/discharge cycles is coincident with the long cycling stability (Figure 3.6a). The exceptional electrochemical performance reveals that the Se/C composite is a promising electrode material for both Li-ion and Na-ion batteries.

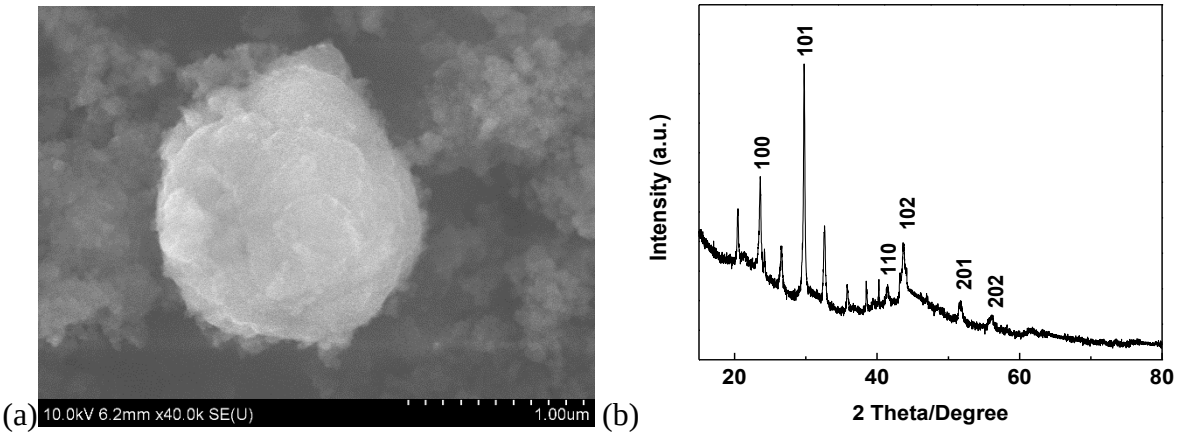

Figure 3.7. (a) SEM image and (b) XRD pattern of the Se/C composite after 1000 cycles in Li-ion batteries.

The good cycling stability of the Se/C composite is believed to be associated with the unique structure of the Se/C composite. Therefore, the morphology and structure of Se/C composite electrodes after 1000 cycles in Li-Se batteries are investigated by SEM, XRD (Figure 3.7) and TEM (Figure 3.8). Compared to Figure 3.1, no obvious morphology change is observed after

1000 cycles (Figure 3.7a), which demonstrates that a robust mesoporous carbon can effectively accommodate the large volume change of Se during lithiation/delithiation. After 1000 cycles, selenium in mesoporous carbon still retains the crystal structure as evidenced by the XRD pattern (Figure 3.7b). The extra peaks in XRD pattern may be assigned to the SEI film. The EDS mapping results (Figure 3.8) exhibit that Se is still uniformly dispersed in porous carbon after 1000 cycles. Similar results are also observed for Na-Se batteries as shown in Figure 3.9.

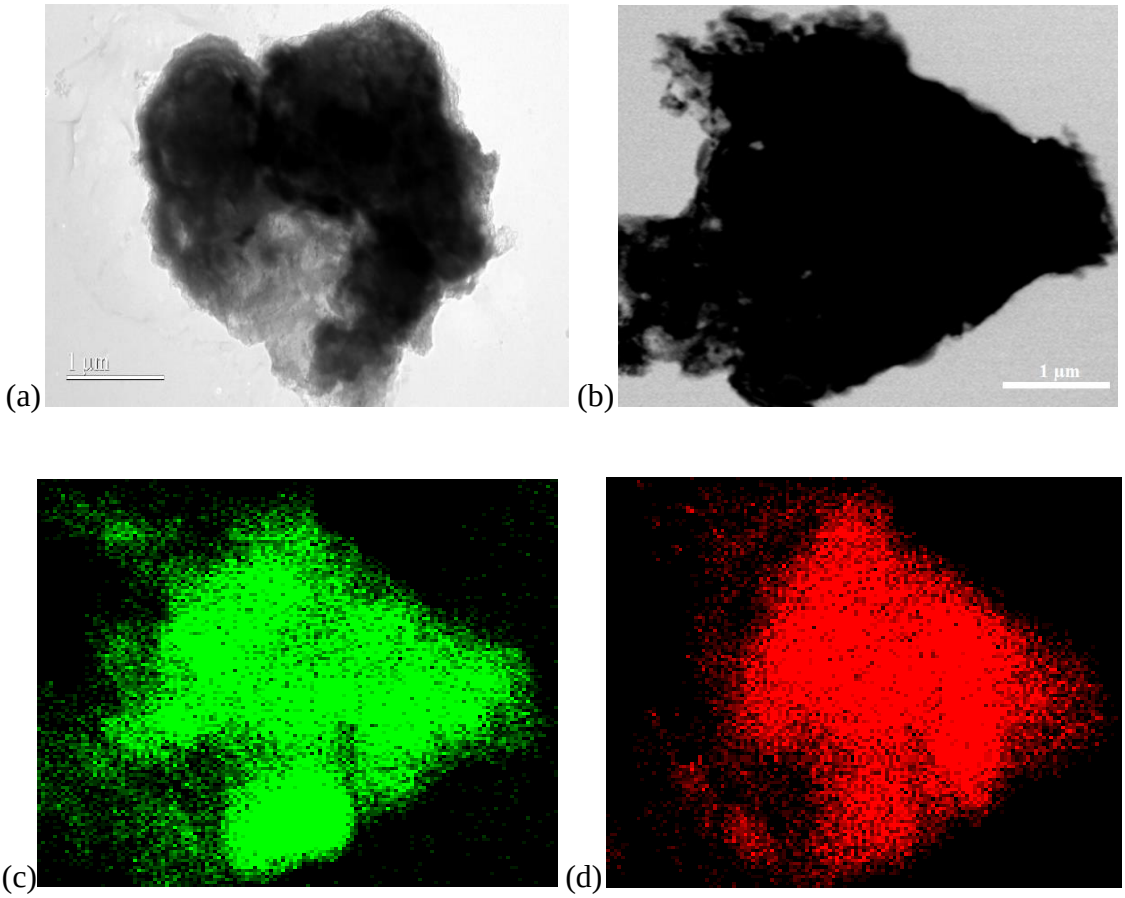

Figure 3.8. (a) TEM image of Se/C composite after 1000 cycles; (b) EDS elemental mapping images of Se/C composite after 1000 cycles, for carbon (c) and selenium (d).

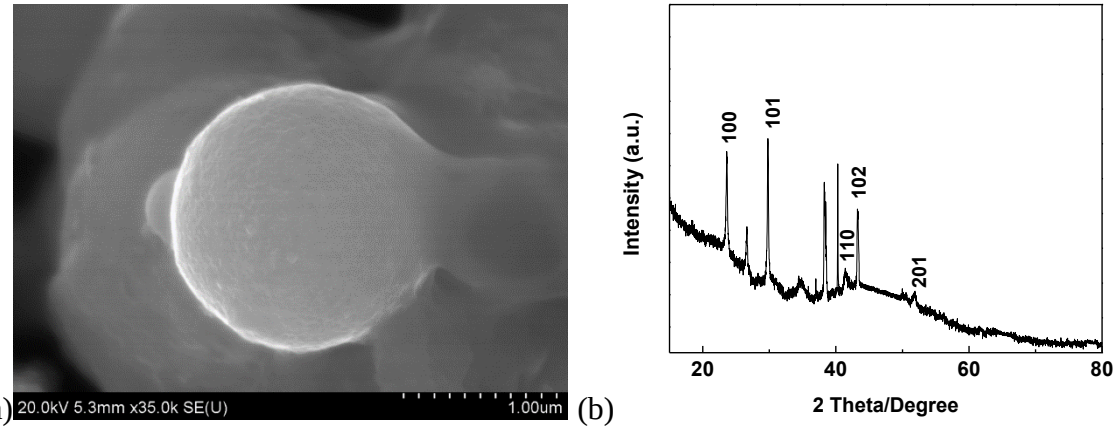

Figure 3.9. (a) SEM images for selenium impregnated carbon composite vs Na after 380 cycles; (b) XRD patterns for selenium impregnated carbon composite vs Na after 380 cycles.

The mechanism behind the exceptional cycling stability and high Coulombic efficiency of the Se_8/C composite was investigated by comparing with the electrochemical performance of the pristine Se_{12} in the same electrolyte ($LiPF_6$-EC/DEC). The pristine Se_{12} electrode was prepared by mixing Se_{12} with carbon black and binder at a component ratio of 80:10:10 (Se: carbon black: binder). The charge/discharge behaviors of Se_{12} electrodes are presented in Figure 3.10. Only very-short sloping lines can be observed in the charge/discharge curves, leading to a very low capacity of 10 mAh g^{-1}, which is 48 times less than that of Se_8/C electrodes. The side reaction between Li_xSe and carbonate electrolyte for less protective Se_{12}/carbon black composite [67] and large particle size of Se_{12} may be responsible for the low capacity. It has been proposed that use of high soluble electrolyte can improve the utilization of insulating S cathode, thus leading to high capacity [105]. Liquid electrolyte (LiTFSI in TEGDME) which has higher solubility for polysulfides than conventional carbonate electrolyte ($LiPF_6$ in EC/DEC) is employed for Se cathode [105]. Se_{12}/carbon black cathode in LiFTSI-TEGDME electrolyte shows two plateaus at 2.2 V and 1.8 V (shown in Figure 3.10b). The two plateau reaction was also observed for Se/C

cycling with LiTFSI in DOL/DME electrolyte by Cui *ect* [67]. The lithiation plateau at high potential of 2.2 V is attributed to reduction of Se to the soluble polyselenides, Li_2Se_n ($n \geqslant 4$), while the plateau at a low potential of 1.8V is due to further reduction of soluble Li_2Se_n ($n \geqslant 4$), to non-soluble Li_2Se_2, and Li_2Se [67]. During the delithiation, Li_2Se is firstly oxidized to Se_n^{2-} ($n \geqslant 4$), and then the high order polyselenide is further oxidized to Se [67]. The high solubility of polyselenides in liquid LiTFSI-TEGDME electrolyte enhances the utilization of Se_{12}, thus increasing the capacity to more than 200 mAh g^{-1} (Figure 3.10b), which is more than 20 times higher than that in $LiPF_6$-EC/DEC electrolyte. However, the high solubility of polyselenides in LiTFSI-TEGDME electrolyte also causes severe shuttle reaction, as evidenced by the endless voltage plateau at 2.2 V. Since the mesoporous carbon host can reduce the side reaction between Li_xSe and carbonate electrolyte and the stable Se-O layer formed on Li_xSe can protect Li_xSe from further side reaction (Se-O layer function as a SEI), the low-cost $LiPF_6$-EC/DEC electrolyte can be used for Se/C cathode which is prepared by infusing Se into mesoporous carbon at a high temperature.

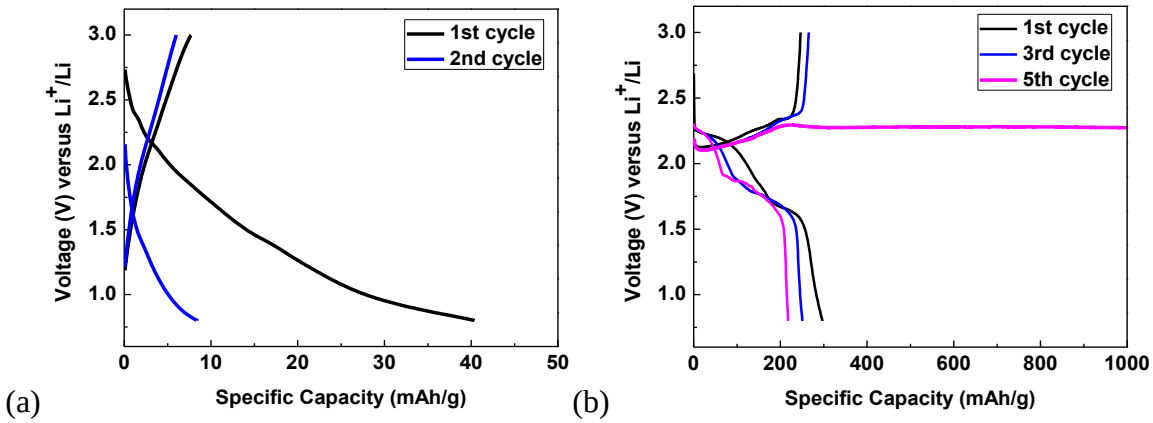

(a) (b)

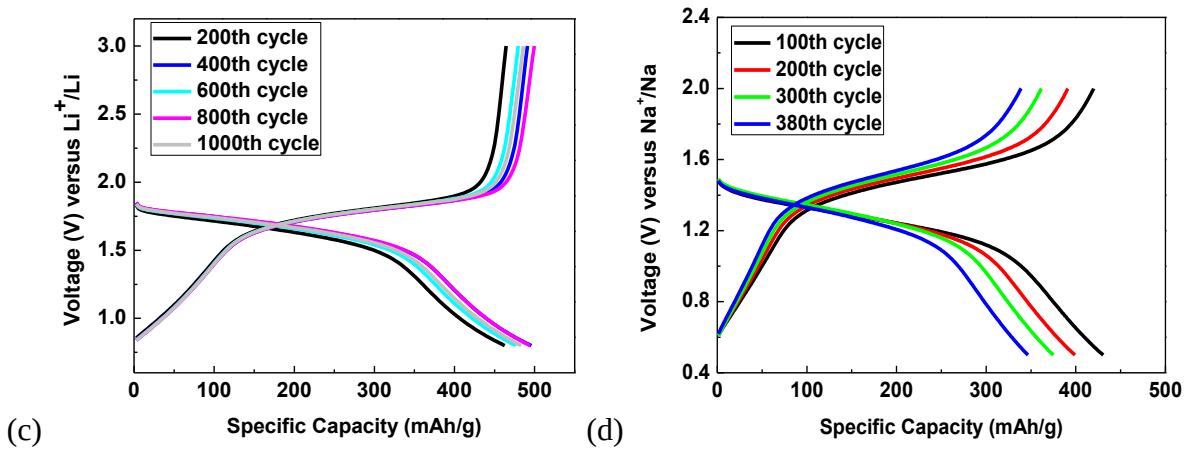

Figure 3.10. Charge/discharge profiles of pristine Se in $LiPF_6$-EC/DEC electrolyte (a) and LiTFSI-TEGDME electrolyte (b); Charge/discharge profiles of Se/C composite in $LiPF_6$-EC/DEC electrolyte for Li-ion batteries (c) and Na-ion batteries (d).

The ideal structure of Se/C nanocomposite has been realized by infusing Se into mesoporous carbon at a temperature of 600^{o}C. The exceptional electrochemical performance of Se/C composite in $LiPF_6$-EC/DEC electrolyte (Figure 3.10c and 3.10d) is due to the uniform distribution of nano-Se_8 in porous carbon and direct generation of insoluble polyselenides. Structure change of Se during charge/discharge cycles in Li-ion battery was measured using Raman spectroscopy. The Raman measurement for Se/C composite before cycling and after 1 and 100 cycles is shown in Figure 3.11. The molecular structure of fresh Se in mesoporous carbon is ring-structured $Se_{8.}$ The ring-structured Se_8 is converted to chain-structured Se_n after 1st cycle, which is confirmed by the sharp peak at 235 cm^{-1} in Raman spectrum. It retains chain-structured Se_n after 100 cycle. The similar result is also reported in the work by Yang *etc* [14]. It is believed that the formation of chain-structured Se_n after 1st cycle leads to the high electrochemical stability of Se/C composite.

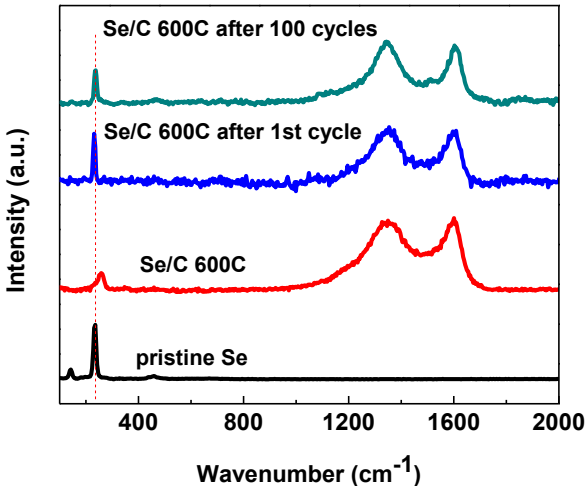

Figure 3.11. Raman spectra of pristine Se, Se/C composite before test, after 1st cycle and after 100 cycles.

3.4 Conclusion

Nano-Se_8 impregnated mesoporous carbon composites for Li-ion and Na-ion batteries are synthesized by infusing Se into mesoporous carbon at 600 ^{o}C under vacuum. Mesoporous carbon is employed to constrain Se_8 in its small pores to alleviate the shuttle effect. The Se_8/C composite cathode in both Li-ion and Na-ion batteries exhibits excellent electrochemical performance in low-cost carbonate-based electrolyte. The Se_8/C in Li-ion batteries can deliver a reversible capacity of 480 mAh g^{-1} and maintains 1000 cycles without any capacity loss. The initial capacity of Se/C composite for sodium ion batteries is as high as 485 mAh g^{-1}, and maintains 340 mAh g^{-1} after 380 cycles. The excellent battery performance of Se/C composite is due to (1) use of small molecular Se_8 and its uniform distribution in mesoporeous carbon which allows most Se_8 molecules to react with Li ions and to protect Li_xSe from side reaction with carbonate

electrolyte; (2) use of low-soluble and low cost $LiPF_6$ in EC/DEC electrolytes which mitigate the dissolution of polyselenides. The exceptional electrochemical performance of the Se/C composite enables its application in lithium/sodium ion batteries.

Chapter 4 In Situ Formed Carbon Bonded and Encapsulated Selenium Composites for Li-Se and Na-Se Batteries

4.1 Introduction

The emerging electric vehicles and smart grids require high power and high capacity energy storage devices [71]. The primary technological bottleneck of state-of-the-art Li-ion and Na-ion batteries comes from the low energy density of ceramic cathodes, which cannot satisfy the critical energy requirement of electric vehicles and smart grids [22, 84]. Even though lithium rich metal oxide, which attracts considerable research interest due to its higher capacity than the commercial lithium metal oxide, can only deliver a reversible capacity of 250 mAh g^{-1} [85, 86], it still cannot match with the anode counterparts such as graphite, Sn and Si [118, 119].

Up to date, sulfur is the most promising cathode material due to its abundance, high theoretical capacity (1675 mAh g^{-1}) and low cost [89, 91]. However, lithium sulfur batteries suffer from two major challenges [90, 111]: (1) the insulating nature of sulfur results in low utilization of sulfur cathode and sluggish kinetics of lithium sulfur batteries; (2) Severe shuttle reaction, triggered by the formation of high solubility polysulfide intermediates during lithiation/delithiation process, results in rapid capacity fading. Although tremendous advances in stabilizing sulfur cathodes have been achieved via carbon coating and nanomaterial fabrication [120, 121], the two challenges still cannot be resolved and sulfur cannot be commercialized as cathodes in Li-ion and Na-ion batteries.

The recent investigation on selenium opens up new opportunities to develop advanced cathode materials for lithium and sodium storage. Abouimrane *et al.* reported selenium, the congener of sulfur, is a promising cathode material for both lithium ion and sodium ion batteries due to comparable volumetric capacity (3253 Ah L^{-1}) to sulfur (3467 Ah L^{-1}) [67, 122]. Though Se cathode suffers from similar dissolution issue with sulfur, its higher electrical conductivity than sulfur is advantageous since it may increase the utilization and power density of Se cathodes. In selenium cathodes, porous carbon as a conductive framework was used to encapsulate Se, thus circumventing the shuttle reaction [14, 123]. Carbon coated Se, nanofibrous Se, free standing graphene/Se film and TiO_2-Se composite were also reported to demonstrate improved electrochemical performance [124-128]. In our previous work, we impregnated Se into mesoporous carbon that delivers a reversible capacity of 480 mAh g^{-1} for 1000 cycles without any capacity loss in Li-ion batteries and 340 mAh g^{-1} for 380 cycles in Na-ion batteries [44]. The exceptional battery performance is ascribed to the synergic physical encapsulation by porous carbon and solid-electrolyte-interphase (SEI) formed from reduction of carbonate based electrolyte. Though such excellent electrochemical performance is achieved by filling Se into mesoporous carbon, the low loading content (30%) of Se in the composite impedes its widespread application in rechargeable batteries.

In this study, the C/Se composites containing 54% of Se were *in situ* synthesized by annealing the mixture of PTCDA and Se in a sealed vacuum glass tube as shown in figure 4.1. One PTCDA molecule contains six oxygen atoms, which are active sites to react with selenium at high temperature. The resulting C/Se composites are collected as black power (figure 4.1b) in the vacuum glass tube after annealing at 600 ^{o}C. The high temperature treatment enables chemical bonding and physical encapsulation of Se by carbon. The *in situ* formed C/Se composites exhibit

very stable cycling performance in commercial carbonate based electrolytes. The C/Se composites with high loading content of Se maintains a reversible capacity of 430 mAh g^{-1} after 250 cycles in Li-ion batteries and 280 mAh g^{-1} after 50 cycles in Na-ion batteries.

(a)

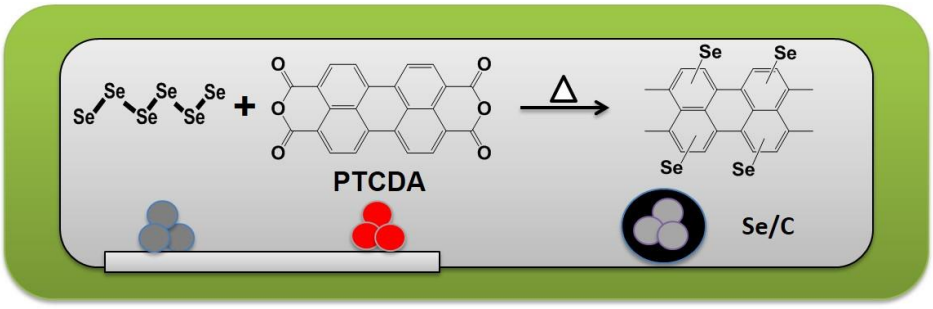

(b)

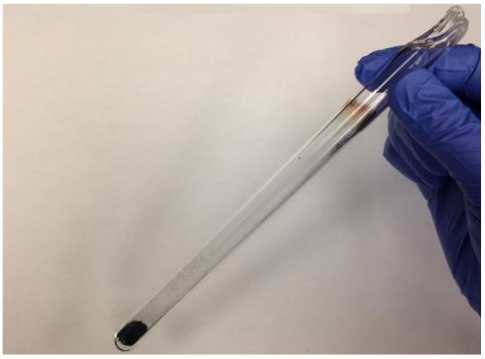

Figure 4.1. (a) Schematic illustration for the *in situ* synthesis of C/Se composites; (b) Photograph of sealed vacuum glass tube after annealing.

4.2 Experimental Section

Synthesis of C/Se composites: All chemicals were purchased from Sigma Aldrich and used as received. Selenium and perylene-3, 4, 9, 10-tetracarboxylic dianhydride were mixed with a ratio of 1.5:1 by weight and sealed in a glass tube under vacuum. The sealed glass tube was annealed in an oven at 600 °C for 3 h, and it was cooled to room temperature in 24 h. C/Se composites were collected as black powder.

Material Characterizations: Scanning electron microscopy (SEM) images were taken by Hitachi SU-70 analytical ultra-high resolution SEM (Japan); Transmission electron microscopy (TEM) images were taken by JEOL (Japan) 2100F field emission TEM; Thermogravimetric analysis (TGA) was carried out using a thermogravimetric analyzer (TA Instruments, USA) with a heating rate of 10 °C min^{-1} in argon; X-ray diffraction (XRD) pattern was recorded by Bruker Smart1000 (Bruker AXS Inc., USA) using CuKα radiation; Raman measurements were performed on a Horiba Jobin Yvon Labram Aramis using a 532 nm diode-pumped solid-state laser, attenuated to give ~900 μW power at the sample surface. The X-Ray Photoelectron Spectroscopy (XPS) analysis was performed on a high sensitivity Kratos AXIS 165 X-ray Photoelectron Spectrometer using monochronic Al Kα radiation.

Electrochemical measurements: The *in situ* formed C/Se composites were mixed with carbon black and sodium alginate binder to form a slurry at the weight ratio of 80:10:10. The electrode was prepared by casting the slurry onto aluminum foil using a doctor blade and dried in a vacuum oven at 60 °C overnight. The slurry coated on aluminum foil was punched into circular electrodes with an area mass loading of 1.2 mg cm^{-2}. Coin cells for lithium selenium batteries were assembled with lithium foil as the counter electrode, 1M $LiPF_6$ in a mixture of ethylene carbonate/diethyl carbonate (EC/DEC, 1:1 by volume) and Celgard®3501 (Celgard, LLC Corp., USA) as the separator. Coin cells for sodium selenium batteries were assembled with sodium metal as the counter electrode, 1M $NaClO_4$ in a mixture of ethylene carbonate/dimethyl carbonate (EC/DMC, 1:1 by volume) and Celgard®3501 (Celgard, LLC Corp., USA) as the separator. Electrochemical performance was tested using Arbin battery test station (BT2000, Arbin Instruments, USA). Capacity was calculated on the basis of the mass of selenium in C/Se

composites. Cyclic voltammograms were recorded using Gamry Reference 3000 Potentiostat/Galvanostat/ZRA with a scan rate of 0.1 mV s^{-1}.

4.3 Results and Discussion

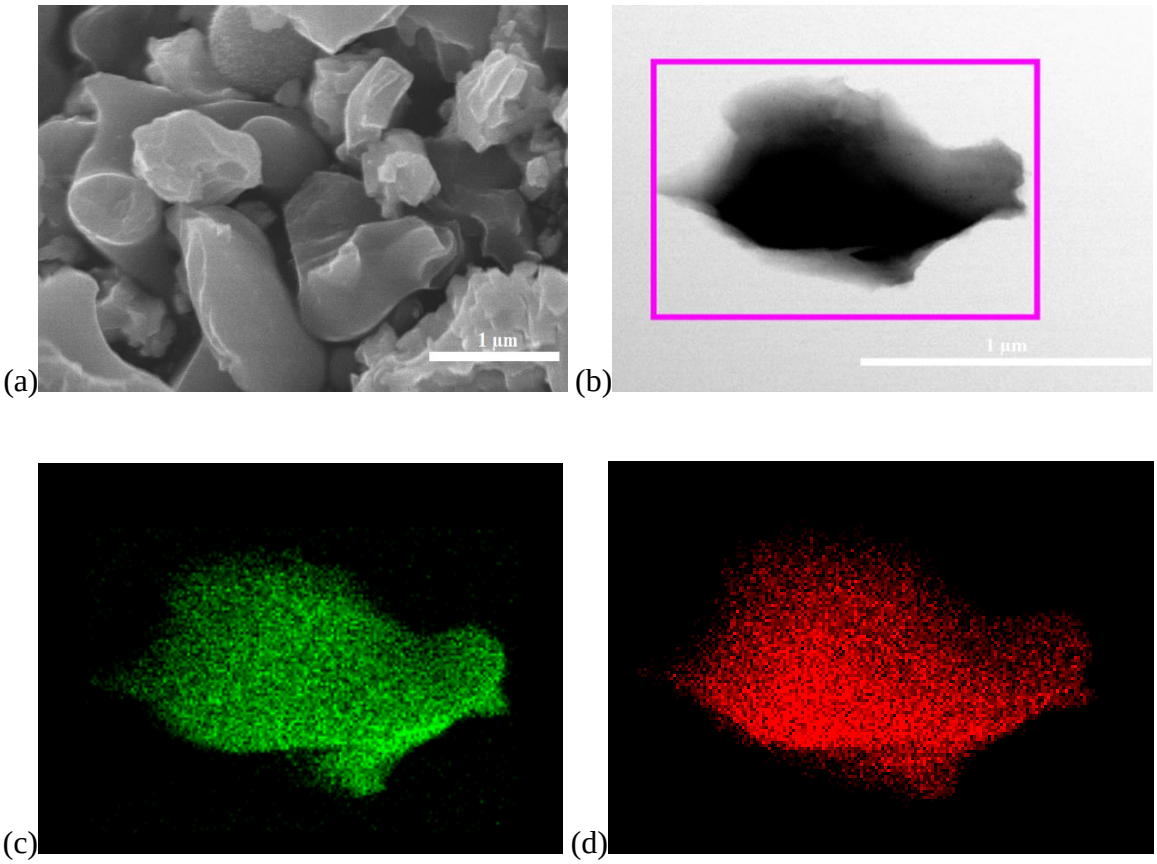

Figure 4.2. (a) SEM image of *in situ* formed C/Se composite; (b) TEM image of *in situ* formed C/Se composite and EDS elemental mapping images of the composites, marked by purple square, for carbon (c) and selenium (d).

Figure 4.2 shows the morphology of C/Se composites that consist of irregular shape particles with a size about 1 µm. The Se is uniformly distributed in the C/Se composite (Figure 4.2b) as

demonstrated in the energy dispersive X-ray spectroscopy (EDS) (Figure 4.2c, and 4.2d). The content of Se in the composite is determined by thermogravimetric analysis (TGA) as shown in figure 4.3. The *in situ* formed C/Se composites contain 54% of Se, which is much higher than that (30%) of Se impregnated mesoporous carbon composite in our previous work [44].

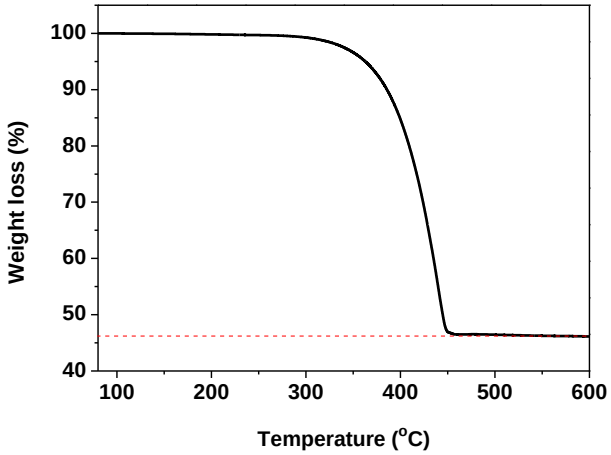

Figure 4.3. The TG analysis for *In Situ* Formed C/Se composites.

The structure of C/Se was characterized using X-ray diffraction (XRD), as shown in figure 4.4a. It shows a broad peak at 26 degree and a few small peaks. The broad peak at 26 degree is attributed to graphitic carbon derived from carbonized PTCDA, while the small peaks are indexed to crystalline Se. Since the intensity of XRD peaks for crystal Se is very weak, only a small portion of Se exists in the form of crystal structure.

The nature of interaction between C and Se was characterized using Raman spectroscopy and X-ray photoelectron spectroscopy (XPS). Se and carbonized PTCDA were used as control samples to identify the Raman spectra of C/Se composites. Figure 4.4b shows the Raman peaks of pristine Se, carbonized PTCDA and *in situ* formed C/Se composites. Two broad carbon peaks at 1345 cm^{-1} and 1595 cm^{-1} appearing in both carbonized PTCDA and C/Se composites represent the disordered graphite (D band) and crystalline graphite (G band), respectively. The similar

peak intensity between D band and G band in C/Se composite is indicative of good electrical conductivity of the carbon matrix derived from carbonized PTCDA. No Raman peaks for pristine Se is observed in the C/Se composites, demonstrating that the small amount of crystal Se is encapsulated by carbon matrix since Raman spectroscopy only collects signals from the surface of material. The interaction between C and Se was characterized by XPS as shown in figure 4.4c and 4.4d. The asymmetry of C 1s peak of C/Se composite in Figure 4.4c indicates the co-existence of sp^2 and sp^3 carbon owing to the graphitic structure of carbon matrix. The binding energies of elemental Se 3d 5/2 is in a range from 55.1 eV to 55.5 eV. However, the binding energies of Se 3d 3/2 and Se 3d 5/2 in C/Se composite are located at 57.0 eV and 56.2 eV, respectively, which are higher than that of elemental Se. The high binding energies of Se is attributed to the strong chemical bond between Se and carbon [129]. The unique synthetic technique of sealed vacuum glass tube enables the formation of C-Se bond at high temperature. The absence of elemental Se in XPS spectrum further confirms that small amount of crystal Se is encapsulated by carbon matrix since XPS only collects signals from the surface of material. Therefore, the *in situ* formed carbon bonded and encapsulated selenium-carbon composites are obtained by using unique synthetic technique of sealed vacuum glass tube.

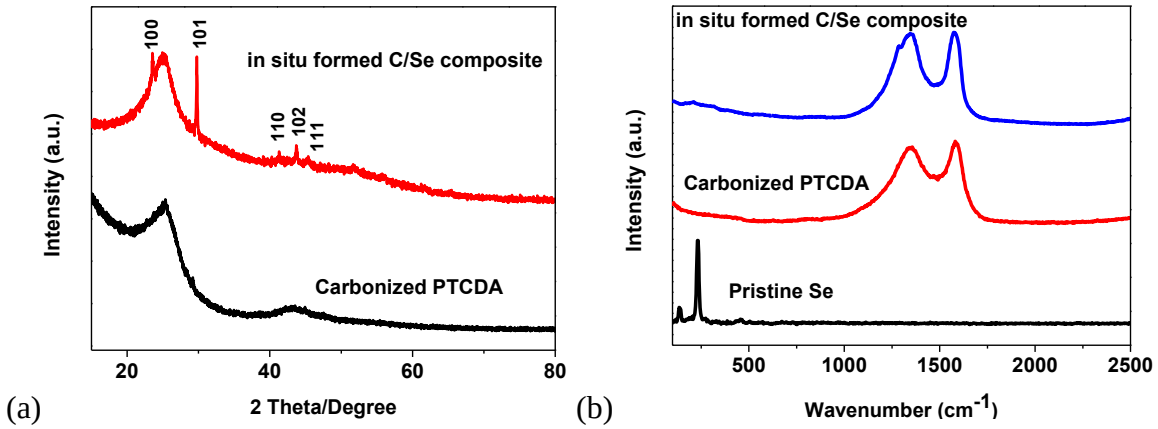

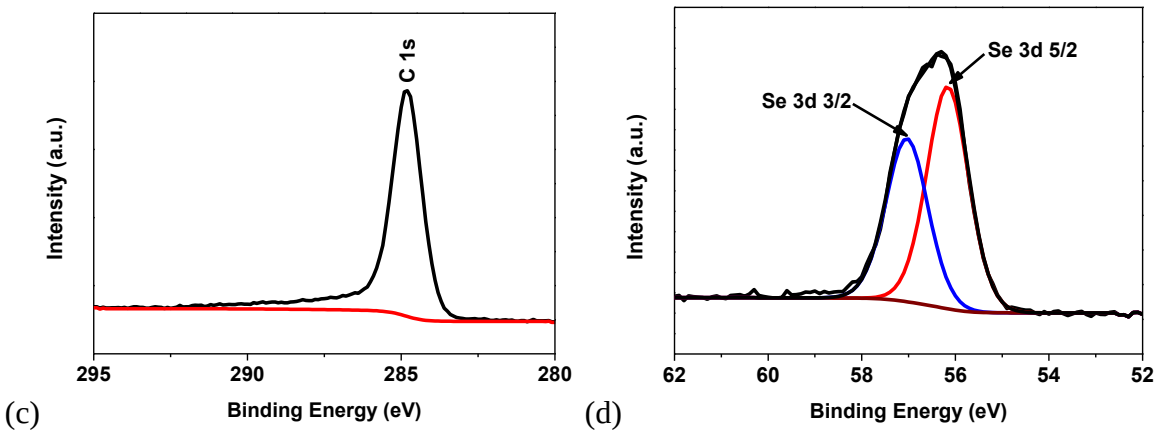

Figure 4.4. XRD patterns (a) and Raman spectra (b) for pristine Se, and *in situ* formed C/Se composite; XPS spectra of *in situ* formed C/Se composite: (c) C 1s, (d) Se 3d. Note: the XPS peaks are calibrated by using C 1s peak at 284.8 eV.

The electrochemical performances of C/Se composites in Li-ion battery and Na-ion batteries were measured in coin cells with carbonate-based electrolytes. Figure 4.5a shows the lithiation/delithiation behavior of C/Se composite in Li-C/Se cell. In the first cycle, two lithiation plateaus centered at 1.6 V and 0.9 V, and a long slopping delithiation plateau centered at 1.8 V are observed. The lithiation plateau at 1.6 V and delithiation plateau at 1.8 V represent the redox reaction between Se and Li-ions, while the plateau at 0.9 V corresponds to the formation of solid electrolyte interphase (SEI) layer and the lithiation of Se that is bonded with carbon. The low Coulombic efficienty of the first cycle (65%) is due to the growth of SEI layer. In the second cycle, the Coulombic efficiency increases to 94%, indicating very small amount of newly formed SEI layer. In the second lithiation, the capacities of plateaus at both 1.8 V and 0.9 V are reduced due to the dissolution of polyselenide caused by incompletely encapsulated Se. The physical encapsulation and chemical bonding of Se by carbon coating suppress the volume expansion in the first few lithiation/delithiation cycles, which require additional overpotential to overcome the stress/strain energy. After the activation process in the few cycles, the deformation of carbon

matrix releases the stress/strain of C/Se composite cathode, shifting the lithiation/delithiation potential to a higher value. After 20 cycles, the lithiation plateau at 0.9 V becomes very short, while the lithiation plateau at 1.6 V shifts to 1.9 V with higher capacity, demonstrating most of Se is activated. The delithiation plateau at 1.8 V also shifts to 1.95 V. The positive shift of both lithiation and delithiation plateaus indicates the relief of the strain/stress in the composite upon cycling. Cyclic votammograms (CV) scans in figure 4.5b confirm that there is only one pair of redox peaks during lithiation/delithiation process. The cathodic peak is at 1.6 V in the first scan, and then it shifts to 1.7 V in the subsequent cycles, while the anodic peak is at 1.83 V with a little positive shift upon cycling. The sharp cathodic peak at 0.8 V represents the formation of solid electrolyte interphase (SEI) layer and the cleavage of C-Se bond by electrochemical reaction between Se and Li-ion. The strong cathodic peak at 0.8 V is recovered in the second and third cycle, demonstrating the contribution of the growth of SEI layer is very small, because the growth of SEI layer mainly occurs in the first cycle. Figure 4.5c and 4.5d show the cycle life and rate capability of *in situ* formed C/Se composites. The composites deliver a charge capacity of 560 mAh g^{-1} at a current density of 100 mA g^{-1} in the first cycle, and remain the reversible capacity of 430 mAh g^{-1} after 250 cycles. Besides superior cycling stability, the composites also exhibit excellent rate capacity. As shown in figure 4.5d, the reversible capacity of the composite is 600 mAh g^{-1} at a current density of 40 mA g^{-1}, while the reversible capacity remains at 280 mAh g^{-1} with the current density increases to 1.2 A g^{-1}, and the reversible capacity recovers to 600 mAh g^{-1} after the current density decreases back to 40 mA g^{-1}. Therefore, the exceptional electrochemical performance of the C/Se composite demonstrates that it is a promising cathode for rechargeable lithium batteries.

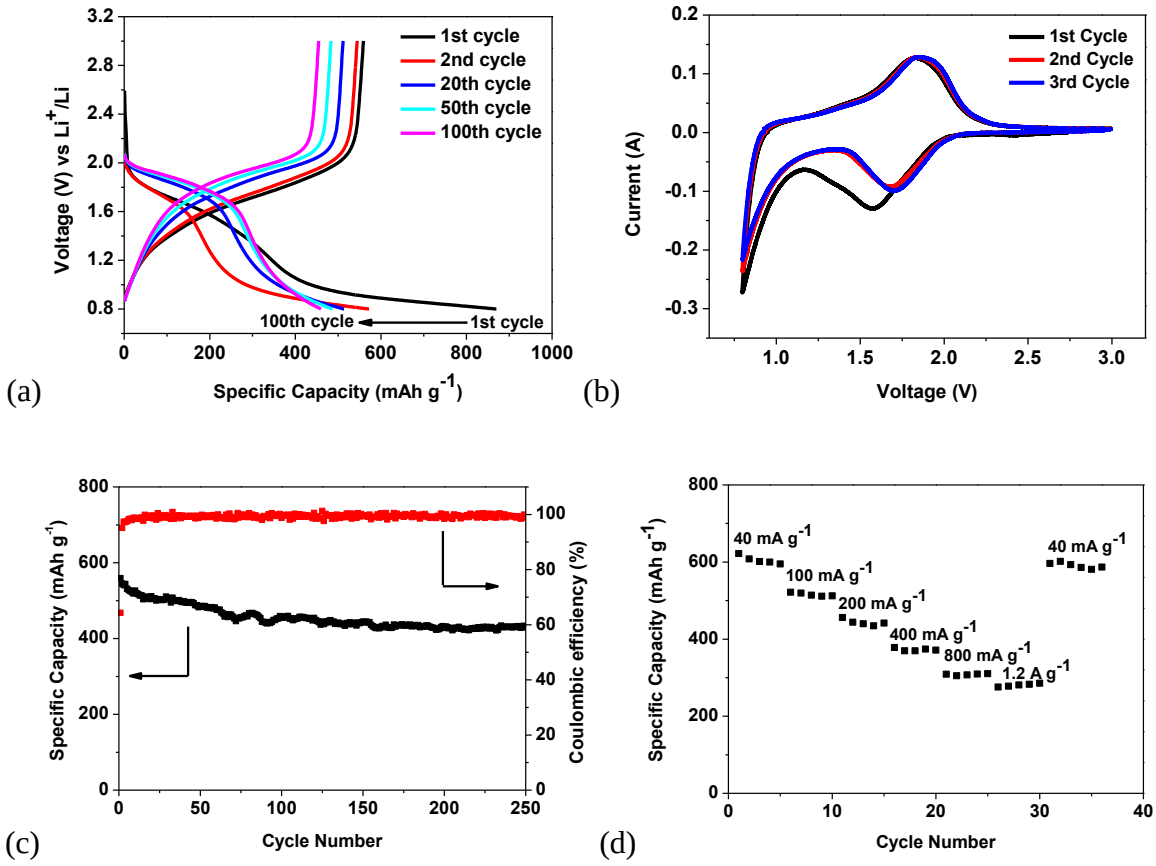

Figure 4.5. Electrochemical performance of *in situ* formed C/Se composite. (a)The galvanostatic charge-discharge curves between 0.8 V and 3.0 V versus Li/Li^+; (b)cyclic voltammograms at 0.1 mV s^{-1} in the potential window from 0.8 V to 3.0 V versus Li/Li^+; (c) delithiation capacity and Coulombic efficiency versus cycle number at the current density of 100 mA g^{-1}; (d) rate performance at various C-rates.

It was reported that Se cathodes have two potential plateaus at ~2.3 V and 3.75 V during delithiation [13]. The plateau at ~2.3 V corresponds to the conversion of Li_2Se to Se, while the plateau at 3.75 V is attributed to the redox shuttle reaction, triggered by the dissolution of polyselenide species in the electrolyte upon cycling. If the dissolution of polyselenide species can be avoided, the plateau at 3.75 V will disappear. Only one plateau at ~2.0 V was reported for carbon encapsulated Se cathode [14], because the small pores of mesoporous carbon confine the

polyselenide species and avoid the dissolution. In our work, Se is bonded and encapsulated by carbon so that the polyselenide species are restrained by carbon matrix, and the plateau at 3.75 V associated with shuttle effect was not observed.

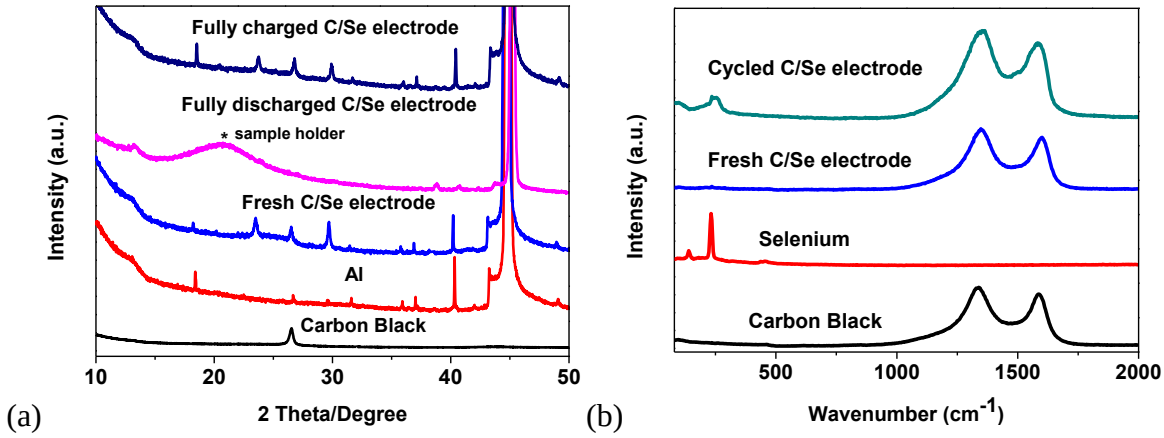

Figure 4.6. (a) XRD patterns for carbon black, Al foil, fresh C/Se electrode and cycled C/Se electrode; (b) Raman spectra for carbon black, selenium, fresh C/Se electrode and cycled C/Se electrode.

The phase structure of C/Se electrodes before cycling and after fully lithiation/delithiation was characterized using XRD and Raman measurements as shown in figure 4.6. The fully discharged C/Se electrode is prepared by disassembling Li-C/Se cell in the Ar filled glovebox after discharging the cell to 0.8 V and maintaining at 0.8 V for 24 h. The fully charged C/Se electrode is prepared after charging the electrode to 3.0 V and maintaining at 3.0 V for 24 hours. Both electrodes are immersed in dimethyl carbonate for 24 h to remove the $LiPF_6$ salt before XRD and Raman measurement. The fresh C/Se electrode shows typical characteristic XRD peaks. All these characteristic XRD peaks of Se disappear in fully discharged C/Se electrode, demonstrating the lithiated Se becomes amorphous Li_2Se after fully lithiation. However, the characteristic XRD peaks of Se recover after fully delithiation, demonstrating the crystal structure of Se recovers upon cycling. The formation of Li_2Se after fully lithiation of C/Se

cathodes was also reported in previous studies [13, 14]. The Raman spectra of fresh and cycled C/Se electrodes are shown in figure 4.6b. In the fresh electrode, two broad carbon peaks at 1345 cm^{-1} and 1595 cm^{-1} can be observed, and the characteristic peak for cyclic Se_8 disappears due to the encapsulation and bonding of Se by carbon matrix. After one change/discharge cycle, a small peak at 256 cm^{-1} representing to the chain-structured Se_n appears. The formation of chain-structured Se_n after the first cycle enhances the electrochemical stability of C/Se composite.

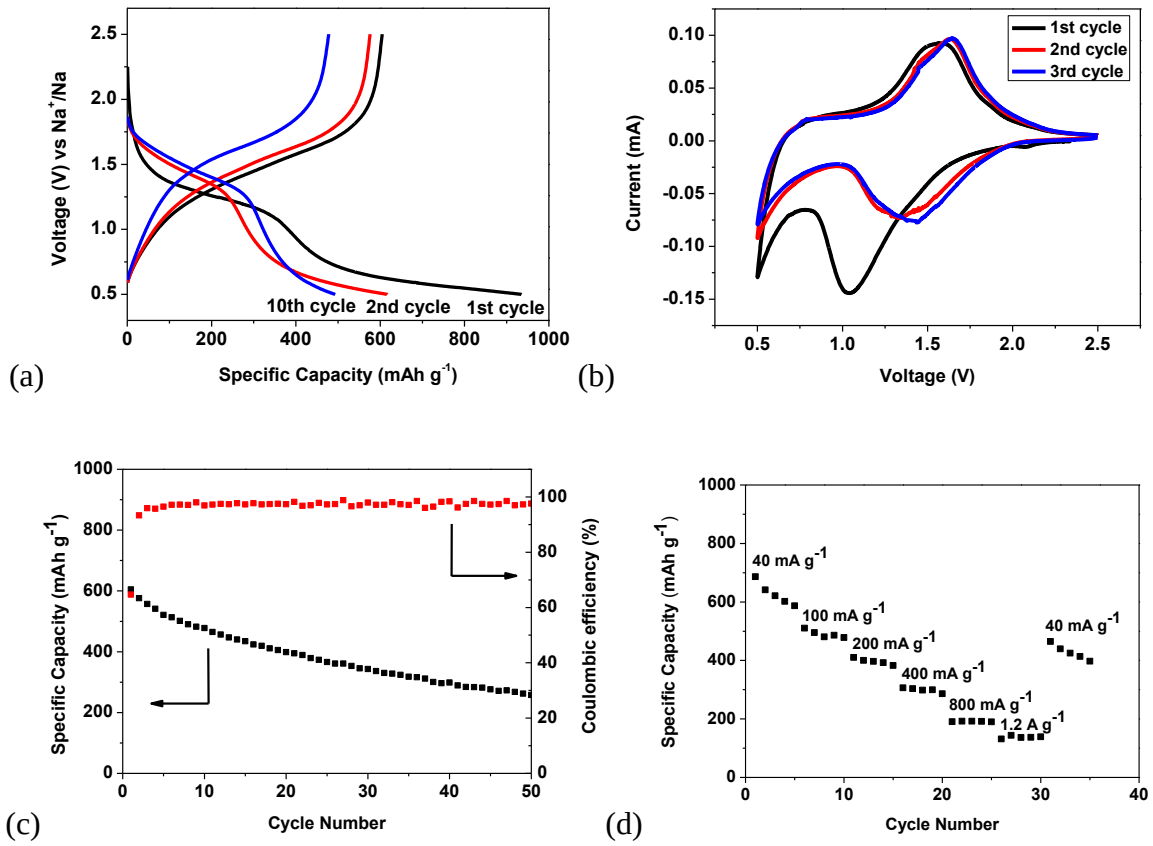

Figure 4.7. Electrochemical performance of *in situ* formed C/Se composite. (a)The galvanostatic charge-discharge curves between 0.5 V and 2.5 V versus Na/Na^+; (b)cyclic voltammograms at 0.1 mV s^{-1} in the potential window from 0.5 V to 2.5 V versus Na/Na^+; (c) desodiation capacity and Coulombic efficiency versus cycle number at the current density of 100 mA g^{-1}; (d) rate performance at various C-rates.

The unique C/Se composites can also be used as a cathode for sodium ion batteries. Figure 4.7 shows the charge/discharge profiles of C/Se composite in $NaClO_4$-EC/DMC electrolyte. Two plateaus centered at 1.3 V and 0.6 V are observed during the first sodiation, while one slopping plateau centered at 1.5 V is observed during the first desodiation, which are 0.3 V lower than lithiation/delithiation plateaus in lithium ion batteries due to the lower potential of sodium metal than lithium metal [130]. The plateau centered at 0.6 V becomes very short from 2^{nd} cycle to 10^{th} cycle, while the plateau centered at 1.5 V becomes longer from 2^{nd} cycle to 10^{th} cycle, demonstrating that most of Se in C-Se composite is activated after 10 cycles. The positive shift of both sodiation and desodiation plateaus indicating the relaxation of the strain/stress in the composite upon cycling. The CV scans in figure 4.7b show that there is only one pair of redox peaks during sodiation/desodiation process. In the first scan, there are a broad cathodic peak at 1.05 V and a conspicous cathodic peak at 0.5 V, corresponding to the two plateaus at 1.3 V and 0.6 V in the first sodiation curve, and an anodic peak at 1.55 V, corresponding to the plateau at 1.5 V in the first desodiation curve. In the following scans, both cathodic peak at 1.05 V and anodic peak at 1.55 V shift to the positive values, and the intensity of the sharp cathodic peak at 0.5 V becomes weaker upon cycling, coincident with the changes in charge/discharge profiles. The long term cycling performance and rate capability are shown in figure 4.7c and 4.7d. The *in situ* formed C/Se composites deliver a charge capacity of 605 mAh g^{-1} in the first cycle at a current density of 100 mA g^{-1}, while it decreases to 258 mAh g^{-1} after 50 cycles. The cycle life in sodium cell is poorer than that in lithium ion cell due to the more severe volume change induced by larger size of sodium ion. When the current density increases from 40 mA g^{-1} to 1.2 A g^{-1}, the desodiation capacity remains 138 mAh g^{-1}. Therefore, the good electrochemical performance of

in situ formed C/Se composite paves the way for the feasibility of high-performance Na-ion batteries.

4.4 Conclusion

In conclusion, carbon bonded and encapsulated C/Se composites with 54% of Se were synthesized by *in situ* carbonizing the mixture of PTCDA and Se in a sealed vacuum glass tube. The unique synthesizing technique enables physical encapsulation and chemically bonding of Se by carbon, which greatly enhances the charge/discharge cycling stability in both lithium and sodium batteries. The exceptional electrochemical performance of *in situ* formed C/Se composite demonstrates that it is a promising cathode material for rechargeable lithium and sodium batteries.

Chapter 5 Carbonized Polyacrylonitrile Stabilized SeS_x Cathodes for Long Cycle Life and High Power Density Lithium Ion Batteries

5.1 Introduction

Lithium ion batteries which drive most portable electronics are promising energy storage devices for electric vehicles and smart grids [2]. To fulfill the large-scale application of lithium ion batteries, energy density and cycle life of current Li-ion batteries have to be improved [71]. Anode materials such as Si and Sn can provide theoretical capacities of 3579 mAh g^{-1} and 993 mAh g^{-1} respectively [34, 83], while the capacities of commercial $LiCoO_2$ (137 mAh/g) and $LiFePO_4$ (170 mAh g^{-1}) are much lower than counterpart anodes [22, 84]. The energy density of current lithium ion batteries is mainly limited by cathode materials. Due to a high theoretical capacity of 1672 mAh g^{-1}, sulfur has been considered as the next generation cathode for high energy Li-ion batteries [131-133], and it has attracted considerable research interest from both academy and industry. However, lithium sulfur batteries suffer from two major problems [111]: (1) low utilization of sulfur and poor power density due to the insulating property of sulfur and lithium sulfide; (2) the dissolution of polysulfide intermediates triggers severe shuttle reaction, resulting in rapid capacity fading during lithiation/delithiation process. Nevertheless, the dissolution of insulating polysulfide intermediates into electrolytes also allows full lithiation of sulfur, thus increasing the sulfur utilization and capacity. The current strategy to achieve both long cycling stability and high capacity is to use highly polysulfide-soluble electrolyte, but physically restrict dissolved polysulfides inside sulfur cathode to prevent shuttle reaction. The most effective

method is to employ conductive porous carbon as a host to constrain polysulfide intermediates and enhance the conductivity of sulfur [62, 112].

Recently, selenium, the congener of sulfur, is introduced as the cathode material for lithium ion batteries due to its higher electrical conductivity than sulfur and its comparable volumetric capacity (3253 Ah L^{-1}) to sulfur (3467 Ah L^{-1}) [13, 14]. As demonstrated in our previous work, selenium impregnated mesoporous carbon composite exhibits excellent capacity retention that there is no capacity loss after 1000 deep charge/discharge cycles [44]. However, the mass capacity (480 mAh g^{-1}) of selenium, is lower than the mass capacity of sulfur (from 800 mAh g^{-1} to 1000 mAh g^{-1}). Since selenium possesses high cycling stability, but low reversible capacity, and sulfur has high reversible capacity, but poor cycling stability, it is desirable to develop a cathode material that combines the advantages of S and Se. As a consequence, selenium sulfide (SeS_2) has been explored as a cathode material for lithium ion batteries [67].

Since SeS_2 has similar chemical properties with sulfur and selenium, it is believed that the method used to stabilize sulfur and selenium should be also effective for SeS_2. It was reported that PAN could react with sulfur at 300 ^oC to form a stable and conductive heterocyclic compound which could confine elemental sulfur and stabilize polysulfides [100, 101]. When the carbonization temperature increases to 600 ^oC, the N-containing carbon (ring) structures in carbonized polyacrylonitrile (PAN) is able to constrain lithium sulfide species [99], which further enhances the cycling stability and electronic conductivity. In this study, we synthesized SeS_x/CPAN composites by annealing the mixture of SeS_2 and PAN at 600 ^oC under vacuum. The x in SeS_x/CPAN is less than 2 due to the property difference between Se and S in high temperature of 600 ^oC. SeS_x is uniformly distributed in the carbonized PAN spheres with a particle size of 200 nm, and the carbonized PAN matrix can effectively confine lithium

polysulfide and lithium polyselenide intermediates, thus improving the cycling stability of SeS_x/CPAN composites in commercial electrolyte ($LiPF_6$ in EC/DEC). The SeS_x/CPAN composite delivers a reversible capacity of 780 mAh g^{-1} at the current density of 600 mA g^{-1}, and maintains the capacity of 780 mAh g^{-1} for 1200 cycles. As the current density increased from 60 mA g^{-1} to 6 A g^{-1}, the capacity retains 50% of the capacity at 60 mA g^{-1}, demonstrating its exceptional rate capability. The superior electrochemical performance of SeS_x/CPAN composite is owing to synergic restriction of SeS_x by both CPAN matrix and SEI layer. This is the first report on detailed electrochemical performance of selenium sulfide cathode. Our results demonstrate that SeS_x/CPAN composite is a promising cathode material for long cycle life and high power density lithium ion batteries.

5.2 Experimental Section

Synthesis of $SeS_{0.7}$/CPAN composites: All chemicals were purchased from Sigma Aldrich and used as received. Selenium sulfide and polyacrylonitrile were mixed with a ratio of 1:1 by weight and sealed in a glass tube under vacuum. The sealed glass tube was annealed in an oven at 600 °C for 3 h, and it was cooled to room temperature in 24 h. $SeS_{0.7}$/CPAN composites were collected as black powder. PCPAN is also synthesized in a sealed glass tube at 600 ^oC for 3 h in vacuum.

Material Characterizations: Scanning electron microscopy (SEM) images were taken by Hitachi SU-70 analytical ultra-high resolution SEM (Japan); Transmission electron microscopy (TEM) images were taken by JEOL (Japan) 2100F field emission TEM; Thermogravimetric analysis (TGA) was carried out using a thermogravimetric analyzer (TA Instruments, USA) with a heating rate of 10 °C min^{-1} in argon; X-ray diffraction (XRD) pattern was recorded by Bruker

Smart1000 (Bruker AXS Inc., USA) using CuKα radiation; Raman measurements were performed on a Horiba Jobin Yvon Labram Aramis using a 532 nm diode-pumped solid-state laser, attenuated to give ~900 μW power at the sample surface. The X-Ray Photoelectron Spectroscopy (XPS) analysis was performed on a high sensitivity Kratos AXIS 165 X-ray Photoelectron Spectrometer using monochronic Al Kα radiation.

Electrochemical measurements: The $SeS_{0.7}$/CPAN composites were mixed with carbon black and sodium alginate binder to form a slurry at the weight ratio of 80:10:10. The electrode was prepared by casting the slurry onto aluminum foil using a doctor blade and dried in a vacuum oven at 60 °C overnight. The slurry coated on aluminum foil was punched into circular electrodes with an area mass loading of 1.2 mg cm^{-2}. The same method is used to fabricate pristine selenium sulfide electrode and carbon black electrode. The pristine selenium sulfide electrode was made by mixing selenium sulfide, carbon black and sodium alginate binder at a weight ratio of 26:64:10. The carbon black electrode was made by mixing carbon black and sodium alginate binder at a weight ratio of 90:10. Coin cells for lithium selenium sulfide batteries were assembled with lithium foil as the counter electrode, 1M $LiPF_6$ in a mixture of ethylene carbonate/diethyl carbonate (EC/DEC, 1:1 by volume) or 1M LiTFSI in tetraethylene glycol dimethyl ether (TEGDME) as the electrolyte, and Celgard®3501 (Celgard, LLC Corp., USA) as the separator. Electrochemical performance was tested using Arbin battery test station (BT2000, Arbin Instruments, USA). Capacity was calculated on the basis of the mass of selenium sulfide in $SeS_{0.7}$/CPAN composites. Cyclic voltammograms were recorded using Gamry Reference 3000 Potentiostat/Galvanostat/ZRA with a scan rate of 0.1 mV s^{-1}. Impedance analysis was also performed by Gamry Reference 3000 Potentiostat/Galvanostat/ZRA.

5.3 Results and Discussion

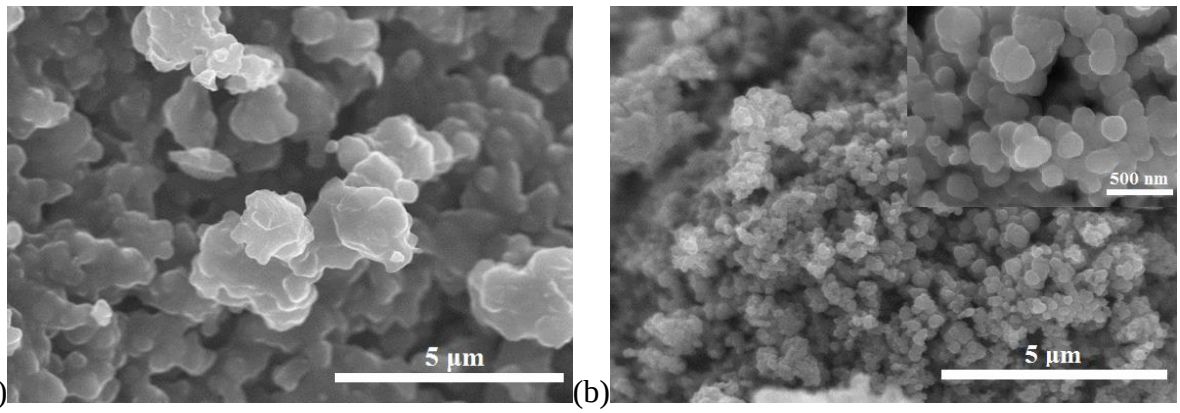

Figure 5.1. SEM images for PCPAN (a) and SeS_x/CPAN composites (b).

The scanning electron microscope (SEM) images in Figure 5.1 show the morphology of pre-carbonized PAN (PCPAN) and SeS_x/CPAN composites. As shown in figure 5.1 (a), PCPAN synthesized under vacuum at a high temperature (600 ^oC) consists of irregular-shape particles with a size about 3 µm. The SeS_x/CPAN composites, synthesized by annealing the mixture of SeS_2 and PAN (1:1 by weight) at the same temperature of 600 ^oC under vacuum, are composed of round-shape particles with a small particle size of 200 nm. The morphology difference is attributed to the reaction between PAN and SeS_2. SeS_2 can dehydrogenate PAN to form a conductive main chain, in the meanwhile, –CN functional groups in PAN are cyclized to form a stable heterocyclic ring at the high temperature [100]. The heterocyclic ring can confine SeS_x and accommodate the volume change caused by the lithiation/delithiation. The transmission electron microscopy (TEM) image of SeS_x/CPAN composites (Figure 5.2a) shows that primary particles are in round-shape with a size about 200 nm, and these particles aggregate into a large cluster, which is consistent with the SEM images. High resolution transmission electron microscopy (HRTEM) and selected area electron diffraction (SAED) are also carried out to investigate the microstructure of the SeS_x/CPAN composite. From the HRTEM image and SAED pattern in figure 5.3, it can be clearly observed that SeS_x/CPAN composite has an amorphous structure.

The energy-dispersive X-ray spectroscopy (EDS) elemental mapping images in figure 5.2b-d reveal that the carbon elemental mapping image overlaps with sulfur and selenium mapping images, demonstrating the uniform distribution of SeS_x in the carbon matrix. Moreover, the EDS mapping also indicates that the ratio of selenium and sulfur is 1:0.7, as shown in figure 5.4, so x is 0.7. The content of $SeS_{0.7}$ in the $SeS_{0.7}$/CPAN composites is 33% as shown in the thermogravimetric analysis (TGA) in figure 5.5.

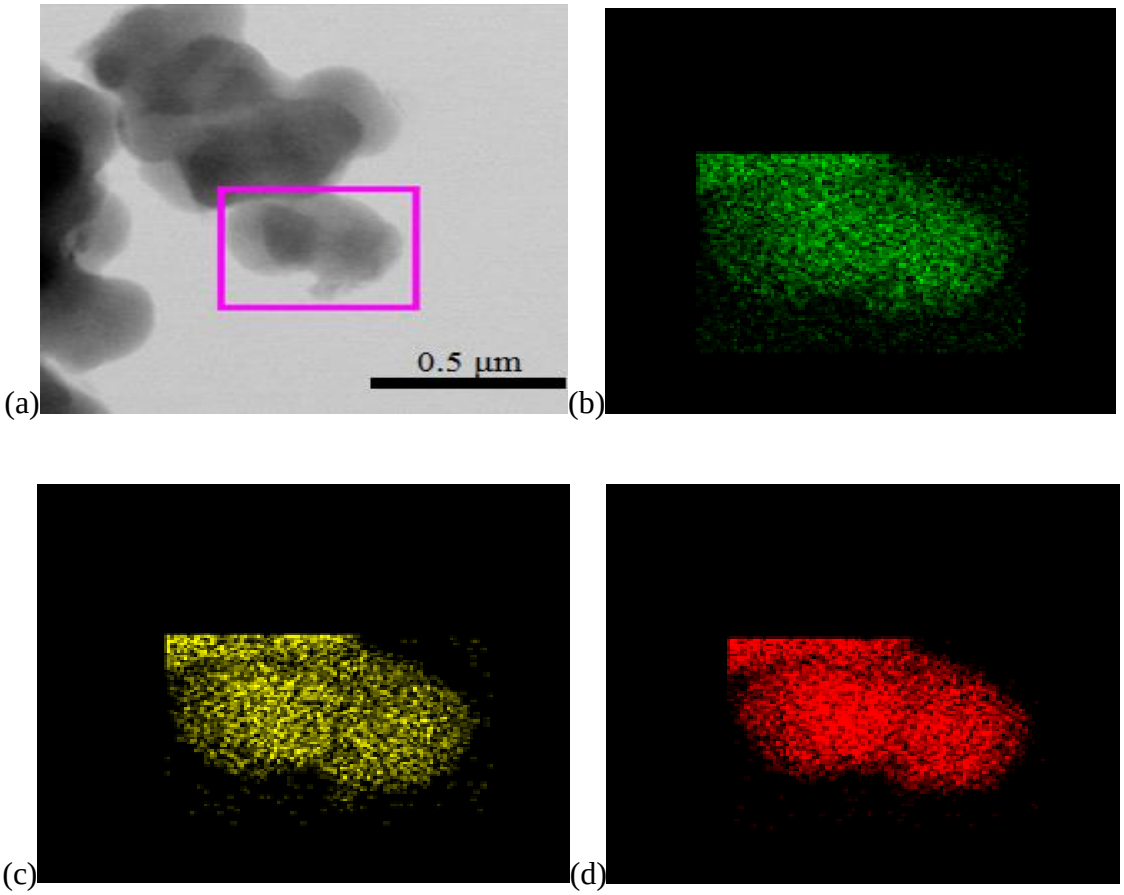

Figure 5.2. TEM image of SeS_x/CPAN composites (a) and EDS elemental mapping images of the SeS_x/CPAN composites, marked by purple square, for carbon (b), sulfur (c) and selenium (d).

(a) 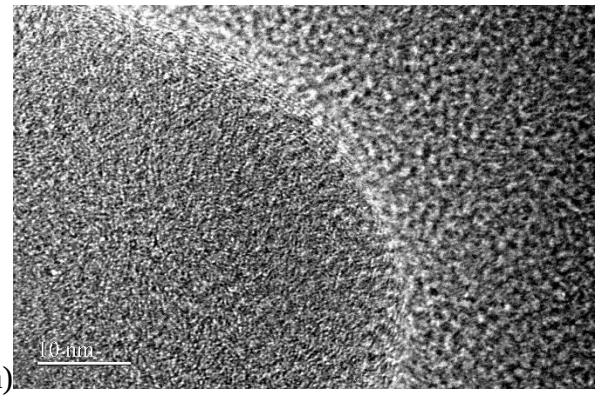

(b) 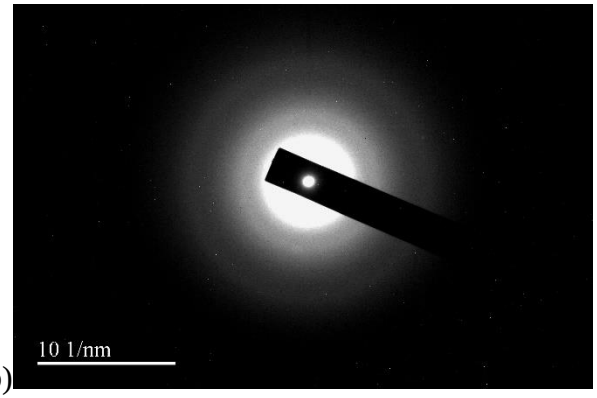

Figure 5.3. HRTEM (a) and SAED pattern (b) for SeS_x/CPAN composite.

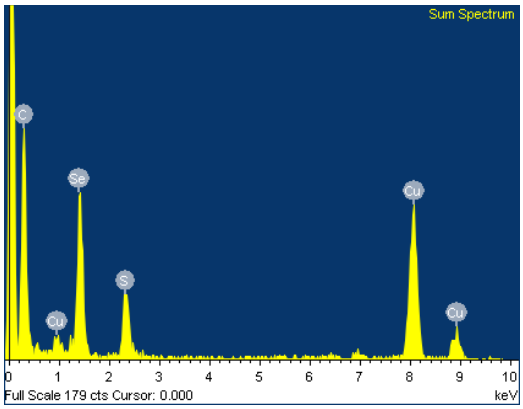

Figure 5.4. EDS analysis for $SeS_{0.7}$/CPAN composites.

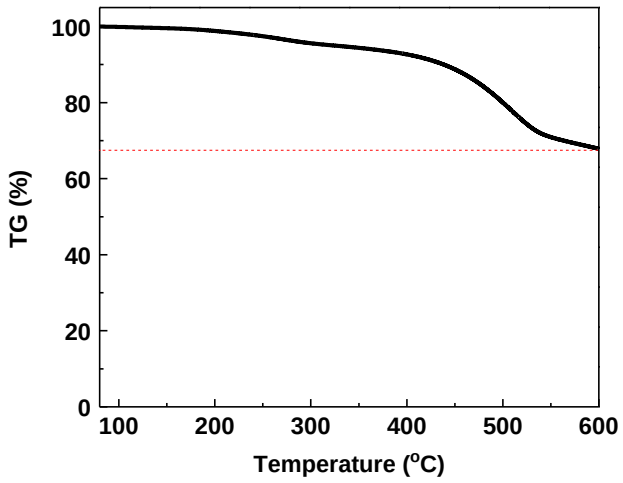

Figure 5.5. The TGA analysis for $SeS_{0.7}$/CPAN composites.

The phase structure of $SeS_{0.7}$/CPAN composites was investigated by X-ray diffraction and Raman spectroscopy. Figure 5.6a and 5.6b show the XRD pattern and Raman spectrum of $SeS_{0.7}$/CPAN composites. XRD patterns and Raman spectra of pristine SeS_2 and PCPAN are also showed in Figure 5.6 as controls. The XRD pattern shows that $SeS_{0.7}$/CPAN composite has an amorphous structure, while pristine SeS_2 possesses a crystal structure. One broad peak at 26 degree in the XRD pattern of $SeS_{0.7}$/CPAN composites is attributed to the carbon matrix formed through carbonization of PAN. The amorphous structure of $SeS_{0.7}$ in $SeS_{0.7}$/CPAN composite may be due to the uniform distribution of $SeS_{0.7}$ at a molecular level in CPAN matrix, leading to strong confinement of $SeS_{0.7}$ in CPAN. Similar to the XRD pattern, characteristic Raman peaks of SeS_2 are not observed in $SeS_{0.7}$/CPAN composites, and only two broad carbon peaks at 1345 cm^{-1} and 1595 cm^{-1} representing the disordered graphite (D band) and crystalline graphite (G band), respectively, appear in the Raman spectrum of $SeS_{0.7}$/CPAN composites. Both XRD and Raman measurements confirm that $SeS_{0.7}$ molecules are constrained by CPAN to form an amorphous structure. The X-Ray Photoelectron Spectroscopy (XPS) analysis was also used to obtain valuable information about the surface of $SeS_{0.7}$/CPAN composites. The peaks for carbon-carbon bond and carbon-nitrogen bond are observed in figure 5.6c. Since CPAN consists of well-formed N-containing carbon (ring) structures [134], the C 1s XPS spectrum is in well agreement with the structure of CPAN. The S 2p and Se 3p XPS spectrum in figure 5.6d shows the XPS peaks for S 2p 1/2, S 2p 3/2, Se 3p 1/2 and Se 3p 3/2, which further confirms the existence of selenium sulfide in $SeS_{0.7}$/CPAN composites. Moreover, the composition of $SeS_{0.7}$ is obtained from the peak fit using relative sensitivity factors from the Kratos vision library, and atomic ratio of S to Se is calculated to be 0.7, which is coincident with the result of EDS analysis. It was reported that sulfur can react with selenium to generate selenium sulfide at a high temperature

[135, 136]. Moreover, the heterocyclic sulfur-selenium molecules such as Se_5S_2, Se_5S_3 and Se_3S_2 do exist as ring molecules with a majority of Se atoms [137]. Therefore, in the $SeS_{0.7}$/CPAN composite, $SeS_{0.7}$ can exist as molecules in the frame of CPAN.

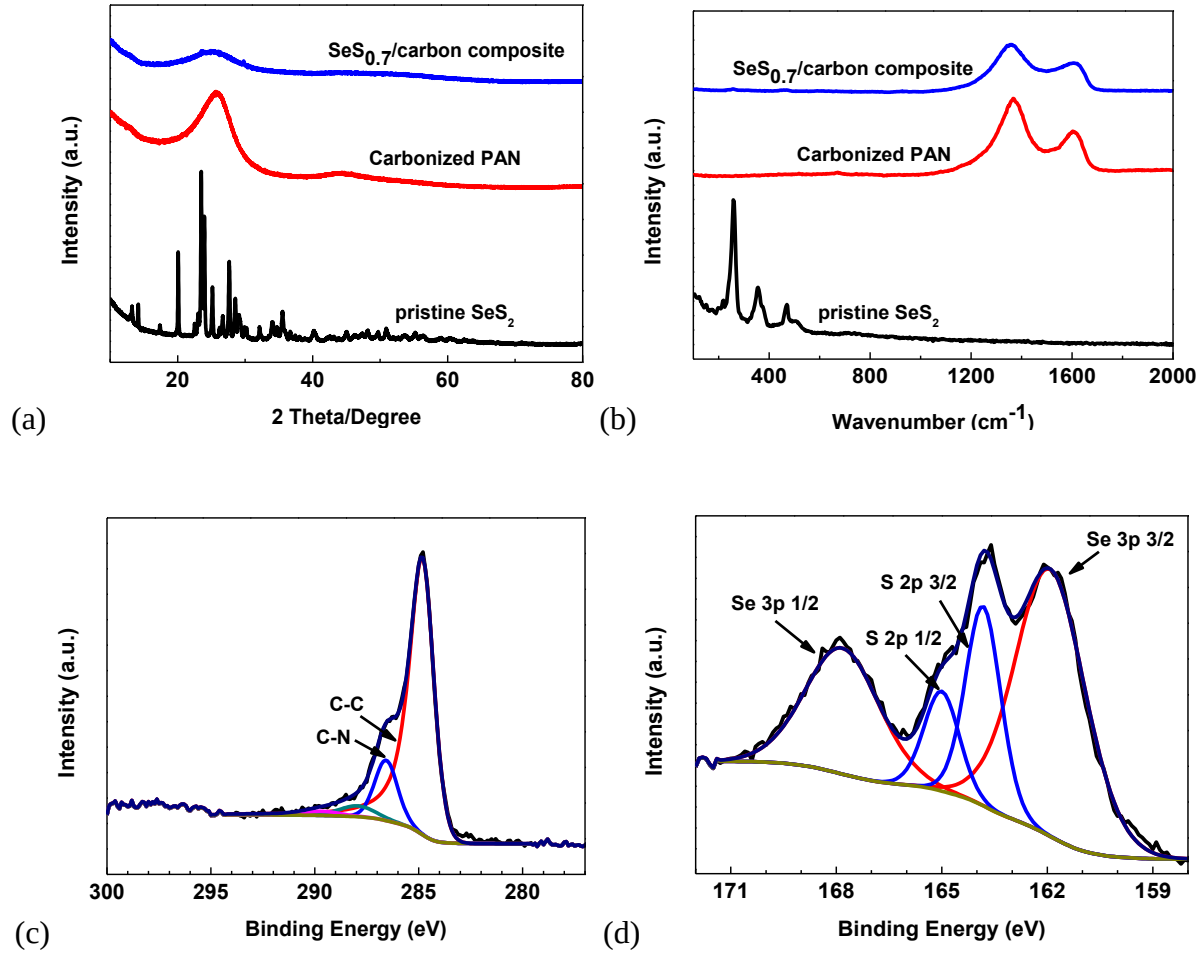

Figure 5.6. XRD patterns (a) and Raman spectra (b) for pristine SeS_2, PCPAN and $SeS_{0.7}$/CPAN composites; XPS spectra of $SeS_{0.7}$/CPAN composites: (c) C 1s, (d) S 2p and Se 3p.

The galvanostatic charge–discharge behaviors of $SeS_{0.7}$/CPAN composites in $LiPF_6$-EC/DEC electrolyte are shown in figure 5.7a. During the first lithiation, a small plateau at 2.35 V and a long flat plateau at 1.7 V are observed. However, the short plateau at 2.35 V disappears, while the flat plateau at 1.7 V becomes a little steeper and shifts to 1.8 V in the subsequent cycles. The

plateau at 2.35 V is assigned to the conversion of $SeS_{0.7}$ to polysulfides/polysenelides and the plateau at 1.7-1.8 V is atributed to conversion of polysulfides to Li_2S and polyselenides to Li_2Se [67]. The disappearence of the small plateau at 2.35 V is probably owing to the dissolution of high-order polysulfide/polyselenide intermediates into the electrolyte [67]. The long sloping line from 1.5 V to 0.8 V in the first lithiation becomes much steeper in the following lithiation cycles, resulting in large irreversible capacity in the first cycle. The large irreversible capacity induced at the potential range from 1.5 V to 0.8 V may be attributed to the formation of SEI layer on the surface of electrode. The low Coulombic efficiency (~58%) in the first cycle quickly increases to 95% in the second cycle, suggesting that SEI layer is well-formed after the first cycle. The SEI layer on $SeS_{0.7}$/CPAN electrode can prevent polysulfides/polysenelides from reacting with carbonate-based electrolyte. Similar SEI formation process is also observed in carbon black electrode. As shown in figure 5.8, a long potential plateau between 1.0 V and 0.8 V in carbon black electrode is observed in the first cycle, but it disappears in the second cycle, resulting in a large irreversible capacity. The large irreversible capacity is ascribed to the formation and growth of SEI layer on the surface of carbon black, which is coincident with the result of $SeS_{0.7}$/CPAN electrode. During delithation, only one sloping plateau centered at 2.1 V can be observed, and this peak remains stable during following lithiation/delithiation cycles. The CV curves in figure 5.7b are consistent with the charge–discharge curves. In the first scan, there are a small anodic peak at 2.45 V, a sharp anodic peak at 1.5 V and a cathodic peak at 2.2 V. The small peak at 2.45 V dissappears after the first scan, while the sharp peak at 1.5 V shifts to 1.75 V in the subsequent scans. The peak shift indicates that there is an activation process due to volume expansion of $SeS_{0.7}$ in the first lithiation process, and then the peaks become very stable, demonstrating high cycling stability of $SeS_{0.7}$/CPAN composites. Figure 5.7c shows the cycling

stability of $SeS_{0.7}$/CPAN composites. It delivers a reversible capacity of 780 mAh g^{-1}, and retains for 1200 cycles. The Coulombic efficiency of $SeS_{0.7}$/CPAN electrode is nearly 100%. Its high reversible capacity, long cycle life and high Coulombic efficiency demonstrate that CPAN can effectively confine $SeS_{0.7}$ and stabilize polysulfide and polyselenide intermediates. The rate performance of $SeS_{0.7}$/CPAN composite is shown in figure 5.7d. At a current density of 60 mA g^{-1}, its reversible capacity can reach 900 mAh g^{-1}. As the current density increases from 60 mA g^{-1} to 6 A g^{-1}, the reversible capacity retains about 50% of the capacity at 60 mA g^{-1}. With the current density increased to 12 A g^{-1}, the capacity decreases to 80 mAh g^{-1}, but the reversible capacity recovers to 900 mAh g^{-1} after the current density returns to 60 mA g^{-1}, demonstrating its superior robustness to tolerate current changes. The excellent electrochemical performance of $SeS_{0.7}$/CPAN composites demonstrates that CPAN is a good carbon host to enhance the kinetics and cycling stability of $SeS_{0.7}$ cathode material. Therefore, the $SeS_{0.7}$/CPAN composite is a promising alternative to sulfur for long cycle life and high power density lithium ion batteries.

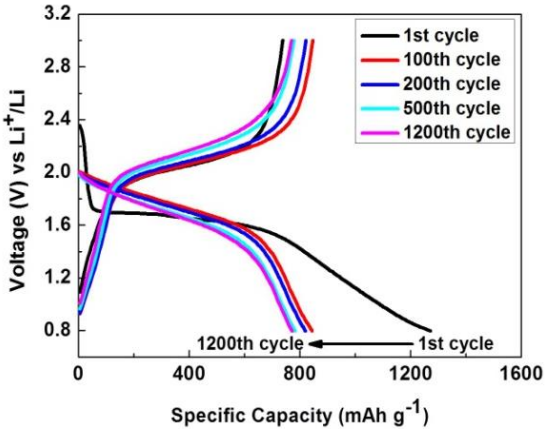

(a)

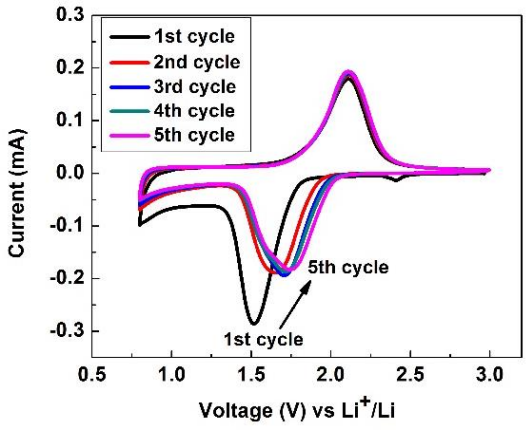

(b)

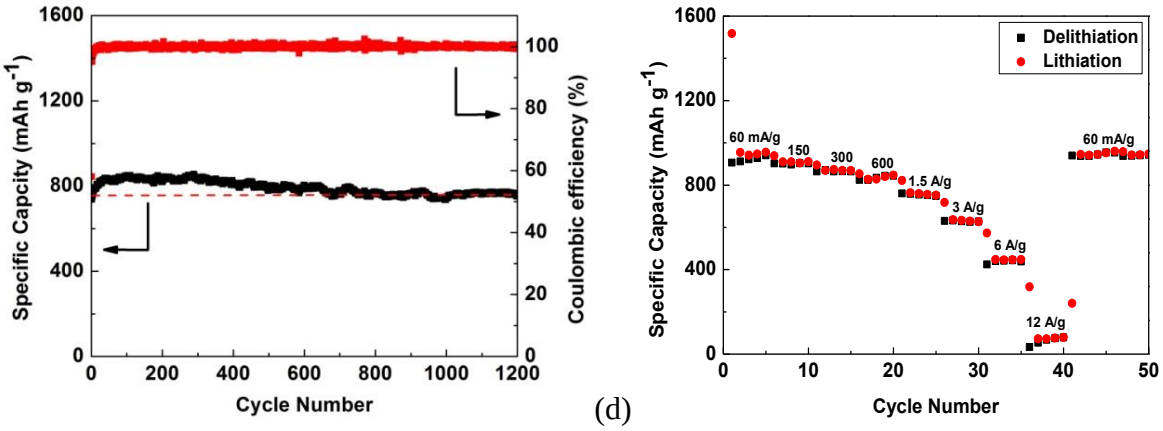

Figure 5.7. Electrochemical performance of $SeS_{0.7}$/CPAN composites. (a) The galvanostatic charge–discharge curves between 0.8 V and 3.0 V versus Li/Li^+; (b) Cyclic voltammograms at 0.1 mV s^{-1} in the potential window from 0.8 V to 3.0 V versus Li/Li^+; (c) Delithiation capacity and coulombic efficiency versus cycle number at the current density of 600 mA g^{-1}; (d) Rate performance at various C-rates.

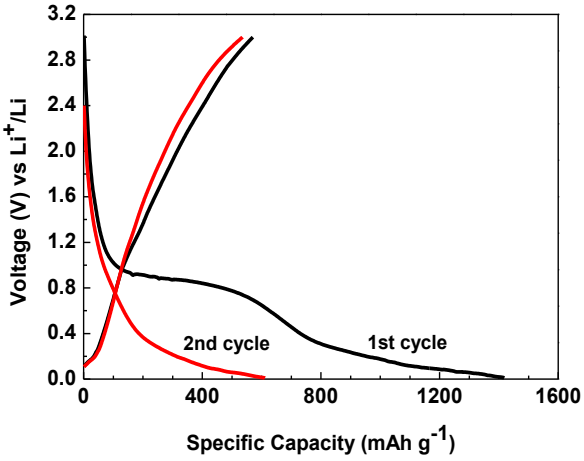

Figure 5.8. Charge/Discharge profile for carbon black at a current density of 200 mA g^{-1}.

It was reported that selenide anions can react with the carbonyl groups in the carbonate solvent and form an insulating SEI layer on the cathode surface [13, 67]. The SEI layer on Se/C cathode continuesly grows during charge/dishcarge cycles, reducing the cycling stability of Se/C cathode.

By the contrary, $SeS_{0.7}$/CPAN electrode shows exceptional cycling stability in carbonate-based electrolyte. To investigate the mechanism behind the long cycle life, XPS, a surface-sensitive spectroscopic technique, was employed to obtain the SEI information on $SeS_{0.7}$/CPAN electrode at a fully charged state (3.0 V) after the 1st deep charge/discharge cycle. To remove $LiPF_6$ salt, cycled $SeS_{0.7}$/CPAN electrode was immersed in propylene carbonate for 48 h before XPS analysis. A control experiment was carried out with a fresh $SeS_{0.7}$/CPAN electrode. As shown in figure 5.9, the XPS peaks for Na and N, resulting from sodium alginate binder and CPAN matrix, are clearly observed in the fresh $SeS_{0.7}$/CPAN electrode, but disappear in cycled $SeS_{0.7}$/CPAN electrode. The sulfur peaks cannot be observed in both fresh and cycled $SeS_{0.7}$/CPAN electrodes because the sulfur peaks overlap with selenium peaks in XPS spectrum. The disappearance of peaks for Na and N in cycled $SeS_{0.7}$/CPAN electrode is attributed to the formation of SEI layer on the surface of $SeS_{0.7}$/CPAN electrode that covers the sodium alginate binder and CPAN matrix. XPS is a surface-sensitive technique (10 nm). If $SeS_{0.7}$/CPAN electrode was covered by SEI layer, XPS cannot detect the material inside $SeS_{0.7}$/CPAN electrode, resulting in the disappearance of XPS peaks for Na and N. The formation of an insulating layer on the surface of Se cathode in carbonate-based electrolyte after the 1st cycle was also reported by Dr. Amine's group [13, 67]. To further investigate the role of SEI layer in $SeS_{0.7}$/CPAN electrodes, LiTFSI-TEGDME is employed as an electrolyte in $SeS_{0.7}$/CPAN coin cells, because TEGDME solvent in LiTFSI-TEGDME electrolyte is stable and will not be reduced to form SEI layer during the lithiation process [138]. As shown in figure 5.10, $SeS_{0.7}$/CPAN electrode in LiTFSI-TEGDME electrolyte suffers from quick capacity decline comparing to the highly stable cycling behavior of $SeS_{0.7}$/CPAN electrode in carbonate-based electrolyte. Moreover, the Coulombic efficiency (calculated based on lithiation capacity over delithiation capacity) in the initial 40 cycles is larger

than 100% due to the dissolution of polysulfides and polyselenides. It demonstrates that CPAN matrix cannot effectively confine polysulfides and polyselenides without a stable SEI layer. Therefore, though the formation of SEI layer induces a large irreversible capacity in the first lithiation/delithiation cycle of $SeS_{0.7}$/CPAN electrode (Figure 5.7a), it can prevent the $SeS_{0.7}$ from reacting with carbonate-based electrolyte, leading to the enhancement of cycling stability.

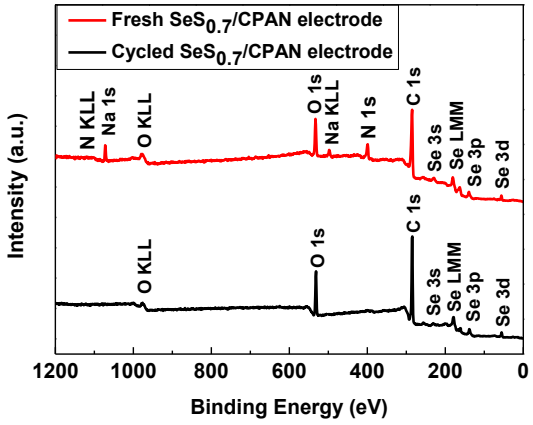

Figure 5.9. XPS spectrum of fresh $SeS_{0.7}$/CPAN electrode and cycled $SeS_{0.7}$/CPAN electrode.

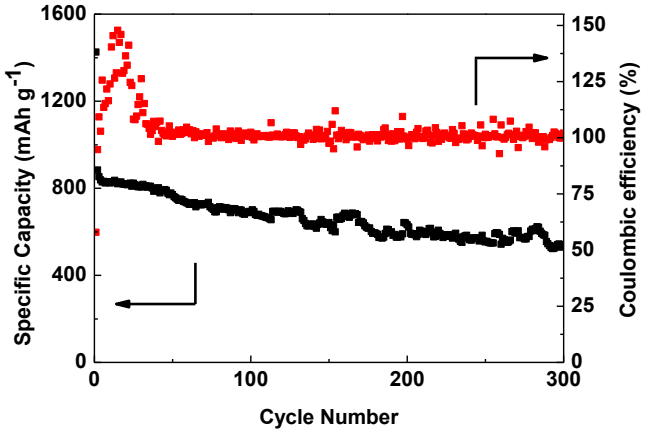

Figure 5.10. Electrochemical performance of $SeS_{0.7}$/CPAN composites in LiTFSI-TEGDME electrolyte. Lithiation capacity and coulombic efficiency versus cycle number at the current density of 600 mA g^{-1}.

The highly stable SEI layer during charge/discharge cycles was confirmed by electrochemical impedance spectroscopy (EIS). As shown in figure 5.11, the impedance curve of fresh $SeS_{0.7}$/CPAN cathodes exhibits two depressed semi-circles in the high and middle frequency regions, and a sloping line in the low frequency region. The two depressed semicircles in the high and middle frequency regions merge into a single depressed semicircle after first charge/discharge cycle, and it remains stable during the rest of cycles. The high-frequency semicircle stands for contact resistance of $SeS_{0.7}$/CPAN particles in fresh $SeS_{0.7}$/CPAN cathode, and sum of SEI layer resistance and particle-to-particle resistance for cycled $SeS_{0.7}$/CPAN cathode. The middle-frequency semicircle is attributed to charge transfer resistance. The low frequency line represents ion diffusion resistance in the $SeS_{0.7}$/CPAN particles. The fresh $SeS_{0.7}$/CPAN cell displays a large charge transfer resistance and ion diffusion resistance due to limit access of liquid electrolyte into $SeS_{0.7}$/CPAN electrode film. After volume expansion/shrinkage in the first cycle, more electrolytes can penetrate into electrode film, leading to lower charge transfer resistance and shorter ion diffusion distance in the following cycles. The reduced impedance in the second cycle decreases the overpotential, and shifts the lithiation potential to a higher value as demonstrated in the CV curves in Figure 5.7b. The slightly impedance increase in the high-frequency semicircle is attributed to the formation of SEI layer. However, the formed SEI layer is very stable during following charge/discharge cycles, as evidenced by the overlapped impedance curves. The low and stable resistance of SEI layer and charge transfer reaction is coincident with the exceptional rate capability of $SeS_{0.7}$/CPAN composites (in figure 5.7d), demonstrating its fast kinetics.

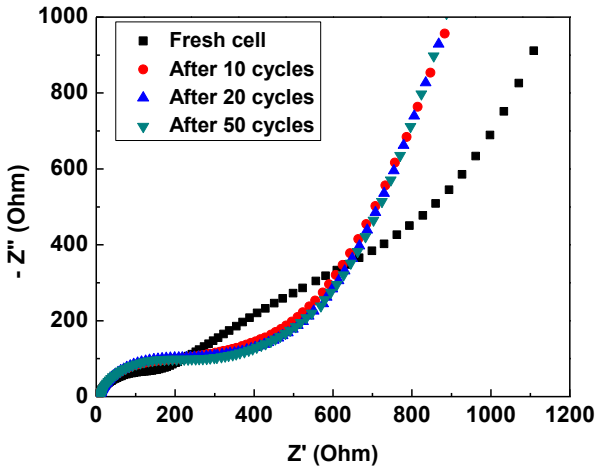

Figure 5.11. Impedance analysis for $SeS_{0.7}$/CPAN cell before test and after fully charge to 3.0 V and rest for 2 h.

The morphology change of $SeS_{0.7}$/CPAN composites during 100 deep charge/discharge cycles was studied by using TEM. From the TEM image in figure 5.12, it can be observed that the cycled $SeS_{0.7}$/CPAN composites still consist of round-shape particles with a size about 200 nm, which is similar to the fresh $SeS_{0.7}$/CPAN composites (Figure 5.2a). It demonstrates that $SeS_{0.7}$/CPAN composite maintains its morphology after 100 cycles, and the good morphology maintenance guarantees high cycling stability of $SeS_{0.7}$/CPAN composite. The rough surface of the $SeS_{0.7}$/CPAN particles is due to formation of the SEI layer. As shown in figure 5.12, A ~20 nm SEI layer can be observed on the surface of $SeS_{0.7}$/CPAN electrode after 100 cycles in $LiPF_6$-EC/DEC electrolyte. Moreover, the fuzzy SEI image of cycled $SeS_{0.7}$/CPAN in figure 5.13 is attributed to the low electronic conductivity of SEI layer. Figure 5.14 shows the TEM image of $SeS_{0.7}$/CPAN electrode after first cycle in LiTFSI-TEGDME electrolyte. A clean surface of $SeS_{0.7}$/CPAN electrode without SEI layer is observed. To further confirm that SEI layer is not formed on this electrode, TEM EDX mapping is employed to check the elemental distribution of this electrode. As shown in figure 5.15, C, S and Se can still be observed in the cycled electrode,

but F which is a main component of SEI layer cannot be observed, demonstrating that SEI layer is not formed on electrodes in LiTFSI-TEGDME electrolyte. The elemental distribution in carbon black and binder (Sodium alginate), surrounding $SeS_{0.7}$/CPAN spheres, is also investigated by TEM EDX. As shown in figure 5.16, C, S and Se are observed in the outside of $SeS_{0.7}$/CPAN spheres. The C peak results from carbon black and binder. The S and Se peaks result from the dissolution of polysulfides and polyselenides in LiTFSI-TEGDME electrolyte, which triggers the shuttle effect. F peak is not observed, further demonstrating the absence of SEI layer.

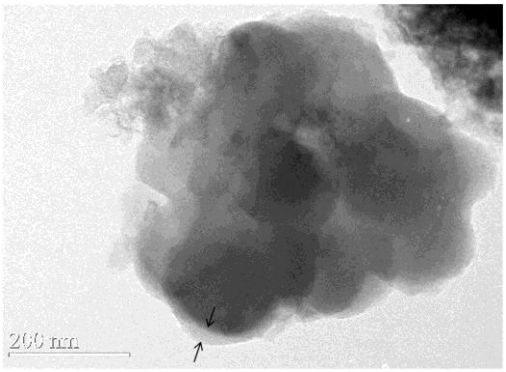

Figure 5.12. TEM image of the $SeS_{0.7}$/CPAN electrode after 100 cycles in Li-ion batteries.

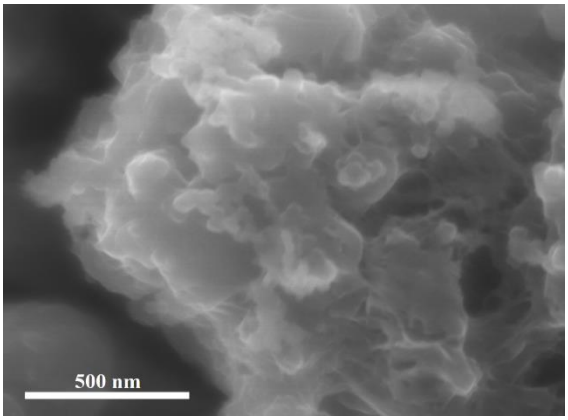

Figure 5.13. SEM image of the $SeS_{0.7}$/CPAN electrode after 100 cycles in Li-ion batteries.

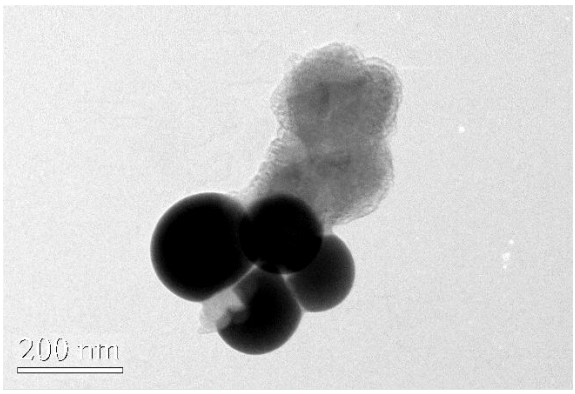

Figure 5.14. TEM image of the $SeS_{0.7}$/CPAN electrode after first cycle in LiTFSI-TEGDME electrolyte.

To investigate how the *in-situ* carbonization of PAN affects the cycling stability, the electrochemical performance of *ex-situ* carbonized SeS_2/pre-carbonized PAN (PCPAN) composite and pristine SeS_2 was also measured as controls to compare with *in-situ* formed $SeS_{0.7}$/CPAN composite. The SeS_2/PCPAN composite was synthesized by pre-carbonization of PAN (PCPAN in Figure 5.1a), and then infusing SeS_2 into PCPAN under the same condition as $SeS_{0.7}$/CPAN composite. TG analysis shows that only 13% of SeS_2 is infused into PCPAN (figure 5.17), which is much lower than the content (33%) of $SeS_{0.7}$ in *in-situ* formed $SeS_{0.7}$/CPAN composite. The low SeS_2 content in *ex-situ* formed SeS_2/PCPAN composite is because the well-formed N-containing carbon (ring) structures in PCPAN hinder the diffusion of SeS_2 into carbonized PAN matrix. The first lithiation/delithiation curves of SeS_2/PCPAN composites in Figure 5.18 (a) exhibit higher overpotential and larger irreversible capacity (~62%) than $SeS_{0.7}$/CPAN composite (Figure 5.7a). The charge/discharge potential of *ex-situ* formed SeS_2/PCPAN in the following charge/discharge cycles is also slightly lower than that of *in-situ* formed $SeS_{0.7}$/CPAN. The reversible capacity of $SeS_{0.7}$/PCPAN composite is 1050 mAh g^{-1}, which is higher than that of $SeS_{0.7}$/CPAN composite. As shown in figure 5.18 (b), SeS_2/PCPAN

composite also exhibits excellent cycling stability. Although *ex-situ* formed SeS_2/PCPAN composite can maintain reversible capacity of 1050 mAh g^{-1} for 700 cycles, the low SeS_2 loading significantly reduces the overall capacity. Therefore, the *in-situ* formed $SeS_{0.7}$/CPAN composite is a more advanced cathode material than *ex-situ* formed SeS_2/PCPAN composite. As another control, the pristine SeS_2 electrode (figure 5.19a) shows much worse battery performance than both *in-situ* formed $SeS_{0.7}$/CPAN and *ex-situ* formed SeS_2/PCPAN electrodes. It delivers high irreversible capacity (~70%) and low lithiation capacity in the first cycle due to the low conductivity of SeS_2. Nevertheless, the formation of SEI layer stabilizes the pristine SeS_2 and increases the Coulombic efficiency to almost 100% by preventing the shuttle reaction.

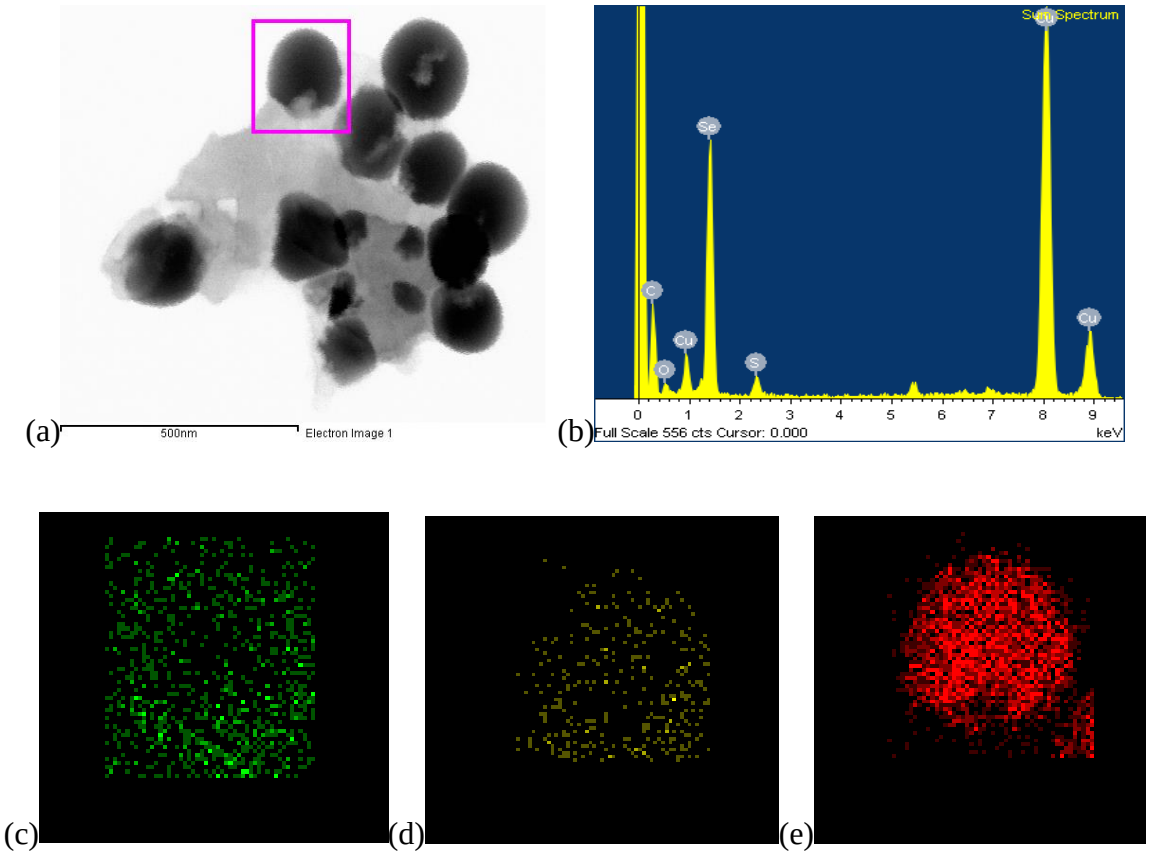

Figure 5.15. TEM EDX mapping for $SeS_{0.7}$/CPAN electrode after first cycle in LiTFSI-TEGDME electrolyte. TEM image of $SeS_{0.7}$/CPAN composites (a) and EDS elemental

distribution (b) and mapping images of the SeS_x/CPAN composites, marked by purple square, for carbon (c), sulfur (d) and selenium (e).

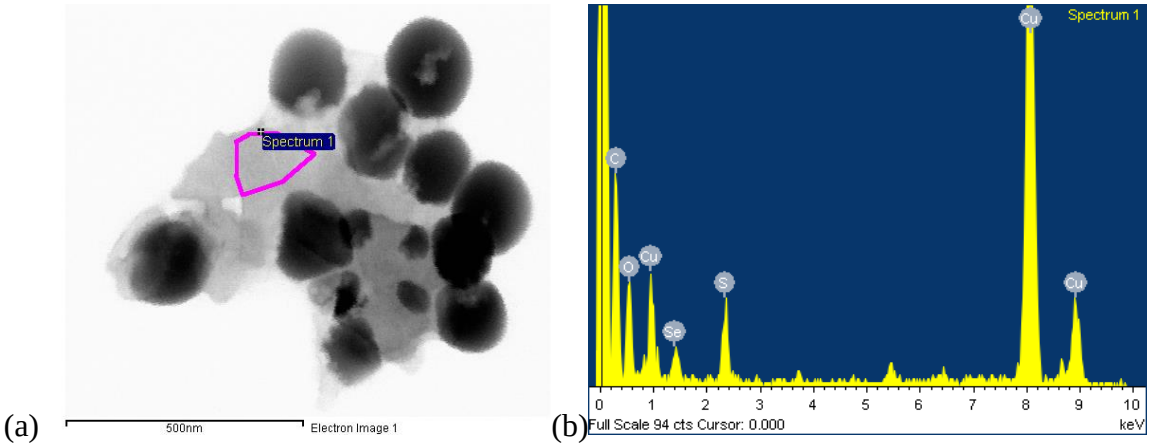

Figure 5.16. TEM EDX for $SeS_{0.7}$/CPAN electrode after first cycle in LiTFSI-TEGDME electrolyte. TEM image of $SeS_{0.7}$/CPAN composites (a) and EDX elemental distribution (b) of the marked purple line.

The effect of SEI layer on preventing the shuttle reaction was investigated by comparing the charge/discharge behaviors of pristine SeS_2 in carbonate-based electrolyte and LiTFSI-TEGDME electrolyte. The sloping lithiation plateau of pristine SeS_2 in $LiPF_6$-EC/DEC electrolyte centered at 1.7 V shifts to flat plateaus centered at 2.0 V in LiTFSI-TEGDME electrolyte (figure 5.19b). LiTFSI-TEGDME is a standard electrolyte for S and SeS_2 cathodes because it does not react with polysulfides/polyselenides [13, 67]. The reversible capacity of pristine SeS_2 in LiTFSI-TEGDME electrolyte continuously decreases from 1st cycle to 10th cycle, while its reversible capacity in $LiPF_6$-EC/DEC electrolyte remains stable after the first cycle. Thus, the SEI layer formed in carbonate-based electrolyte stablizes the SeS_2 electrode and increases the Coulombic efficiency.

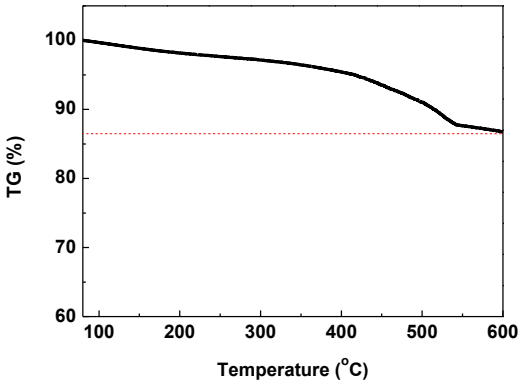

Figure 5.17. The TGA analysis for $SeS_{0.7}$/PCPAN composites.

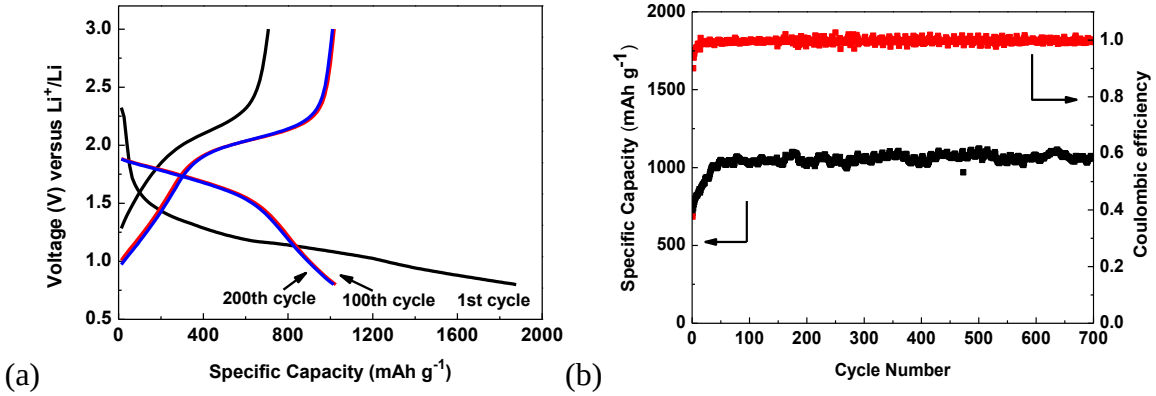

Figure 5.18. (a) The charge-discharge profiles for $SeS_{0.7}$/PCPAN composite in $LiPF_6$ electrolyte; (b) cycle life for $SeS_{0.7}$/PCPAN composite in $LiPF_6$ electrolyte at a current density of 1.5 A g^{-1}.

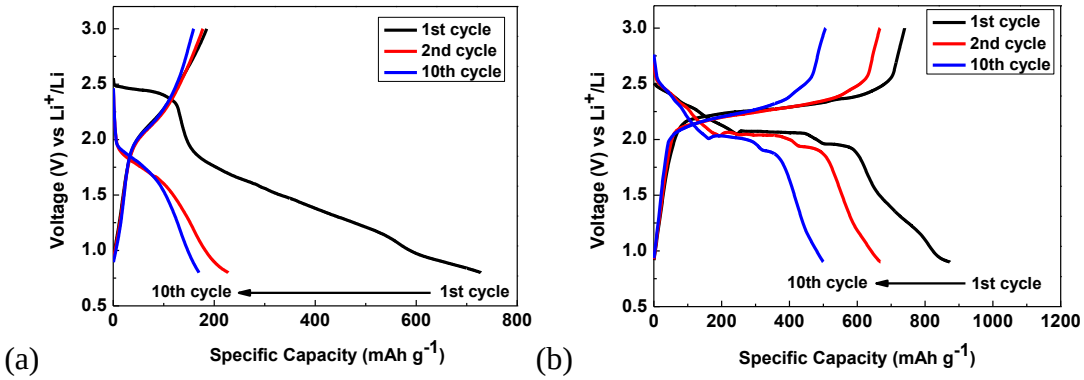

Figure 5.19. The charge-discharge profiles for pristine SeS_2 in $LiPF_6$-EC/DEC electrolyte (a) and LiTFSI-TEGDME electrolyte (b) at a current density of 60 mA g^{-1}.

5.4 Conclusion

The $SeS_{0.7}$/CPAN composites are synthesized by annealing the mixture of SeS_2 and PAN at 600 °C under vacuum. The CPAN matrix can enhance the electrical conductivity of $SeS_{0.7}$ material and constrain the polysulfide and polyselenide intermediates during the lithiation/delithiation process, leading to superior electrochemical performance of $SeS_{0.7}$/CPAN composites. The formation of stable SEI layer on the surface of $SeS_{0.7}$/CPAN electrode further contributes to the long cycle life and high Coulombic efficiency. The composite delivers a reversible capacity of 780 mAh g^{-1} and retains for 1200 cycles. As the current density increases from 60 mA g^{-1} to 6 A g^{-1}, its capacity retention is about 50%, demonstrating its high rate capability. Therefore, $SeS_{0.7}$/CPAN composite is a promising cathode material for long cycle life and high power density lithium ion batteries.

Chapter 6 Self-assembled Organic Nanowires for High Power Density Lithium Ion Batteries

6.1 Introduction

Lithium ion batteries, the best power sources for portable electronics, are considered as the most promising energy storage devices for emerging electric vehicles and smart grids [2, 71]. Currently, lithium ion batteries largely rely on inorganic compounds as electrodes such as $LiCoO_2$ and $LiFePO_4$ [22, 139]. Most of these compounds are synthesized using non-earth-abundant resources via energy-demanding ceramic processes [72]. Recycling of used batteries further consumes large quantities of energy and chemicals, releasing more CO_2. To satisfy the urgent demand for rechargeable energy storage devices in electric vehicles and smart grids, next generation battery electrodes should be made from renewable or recyclable resources via low energy consumption processes. One possible approach is to use biomass or recyclable organic materials as electrode materials via solution phase routes [73]. In addition, most of organic compounds are degradable in the environment, so the organic electrode materials are environmentally benign.

Recently, carbonyl group based organic materials such as purpurin [74], tribrominated trioxotriangulene [75], perylenetetracarboxylic anhydride [76] and other compounds [140-151] have been investigated as electrodes for Li-ion batteries, and some organic materials can also been used for Na-ion battery electrodes [80, 130]. However, due to dissolution of organic compounds in electrolyte and very low electronic conductivity, the electrochemical performance of these sustainable organic electrode materials is much worse than their inorganic counterparts. The solubility of organic compounds could be reduced by enhancing their polarities via salt

formation [77] and solubility of organic salt in organic electrolyte can be further reduced by increasing the concentration of lithium salt in organic electrolyte that has effectively suppressed dissolution of polysulfide in lithium sulfur batteries [66]. Although use of organic salts such as lithium salt of tetrahydroxybenzoquinone [79] can mitigate the dissolution issue [72], the low electronic conductivity of organic salts and volume change during lithiation/delithiation still limits the power density and cycling stability of organic electrodes. Due to the very low electrical conductivity of most organic compounds, up to 30 wt% of conductive carbon black is normally mixed into organic electrode to provide electron pathways for the electrochemical reactions and another ~5-10% (by weight) nonconductive polymer binders are also needed to mechanically bind all the components into an electrode. Even adding 30 wt% of carbon black, there is only a portion of active materials contributes to the output power of a battery in organic electrodes due to large size of organic salt particles. A recent work of organic $Li_4C_8H_2O_6$ nanosheets for Li-ion batteries has demonstrated that nanosheet structure provides short Li ion diffusion pathways and large contact areas for both conductive carbon and electrolyte, leading to high rate capability [78].

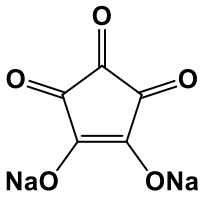

Scheme 6.1. Molecular structure of croconic acid disodium salt.

In this study, croconic acid disodium salt (CADS) wires are used as models to investigate the size effect on the battery performance of organic electrodes. CADS has a cyclopentene backbone with three carbonyl groups, and two of them are connected by a conjugated chemical bond as shown in scheme 6.1. The two carbonyl groups in CADS can participate in the reversible reaction with lithium ions [73], providing a theoretical capacity of 288 mAh g^{-1}. According to the

reported reaction mechanism for carbonyl group based organic electrodes, only carbonyl groups that are connected by conjugated structure such as carbon-carbon double bond or benzene ring can participate in the lithiation reaction [77]. There are three carbonyl groups in CADS. Only two of them are connected by conjugated structure, thus active for the lithiation reaction. In addition, the specific capacity of CADS nanowire shown in figure 6.5 also support the reaction mechanism. The specific capacity of CADS nanowire is 200 mAh g^{-1} at a low current density of 0.1 C, which is close to the theoretical capacity (288 mAh g^{-1}) of CADS based on lithiation reaction of two carbonyl groups. CADS nanowires with diameter size ranging from 150 nm to 4 μm were synthesized by anti-solvent crystallization method to reduce the strain and Li-ion diffusion length. 150 nm CADS nanowire exhibits the superior capacity, rate capability and cycling stability. The theoretical calculation for lithiation and delithiation of CADS suggests that sodium ions in CADS will be gradually replaced by lithium during the lithiation and delithiation of CADS electrode, which is confirmed by Inductively Coupled Plasma test. Since Li croconate has a more stable crystal structure than Na croconate, the formation of Li croconate further enhances the cycling stability of CADS electrode. To our best knowledge, CADS nanowires demonstrate one of the best battery performances for reported organic compounds in terms of cycling stability and rate performance at a low carbon content [144].

6.2 Experimental Section

Fabrication of CADS nanowires: all materials are purchased from Sigma Aldrich, and used without further purification. 0.75 mL CADS aqueous solution with a concentration of 0.8 mg mL^{-1} was added into 12 mL acetone with bath sonication. After 10 minutes sonication, the yellow precipitation was collected through filtration. Several bottles of above sample were

collected for further characterization. CADS microwire was prepared with the same method, but a higher concentration (2 mg mL^{-1}) of CADS aqueous solution was used.

Fabrication of CADS micropillar: the as received CADS powder was directly dissolved in water to prepare 5mg/ml CADS water solution. Then, the 5mg/ml CADS water solution was cast on the stainless steel foil and kept at room temperature for 48 hours to evaporate water. The resulting sample was collected for further characterization.

Material Characterizations: Scanning electron microscopy (SEM) image was taken by Hitachi SU-70 analytical ultra-high resolution SEM (Japan). X-ray diffraction (XRD) pattern was recorded by Bruker Smart1000 (Bruker AXS Inc., USA) using CuKα radiation.

Inductively Coupled Plasma test: Inductively Coupled Plasma (ICP) test was performed on PerkinElmer Optima 4300 DV ICP-Optical Emission Spectrometer. Both the fresh and cycled electrodes were dissolved in deionized water by sonication. Before ICP test, the cycled electrode was immersed in diethyl carbonate for 48 h to remove the $LiPF_6$ salt. Six standard solutions with the Li^+ or Na^+ concentration of 0.0 mg L^{-1}, 0.025 mg L^{-1}, 0.05 mg L^{-1}, 0.1 mg L^{-1}, 0.25 mg L^{-1}, 0.5 mg L^{-1} were prepared to obtain a standard curve of peak intensity vs. ion concentration (relationship between peak intensity and the concentrations of lithium ion or sodium ion). The concentrations of lithium ion and sodium ion in fresh and cycled electrodes were obtained by comparing the peak intensity of fresh and cycled electrodes to the standard peak intensity in the standard curve of peak intensity vs. ion concentration.

Electrochemical Measurements: The recrystallized CADS, CADS microwire and CADS nanowire were mixed with carbon black and Polyvinylidene fluoride (PVDF) binder to form slurry at the weight ratio of 70:20:10, respectively. The electrode was prepared by casting the slurry onto aluminum foil using a doctor blade and dried in a vacuum oven at 100 °C overnight.

The electrode was cut into circular pieces with diameter of 1.2 cm for coin cell testing, and the area mass loading of the electrode is ~0.8 mg cm^{-2}. Li ion batteries were assembled with lithium metal as the counter electrode, 1 M $LiPF_6$ in a mixture of ethylene carbonate/diethyl carbonate (EC/DEC, 1:1 by volume) as the electrolyte, and Celgard®3501 (Celgard, LLC Corp., USA) as the separator. Electrochemical performance was tested using Arbin battery test station (BT2000, Arbin Instruments, USA). Capacity was calculated on the basis of the mass of CADS micropillar, CADS microwire or CADS nanowire. Cyclic voltammogram were recorded at a scan rate of 0.1 mV/s between 0.8 – 2.8 V using Solatron 1260/1287 Electrochemical Interface (Solatron Metrology, UK). Impedance analysis was also performed by Solatron 1260/1287 Electrochemical Interface.

Calculations were performed with the Amsterdam Density Functional (ADF) suite of softwares [1], using a triple-zeta with polarization basis set. ADF uses Slater-type orbitals (STOs), as opposed to most quantum-chemistry codes which use Gaussian-type orbitals. STOs feature correct decay at long distances and correctly describe the nuclear-electron cusp.

6.3 Results and Discussion

(a) 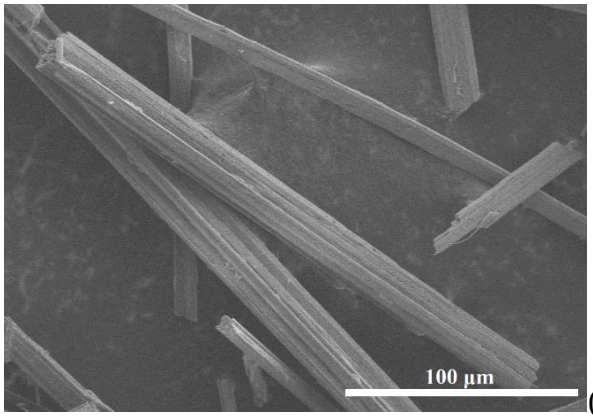

(b) 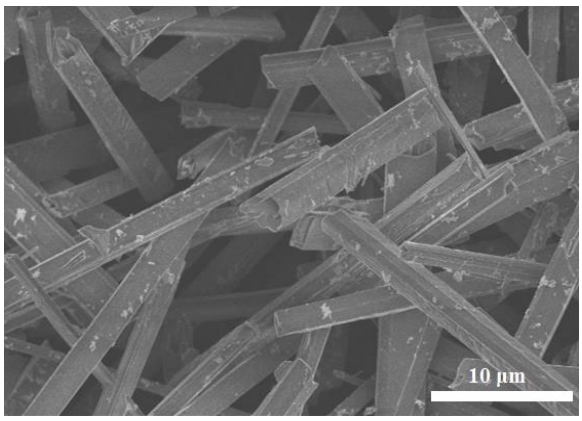

(c) 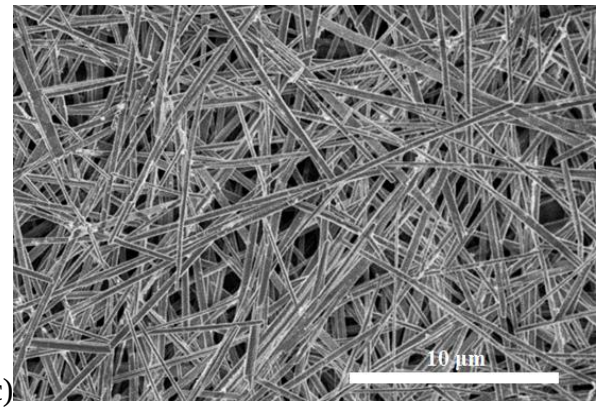

(d) 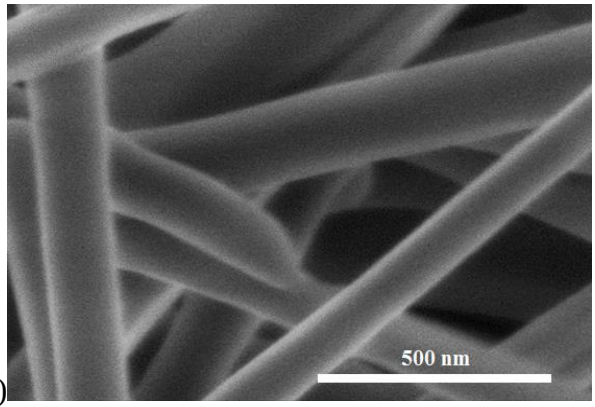

Figure 6.1. SEM images for CADS micropillar (a), CADS microwire (b) and CADS nanowire (c, d).

Crystal CADS micropillars with the width of 10 μm and length longer than 100μm (Figure 6.1a) were prepared by directly recrystallizing CADS from water, and are used as control samples. Due to the insulating nature of CADS, the large particle size will significantly increase the transportation resistance of Li-ion and electron in the CADS micropillars. The large size and small surface area of CADS micropillar also results in poor contact between CADS and conductive carbon, thus remarkably reducing the charge transfer reaction kinetics. To improve the lithiation/delithiation kinetics, CADS microwire with an average diameter about 4 μm (Figure 6.1b) and CADS nanowire with a mean diameter about 150 nm (Figure 6.1c & 6.1d) were fabricated at room temperature using anti-solvent crystallization method, a facile synthetic route. The growth of CADS nanowires is driven by the reduction of the solubility of CADS when CADS aqueous solution is added into acetone (a poor solvent for CADS). Under bath sonication, CADS starts to crystallize within a few minutes due to the poor solubility in the water/acetone mixture solvent and self-assemble into nanowires, which is possibly due to π-π interaction between CADS molecules [152]. The CADS wires synthesized by anti-solvent crystallization method have very uniform diameters (Figure 1b and1c). The diameter of CADS

wires can be manipulated by tuning the concentration of CADS in aqueous solution. The lower concentration CADS aqueous solution yields thinner CADS nanowires.

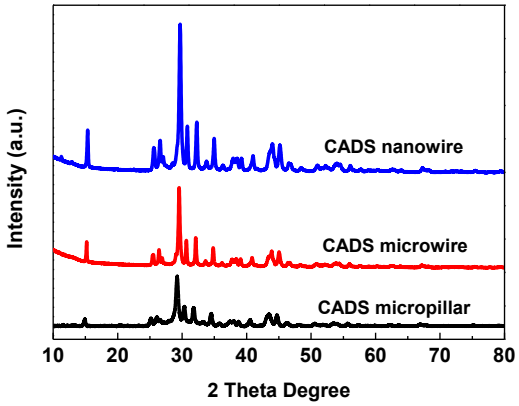

Figure 6.2. XRD patterns of CADS micropillar, CADS microwire and CADS nanowire.

The crystal structures of three CADS samples are identified by X-ray diffraction (XRD). The XRD patterns in figure 6.2 reveal that the CADS micropillar, CADS microwire and CADS nanowire have the same crystal structure. No impurity peak is observed in all three CADS samples. The peak intensity of CADS nanowire is stronger than that of CADS micropillar and CADS microwire, demonstrating that CADS nanowires have high crystallinity and relatively uniform crystal size.

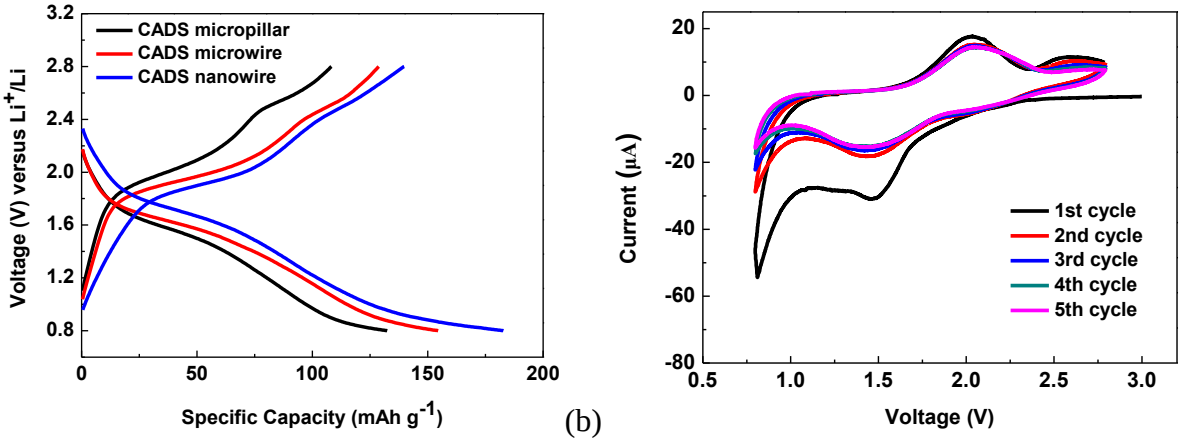

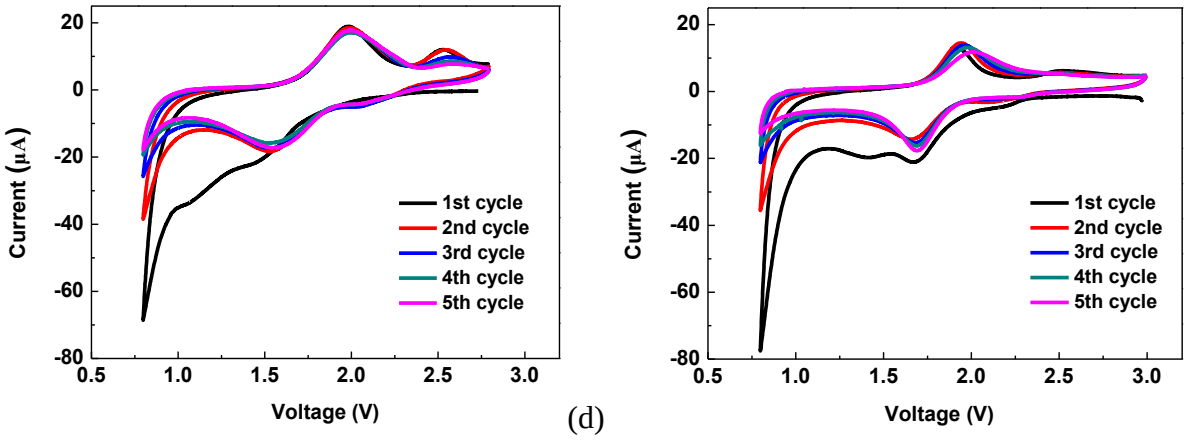

Figure 6.3. Electrochemical performance of CADS micropillar, CADS microwire and CADS nanowire. (a) Charge and discharge curves of CADS micropillar, CADS microwire and CADS nanowire for the second cycle; Cyclic voltammograms for CADS micropillar (b), CADS microwire (c), CADS nanowire (d).

The charge and discharge profiles for CADS micropillar, CADS microwire and CADS nanowire in the second cycle were measured at a current density of 0.2 C (1 C is defined as 288 mA g^{-1}) and are shown in Figure 6.3a. The lithiation potential decreases and delithiation potential increases with the size of CADS nanowire increases from 150 nm to 4 μm and then to 10 μm. The cyclic voltammetry (CV) of three CADSs with different diameter in figure 6.3b-d shows a peak at 1.6 V with a small shoulder at 2.1 V during lithiation, and a peak at 2.0 V with a small shoulder at 2.6 V during delithiation, demonstrating that CADS undergoes a two-step reaction with lithium ions. The two carbonyl groups connected by carbon-carbon double bond react with lithium ions step by step. The potential hysteresis (ΔV) between the cathodic peak and anodic peak is 0.62 V for CADS micropillar, 0.47 V for CADS microwire and 0.30 V for CADS nanowire, indicating that the overpotential of CADS nanowire is smaller than CADS micropillar and CADS microwire. The increase of potential hysteresis with wire size confirms that lithiation/delithiation kinetics decreases with the increase of wire size. The equilibrium potentials

of CADS are estimated by averaging the lithiation and delithiation potential. The equilibrium lithiation potentials of CADS are 1.8 V and 2.35 V. As shown in CV curves in Figure 6.3, the lithiation peak potential slightly increases to more positive value with lithiation and delithiation cycles. To explore the mechanism for two-step reaction and potential shift, the first principle DFT calculation is applied to calculate the lithiation process. Table 6.1 collects the values of the total electronic bonding energy of various species involved in the reduction of CADS. Table 6.2 collects the calculated reduction potential of the CADS with respect to a lithium electrode potential. Figure 6.4 schematically reports the energy levels of Na and Li croconate for the three reduced forms considered. The potentials in Table 6.2 indicate that the one-electron and the two-electron reduction of CADS occur at very similar potentials. The sequential one-electron reductions are estimated to be 2.42 V and 2.36 V, which is higher than the equilibrium potential demonstrated by CV scans (2.35 V and 1.8 V). The large potential difference (2.36-1.8=0.56V) in second step reaction is probably attributed to the strain overpotential induced by the volume expansion at high lithiation levels. A large strain overpotential of 0.6 V was reported for lithiation of Sn [153]. Due to the low strain at low lithiation level, the calculated potential in the first step reaction is similar to measured potential in CV. However, the calculations are unable to ascertain whether the electrochemical potentials are due to a concerted two-electron process or two sequential one-electron processes. Analyzing the overall stability of the sodium and lithium croconate indicates (see Table 6.1) that lithium croconate forms a more stable crystal than the sodium salt. Thus, it is possible that the CADS undergoes a chemical exchange from sodium croconiate to lithium croconate. For this reason, additional simulations were carried out for the reduction of lithium croconate. The simulations show that the reduction potential for Lithium croconate is 2.56 V and 2.49 V for the single one-electron processes, respectively. Thus, if a

counter ion exchange occurs during the CV scans, the reduction potential should slightly increases, which is in well agreement with CV scans in Figure 6.3. The simulations qualitatively reproduce the potentials determined experimentally and predict a possible Sodium-Lithium exchange during the lithiation and delithiation of CADS electrode. Such a prediction is further confirmed by Inductively Coupled Plasma (ICP) test. A fresh CADS electrode and a CADS electrode after first cycle are dissolved in water separately, and then Li^+ and Na^+ concentration in water was measured by ICP. The result shows that the concentrations of Li^+ and Na^+ in fresh electrode are 0 and 0.135 mg L^{-1}, respectively, while the concentrations of Li^+ and Na^+ in cycled electrode are 0.103 mg L^{-1} and 0.020 mg L^{-1}, demonstrating that most of sodium ions in CADS are exchanged by lithium ions.

Compound	Bonding Energy (eV)	Homo-Lumo gap (eV)
Na_2CA	-96.2954	3.39
Li_2CA	-98.4320	3.88
Li_3CA	-101.4177	2.13
Na_2LiCA	-99.1397	1.25
Na_3LiCA	-100.6417	0.61
Na_2Li_2CA	-101.9261	0.96
Li_4CA	-104.3329	1.94
Li	-0.4295	

Table 6.1. Total bonding energy and HOMO-LUMO gap in eV.

Electrochemical process	Potential	# of electrons
$Na_2CA + Li \rightarrow Na_2LiCA$	2.42	1
$Na_2LiCA + Li \rightarrow Na_2Li_2CA$	2.36	1
$Na_2CA + 2Li \rightarrow Na_2Li_2CA$	2.39	2
$Li_2CA + Li \rightarrow Li_3CA$	2.56	1
$Li_3CA + Li \rightarrow Li_4CA$	2.49	1
$Li_2CA + 2Li \rightarrow Li_4CA$	2.52	2

Table 6.2. Summary of the calculated electrochemical potentials from the energies in Table 6.1.

The formation and growth of solid electrolyte interphase (SEI) layer on the surface of CADS is also evidenced by CV in Figure 6.3b-d. A sharp peak at 0.8 V in the first anodic scan without corresponding cathodic peak is observed in the cyclic voltammograms of CADS micropillar, CADS microwire and CADS nanowire. The sharp peak at 0.8 V becomes weaker after each cycle, suggesting that stable SEI layer is formed during the first cycle.

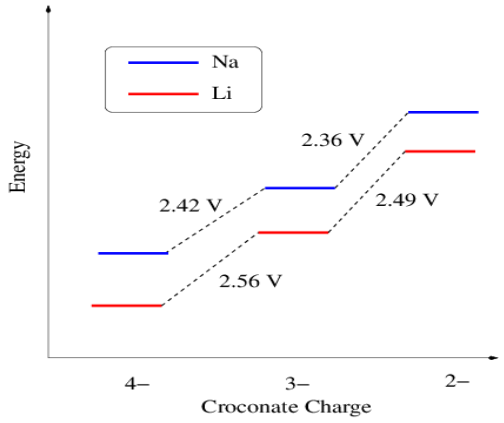

Figure 6.4. Calculated energy levels of NaCA and LiCA. Potentials shown are referenced to the Li electrode.

The cycling performance of CADS electrodes is shown in figure 6.5a. The specific capacities of CADS micropillar, CADS microwire and CADS nanowire decrease a little in the first 20 cycles,

and then it becomes very stable for CADS micropillar, and even increase back to original capacity at 110 cycles for CADS nanowires, and slightly lower than initial capacity at 110 cycles for CADS microwires. This kind of cycling behavior is also observed in nano-Si/C composite [154]. As indicated by Fig. 6.3b-d, the reductive peak at 0.8 V, corresponding to the formation of SEI layer, decays rapidly during the initial cycles, resulting in capacity decline. To identify the mechanism for capacity increase of CADS after 20 cycles, the charge/discharge profiles of CADS nanowire, CADS microwire and CADS micropillar from 5^{th} cycle to 30^{th} cycle are shown in figure 6.6. From the charge/discharge curves of CADS nanowires at different cycles in figure 6.6 (a), it can be clearly observed that the lithiation plateau and delithiation plateau shift close to each other upon cycling, indicating smaller overpotential and faster kinetics. At initial cycles, the electrolyte does not fully penetrate to the entire electrode, leading to large overpotential and slow kinetics. Upon cycling, the large volume expansion and shrinkage of CADS increase the porosity of the CADS electrodes, allowing electrolyte to penetrate the entire electrode, thus shortening the ion diffusion pathway and lowering the overpotential after 30 cycles. The fast kinetics enhances the utilization of organic electrode, resulting in increase of capacity. However, for micro-size CADS electrode, the large volume change also generates cracks, resulting in capacity decline in the initial cycles. The formation of cracks offsets the kinetic enhancement induced by electrolyte penetration so that the overpotential change from 5^{th} cycle to 30^{th} cycle is very small as evidenced by the little plateau shift in figure 6.6 (b) and (c). The reversible capabilities of CADS micropillar, CADS microwire and CADS nanowire measured at a current density of 0.2 C are 85 mAh g^{-1}, 132 mAh g^{-1} and 177 mAh g^{-1}, respectively. CADS nanowire retains its initial capacity after 110 deep charge/discharge cycles.

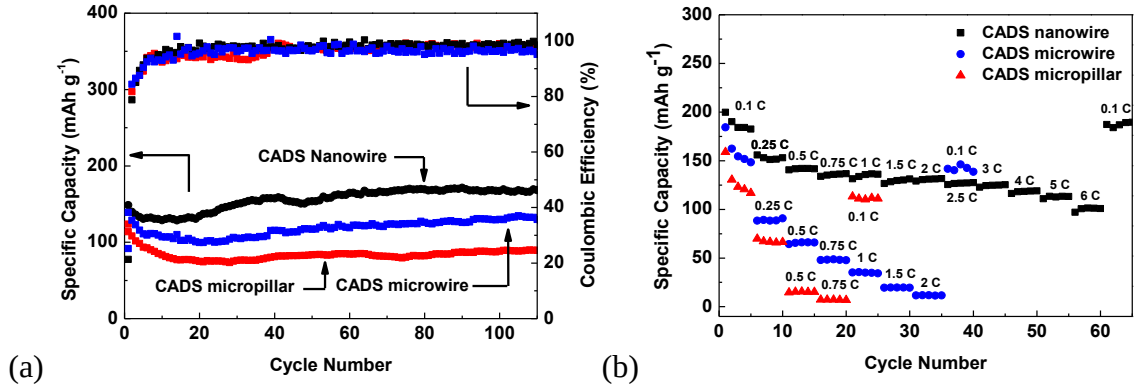

Figure 6.5. Cycle life (a) and rate capability (b) of CADS micropillar, CADS microwire and CADS nanowire. (1 C is defined as 288 mA g^{-1})

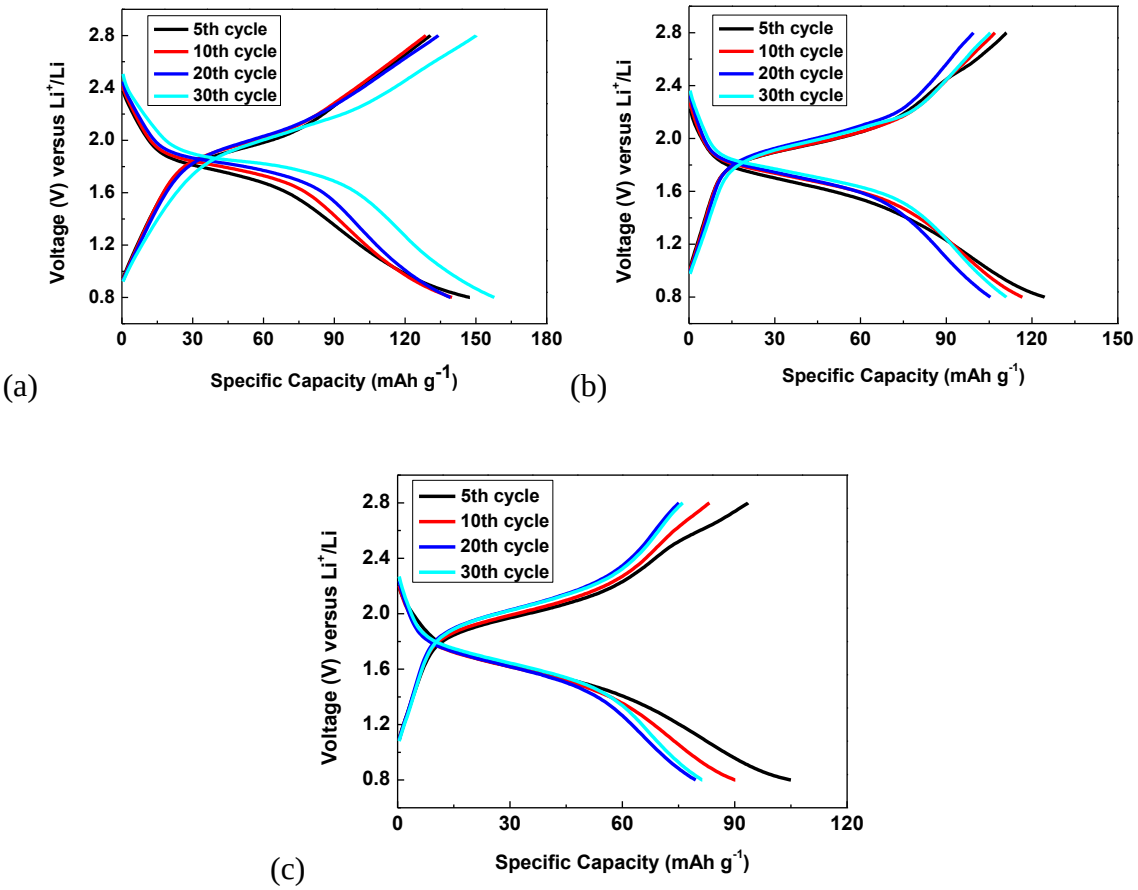

Figure 6.6. The charge/discharge profiles from 5th cycle to 30th cycle for CADS nanowire (a), CADS microwire (b) and CADS micropillar (c).

Since CADS is an insulating material, lithium ions and electrons cannot be easily transported into the inside of bulk CADS material, but the smaller size and larger surface area of CADS nanowire enables more CADS to react with lithium ions, and lithium ions can quickly transfer to inside of CADS, so the specific capacity and rate capability of CADS nanowire is much higher than that of CADS micropillar and CADS microwire. The rate capability of CADS micropillar, CADS microwire and CADS nanowire is shown in figure 6.5b. With the current density increases from 0.1 C to 0.75 C, the specific capacity of CADS micropillar decreases rapidly from 125 mAh g^{-1} to 7 mAh g^{-1}. Although the capacity of CADS microwire is still 48 mAh g^{-1} at the current density of 0.75 C, the specific capacity of CADS microwire decreases from 160 mAh g^{-1} to 11 mAh g^{-1} when the current density increases from 0.1 C to 2 C, indicating the inferior rate performance of CADS microwire due to the large diameter (~4 μm) of microwire. On the contrary, the smaller size and larger surface area of CADS nanowire can shorten the lithium ion diffusion length and enables better contact between CADS and conductive carbon. Therefore, CADS nanowire retains 50% of its initial capacity (200 mAh g^{-1}) subjected to the current density up to 6 C. After the current density returns to 0.1 C, the capacity of CADS nanowire recovers to its initial capacity immediately. Hence, from the electrochemical performance of CADS micropillar, CADS microwire and CADS nanowire, we can conclude that nanowire structure makes great contribution to the high capacity and high power density of CADS material.

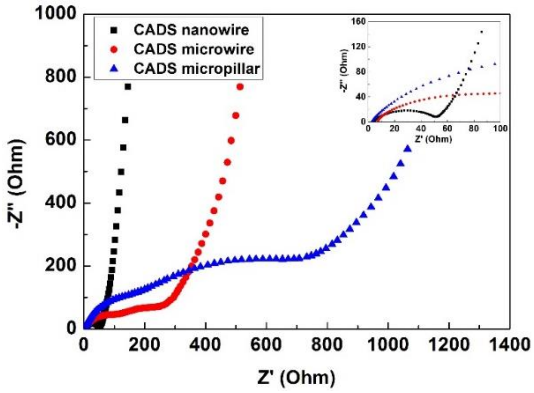

Figure 6.7. EIS spectra for CADS micropillar electrode, CADS microwire electrode and CADS nanowire electrode. (The inset is magnification of the semi-circle of CADS Nanowire)

The reaction kinetics of CADS materials was investigated using electrochemical impedance spectroscopy. The high frequency semicircle represents interface resistance includes contact impedance or SEI impedance, and charge transfer impedance, while the low frequency line stands for ion diffusion resistance. As shown in figure 6.7, both the interface and diffusion impedances of CADS nanowire are much lower than that of CADS micropillar and CADS microwire, indicating the lower interface resistance and better kinetics of CADS nanowire. The interface resistance of CADS nanowire is about 50 Ohm, while that for CADS micropillar electrode and CADS microwire electrode have much higher value of 300 Ohm and 750 Ohm, respectively. The impedance results convince that the high capacity and superior rate capability of CADS nanowire is due to the large electrochemical reaction interface and short Li diffusion pathway.

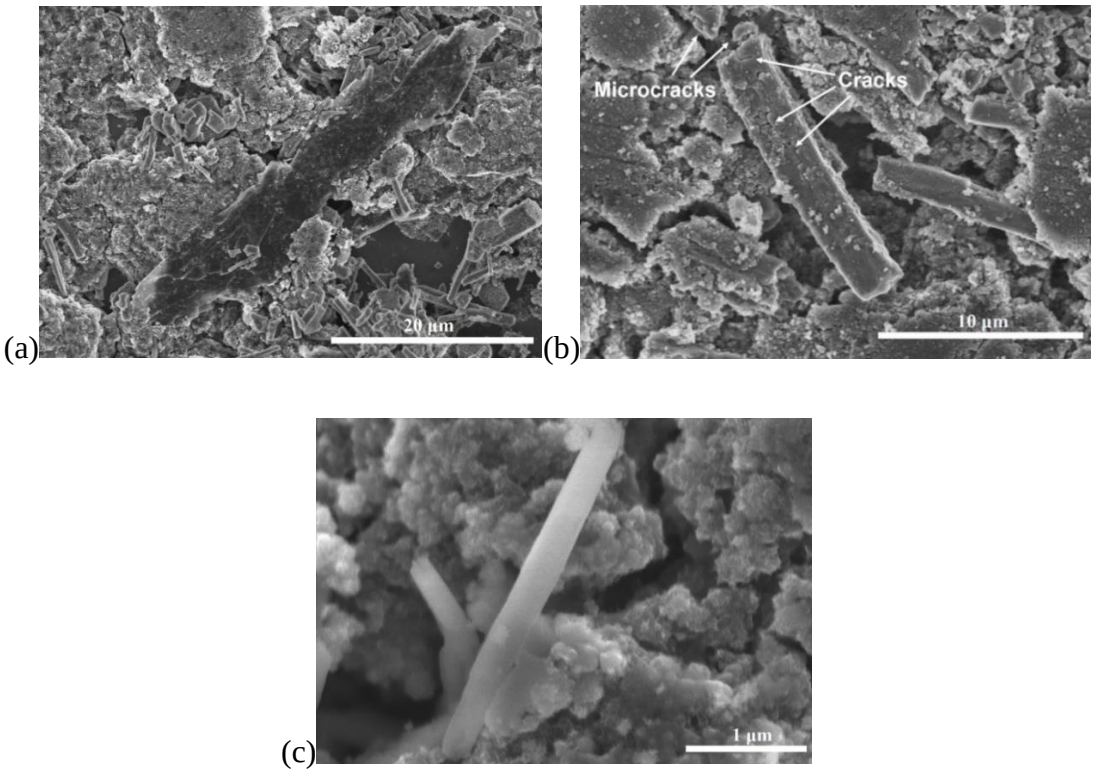

Figure 6.8. SEM images for CADS micropillar (a), CADS microwire (b) and CADS nanowire (c) after 100 cycles.

The morphology of CADS micropillar, CADS microwire and CADS nanowire after 110 cycles were investigated by SEM. As shown in figure 6.8a, there are a number of micro-size short rods around the large size CADS micropillar, demonstrating severe pulverization occurs after 110 charge/discharge cycles. The CADS microwires maintains its morphology after 110 cycles (Figure 6.8b), but few short CADS rods and microcracks induced by the large strain during repeated charge/discharge cycles can still be observed. Different from CADS microwires, CADS nanowire preserves its morphology after 110 cycles in figure 6.8c, no cracks and pulverization can be observed. The good morphology maintenance of CADS nanowires enables its high cycling stability.

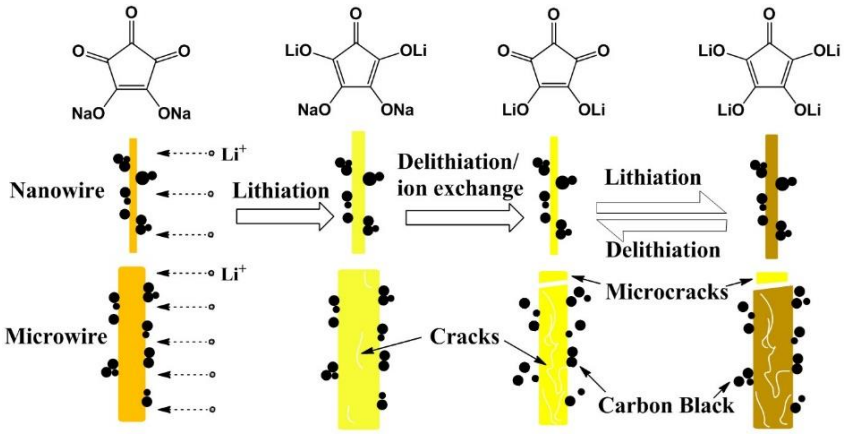

Scheme 6.2. Schematic illustration of lithiation/de-lithiation mechanism for croconic acid disodium salt.

6.4 Conclusion

In summary, during repeated lithiation/delithiation, CADS will gradually convert to croconic acid dilithium salt through ion exchange (Scheme 6.2), as suggested by theoretical calculation and evidenced by the potential shift in CV scans and reduction of Na^+ concentration in cycled CADS electrode. More importantly, CADS nanowire with small size (150nm) and large surface area, can effectively avoid pulverization and enables stable contact between CADS and carbon black, providing high capacity, high rate capability and long cycling stability. Due to the large size of CADS microwire, large volume change exists and leads to the formation of cracks and microcracks, as evidenced by SEM images of cycled CADS microwires. The microcracks which lose contact with carbon black are not electroative, resulting in capacity decline in the initial cycles. Therefore, nano-size CADS has much better electrochemical performance than micro-size CADS.

The CADS wires with diameters from 10 μm to 150 nm were synthesized using a facile anti-solvent crystallization method. The CADS nanowire with small diameter and large surface area shows high capacity, long cycle life and excellent rate capability due to its short Li-ion and electron diffusion pathway, large surface area and low strain. CADS nanowire can retain its initial capacity after 110 deep charge/discharge cycles at a low current density of 0.2 C, and deliver a high capacity of 100 mAh g^{-1} at 6 C. The theoretical calculation shows that the CADS gradually changes into more stable lithium croconate through ion exchange process during lithiation/delithiation. The ion exchange process is confirmed by ICP result, which shows the high content of lithium ion and low content of sodium ion in the cycled CADS electrode. Since the nano-organic material exhibits superior electrochemical performance, our research work paves the way for further improvement of organic battery performance in the future.

Chapter 7 Graphene Oxide Wrapped Croconic Acid Disodium Salt for Sodium Ion Battery Electrodes

7.1 Introduction

Sodium ion batteries are the most promising alternatives to lithium ion batteries due to the low cost and abundance of sodium element in the earth [155]. The chemical similarity of sodium ion toward lithium ion enables some electrode materials used in Li ion batteries to be applied for Na ion batteries [34, 47]. Inorganic materials synthesized through energy-demanding ceramic processes [72] are the most common Li ion electrode materials. However, to satisfy the emerging large-scale applications of energy storage, next generation battery electrodes should be made from renewable or recyclable resources via low energy consumption processes. One possible approach is to use electrode materials fabricated from biomass or recyclable organic materials via solution phase routes [73].

Several organic materials have been investigated as electrodes for Li ion batteries [140-144], but very few organic materials were explored for Na-ion batteries. The organic electrodes face two major challenges in organic electrolyte batteries: (1) low power density due to poor electronic conductivity of organic compounds, (2) fast capacity decay during charge/discharge cycles which is generally attributed to dissolution of organic compounds into organic electrolytes [72]. One way to mitigate the dissolution of organic materials in organic electrolytes is use of organic salts [72]. Among the salts, carbonyl group based organic compounds such as lithium salt of tetrahydroxy-benzoquinone [79], lithium ethoxycarbonyl-based compound [147], dilithium trans-trans-muconate and dilithium terephthalate [77] have been investigated as electrodes for Li ion

batteries. These organic salts normally contain more than two carbonyl groups which are connected by conjugated carbon matrix. These carbonyl groups are redox centers which enable the electrochemical reaction to take place in the electrodes. During the discharge process, each carbonyl group can obtain an electron and a lithium ion that induces electron transfer in the conjugated carbon matrix. The reaction between carbonyl group and lithium ion enables the ion transfer and electron transfer in Li ion batteries. Although the solubility of organic salts in the electrolyte has been reduced, these organic salts still suffer from fast and continuous capacity decline during charge/discharge cycles [77, 79]. The mechanism behind the fast capacity decline is still not fully understood.

Most reported organic salts experience phase transformation during lithiation/delithiation as evidenced by a flat voltage plateau in charge/discharge profile and structure change in X-ray diffraction (XRD) patterns [77]. The phase transformation is normally accompanied with volume change. The large volume expansion in the first lithiation can even change the crystal structure of organic salts into amorphous structure and retain amorphous structure in the following charge/discharge cycles [77], which is also observed in Si anodes [82]. The structure change of Si from crystal to amorphous structure is attributed to the large volume change (300%) of Si during lithiation [82]. The severe volume change of Si pulverizes the Si particle, resulting in rapid capacity decline during charge/discharge cycles [83]. Therefore, the volume change of organic salts during lithiation/delithiation may be also responsible for the capacity decay.

In principle, the carbonyl group based organic electrode compounds used in lithium ion batteries can potentially be applied to sodium ion batteries [156, 157]. However, due to larger ion size of Na^+ than Li^+, only few organic salts are suitable for Na ion batteries. In addition, the larger ion size of Na^+ causes much more severe volume change of organic salts, resulting in fast capacity decay of

organic compounds in Na ion batteries [157]. Therefore, only few organic compounds were explored for Na-ion batteries. Due to the large volume change, these organic compounds showed quick capacity decline during Na insertion/extraction [157]. However, how the volume change of organic salts affects the cycling stability has not been investigated yet.

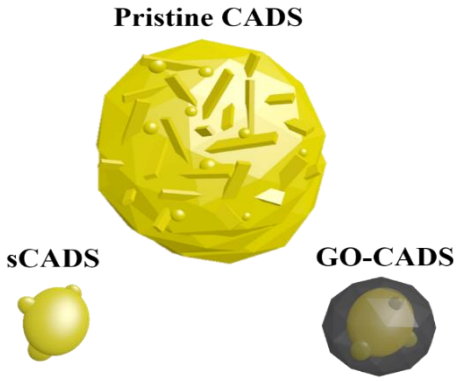

Figure 7.1. Schematic illustration for pristine CADS, sCADS and GO-CADS.

In this paper, croconic acid disodium salt (CADS) is used as a model electrode to investigate the capacity decline mechanism of organic salt electrodes in Na ion batteries. To our best knowledge, CADS has never been studied as a battery electrode material in Li-ion and Na-ion batteries. In addition, this is also the first effort to study the effects of phase change on capacity decay of organic salt electrodes in Na ion batteries. As shown in figure 7.1, three CADS samples, micro-sized pristine CADS, submicrometer-size CADS (sCADS), and graphene oxide wrapped CADS (GO-CADS), are employed to investigate their electrochemical behaviors toward Na. sCADS and GO-CADS are fabricated by ultrasonic spray pyrolysis. Our results show that the particle pulverization is a main reason for capacity decline. Minimizing particle size and wrapping CADS with graphene oxide can effectively stabilize the electrodes during Na ion insertion/extraction, thus improving the cycling stability.

7.2 Experimental Section

All chemicals were purchased from Sigma Aldrich and used as received. The CADS with small particle size of 0.5-1.0μm (denote as sCADS) was prepared by an ultrasonic spray pyrolysis method [158]. The ultrasonic spray pyrolysis apparatus consisted of ultrasonic droplet generator, tube furnaces, and filtration system for particle collection. The ultrasonic generator operated 1.7 MHz frequency atomized the precursor solution to droplets with average diameter of approximately 1 microns. Two tube furnaces were connected in series with a total length of 81 cm. Particle collection was set at the end of the system, allowing gas to pass through and collecting particles from 10 nm to 100 μm. 200 mg CADS with average particle size of 5μm were dissolved into 10 mL water. Aerosol droplets containing the dissolved precursors were generated using compressed nitrogen gas at a pressure of 35 psi in a collision type atomizer. The geometric mean diameter of the droplets was measured to be ~1 μm by a laser aerosol spectrometer. The produced aerosol droplets passed through a silica-gel diffusion dryer and a tube furnace preheated to 200 °C to remove most of the solvent. The products were collected on a 0.4 μm (pore size) DTTP Millipore filter and dried in a vacuum oven at 100 °C overnight.

Graphene oxide was synthesized following the modified hummer's method [159]. The graphene oxide wrapped CADS was also synthesized using ultrasonic spray pyrolysis. 100 mg CADS were dissolved in 100 mL graphene oxide aqueous solution to prepare the precursor. Nitrogen gas (2.5 L min^{-1} flow rate) was used to carry the solution droplets to the furnace series which was operated at 200 °C. In the furnace, water was evaporated, and then graphene wrapped CADS particles were generated in a residential time around 1.5 s.

Scanning electron microscopy (SEM) image was taken by Hitachi SU-70 analytical ultra-high resolution SEM (Japan); Transmission electron microscopy (TEM) images were taken by JEOL

(Japan) 2100F field emission TEM; X-ray diffraction (XRD) pattern was recorded by Bruker Smart1000 (Bruker AXS Inc., USA) using CuKα radiation; Fourier transform infrared spectroscopy (FTIR) was recorded by NEXUS 670 FT-IR Instrument; UV/vis spectra were recorded on an UV-1700 spectrophotometer; Thermogravimetric analysis (TGA) was carried out using a thermogravimetric analyzer (TA Instruments, USA) with a heating rate of 10 °C min^{-1} in argon.

The CADS and sCADS were mixed with carbon black and Polyvinylidene fluoride (PVDF) binder to form slurry at the weight ratio of 45:45:10, separately. The GO-CADS was mixed with carbon black and Polyvinylidene fluoride (PVDF) binder to form slurry at the weight ratio of 70:20:10. The electrode was prepared by casting the slurry onto copper foil using a doctor blade and dried in a vacuum oven at 100°C overnight. The electrode was cut into circular pieces with diameter of 1.2 cm for coin cell testing. Na ion batteries were assembled with sodium metal as the counter electrode, 1 M $NaClO_4$ in a mixture of ethylene carbonate/dimethyl carbonate (EC/DMC, 1:1 by volume) as the electrolyte, and Celgard®3501 (Celgard, LLC Corp., USA) as the separator. Electrochemical performance was tested using Arbin battery test station (BT2000, Arbin Instruments, USA). 0.7 V and 2.0 V (vs. Na/Na^+) were used as low and high cutoff voltages for the galvanostatic tests. After the cell reached the cutoff voltage, it was rested for 10 min for subsequent charge or discharge. Both the charge-discharge current density and specific capacity were calculated on the basis of the mass of CADS in the electrode. Cyclic voltammogram at a scan rate of 0.1 mV s^{-1} between 0.7 – 2 V (versus Na/Na^+) was recorded using Solatron 1260/1287 Electrochemical Interface (Solatron Metrology, UK).

7.3 Results and Discussion

7.3.1 Morphology and Structure

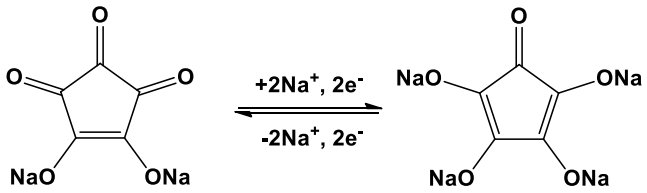

Scheme 7.1. The sodiation/de-sodiation mechanism for croconic acid based molecule.

Croconic acid disodium salt has a five-member ring structure with three carbonyl groups and a carbon-carbon double bond (scheme 7.1). Its chemical structure is very similar to dilithium rhodizonate which has been reported as an organic electrode for Li ion batteries [73]. The carbonyl groups in this compound are redox centers which can react with Na ions and gain electrons through the reaction as shown in scheme 7.1. During the sodiation, each carbonyl group, connected by the carbon-carbon double bond, gains a sodium ion and an electron. At the meanwhile, the carbon-carbon double bond is broken, and two new carbon-carbon double bonds are generated. During the desodiation, CADS molecule is recovered. The reversible reaction between CADS molecule and sodium ions enables CADS to be an electrode material for Na ion batteries.

(a) 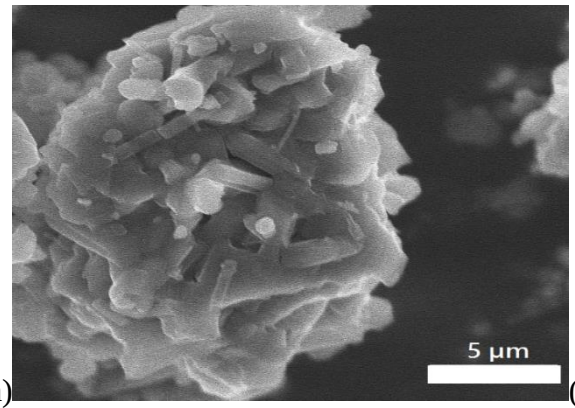

(b) 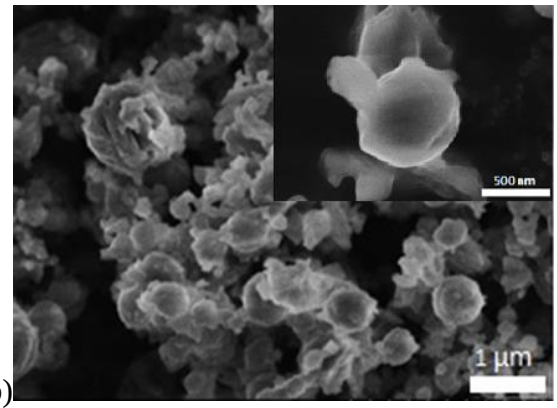

(c) 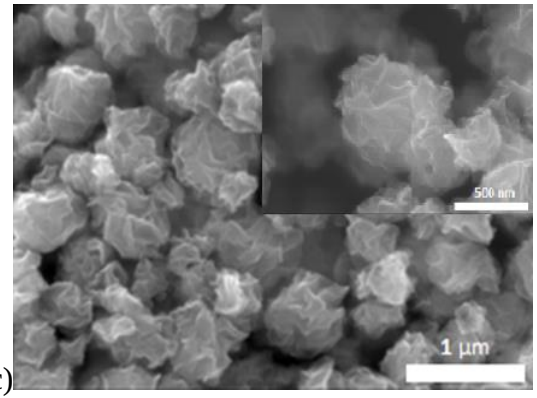

Figure 7.2. The SEM images of pristine CADS (a), sCADS(b), and GO-CADS(c).

Three CADS samples, micro-sized pristine CADS, submicrometer-size CADS (sCADS), and graphene oxide wrapped CADS (GO-CADS), were used to investigate the capacity decline mechanism. The sCADS particles were synthesized by dissolving pristine CADS into water, and then rapidly evaporating the CADS solution using the ultrasonic spray pyrolysis. The GO-CADSs were synthesized by rapidly drying the graphene oxide and CADS aqueous solution at 200 ^{o}C using the ultrasonic spray pyrolysis. The morphology of three CADS samples was characterized by scanning electron microscopy (SEM) as shown in Figure 7.2. The pristine CADS consist of long bars and some irregular-structured particles which tend to aggregate to form micro-size particles (Figure 7.2a). As shown in Figure 7.2b, the sCADS particles have spherical morphology with the particle size of 0.5-1.0 µm, which is about ten times smaller than that of pristine CADS. Figure 7.2c shows the SEM images of GO-CADS, in which all the CADS particles are encapsulated by the folded and winkled graphene oxide. The morphology of the GO-CADS composite is very uniform with particle size typically less than 1µm, which is similar to sCADS. This is attributed to the unique ultrasonic spray pyrolysis. As water evaporates, the amphiphilic GO sheets would migrate to the surface of the droplets to form a shell. Since the diameter of the precipitated CADS particles was much smaller than that of the aerosol droplets,

further water evaporation could collapse the GO shell, resulting in a crumpled morphology that encapsulates the CADS particles [160]. The transmission electron microscopy (TEM) images of GO-CADS in Figure 7.3 also confirm that all the CADS particles are encapsulated by the folded and winkled graphene oxide. The energy-dispersive X-ray spectroscopy (EDS) elemental mapping images (Figure 7.3c, 7.3d and 7.3e) reveal that CADS is uniformly distributed in the GO shell since sodium mapping image overlaps with carbon and oxygen mapping images. The content of CADS in GO-CADS is 37 wt% as determined by thermogravimetric analysis (TGA) results for GO, CADS and GO-CADS as shown in Figure 7.4. The GO is treated by ultrasonic spray pyrolysis under the same condition as GO-CADS. For GO-CADS, the Na ion can penetrate through the defects and open-end of GO to react with the inner CADS [161].

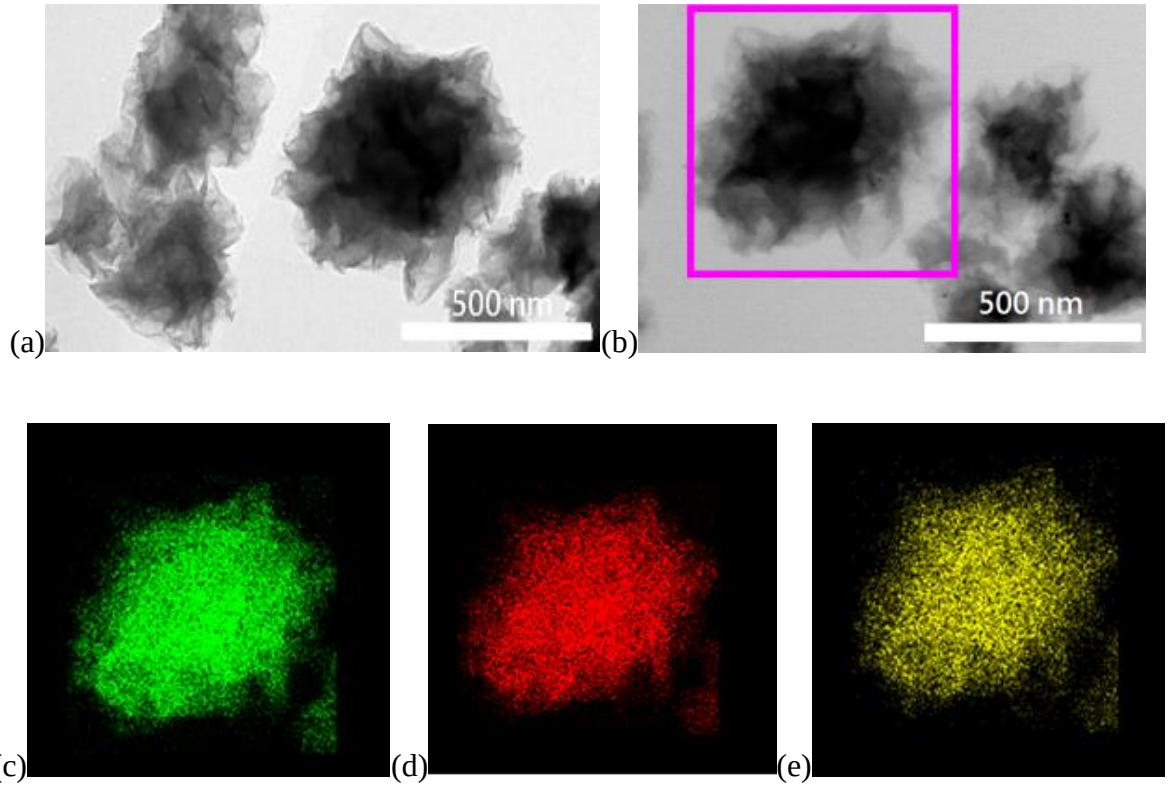

Figure 7.3. TEM images of GO-CADS (a, b) and EDS elemental mapping images of the GO-CADS particle, marked by purple square in (b), for carbon (c), oxygen (d) and sodium (e).

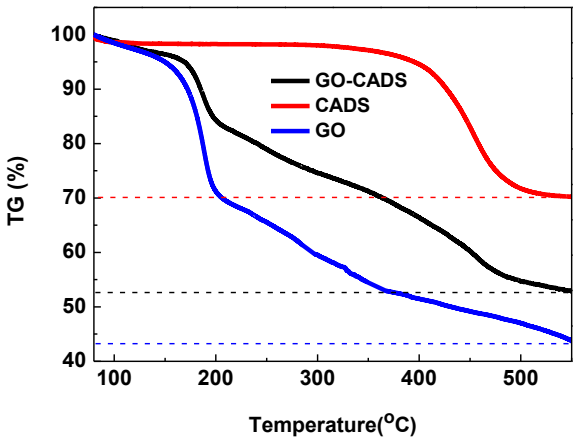

Figure 7.4. The TGA analysis for graphene oxide (GO), CADS and graphene oxide wrapped CADS (GO-CADS).

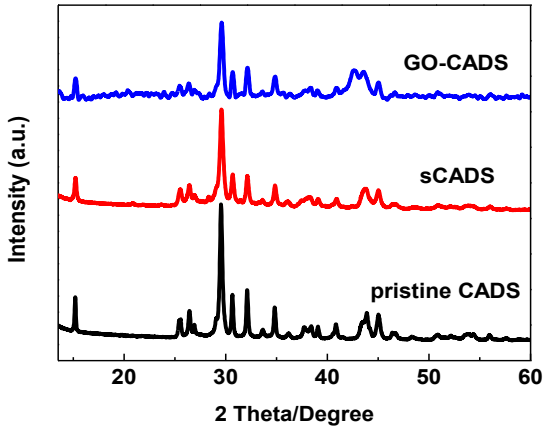

Figure 7.5. The XRD patterns for CADS (black line), sCADS (red line), and GO-CADS (blue line).

The structures of three CADS samples are identified by the XRD. The XRD patterns of sCADS and GO-CADS are the same as the pristine CADS as shown in Figure 7.5, indicating that the sCADS, GO-CADS and pristine CADS have the same crystal structure. However, the XRD peak of pristine CADS is slightly sharper than that of sCADS and GO-CADS, demonstrating the

crystalline structures of CADS were not well-developed due to rapid precipitation (1.0 s of residential time) in ultrasonic spray pyrolysis process.

7.3.2 Sodiation/Desodiation Behaviors

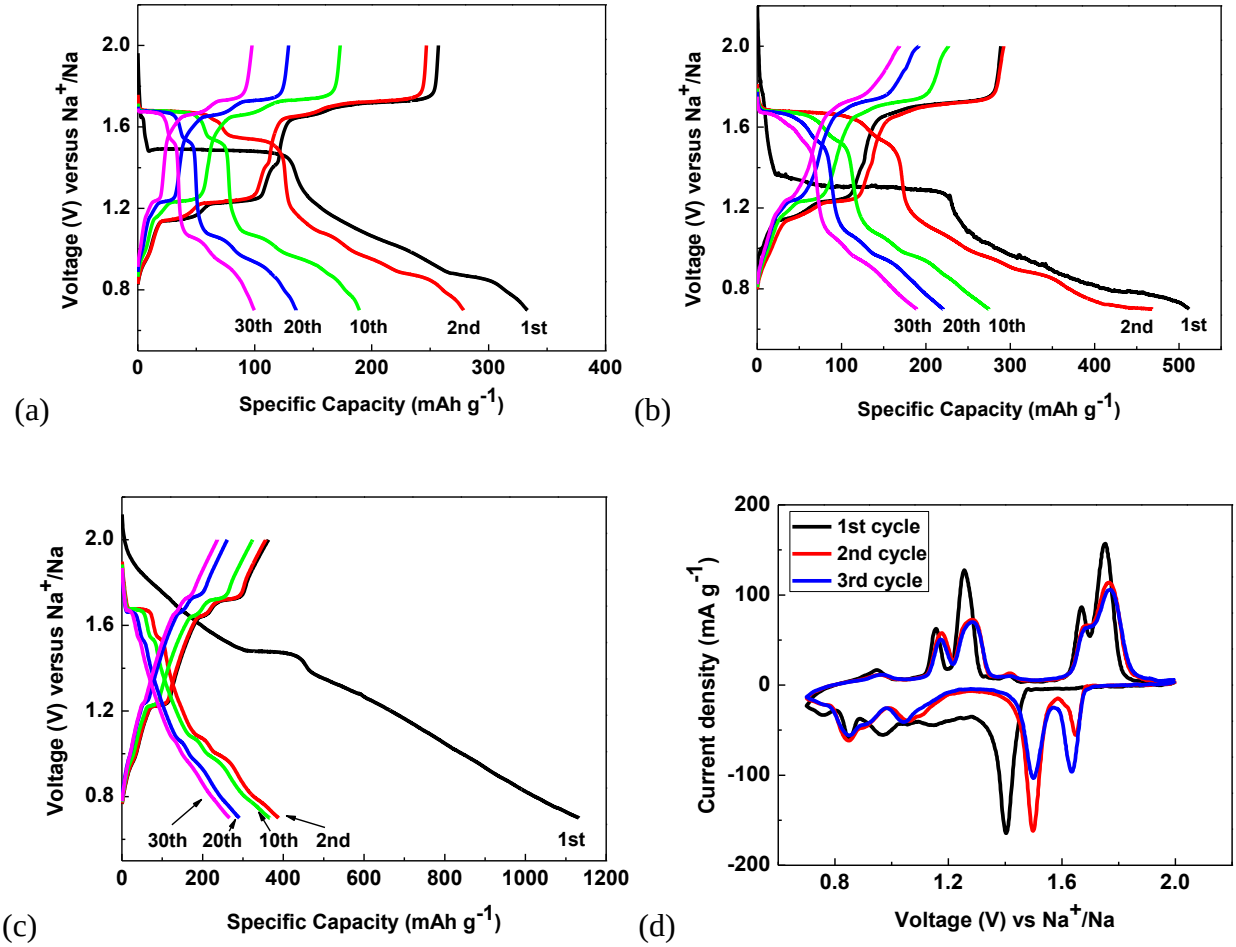

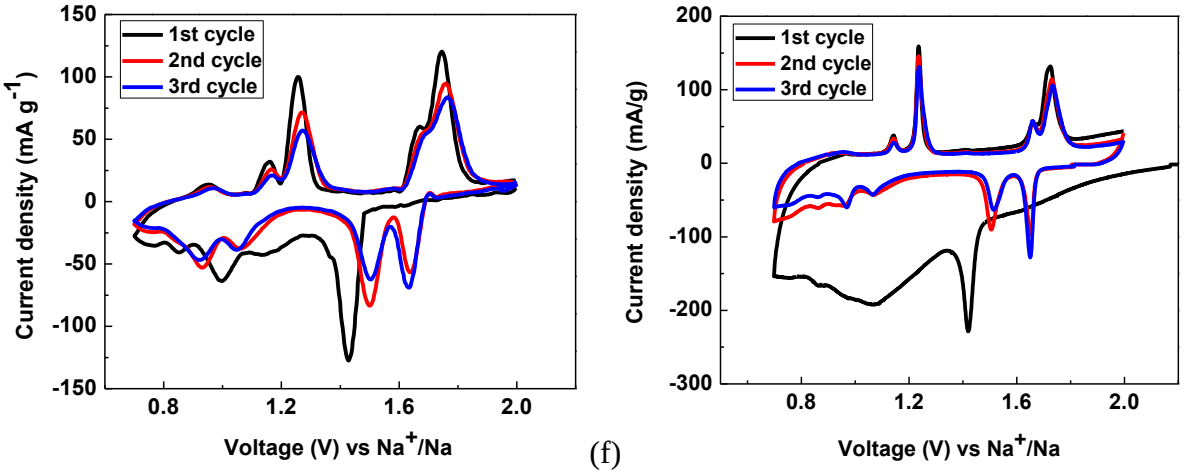

Figure 7.6. Electrochemical performances of materials. The galvanostatic charge–discharge curves of pristine CADS (a), sCADS (b) and GO-CADS (c) between 0.7 V and 2.0 V versus Na/Na^+ at room temperature. Cyclic voltammograms of pristine CADS (d), sCADS (e) and GO-CADS (f) at 0.1 mV s^{-1} in the potential window from 0.7 V to 2.0 V versus Na/Na^+.

The charge/discharge behaviors of pristine CADS, sCADS and GO-CADS in different cycles at a current density of 20 mA g^{-1} are shown in Figure 7.6. The voltage profiles of all three CADS samples show serials voltage plateaus and the potentials of first sodiation plateau are lower than that in the subsequent sodiation process, demonstrating that all three CADS samples experience successive and reversible phase transformations during sodiation/desodiation and the stress/strain due to large volume expansion in the first sodiation induces a large overpotential. The large overpotential is significantly reduced in the subsequent cycles due to the introduction of defects in the first sodiation. The sCADS has larger overpotential than pristine CADS, because more Na ion (250 mAh/g) is inserted into sCADS in the first plateau than that (150 mAh/g) in pristine CADS. Minimization of the CADS particle size from 5.0-10 μm to 0.5-1.0 μm does not change the voltage plateaus (Figure 7.6a and 7.6b), but the capacity (287.8 mAh g^{-1}) of sCADS is larger than that (246.7 mAh g^{-1}) of pristine CADS due to the reduced particle size and consequently

improved kinetics of the former. The capacity of sCADS is very close to the theoretical capacity (288 mAh g^{-1}) of CADS, which is calculated based on one CADS molecule can react with two sodium ions. Since GO can reversibly react with Na^+, and deliver a reversible capacity of 39 mAh g^{-1} (Figure 7.7), the initial capacity of CADS in GO-CADS after subtracting the capacity of GO is about 293 mAh g^{-1}, which is higher than theoretical capacity, probably due to the fact that carbon black additive is also active for Na ion storage. The high capacity of CADS in GO-CADS demonstrates that GO shell can effectively enhance the utilization of inside CADS due to the core shell structure and the higher conductivity of GO than CADS. The slight change in the voltage profile of GO-CADS compared with that of CADS is attributed to the sloping voltage curves of GO capsular [162]. The voltage plateaus and reaction reversibility of CADS, sCADS, GO-CADS can be more clearly observed in cyclic voltammogram profiles (Figure 7.6d, 7.6e and 7.6f). In the first sodiation/desodiation cycle of CADS, there are three clear cathodic peaks at 1.42 V, 1.0 V, 0.85 V and a shoulder at 1.15 V, and four anodic peaks at 1.15 V, 1.25 V, 1.7 V and 1.8V are also observed. However, the shoulder at 1.15 V disappears after the first cycle, and the cathodic peak at 1.42 V in the first cycle shifts to high voltage to split into two new peaks at 1.5 V and 1.65 V in the following cycles. This result suggests that the CADS experiences an activation process during the first sodiation, which has been observed in many high capacity electrodes with large volume changes such as Sn and Sb [33, 55]. The activation process characterized by the high overpotential in the first sodiation process is induced by the high stress/strain raised by the first sodiation. The high stress/strain in the first sodiation generates a large amount of defects (cracks, dislocations, plastic deformations, etc) in host to release the strain/stress. Therefore, the relaxation of the strain/stress in the first solidation decreases the overpotential and moves solidation potential to more positive values in the following sodiation

process. After the first cycle, there are four peaks in the desodiation scans, which are corresponding to the four peaks in the sodiation scans, demonstrating the high reversibility of sodiation and desodiation of CADS. The cyclic voltammograms of sCADS and GO-CADS are similar with pristine CADS. There is a broad shoulder at 1.1 V in the first sodiation process of GO-CADS owing to the irreversible reaction on the surface of GO. After the first sodiation, GO-CADS displays similar anodic and cathodic peaks as pristine CADS and sCADS. The highly reversible peaks in the cyclic voltammetry curves and the highly reversible plateaus in the galvanostatic charge–discharge curves suggest that CADS experiences highly reversible phase transformation during sodiation/desodiation.

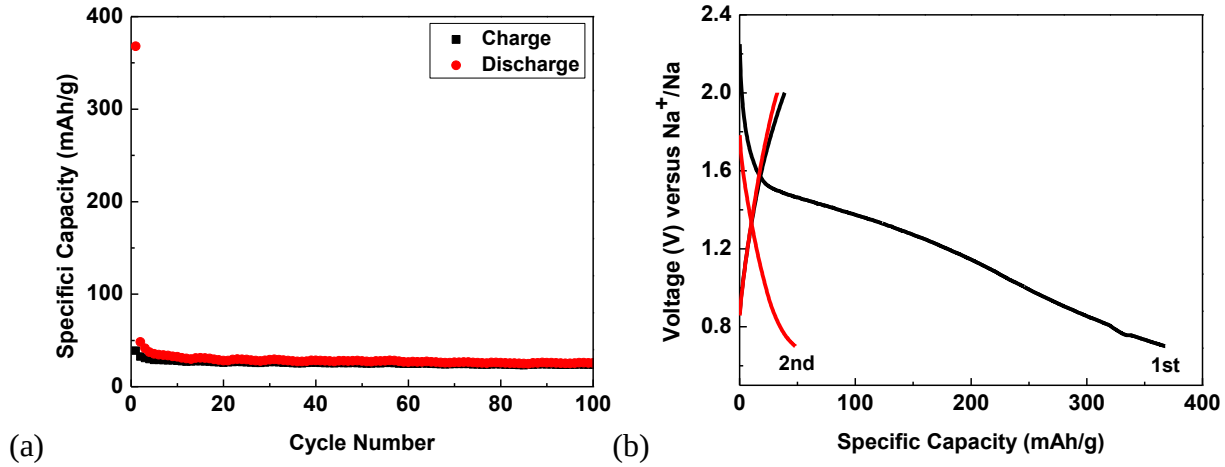

Figure 7.7. Electrochemical performance of graphene oxide. Charge and discharge capacity versus cycle number (current density: 20 mAh g^{-1}) for GO; (b) The galvanostatic charge–discharge curves of GO.

The reversible phase change during sodiation/desodiation is also confirmed by XRD (Figure 7.8). In the full sodiation state, the original peaks of pristine CADS at 28 degree and 30 degree shift to 24 degree and 26 degree. Moreover, the two peaks at ~32 degree of pristine CADS salt merge together to form a new peak at ~28 degree after full sodiation. Therefore, XRD data confirm the

phase change of CADS during sodiation. After the desodiation, the XRD peaks of CADS shift back to their original positions, and maitain the positions after 50th full desodiations, illustrating that the phase transformation is highly reversible. Comparing to fresh CADS, a few extra XRD peaks in full desodiated CADS might imply the uncompleted phase transformation in the active material.

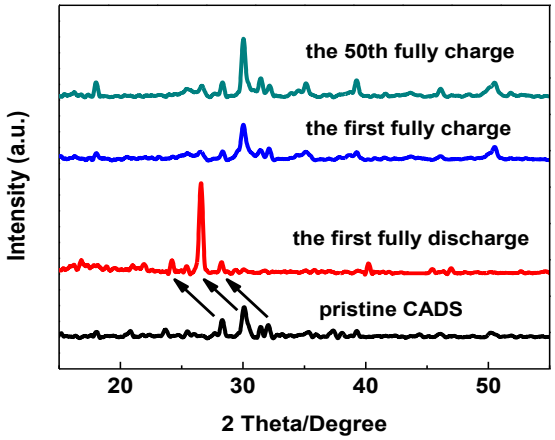

Figure 7.8. The XRD patterns of pristine CADS (black line), the first fully discharged CADS (red line), the first fully charged CADS (blue line) and the 50th fully charged CADs (green line).

7.3.3 Cycling Stability and Mechanism for Capacity Decay

The cycling stability of three CADS samples is tested at a current density of 20 mA g^{-1} (Figure 7.9). The capacity of pristine CADS quickly decreases from 250 mAh g^{-1} to 50 mAh g^{-1} after 60 cycles. If the dissolution of organic salts into organic electrolyte is responsible for the fast capacity decay, the capacity decline of sCADS should be much faster than pristine CADS due to the reduced particle size and thus enhanced contact surface between sCADS and electrolyte. However, the sCADS has much better cycling stability, demonstrating that the dissolution of

CADS is not the major reason for the capacity decay. The insolubility of CADS in electrolyte is directly tested by comparing the Fourier transform infrared spectroscopy (FTIR) spectra of fresh electrolyte and the electrolyte after 50 sodiation/desodiation cycles. Figure 7.10a shows the FTIR spectrum of CADS. There is a very sharp peak at 1500 cm^{-1} which represents the stretching vibration of the carbonyl groups and carbon-carbon double bond in CADS. If CADS dissolves in the electrolyte, there should be a peak at 1500 cm^{-1} in the FTIR spectrum of the electrolyte after 50 cycles, whereas the spectra of the electrolyte before test and after 50 cycles are nearly the same in the range from 800 to 2000 cm^{-1} in Figure 7.10b. UV-vis spectroscopy is also employed to measure the active material in the electrolyte. As shown in figure 7.11, the UV-vis spectra of cycled electrolyte (50 cycles) are almost the same to that of the fresh electrolyte, indicating no active material is dissolved in the electrolyte during cycles. Thus, this evidence confirms that CADS is not dissolved in the electrolyte during the charge and discharge.

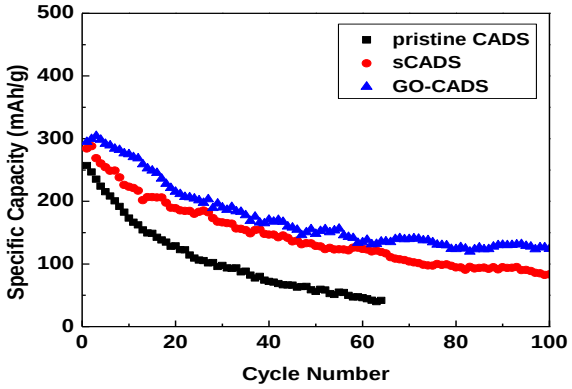

Figure 7.9. Desodiation capacity versus cycle number (current density: 20 mA g^{-1}) for pristine CADS, sCADS and GO-CADS, respectively.

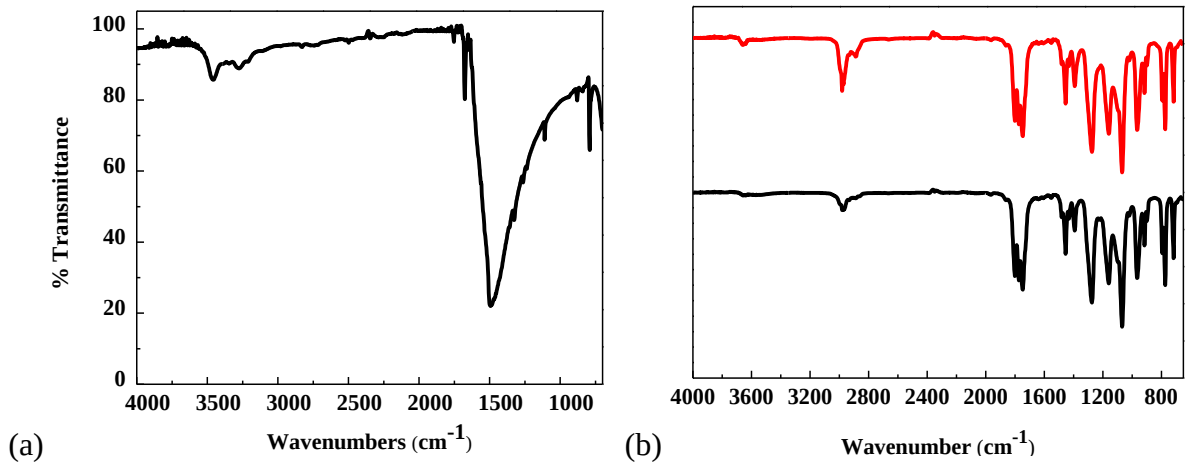

Figure 7.10. (a) FTIR spectrum for CADS; (b) FTIR spectra for the electrolyte used in CADS coin cell before test (red line) and after 50 cycles (black line).

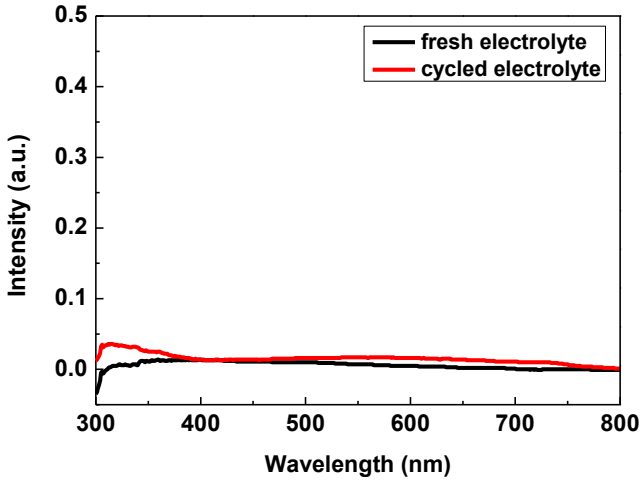

Figure 7.11. UV-vis spectra for fresh electrolyte and electrolyte after 50 cycles in N-Methyl-2-pyrrolidone solution.

Another possibility for capacity decline is the pulverization of CADS particles due to the volume change induced by repeating phase transformation during sodiation/desodiation process. Pulverization-induced capacity decay has been observed in high capacity anodes such as Sn in Na-ion battery [163]. The pulverization of CADS particles will demolish the integrity of electrode

structure, resulting in poor cycling stability. The morphology change of CADS before and after 50 sodiation/desodiation cycles is observed by SEM. As shown by SEM images in Figure 7.12a and 7.12b, the pristine CADS in the electrode has the long bar-like shape, but after 50 cycles the long bar is severely cracked. The long bar is broken into numerous small fragmentations, most of which do not connect with conductive carbon. The most effective method to reduce the particle pulverization is to minimize the particle sizes [83]. Figure 7.12c and 7.12d show the SEM images of the fresh sCADS material and cycled sCADS. sCADS particles maintain the similar particle morphology after 50 cycles and no cracks are observed, thus the sCADS has much better cycling stability than CADS as demonstrated in Figure 7.9. The GO encapsulation of sCADS can further enhance morphology stability of sCADS as demonstrated in Figure 7.12e and 7.12f. After 50 charge/discharge cycles, no obvious morphology change can be observed. The good morphology stability of GO-CADS is consistent with the best cycle life of GO-CADS electrode as shown in figure 7.9. The FTIR, UV-vis and SEM images in Figure 7.10, 7.11 and 7.12 demonstrate that the capacity fading is not due to the dissolution of sCADS and GO-CADS in the electrolyte, but the large stress/strain of CADS during repeating phase changes.

Since the particle pulverization will isolate the small pulverized CADS particles from carbon additive and current collector during sodiation/desodiation process, the isolated CADS particles are not able to electrochemically react with Na^+ in the following cycles, thus dramatically decreasing the battery performance. However, if CADS particles are encapsulated by a conductive graphene oxides, the void in the crumpled graphene oxide coating can accommodate the volume expansion of CADS upon sodiation and maintain the connection between inner CADS particles and outer graphene oxide cover (even they are pulverized), thus improving cycling stability. As demonstrated in Figure 7.9, the graphene oxide encapsulated CADS shows

the best cycling stability. Further improvement for cycling stability is under investigation by optimizing the ratio of graphene oxide and CADS, increasing the aerosol spray temperature, and adjusting the residential time.

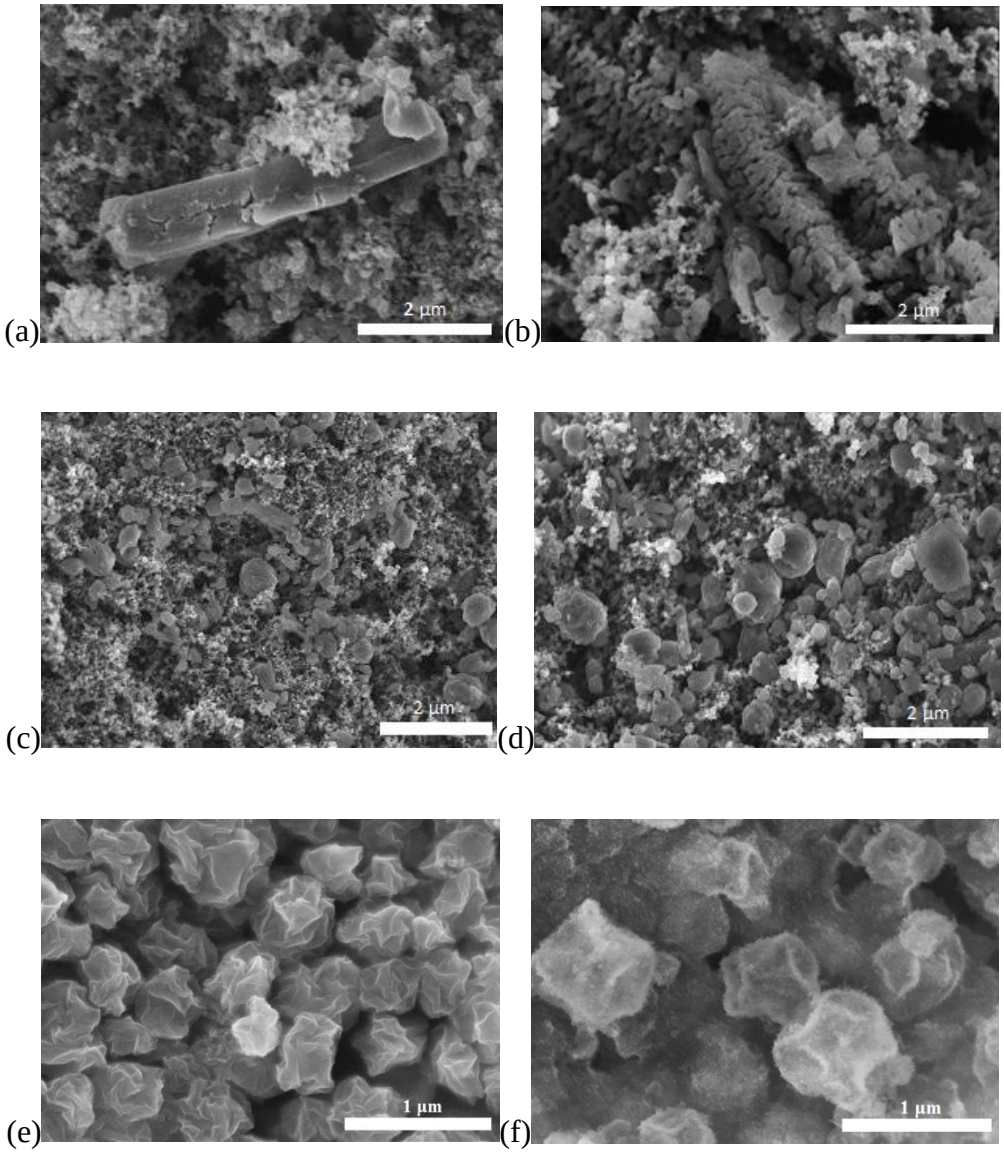

Figure 7.12. SEM images of the pristine CADS electrode materials before test (a) and after 50 cycles (b); SEM images of the sCADS electrode materials before test (c) and after 50 cycles (d); SEM images of GO-CADS electrode materials before test (e) and after 50 cycles (f).

7.4 Conclusion

Croconic acid disodium salt, a carbonyl group based organic compound, was used as an anode material for the first time. It is shown that the rapid capacity fading of pristine CADS in sodium ion batteries is due to the particle pulverization rather than the dissolution in organic electrolyte. The CADS experiences a serial phase transformations during sodiation/desodiation process. The volume change during phase transformations triggers the particle pulverization, which is confirmed by SEM results. The sCADS and GO-CADS fabricated by ultrasonic spray pyrolysis have much smaller particle size than pristine CADS, and provide much better cycling stability due to the suppression of pulverization and improvement of electronic conductivity. Hence, minimizing the CADS particle size and encapsulating CADS particles by graphene oxide are two effective methods to enhance the electrochemical performance of CADS.

Chapter 8 One-step Fabrication of Organic Nanorod Electrodes for Sodium Ion Batteries

8.1 Introduction

Li-ion batteries (LIB) are the promising energy storage devices for emerging electric vehicles and smart grids. However, the high cost and limited availability of lithium sources hinder the large-scale application of LIB for renewable energy storage [42, 155]. Na-ion batteries (NIB), which share similar chemistry as LIB, are the most promising energy storage devices for renewable energy due to the low cost and abundance of sodium sources [108]. Recently, considerable research efforts have been devoted to developing advanced cathode materials for NIB [130]. Among them, sulfur [110, 164], selenium [13, 44], O3-type and P2-type sodium metal oxides [45, 165], sodium metal phosphate [47, 48] and sodium metal sulfate [49] cathodes showed excellent electrochemical performance. However, there are only a few reports on the anode materials. Although the nongraphitic carbonaceous materials [166, 167], tin [33, 168], antimony [169], red phosphorous [170, 171] and metal sulfides [57, 172] anodes show promising performance in NIB, the high energy-consuming synthetic process, material scarcity, and high cost limit the wide application of these anode materials in NIB. As a consequence, it is of great significance to explore energy- and cost-effective organic anode materials for NIB.

Organic materials derived from biomasses are the best candidates for next generation green NIB due to their abundance, sustainability, environmental benignity and low cost [72]. Although several carbonyl group based organic anodes have been reported for NIB [173-175], the limited cycling stability, low capacity and inferior rate capability impede the application of these

carbonyl based organic anodes. The organic anodes face three major challenges [176-178]: (1) The extremely low conductivity of organic materials seriously reduces reaction kinetics, resulting in large overpotentials; (2) Particle pulverization induced by large volume change during sodium ion insertion/extraction accelerates capacity decay; (3) The high solubility of organic materials in organic electrolyte induces active material loss upon cycling, resulting in fast capacity fading. Due to the very low conductivity of organic anodes, 20 wt%~30 wt% of conductive carbon has to be added into organic electrodes and the particle size of organic materials has to be reduced into nano-scale to increase the contact surface among organic materials, conductive carbon and electrolytes, thus enhancing electrochemical reaction kinetics [78]. The decrease of organic particle size into nano-scale can also alleviate particle pulverization, further improving cycling stability. Current technology to reduce the solubility of organic compounds in the electrolyte is to increase the polarity of organic compounds by formation of organic salts. Up to date, only nano-size organic salt electrodes show reasonable performance. As battery electrode, the nano-size organic salt electrodes are fabricated through two steps: (1) Synthesizing nano-size organic salts using chemical/physical process; (2) Mixing nano-size organic salts with conductive carbon, binder and solvent to form a slurry-ink, and then casting onto current collector.

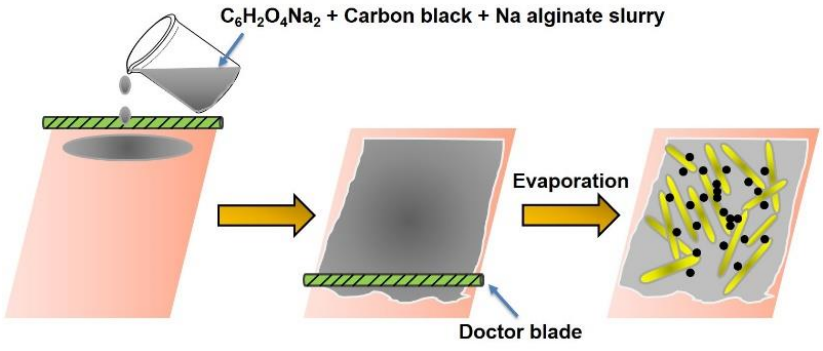

Figure 8.1. Schematic illustration of nanorod electrode preparation process.

In this work, 2,5-Dihydroxy-1,4-benzoquinone disodium salt (DHBQDS) nanorod anodes were *in situ* fabricated for the first time by one-step process through integrating the nanomaterial synthetic process into electrode casting process, simplifying the electrode preparation process. Due to the high solubility of DHBQDS and sodium alginate binder in water, the DHBQDS-carbon black-sodium alginate aqueous slurry was casted on the Cu foil, and the DHBQDS nanorod crystals and nano-size sodium alginate were uniformly co-precipitated on the carbon surface during the electrode drying process as shown in figure 8.1. Due to the fast ionic and electronic conductivity of DHBQDS nanorod-carbon nanocomposite and uniform distribution of DHBQDS, sodium alginate and carbon black, the DHBQDS nanorod electrodes deliver a reversible capacity of 167 mAh g^{-1} at a high current density of 200 mA g^{-1} after 300 cycles, which is 87% of its initial capacity (capacity decay rate of 0.051% per cycle). To reduce the dissolution of DHBQDS in the electrolyte upon cycling, a thin layer of Al_2O_3 with thickness of 1 nm or 2 nm was coated on the DHBQDS nanorod electrodes using ALD. The reversible capacity of Al_2O_3 coated DHBQDS nanorod electrodes remains at 212 mAh g^{-1} at a low current density of 50 mA g^{-1} after 300 cycles with a very low capacity decay rate of 0.049% per cycle. The Al_2O_3 coating remarkably suppresses the dissolution issue as evidenced by the fact that the Coulombic efficiency achieves ~100% for Al_2O_3 coated electrodes after first few cycles. The ALD enhanced organic nanorods represent the best organic anode in Na-ion batteries in terms of reversible capacity and cycle life.

8.2 Experimental Section

Synthesis of 2,5-Dihydroxy-1,4-benzoquinone disodium salt: All chemicals were purchased from Sigma Aldrich and used as received. 2,5-Dihydroxy-1,4-benzoquinone was dispersed in ethanol alcohol with sodium hydroxide powders in 5% excess. The solution was stirred at room temperature for 24 h, and then the solution was filtered to collect the precipitation. The precipitation was washed with ethanol and dried in the vacuum oven at 100 ^{o}C overnight. 2,5-Dihydroxy-1,4-benzoquinone disodium salt was collected as orange powder.

Atomic Layer Deposition: The DHBQDS electrodes were placed into an atomic layer deposition system (Beneq TFS 500) for Al_2O_3 deposition. High-purity nitrogen at 150 ^{o}C was used as carrier gas for the whole process. To obtain the Al_2O_3 layer with a thickness of 1 nm or 2 nm, 10 or 20 precursor pulse cycles of ALD-Al_2O_3 were performed. Each cycle included alternating flows of trimethylaluminum (TMA, 4 sec, Al precursor) and water (4 sec, oxidant) separated by flows of pure nitrogen gas (4 and 10 sec, respectively, carrier and cleaning gas). The thickness of Al_2O_3 layer was about 1 Å for each precursor pulse cycle.

Material Characterizations: Scanning electron microscopy (SEM) images were taken by Hitachi SU-70 analytical ultra-high resolution SEM (Japan); Thermogravimetric analysis (TGA) was carried out using a thermogravimetric analyzer (TA Instruments, USA) with a heating rate of 5 °C min^{-1} in argon; X-ray diffraction (XRD) pattern was recorded by Bruker Smart1000 (Bruker AXS Inc., USA) using CuKα radiation. An XRD sample holder with cover is used for the fully sodiated DHBQDS nanorod electrode to avoid its contact with air.

Electrochemical measurements: The DHBQDS powder was mixed with carbon black and sodium alginate/PVDF binder to form a slurry at the weight ratio of 60:25:15. The electrode was

prepared by casting the slurry onto copper foil using a doctor blade and dried in a vacuum oven at 100 °C overnight. The slurry coated on copper foil was punched into circular electrodes with an area mass loading of 1.0 mg cm^{-2}. Coin cells for sodium ion batteries were assembled with sodium foil as the counter electrode, 1M $NaClO_4$ in a mixture of ethylene carbonate/dimethyl carbonate (EC/DMC, 1:1 by volume) or fluoroethylene carbonate/dimethyl carbonate (FEC/DMC, 1:1 by volume) and Celgard®3501 (Celgard, LLC Corp., USA) as the separator. Electrochemical performance was tested using Arbin battery test station (BT2000, Arbin Instruments, USA). Capacity was calculated on the basis of the mass of DHBQDS. Cyclic voltammograms were recorded using Gamry Reference 3000 Potentiostat/Galvanostat/ZRA with a scan rate of 0.1 mV s^{-1}.

8.3 Results and Discussion

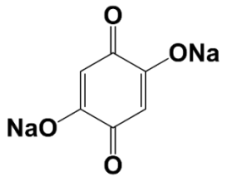

Scheme 8.1. The molecular structure of DHBQDS.

2,5-Dihydroxy-1,4-benzoquinone disodium salt is synthesized by neutralizing 2,5-Dihydroxy-1,4-benzoquinone (DHBQ) with sodium hydroxide in ethanol alcohol solution. DHBQDS contains two carbonyl groups, connected by a benzene ring, and two sodium ions, bonding with phenol groups, as shown in scheme 8.1. The 1,4-benzoquinone structure provides two active sites for the redox reaction with electrons and sodium ions, while the sodium-oxygen ionic bonds remarkably decrease its dissolution in organic electrolyte, but maintain high solubility in water.

The pristine DHBQDS precipitated from sodium hydroxide-ethanol alcohol solution has a crystal structure as demonstrated by the X-ray diffraction (XRD) pattern in figure 8.2a. As shown in Figure 8.2b, the pristine DHBQDS particles have irregular rods and particles morphology with an average size about 1 μm. The thermal stability of pristine DHBQDS is measured by thermogravimetric analysis as shown in figure 8.2c. Decomposition of DHBQDS molecules starts at the temperature of 150 ^{o}C. The DHBQDS lose 4% of weight from 150 ^{o}C to 450 ^{o}C and 15% of weight from 450 ^{o}C to 550 ^{o}C during heating in argon.

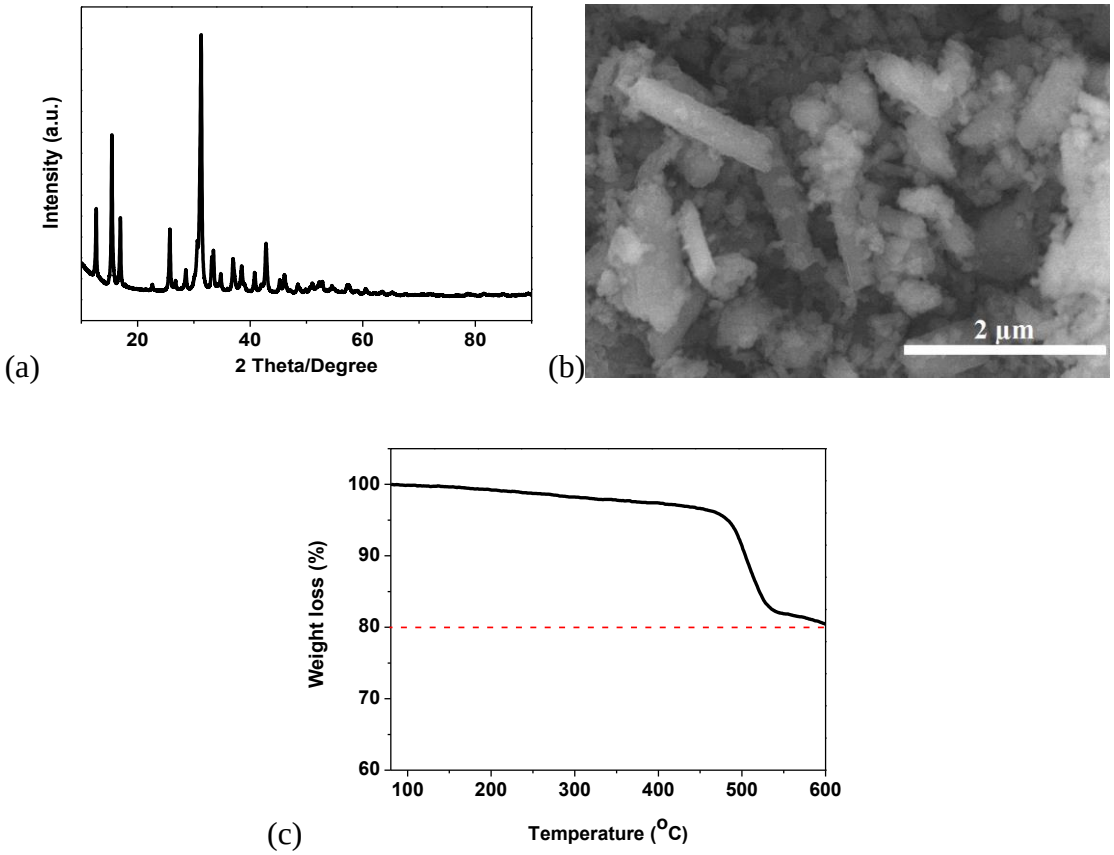

Figure 8.2. (a) XRD pattern for DHBQDS; (b) SEM image of DHBQDS; (c) Thermogravimetric analysis (TGA) curve of DHBQDS in Ar.

To investigate the role of carbon black and sodium alginate in precipitation of nano-size DHBQDS, the pristine DHBQDS was recrystallized from four different aqueous solutions/slurries due to the high solubility of DHBQDS in water: (1) DHBQDS-carbon black-sodium alginate aqueous slurry with the weight ratio of 60:25:15; (2) DHBQDS-carbon black aqueous slurry with the same weight ratio (70:30) of DHBQDS to carbon black as in (1); (3) DHBQDS-sodium alginate aqueous solution with the same ratio (80:20) of DHBQDS to sodium alginate as in (1), and (4) aqueous DHBQDS solution. Each slurry/solution was casted on Cu foils and then dried in the vacuum oven at 100 ^{o}C for 12 h that is the same procedure as the electrode fabrication process. As shown in figure 8.3, DHBQDS precipitated from DHBQDS-carbon black-sodium alginate aqueous solution has nanorod structure with a diameter of 200-300 nm and a length of ~1 μm. However, the DHBQDS precipitated from other three aqueous slurry/solutions have irregular shapes (Figure 8.4a-c), demonstrating the synergic effect of carbon black and sodium alginate in the formation of DHBQDS nanorods. Therefore, carbon black and sodium alginate binder not only enhance the conductivity and integrity of the electrode, but also assist the growth of DHBQDS nanorods. The exact synergic mechanism of carbon black and sodium alginate for the formation of DHBQDS nanorods is still under investigation. The high solubility of DHBQDS and sodium alginate in water enables the uniform distribution of DHBQDS nanorods, sodium alginate and carbon black in the electrode, which will contribute to the robustness of electrode and superior rate performance of DHBQDS nanorod electrodes.

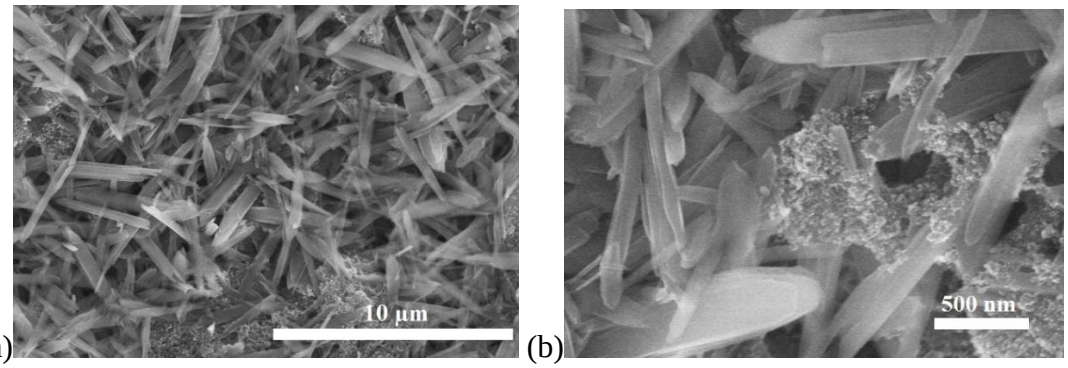

Figure 8.3. SEM images of DHBQDS nanorod electrode.

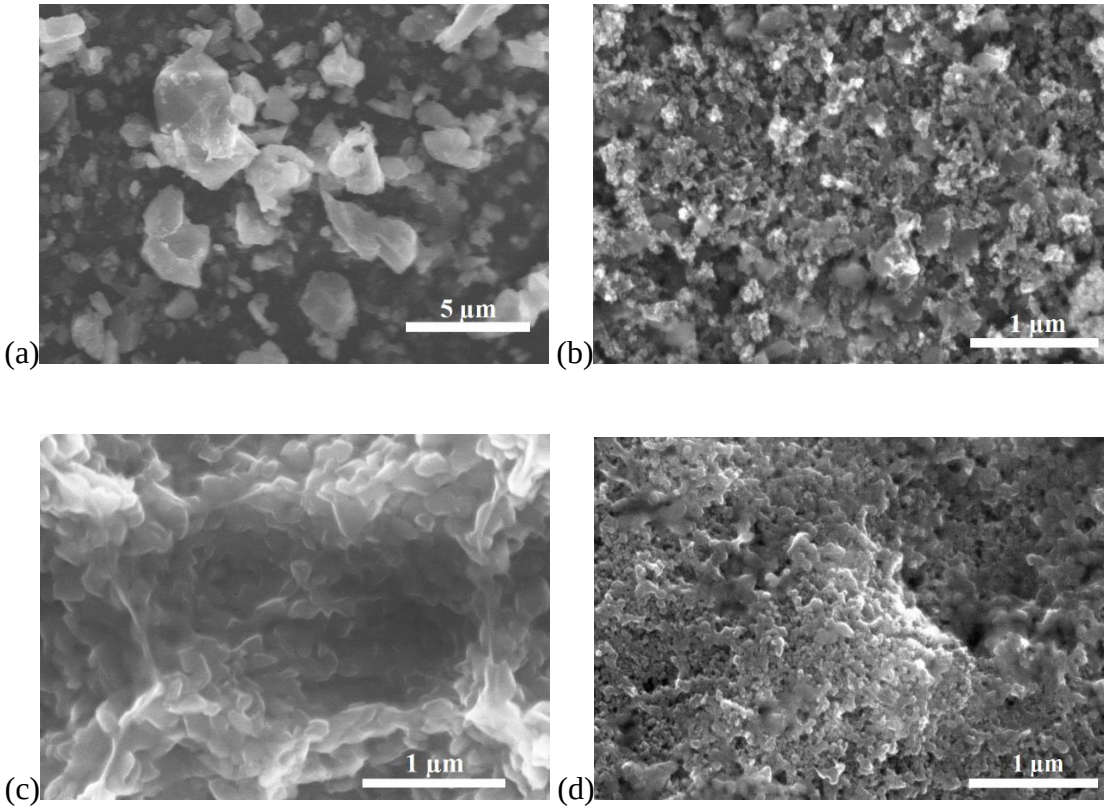

Figure 8.4. SEM images of recrystallized DHBQDS from aqueous DHBQDS solution (a), DHBQDS recrystallized from aqueous DHBQDS-carbon black suspension (b), DHBQDS recrystallized from aqueous DHBQDS-sodium alginate solution (c) and DHBQDS electrode with PVDF and carbon black (d).

As shown in figure 8.5a, the quinone-based DHBQDS molecule has two carbonyl groups, connected by conjugated structure. Both carbonyl groups can react with sodium ions during sodiation/desodiation process. Therefore, single DHBQDS molecule can reversibly react with two sodium ions and electrons, providing a theoretical capacity of 291 mAh g^{-1}. The cyclic voltammogram (CV) of DHBQDS nanorod electrodes in FEC-based electrolyte in figure 8.5b clearly show two desodiation peaks at 1.39 V and 1.62 V possibly due to the two active carbonyl groups, and two corresponding sodiation peaks can be observed at 1.10 V and 1.16 V after two activation cycles (in the third cycles). The two sodiation peaks are very close to each other, so that they overlap and merge into one broad peak in the following cycles. CV scans demonstrate two pairs of redox peaks, representing two active sites in DHBQDS. The two active carbonyl groups react with sodium ions and electrons step by step to undergo a two-phase transition process.

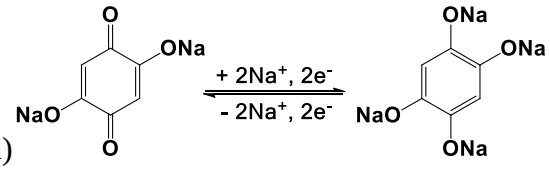

(a)

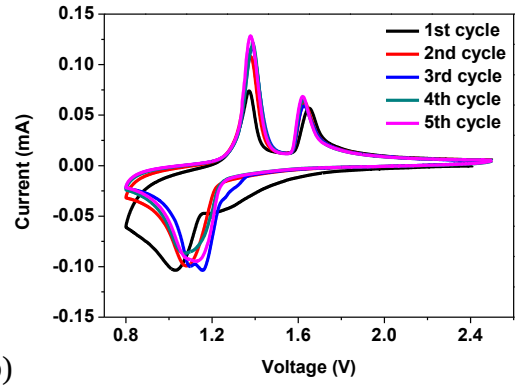

(b)

Figure 8.5. (a)The sodiation/desodiation mechanism for DHBQDS; (b) Cyclic voltammogram of DHBQDS electrode with sodium alginate binder in $NaClO_4$-FEC/DMC electrolyte at 0.1 mV s^{-1} in the potential window from 0.5 V to 2.5 V versus Na/Na^+.

The electrochemical performance of DHBQDS nanorod electrodes is measured in the coin cells at a current density of 50 mA g^{-1} using sodium metal as a counter electrode. Two electrolytes ($NaClO_4$-EC/DMC and $NaClO_4$-FEC/DMC) are used to investigate the role of FEC on the performance of DHBQDS electrodes. DHBQDS micro-electrode with PVDF binder (Figure 8.4d) is used as a control to compare with the DHBQDS nanorod electrode. The galvanostatic charge-discharge curves of DHBQDS electrodes at different sodiation/desodiation cycles are shown in figure 8.6. One sloping sodiation plateau centered at 1.2 V and two flat desodiation plateaus at 1.3 V and 1.6 V are observed for DHBQDS electrodes in both electrolytes after the first charge/discharge activation cycle, which is consistent with the CV scans in the Figure 8.5. In the first sodiation curve, only one sodiation plateau at 1.2 V is observed in the EC-based electrolyte, while an extra slopping sodiation plateau centered at 1.4 V followed by the regular flat sodiation plateau at 1.2 V can be found in the FEC-based electrolyte, which could be associated to the formation of a thick solid electrolyte interphase (SEI) layer, as evidenced by the larger potential hysteresis between sodiation/desodiation plateaus. Table 8.1 summarizes the capacity and Coulombic efficiency of DHBQDS nanorod electrode and micro-electrode in $NaClO_4$-FEC/DMC and $NaClO_4$-EC/DMC. The first cycle Coulombic efficiencies of DHBQDS nanorod electrode and micro-electrode in $NaClO_4$-FEC/DMC electrolyte are lower than that in EC-based electrolyte, indicating formation of thick SEI layer in FEC-based electrolyte. Moreover, larger overpotential of sodiation/desodiation plateaus can be observed in FEC-based electrolyte owing to the thicker insulating SEI layer. However, SEI layer can reduce the dissolution of DHBQDS

and stabilize the electrode, which is beneficial to the long-term cycle life. Table 8.1 also demonstrates that the reversible capacity of DHBQDS nanorod electrode is higher than that of DHBQDS micro-electrode due to the uniform distribution of DHBQDS nanorods and carbon black after recrystallization.

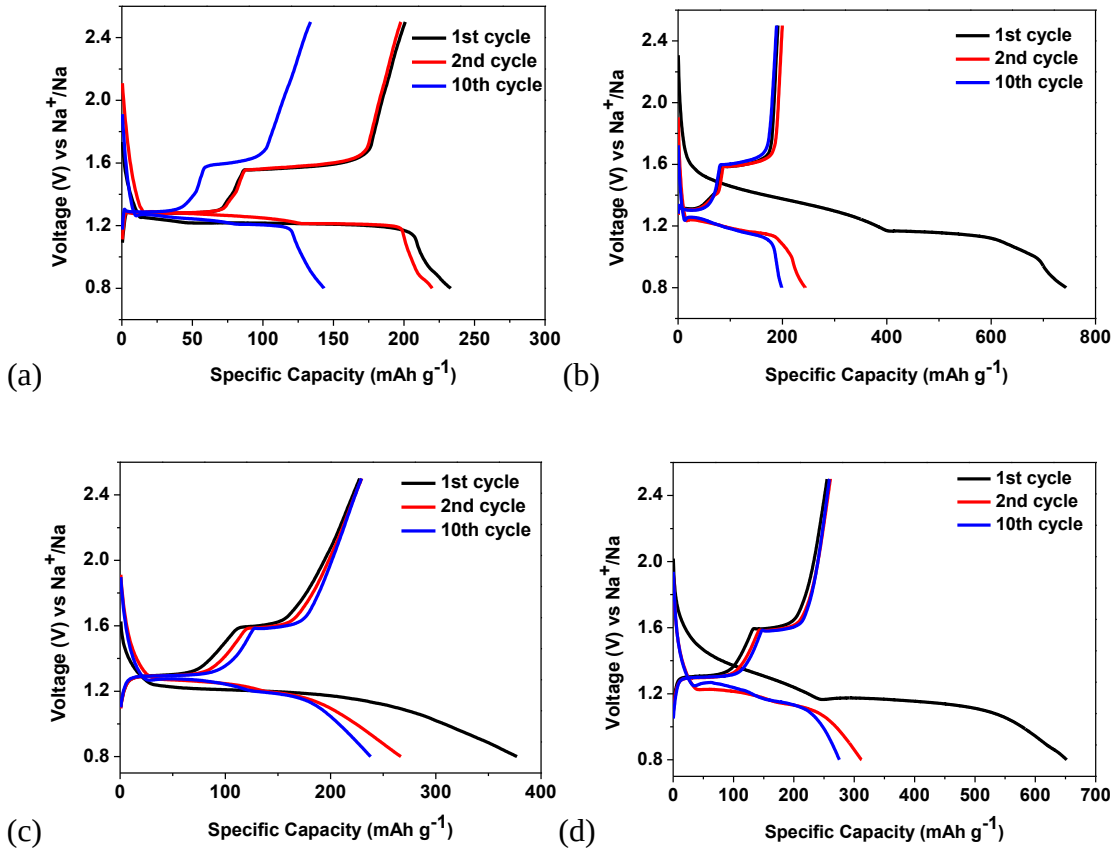

Figure 8.6. The galvanostatic charge-discharge curves between 0.8 V and 2.5 V versus Na/Na^+ for DHBQDS micro-electrode with PVDF binder in $NaClO_4$-EC/DMC electrolyte (a) and $NaClO_4$-FEC/DMC electrolyte (b) and DHBQDS nanorod electrode with sodium alginate binder in $NaClO_4$-EC/DMC electrolyte (c) and $NaClO_4$-FEC/DMC electrolyte (d).

DHBQDS	Capacity (decay rate per cycle)		1st Coulombic efficiency	
	FEC-based Electrolyte	EC-based electrolyte	FEC-based Electrolyte	EC-based electrolyte
DHBQDS micro-electrode with PVDF binder	203 mAh g^{-1} (0.64%)	201 mAh g^{-1} (0.85%)	26%	86%
DHBQDS nanorod electrode with sodium alginate binder	276 mAh g^{-1} (0.13%)	246 mAh g^{-1} (0.27%)	40%	60%

Table 8.1. The capacity decay rate and Coulombic efficiency of DHBQDS micro-electrode and DHBQDS nanorod electrode at a current density of 50 mA g^{-1} in $NaClO_4$-FEC/DMC and $NaClO_4$-EC/DMC.

The cycling stability of DHBQDS electrodes using PVDF and sodium alginate binders was measured in $NaClO_4$-EC/DMC and $NaClO_4$-FEC/DMC electrolytes (Figure 8.7). As shown in figure 8.7a, DHBQDS micro-electrodes using PVDF binder suffers from fast capacity decline in both electrolytes. However, the capacity decay rate of DHBQDS in FEC-based electrolyte is slower than that in EC-based electrolyte, demonstrating that FEC-based electrolyte can improve the cycling stability. Analogous to DHBQDS micro-electrodes with PVDF binder, the cycling performance of DHBQDS nanorod electrodes with sodium alginate binder in the FEC-based electrolyte is also better than that in the EC-based electrolyte (Figure 8.7b). The reversible capacity of DHBQDS nanorod electrodes in EC-based electrolyte decreases from initial 220 mAh g^{-1} to 92 mAh g^{-1} after 240 cycles, while the reversible capacity of DHBQDS electrodes in FEC electrolyte remains at 190 mAh g^{-1} after 240 cycles corresponding to a low capacity decay rate of 0.13% per cycle. The DHBQDS nanorod electrode using sodium alginate binder show better cycling stability than DHBQDS micro-electrode using PVDF binder in both electrolytes, and DHBQDS nanorod electrodes show the best performance in FEC-based electrolyte. The DHBQDS nanorod formed with the assistance of sodium alginate and carbon black provides larger surface area and shorter ionic/electronic diffusion pathways compared to micro-sized

DHBQDS, resulting in fast reaction kinetics. Moreover, the nanostructure can accommodate the volume expansion/shrinkage during sodiation/desodiation process, alleviating the particle pulverization. Since DHBQDS nanorod electrode in FEC-based electrolyte exhibits the best cycle life, it is selected to measure the rate capability. As shown in figure 8.7c, with the current density increases from 20 mA g^{-1} to 1 A g^{-1}, the reversible capacity decreases from 290 mAh g^{-1} to 68 mAh g^{-1}, while the reversible capacity recovers to 290 mAh g^{-1} after the current density returns to 20 mA g^{-1}, demonstrating the excellent robustness and integrity of DHBQDS nanorod electrode at various current densities. After 45 cycles, the current density is increased to 200 mA g^{-1} for long term cycling stability test as shown in figure 8.7d. By comparing figure 8.7b and figure 8.7d, we can conclude that both the cycling stability and Coulombic efficiency of DHBQDS nanorod electrode increase with the elevated current density. The Coulombic efficiency improves from 94% at 50 mA g^{-1} to ~100% at 200 mA g^{-1}, while the reversible capacity remains at 167 mAh g^{-1} at 200 mA g^{-1} after 300 cycles (255 cycles after the rate capability test), which is 87% of its initial capacity (capacity decay rate of 0.051% per cycle). The improved Coulombic efficiency and cycle life at a high charge/discharge current density demonstrate that DHBQDS nanorods still slightly dissolve into the FEC-based electrolyte even SEI protection layer is formed. At low current density, more DHBQDS nanorods can dissolve into the electrolyte, resulting in capacity fading, while the dissolution of DHBQDS nanorods in the electrolyte becomes much slower at high current density due to the shorter charge/discharge period.

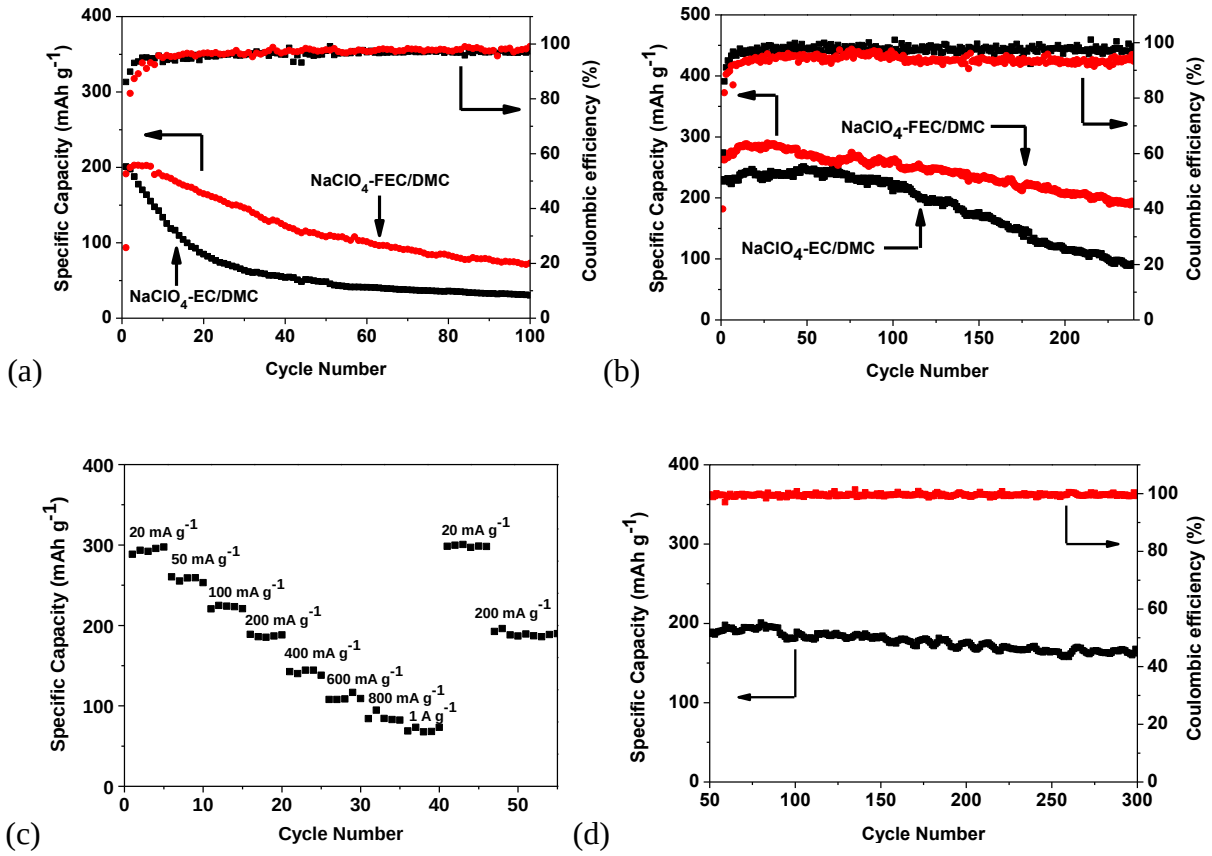

Figure 8.7. Electrochemical performance of DHBQDS electrode. Desodiation capacity and Coulombic efficiency of DHBQDS micro-electrode with PVDF binder (a) and nanorod electrode with sodium alginate binder (b) in $NaClO_4$-EC/DMC electrolyte and $NaClO_4$-FEC/DMC electrolyte at the current density of 50 mA g^{-1}; (c) rate performance of DHBQDS nanorod electrode with sodium alginate binder in $NaClO_4$-FEC/DMC electrolyte at various current rates; (d) Desodiation capacity and Coulombic efficiency after rate measurement at the current density of 200 mA g^{-1}.

The impedance analysis for DHBQDS nano-electrode and micro-electrode in FEC-based electrolyte was performed using electrochemical impedance spectroscopy (EIS). In the impedance plots, the depressed semi-circle in high frequency region represents interface resistance including contact impedance or SEI impedance, and charge transfer impedance, while

the low frequency line stands for ion diffusion resistance. As shown in figure 8.8, both the interface and diffusion impedances of DHBQDS nano-electrode are much lower than that of DHBQDS micro-electrode, indicating the lower interface resistance and better kinetics of DHBQDS nanorods. The interface resistance of DHBQDS nano-electrode is about 140 Ohm, while that for DHBQDS micro-electrode has much higher value of 280 Ohm. The impedance results convince that the high capacity and superior rate capability of DHBQDS nanorod electrode is due to the large electrochemical reaction interface and short lithium ion diffusion pathway.

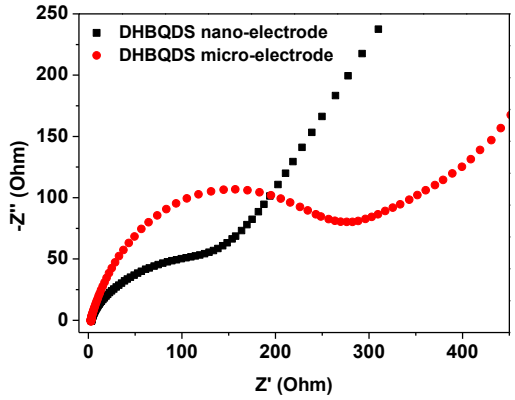

Figure 8.8. Impedance analysis for DHBQDS nanorod electrode and micro-electrode.

To prevent the DHBQDS nanorods from dissolution into the electrolyte, ALD is employed to deposit a thin layer (1 nm or 2 nm) of Al_2O_3 on the surface of DHBQDS nanorod electrode at 150 ^oC under vacuum. As shown in figure 8.9, negligible morphology change can be observed after uniform Al_2O_3 deposition. The electrochemical performance of Al_2O_3 coated DHBQDS nanorod electrode at a low current density of 50 mA g^{-1} in $NaClO_4$-FEC/DMC electrolyte is shown in figure 8.10. The charge/discharge curves of Al_2O_3 covered DHBQDS nanorod electrodes in figure 8.10a and 8.10b are similar to that of bare DHBQDS nanorod electrodes in figure 8.6d, but the sodiation plateaus shift to negative value and a larger potential hysteresis can

be observed, demonstrating the worse reaction kinetics after insulating Al_2O_3 coating. Figure 8.10c and 8.10d show the cycle life of ALD treated DHBQDS nanorod electrodes. The reversible capacity of both ALD treated electrodes increases in the first twenty cycles due to poor reaction kinetics after insulating Al_2O_3 coating, but the Coulombic efficiency of two electrodes with 1nm and 2nm Al_2O_3 increases from 94% of bare DHBQDS to ~100% after nano-layer Al_2O_3 coating, demonstrating the dissolution is alleviated by Al_2O_3 coating. More importantly, the reversible capacities of DHBQDS nanorod electrode with 1nm and 2 nm Al_2O_3 layer remain at 209 mAh g^{-1} and 212 mAh g^{-1} after 300 cycles. The improved Coulombic efficiency and cycle life are attributed to the encapsulation of DHBQDS nanorod by Al_2O_3 layer, which prevents the dissolution of DHBQDS upon cycling. Therefore, a high capacity and long cycle life organic anode is obtained by using organic nanorod material in $NaClO_4$-FEC/DMC electrolyte with Al_2O_3 deposition.

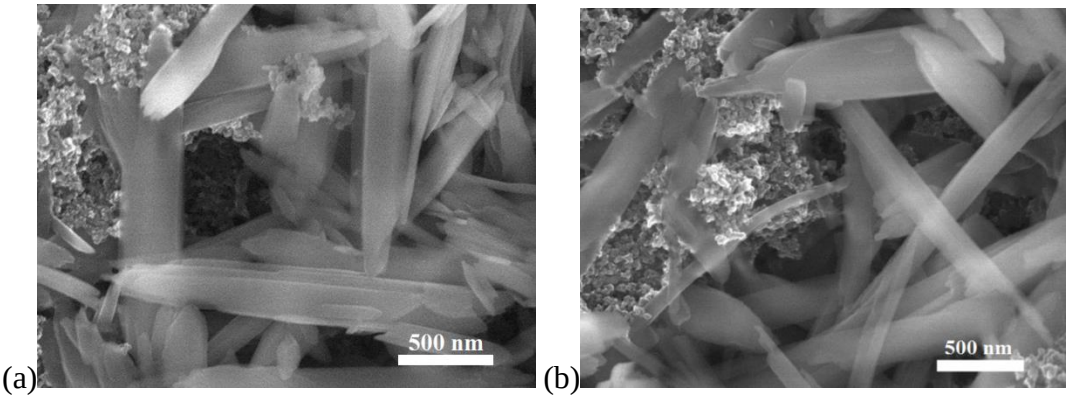

Figure 8.9. SEM images of DHBQDS nanorod electrode covered with 1 nm Al_2O_3 (a) and DHBQDS nanorod electrode covered with 2 nm Al_2O_3 (b).

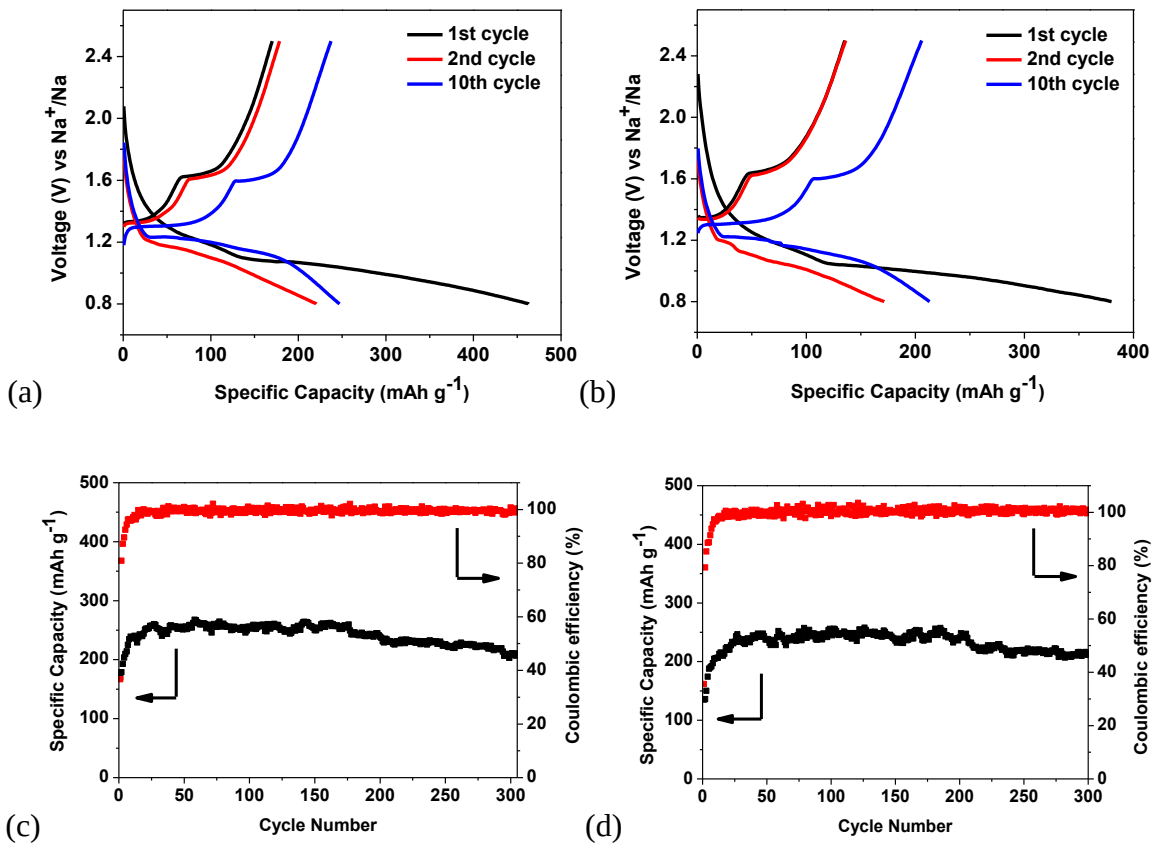

Figure 8.10. The galvanostatic charge-discharge curves between 0.8 V and 2.5 V versus Na/Na^+ for DHBQDS nanorod electrode covered with 1 nm Al_2O_3 layer (a) and 2 nm Al_2O_3 layer (b) with sodium alginate binder in $NaClO_4$-FEC/DMC electrolyte at the current density of 50 mA g^{-1}; Desodiation capacity and Coulombic efficiency of DHBQDS nanorod electrode covered with 1 nm Al_2O_3 layer (c) and 2 nm Al_2O_3 layer (d).

The *ex situ* XRD is performed to study the phase change of DHBQDS nanorod electrode upon sodiation/desodiation process. The fully sodiated DHBQDS nanorod electrode is prepared by sodiating the electrode to 0.8 V and maintaining the voltage at 0.8 V for 12 h. Similarly, the fully desodiated DHBQDS nanorod electrode is prepared by desodiating the electrodes to 2.5 V and maintaining the voltage at 2.5 V for 12 h. Both fully sodiated and fully desodiated electrodes are immersed in dimethyl carbonate for 48 h to remove $NaClO_4$ from the surface of the electrode.

From figure 8.11, we can observe that the three XRD peaks for fresh DHBQDS at 12.5, 15.5 and 17 degree disappear after sodiation, while a small shoulder at 13.3 degree appears, demonstrating the phase change occurs after sodiation. After desodiation, the small shoulder at 13.3 degree disappears, and the three XRD peaks for fresh DHBQDS recover, demonstrating DHBQDS nanorods can maintain its crystal structure upon solidation/desolidation cycles. Therefore, the result of *ex situ* XRD confirms that phase change occurs during sodiation/desodiation process, and the crystal structure of DHBQDS nanorod can be maintained after sodiation/desodiation.

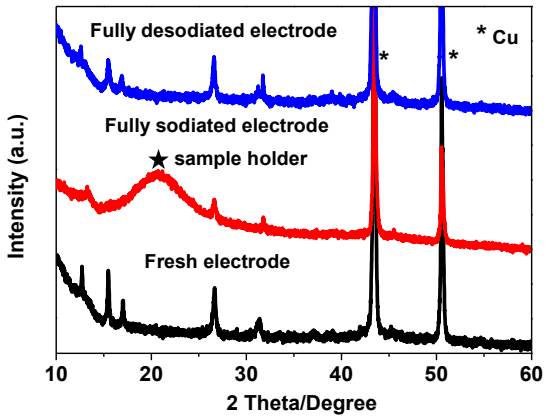

Figure 8.11. XRD patterns for fresh DHBQDS electrode, fully sodiated DHBQDS electrode and fully desodiated DHBQDS electrode.

8.4 Conclusion

A new organic anode material, 2,5-Dihydroxy-1,4-benzoquinone disodium salt, was synthesized by neutralizing 2,5-Dihydroxy-1,4-benzoquinone with sodium hydroxide in ethanol alcohol solution. For the first time, DHBQDS nanorods were *in situ* synthesized in the electrode fabrication process, which uniquely integrates the nanomaterial synthetic procedure into electrode fabrication process. With the assistance of carbon black and sodium alginate, crystal

DHBQDS nanorods were recrystallized from DHBQDS aqueous solution during electrode drying process. The *in situ* formed carbon black-sodium alginate-DHBQDS nanorod composite electrodes have high electronic and ionic conductivity, less particle pulverization, thus high rate capability and excellent cycling stability in $NaClO_4$-FEC/DMC electrolyte. The DHBQDS nanorod electrodes deliver a reversible capacity of 190 mAh g^{-1} at a high current density of 200 mA g^{-1} and maintain 87% of its initial capacity after 300 cycles with capacity decay rate of 0.051% per cycle. ALD is employed to deposit a thin layer (1~2 nm) of Al_2O_3 on the electrode surface, which greatly enhances the Coulombic efficiency from 94% to almost 100% even at a low current density of 50 mA g^{-1}. The reversible capacities of DHBQDS nanorods covered with 1 nm and 2 nm Al_2O_3 layer remain at 209 mAh g^{-1} and 212 mAh g^{-1} after 300 cycles, which represent the best battery performance among all organic anodes. The excellent electrochemical performance of DHBQDS anode demonstrates that it is a promising candidate for advanced NIB. This *in situ* fabrication method can apply to other electrodes if the active materials in electrodes are highly soluble in the solvent of casting slurry.

Chapter 9 Summary and Future Work

9.1 Summary of Work

9.1.1 Sulfur Cathode

Li-sulfur and Na-sulfur batteries are considered as promising energy storage devices for emerging electric vehicles and smart grids due to the low cost and high capacity of sulfur. However, sulfur cathodes for both Li-S and Na-S batteries still suffer from poor cyclic stability and low sulfur utilization. The poor cyclic stability and low sulfur utilization of sulfur cathodes were significantly improved by forming oxygen stabilized C/S composite where sulfur is bonded with oxygen and uniformly distributed in carbon matrix in nano (or even in molecular) levels through annealing the mixture of sulfur and perylene-3, 4, 9, 10-tetracarboxylic dianhydride (PTCDA) at 600 ^{o}C in a sealed vacuum glass tube. The strong interaction between sulfur and oxygen requires extra energy (low potential) to activate sulfur. During initial deep lithiation/delithiation pre-cycles, the strong interaction between sulfur and oxygen is vanished, and the S becomes active even if the discharge potential increased back to normal 1.0 V. The pre-activation of the oxygen stabilized C/S composites also increases the S utilization for Na-sulfur batteries. Therefore, the oxygen stabilized C/S composites are promising cathode materials for Li-sulfur and Na-sulfur batteries.

9.1.2 Selenium Cathode

Selenium (Se) impregnated carbon composites were synthesized by infusing Se into mesoporous carbon at a temperature of 600 ^{o}C under vacuum. Ring-structured Se_8 was produced and

confined in the mesoporous carbon, which acts as an electronic conductive matrix. During the electrochemical process in low-cost $LiPF_6$/EC/DEC electrolyte, low-order polyselenide intermediates formed and were stabilized by mesoporous carbon, which avoided the shuttle reaction of polyselenides. Exceptional electrochemical performance of Se/mesoporous carbon composites was demonstrated in both Li-ion and Na-ion batteries. The Se_8/mesoporous carbon composites also showed excellent rate capability. As the current density increased from 0.1 to 5 C, the capacity retained about 46% in Li-ion batteries and 34% in Na-ion batteries.

As high capacity cathodes for Li-ion and Na-ion batteries, carbon bonded and encapsulated selenium composites (C/Se) with high loading content of 54% Se were synthesized by *in situ* carbonizing the mixture of perylene-3, 4, 9, 10-tetracarboxylic dianhydride (PTCDA) and selenium (Se) in a sealed vacuum glass tube. Since Se is physically encapsulated and chemically bonded by carbon, the shuttle reaction of polyselenide is effectively mitigated. The *in situ* formed C/Se composites exhibit superior cycling stability for both Li-ion and Na-ion batteries in carbonate-based electrolytes. The reversible capacity of the *in situ* formed C/Se composites maintains at 430 mAh g^{-1} after 250 cycles in Li-ion batteries and 280 mAh g^{-1} after 50 cycles in Na-ion batteries at a current density of 100 mA g^{-1}.

9.1.3 Selenium Sulfide Cathode

A facile synthesis of selenium sulfide (SeS_x)/carbonized polyacrylonitrile (CPAN) composites is achieved by annealing the mixture of SeS_2 and polyacrylonitrile (PAN) at 600 ^oC under vacuum. The SeS_x molecules are confined by N-containing carbon (ring) structures in the carbonized PAN to mitigate the dissolution of polysulfide and polyselenide intermediates in carbonate-based

electrolyte. In addition, formation of solid electrolyte interphase (SEI) on the surface of SeS_x/CPAN electrode in the first cycle further prevents polysulfide and polyselenide intermediates from dissolution. The synergic restriction of SeS_x by both CPAN matrix and SEI layer allows SeS_x/CPAN composites to be charged and discharged in a low-cost carbonate-based electrolyte ($LiPF_6$ in EC/DEC) with long cycling stability and high rate capability. The superior electrochemical performance of SeS_x/CPAN composite demonstrates that it is a promising cathode material for long cycle life and high power density lithium ion batteries.

9.1.4 Organic Electrodes

The electroactive organic materials are promising alternatives to inorganic electrode materials for the new generation of green Li-ion batteries due to their sustainability, environmental benignity and low cost. Croconic acid disodium salt (CADS) was used as Li-ion battery electrode, and CADS organic wires with different diameters were fabricated through a facile synthetic route using anti-solvent crystallization method to overcome the challenges of low electronic conductivity of CADS and lithiation induced strain. The CADS nanowire exhibits much better electrochemical performance than its crystal bulk material and microwire counterpart. The nanowire structure also remarkably enhances the kinetics of croconic acid disodium salt. The CADS nanowire retains 50% of the 0.1 C capacity even when the current density increases to 6 C. In contrast, the crystal bulk and microwire material completely lose their capacities when the current density merely increases to 2 C. Such a high rate performance of CADS nanowire is attributed to its short ion diffusion pathway and large surface area, which enable fast ion and electron transport in the electrode. The theoretical calculation suggested that lithiation of CADS experiences an ion exchange process. The sodium ions in CADS will be

gradually replaced by lithium ions during the lithiation and delithiation of CADS electrode, which is confirmed by Inductively Coupled Plasma test.

Croconic acid disodium salt (CADS), a renewable or recyclable organic compound, is investigated as an anode material in sodium ion battery for the first time. The pristine micro-sized CADS delivers a high capacity of 246.7 mAh g^{-1}, but it suffers from fast capacity decay during charge/discharge cycles. The detail investigation reveals that the severe capacity loss is mainly attributed to the pulverization of CADS particles induced by the large volume change during sodiation/desodiation rather than the generally believed dissolution of CADS in the organic electrolyte. Minimizing the particle size can effectively suppress the pulverization, thus improving the cycling stability. Wrapping CADS with graphene oxide by ultrasonic spray pyrolysis can enhance the integration and conductivity of CADS electrodes, thus providing a high capacity of 293 mAh g^{-1}.

Since organic materials have very low electronic conductivity, they are normally synthesized into nano-scale and mixed with conductive carbon before electrode fabrication. I firstly reported a unique one-step fabrication technology by taking advantage of the high solubility of organic materials in water. The synthetic process of nano-size organic materials is merged into the organic electrode fabrication process. 2,5-Dihydroxy-1,4-benzoquinone disodium salt (DHBQDS) is used as a model, and the DHBQDS nanorod electrode is *in situ* formed by precipitating DHBQDS nanorods from DHBQDS-sodium alginate-carbon black aqueous slurry film on a Cu current collector during electrode drying process. To reduce the dissolution of DHBQDS in the electrolyte upon cycling, a thin layer of Al_2O_3 with thickness of 1 nm or 2 nm is coated on the DHBQDS nanorod electrodes using ALD. The ALD enhanced organic nanorods exhibit the best reversible capacity and cycle life among the organic electrodes reported for Na-ion batteries.

9.2 Future Work

High capacity organic compounds based on carbonyl groups (Figure 9.1) will be investigated as electrode materials for Na-ion batteries. In proposed organic Na-ion batteries, pre-sodiated rhodizonic acid disodium salt and 2,5-dihydroxy-1,4-benzoquinone disodium salt will be used as cathode and anode in the sodium ion full cell, respectively. The structures of proposed organic electrode materials are shown in Figure 9.1.

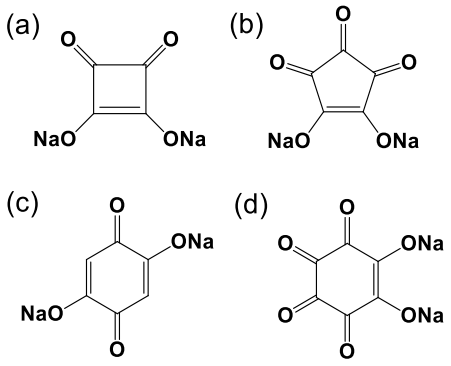

Figure 9.1. Structures of four carbonyl based organic compounds for Na-ion batteries. (a) Squaric acid disodium salt; (b) Croconic acid disodium salt; (c) 2,5-Dihydroxy-1,4-benzoquinone disodium salt; (d) Rhodizonic acid disodium salt.

The organic compounds in figure 9.1 a-c are candidates for anodes, while the organic compound in figure 9.1 d is a candidate for cathode. Since all these compounds are water soluble, the anti-solvent recrystallization method will be used to fabricate organic nanomaterials. Several different electrolytes such as $NaClO_4$-EC/DMC, $NaClO_4$-FEC/DMC, $NaPF_6$-EC/DMC and $NaPF_6$-FEC/DMC will be utilized to compare the electrochemical performance of organic electrodes, and the best electrolyte will be used in the all organic sodium ion full cell. In addition, several different binders such as polyvinylidene fluoride (PVDF), carboxymethyl cellulose (CMC) and sodium alginate (SA) will be used to prepare the electrodes. The battery performance of cathode

and anode with different binders will be compared, and the best binder will be used in the all organic sodium ion full cell. After obtaining electrochemical stable and high capacity cathode and anode materials, an all organic sodium ion full cell will be assembled. As shown in figure 9.2, the organic cathode will be pre-sodiated before use due to the lack of sodium ions. The weight of cathode and anode electrodes will be calculated based on the capacities of each electrode and the first cycle coulombic efficiency of anode. The battery performance of the all organic full cell will be recorded by Arbin battery test station and Gamry Reference 3000. A high performance all organic sodium ion full cell will be achieved for future application in lightweight, flexible, transparent and green batteries.

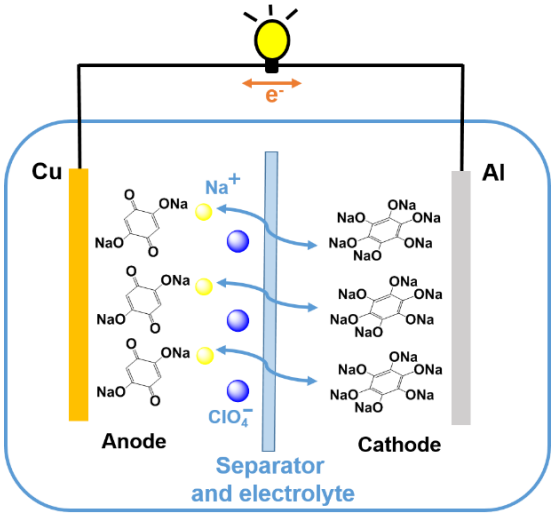

Figure 9.2. An all organic sodium full cell.

Task 1. The electrochemical performance of the proposed organic compounds will be evaluated by galvanostatic charge-discharge tests, cyclic voltammetry, electrochemical impedance spectroscopy and galvanostatic intermittent titration technique.

Task 2. The electrochemical performance will be enhanced by optimizing the electrolyte, binder and morphology of electrode materials. Nano-structure organic materials will be fabricated to improve the kinetics of Na-ion batteries.

Task 3. The reaction mechanism of the proposed organic compounds will be investigated by *in-situ* XRD, TEM and Raman spectroscopy.

Task 4. The all organic sodium ion full cell will be assembled based on the proposed organic compounds, and the electrochemical performance of the full cell will be evaluated.

Bibliography

1. Whittingham, M. S., *Chem. Rev.* **2014**, *114*, 11414-11443.
2. Scrosati, B.; Hassoun, J.; Sun, Y.-K., *Energy Environ. Sci.* **2011**, *4*, 3287-3295.
3. Jung, Y. S.; Cavanagh, A. S.; Dillon, A. C.; Groner, M. D.; George, S. M.; Lee, S.-H., *J. Electrochem. Soc.* **2010**, *157*, A75-A81.
4. Wang, C.; Appleby, A. J.; Little, F. E., *J. Electroanal. Chem.* **2001**, *497*, 33-46.
5. Ji, X.; Nazar, L. F., *J. Mater. Chem.* **2010**, *20*, 9821-9826.
6. Zhang, S. S., *Front. Energy Res.* **2013**, *1*, 10.
7. Manthiram, A.; Fu, Y.; Chung, S. H.; Zu, C.; Su, Y. S., *Chem. Rev.* **2014**, *114*, 11751-11787.
8. Jayaprakash, N.; Shen, J.; Moganty, S. S.; Corona, A.; Archer, L. A., *Angew. Chem. Int. Ed.* **2011**, *50*, 5904-5908.
9. Guo, J.; Xu, Y.; Wang, C., *Nano Lett.* **2011**, *11*, 4288-4294.
10. Wang, H.; Yang, Y.; Liang, Y.; Robinson, J. T.; Li, Y.; Jackson, A.; Cui, Y.; Dai, H., *Nano Lett.* **2011**, *11*, 2644-2647.
11. Ji, L.; Rao, M.; Zheng, H.; Zhang, L.; Li, Y.; Duan, W.; Guo, J.; Cairns, E. J.; Zhang, Y., *J. Am. Chem. Soc.* **2011**, *133*, 18522-18525.
12. Zheng, G.; Yang, Y.; Cha, J. J.; Hong, S. S.; Cui, Y., *Nano Lett.* **2011**, *11*, 4462-4467.
13. Abouimrane, A.; Dambournet, D.; Chapman, K. W.; Chupas, P. J.; Weng, W.; Amine, K., *J. Am. Chem. Soc.* **2012**, *134*, 4505-4508.
14. Yang, C.; Xin, S.; Yin, Y.; Ye, H.; Zhang, J.; Guo, Y., *Angew. Chem. Int. Ed.* **2013**, *52*, 8363-8367.
15. Wang, X.; Zhang, Z.; Qu, Y.; Wang, G.; Lai, Y.; Li, J., *J. Power Sources* **2015**, *287*, 247-252.

16. Han, K.; Liu, Z.; Shen, J.; Lin, Y.; Dai, F.; Ye, H., *Adv. Funct. Mater.* **2015**, *25*, 455-463.

17. Peng, X.; Wang, L.; Zhang, X.; Gao, B.; Fu, J.; Xiao, S.; Huo, K.; Chu, P. K., *J. Power Sources* **2015**, *288*, 214-220.

18. Zeng, L.; Zeng, W.; Jiang, Y.; Wei, X.; Li, W.; Yang, C.; Zhu, Y.; Yu, Y., *Adv. Energy Mater.* **2015**, *5*, 1401377.

19. Yuan, L.-X.; Wang, Z.-H.; Zhang, W.-X.; Hu, X.-L.; Chen, J.-T.; Huang, Y.-H.; Goodenough, J. B., *Energy Environ. Sci.* **2011**, *4*, 269-284.

20. Aravindan, V.; Gnanaraj, J.; Lee, Y.-S.; Madhavi, S., *J. Mater. Chem. A* **2013**, *1*, 3518-3539.

21. Gaubicher, J.; Wurm, C.; Goward, G.; Masquelier, C.; Nazar, L., *Chem. Mater.* **2000**, *12*, 3240-3242.

22. Kang, B.; Ceder, G., *Nature* **2009**, *458*, 190-193.

23. Hu, L. H.; Wu, F. Y.; Lin, C. T.; Khlobystov, A. N.; Li, L. J., *Nat. Commun.* **2013**, *4*, 1687.

24. Periasamy, P.; Kalaiselvi, N.; Kim, H. S., *Int. J. Electrochem. Sci.* **2007**, *2*, 689-699.

25. Manthiram, A.; Chemelewski, K.; Lee, E.-S., *Energy Environ. Sci.* **2014**, *7*, 1339-1350.

26. Lee, E.-S.; Manthiram, A., *J. Mater. Chem. A* **2014**, *2*, 3932-3939.

27. Zheng, J.; Xu, P.; Gu, M.; Xiao, J.; Browning, N. D.; Yan, P.; Wang, C.; Zhang, J.-G., *Chem. Mater.* **2015**, *27*, 1381-1390.

28. Palacín, M. R., *Chem. Soc. Rev.* **2009**, *38*, 2565-2575.

29. Yang, Z.; Choi, D.; Kerisit, S.; Rosso, K. M.; Wang, D.; Zhang, J.; Graff, G.; Liu, J., *J. Power Sources* **2009**, *192*, 588-598.

30. Wu, H.; Cui, Y., *Nano Today* **2012**, *7*, 414-429.

31. Chan, C. K.; Peng, H.; Liu, G.; McIlwrath, K.; Zhang, X. F.; Huggins, R. A.; Cui, Y., *Nat. Nanotechnol.* **2008**, *3*, 31-35.

32. Xu, Y.; Guo, J.; Wang, C., *J. Mater. Chem.* **2012**, *22*, 9562-9567.

33. Xu, Y.; Zhu, Y.; Liu, Y.; Wang, C., *Adv. Energy Mater.* **2013**, *3*, 128-133.

34. Xu, Y.; Liu, Q.; Zhu, Y.; Liu, Y.; Langrock, A.; Zachariah, M. R.; Wang, C., *Nano Lett.* **2013**, *13*, 470-474.

35. Zhu, Z.; Wang, S.; Du, J.; Jin, Q.; Zhang, T.; Cheng, F.; Chen, J., *Nano Lett.* **2014**, *14*, 153-157.

36. Dong, Q.; Wu, C.; Jin, M.; Huang, Z.; Zheng, M.; You, J.; Lin, Z., *Solid State Ionics* **2004**, *167*, 49-54.

37. Xu, Y.; Jian, G.; Liu, Y.; Zhu, Y.; Zachariah, M. R.; Wang, C., *Nano Energy* **2014**, *3*, 26-35.

38. Lin, F.; Nordlund, D.; Weng, T. C.; Zhu, Y.; Ban, C.; Richards, R. M.; Xin, H. L., *Nat. Commun.* **2014**, *5*, 3358.

39. Xiao, J.; Choi, D.; Cosimbescu, L.; Koech, P.; Liu, J.; Lemmon, J. P., *Chem. Mater.* **2010**, *22*, 4522-4524.

40. Bieker, G.; Winter, M.; Bieker, P., *Phys. Chem. Chem. Phys.*, **2015**, *17*, 8670-8679.

41. Zheng, G.; Lee, S. W.; Liang, Z.; Lee, H.; Yan, K.; Yao, H.; Wang, H.; Li, W.; Chu, S.; Cui, Y., *Nat. Nanotechnol.*, **2014**, *9*, 618-623.

42. Slater, M. D.; Kim, D.; Lee, E.; Johnson, C. S., *Adv. Funct. Mater.* **2013**, *23*, 947-958.

43. Xin, S.; Yin, Y. X.; Guo, Y. G.; Wan, L. J., *Adv Mater* **2014**, *26*, 1261-1265.

44. Luo, C.; Xu, Y.; Zhu, Y.; Liu, Y.; Zheng, S.; Liu, Y.; Langrock, A.; Wang, C., *ACS Nano* **2013**, *7*, 8003-8010.

45. Yabuuchi, N.; Kajiyama, M.; Iwatate, J.; Nishikawa, H.; Hitomi, S.; Okuyama, R.; Usui, R.; Yamada, Y.; Komaba, S., *Nat. Mater.* **2012**, *11*, 512-517.

46. Guignard, M.; Didier, C.; Darriet, J.; Bordet, P.; Elkaïm, E.; Delmas, C., *Nat. Mater.* **2013**, *12*, 74-80.

47. Zhu, Y.; Xu, Y.; Liu, Y.; Luo, C.; Wang, C., *Nanoscale* **2013**, *5*, 780-787.

48. Langrock, A.; Xu, Y.; Liu, Y.; Ehrman, S.; Manivannan, A.; Wang, C., *J. Power Sources* **2013**, *223*, 62-67.

49. Barpanda, P.; Oyama, G.; Nishimura, S.; Chung, S. C.; Yamada, A., *Nat. Commun.* **2014**, *5*, 4358.

50. Ellis, B. L.; Makahnouk, W. R.; Makimura, Y.; Toghill, K.; Nazar, L. F., *Nat. Mater.* **2007**, *6*, 749-753.

51. Luo, W.; Bommier, C.; Jian, Z.; Li, X.; Carter, R.; Vail, S.; Lu, Y.; Lee, J. J.; Ji, X., *ACS Appl. Mater. Interfaces* **2015**, *7*, 2626-2631.

52. Xu, J.; Wang, M.; Wickramaratne, N. P.; Jaroniec, M.; Dou, S.; Dai, L., *Adv. Mater.* **2015**, *27*, 2042-2048.

53. Wen, Y.; He, K.; Zhu, Y.; Han, F.; Xu, Y.; Matsuda, I.; Ishii, Y.; Cumings, J.; Wang, C., *Nat. Commun.* **2014**, *5*, 4033.

54. Liu, Y.; Zhang, N.; Jiao, L.; Tao, Z.; Chen, J., *Adv. Funct. Mater.* **2015**, *25*, 214-220.

55. Zhu, Y.; Han, X.; Xu, Y.; Liu, Y.; Zheng, S.; Xu, K.; Hu, L.; Wang, C., *ACS Nano* **2013**, *7*, 6378-6386.

56. Zhu, Y.; Wen, Y.; Fan, X.; Gao, T.; Han, F.; Luo, C.; Liou, S.; Wang, C., *ACS Nano* **2015**, *9*, 3254-3264.

57. Wang, J.; Luo, C.; Gao, T.; Langrock, A.; Mignerey, A. C.; Wang, C., *Small* **2015**, *11*, 473-481.

58. Manthiram, A.; Fu, Y.; Su, Y., *Acc. Chem. Res.* **2013**, *46*, 1125-1134.

59. Yin, Y. X.; Xin, S.; Guo, Y. G.; Wan, L. J., *Angew. Chem. Int. Ed.* **2013**, *52*, 13186-13200.

60. Yang, Y.; Zheng, G.; Cui, Y., *Chem. Soc. Rev.* **2013**, *42*, 3018-3032.

61. Seh, Z. W.; Li, W.; Cha, J. J.; Zheng, G.; Yang, Y.; McDowell, M. T.; Hsu, P. C.; Cui, Y., *Nat. Commun.* **2013**, *4*, 1331.

62. Ji, X.; Lee, K. T.; Nazar, L. F., *Nat. Mater.* **2009**, *8*, 500-506.

63. Wu, F.; Chen, J.; Chen, R.; Wu, S.; Li, L.; Chen, S.; Zhao, T., *J. Phys. Chem. C* **2011**, *115*, 6057-6063.

64. Zhang, S. S., *J. Electrochem. Soc.* **2012**, *159*, A920-A923.

65. Shin, E. S.; Kim, K.; Oh, S. H.; Cho, W. I., *Chem. Commun.* **2013**, *49*, 2004-2006.

66. Suo, L.; Hu, Y. S.; Li, H.; Armand, M.; Chen, L., *Nat. Commun.* **2013**, *4*, 1481.

67. Cui, Y.; Abouimrane, A.; Lu, J.; Bolin, T.; Ren, Y.; Weng, W.; Sun, C.; Maroni, V. A.; Heald, S. M.; Amine, K., *J. Am. Chem. Soc.* **2013**, *135*, 8047-8056.

68. Kundu, D.; Krumeich, F.; Nesper, R., *J. Power Sources* **2013**, *236*, 112-117.

69. Han, K.; Liu, Z.; Ye, H.; Dai, F., *J. Power Sources* **2014**, *263*, 85-89.

70. Zeng, L.; Wei, X.; Wang, J.; Jiang, Y.; Li, W.; Yu, Y., *J. Power Sources* **2015**, *281*, 461-469.

71. Goodenough, J. B.; Kim, Y., *Chem. Mater.* **2010**, *22*, 587-603.

72. Liang, Y.; Tao, Z.; Chen, J., *Adv. Energy Mater.* **2012**, *2*, 742-769.

73. Chen, H.; Armand, M.; Demailly, G.; Dolhem, F.; Poizot, P.; Tarascon, J. M., *ChemSusChem* **2008**, *1*, 348-355.

74. Reddy, A. L.; Nagarajan, S.; Chumyim, P.; Gowda, S. R.; Pradhan, P.; Jadhav, S. R.; Dubey, M.; John, G.; Ajayan, P. M., *Sci. Rep.* **2012**, *2*, 960.

75. Morita, Y.; Nishida, S.; Murata, T.; Moriguchi, M.; Ueda, A.; Satoh, M.; Arifuku, K.; Sato, K.; Takui, T. *Nat. Mater.* **2011**, *10*, 947-951.

76. Han, X.; Chang, C.; Yuan, L.; Sun, T.; Sun, J., *Adv. Mater.* **2007**, *19*, 1616-1621.

77. Armand, M.; Grugeon, S.; Vezin, H.; Laruelle, S.; Ribière, P.; Poizot, P.; Tarascon, J.-M., *Nat. Mater.* **2009**, *8*, 120-125.

78. Wang, S.; Wang, L.; Zhang, K.; Zhu, Z.; Tao, Z.; Chen, J., *Nano Lett.* **2013**, *13*, 4404-4409.

79. Chen, H.; Armand, M.; Courty, M.; Jiang, M.; Grey, C. P.; Dolhem, F.; Tarascon, J.-M.; Poizot, P., *J. Am. Chem. Soc.* **2009**, *131*, 8984-8988.

80. Zhao, L.; Zhao, J.; Hu, Y.-S.; Li, H.; Zhou, Z.; Armand, M.; Chen, L., *Adv. Energy Mater.* **2012**, *2*, 962-965.

81. Wang, S.; Wang, L.; Zhu, Z.; Hu, Z.; Zhao, Q.; Chen, J., *Angew. Chem. Int. Ed.* **2014**, *53*, 5892-5896.

82. Chen, X.; Gerasopoulos, K.; Guo, J.; Brown, A.; Wang, C.; Ghodssi, R.; Culver, J. N., *Adv. Funct. Mater.* **2011**, *21*, 380-387.

83. Kasavajjula, U.; Wang, C.; Appleby, A. J., *J. Power Sources* **2007**, *163*, 1003-1039.

84. Ellis, B. L.; Lee, K. T.; Nazar, L. F., *Chem. Mater.* **2010,** *22*, 691-714.

85. Shi, S. J.; Lou, Z. R.; Xia, T. F.; Wang, X. L.; Gu, C. D.; Tu, J. P., *J. Power Sources* **2014,** *257*, 198-204.

86. Wu, F.; Li, N.; Su, Y.; Zhang, L.; Bao, L.; Wang, J.; Chen, L.; Zheng, Y.; Dai, L.; Peng, J.; Chen, S., *Nano lett.* **2014,** *14*, 3550-3555.

87. Wang, C.; Wu, H.; Chen, Z.; McDowell, M. T.; Cui, Y.; Bao, Z., *Nat. Chem.* **2013**, *5*, 1042-1048.

88. Chen, X.; Guo, J.; Gerasopoulos, K.; Langrock, A.; Brown, A.; Ghodssi, R.; Culver, J. N.; Wang, C., *J. Power Sources* **2012,** *211*, 129-132.

89. Zheng, S.; Yi, F.; Li, Z.; Zhu, Y.; Xu, Y.; Luo, C.; Yang, J.; Wang, C., *Adv. Funct. Mater.*

2014, *24*, 4156-4163.

90. Bruce, P. G.; Freunberger, S. A.; Hardwick, L. J.; Tarascon, J. M., *Nat. Mater.* **2012,** *11*, 19-29.
91. Zhao, Y.; Wu, W.; Li, J.; Xu, Z.; Guan, L., *Adv. Mater.* **2014,** *26*, 5113-5118.
92. Luo, C.; Zhu, Y.; Wen, Y.; Wang, J.; Wang, C., *Adv. Funct. Mater.* **2014,** *24*, 4082-4089.
93. Gao, J.; Lowe, M. A.; Kiya, Y.; Abruña, H. D., *J. Phys. Chem. C* **2011,** *115*, 25132-25137.
94. Schuster, J.; He, G.; Mandlmeier, B.; Yim, T.; Lee, K. T.; Bein, T.; Nazar, L. F., *Angew. Chem. Int. Ed.* **2012,** *51*, 3591-3595.
95. Zhao, M. Q.; Zhang, Q.; Huang, J. Q.; Tian, G. L.; Nie, J. Q.; Peng, H. J.; Wei, F., *Nat. Commun.* **2014,** *5*, 3410.
96. Ji, L.; Rao, M.; Aloni, S.; Wang, L.; Cairns, E. J.; Zhang, Y., *Energy Environ. Sci.* **2011,** *4*, 5053-5059.
97. Elazari, R.; Salitra, G.; Garsuch, A.; Panchenko, A.; Aurbach, D., *Adv. Mater.* **2011,** *23*, 5641-5644.
98. Ji, X.; Evers, S.; Black, R.; Nazar, L. F., *Nat. Commun.* **2011,** *2*, 325.
99. Guo, J.; Yang, Z.; Yu, Y.; Abruna, H. D.; Archer, L. A., *J. Am. Chem. Soc.* **2013,** *135*, 763-767.
100. Wang, J.; Yang, J.; Wan, C.; Du K.; Xie, J.; Xu, N., *Adv. Funct. Mater.* **2003**, *13*, 487-492.
101. Yin, L.; Wang, J.; Lin, F.; Yang, J.; Nuli, Y., *Energy Environ. Sci.* **2012,** *5*, 6966-6972.
102. Xin, S.; Gu, L.; Zhao, N. H.; Yin, Y. X.; Zhou, L. J.; Guo, Y. G.; Wan, L. J., *J. Am. Chem. Soc.* **2012,** *134*, 18510-18513.
103. Lu, L. Q.; Lu, L. J.; Wang, Y., *J. Mater. Chem. A* **2013,** *1*, 9173-9181.
104. Nan, C.; Lin, Z.; Liao, H.; Song, M. K.; Li, Y.; Cairns, E. J., *J. Am. Chem. Soc.* **2014,** *136*,

4659-4663.

105. Zhang, S. S., *J. Power Sources* **2013,** *231*, 153-162.

106. Xu, Y.; Wen, Y.; Zhu, Y.; Gaskell, K.; Cychosz, K. A.; Eichhorn, B.; Xu, K.; Wang, C., *Adv. Funct. Mater.* **2015**, DOI: 10.1002/adfm.201500983.

107. Liu, C.; Li, F.; Ma, L.; Cheng, H., *Adv. Mater.* **2010**, *22*, E28-E62.

108. Ellis, B. L.; Nazar, L. F., *Curr. Opin. Solid State Mater. Sci.* **2012**, *1*6, 168-177.

109. Akridge, J. R.; Mikhaylik, Y. V.; White, N., *Solid State Ionics* **2004**, *175*, 243-245.

110. Lu, X.; Kirby, B. W.; Xu, W.; Li. G.; Kim, J. Y.; Lemmon, J. P.; Sprenkle, V. L.; Yang, Z., *Energy Environ. Sci.* **2013**, *6*, 299-306.

111. Wang, D.; Zeng, Q.; Zhou, G.; Yin, L.; Li, F.; Cheng, H.; Gentle, I. R.; Lu, G. Q., *J. Mater. Chem. A* **2013**, *1*, 9382-9394.

112. Zhang, B.; Qin, X.; Li, G. R.; Gao, X. P., *Energy Environ. Sci.* **2010**, *3*, 1531-1537.

113. Poborchii, V. V., Solid State Commun. **1998**, *107*, 513-518.

114. Lukács, R.; Veres, M.; Shimakawa, K.; Kugler, S., *J. Appl. Phys.* **2010**, *107*, 073517.

115. Lin, Z.; Wang, Z.; Chen, W.; Lir, L.; Li, G.; Liu, Z.; Han, H.; Wang, Z., Solid State Commun. **1996**, *100*, 841-843.

116. Guo, J.; Sun, A.; Chen, X.; Wang, C.; Manivannanb, A. *Electrochim. Acta* **2011**, *56*, 3981-3987.

117. Guo, J.; Liu, Q.; Wang, C.; Zachariah M. R., *Adv. Funct. Mater.* **2012**, *22*, 803-811.

118. Chen, Y.; Li, X.; Park, K.; Song, J.; Hong, J.; Zhou, L.; Mai, Y. W.; Huang, H.; Goodenough, J. B., *J. Am. Chem. Soc.* **2013**, *135*, 16280-16283.

119. Wang, C.; Wu, H.; Chen, Z.; McDowell, M. T.; Cui, Y.; Bao, Z., *Nat. Chem.* **2013**, *5*,1042-1048.

120. Zheng, G.; Zhang, Q.; Cha, J. J.; Yang, Y.; Li, W.; Seh, Z. W.; Cui, Y., *Nano Lett.* **2013**, *13*, 1265-1270.

121. Yao, H.; Zheng, G.; Hsu, P. C.; Kong, D.; Cha, J. J.; Li, W.; Seh, Z. W.; McDowell, M. T.; Yan, K.; Liang, Z.; Narasimhan, V. K.; Cui, Y., *Nat. Comm.* **2014**, *5*, 3943.

122. Cui, Y.; Abouimrane, A.; Sun, C. J.; Ren, Y.; Amine, K., Chem. Comm. 2014, 50, 5576-5579.

123. Lee, J. T.; Kim, H.; Oschatz, M.; Lee, D.; Wu, F.; Lin, H.; Zdyrko, B.; Cho, W.; Kaskel, S.; Yushin, G., *Adv. Energy Mater.* **2015**, *5*, DOI: 10.1002/aenm.201400981.

124. Liu, L.; Hou, Y.; Wu, X.; Xiao, S.; Chang, Z.; Yang, Y.; Wu, Y., *Chem. Comm.* **2013**, *49*, 11515-11517.

125. Zhang, Z.; Yang, X.; Wang, X.; Li, Q.; Zhang, Z., *Solid State Ionics* **2014**, *260*, 101-106.

126. Zhang, Z.; Zhang, Z.; Zhang, K.; Yang, X.; Li, Q., *RSC Adv.* **2014**, *4*, 15489-15492.

127. Liu, L.; Hou, Y.; Yang, Y.; Li, M.; Wang, X.; Wu, Y., *RSC Adv.* **2014**, *4*, 9086-9091.

128. Li, Z.; Yuan, L.; Yi, Z.; Liu, Y.; Huang, Y., *Nano Energy* **2014**, *9*, 229-236.

129. J. F. Moulder, W. F. Stickle, P. E. Sobol, K. D. Bomben, Handbook of X-ray Photoelectron Spectroscopy.

130. Pan, H.; Hu, Y.; Chen, L., *Energy Environ. Sci.* **2013**, *6*, 2338-2360.

131. Lin, Z.; Liu, Z.; Fu, W.; Dudney, J. N.; Liang, C., *Adv. Funct. Mater.* **2013**, *23*, 1064-1069.

132. Kim, J.; Lee, D.; Jung, H.; Sun, Y.; Hassoun J.; Scrosati, B., *Adv. Funct. Mater.* **2013**, *23*, 1076-1080.

133. Song, J.; Xu, T.; Gordin, M. L.; Zhu, P.; Lv, D.; Jiang, Y.; Chen, Y.; Duan, Y.; Wang, D., *Adv. Funct. Mater.* **2014**, *24*, 1243-1250.

134. Rahaman, M. S. A.; Ismail, A. F.; Mustafa, A., *Polym. Degrad. Stab.* **2007**, *92*, 1421-1432.

135. Laitinen, R.; Pakkanen, T., *J. Mol. Struct. : THEOCHEM* **1983**, *91*, 337-352.

136. Drowart, J.; Smoes, S., *J. Chem. Soc., Faraday Trans.* **1977**, *73*, 1755-1767.

137. Jones, R. O.; Hohl, D., *J. Am. Chem. Soc.* **1990**, *112*, 2590-2596.

138. Xu, K., *Chem. Rev.* **2004**, *104*, 4303-4417.

139. Chung, S.; Bloking, J. T.; Chiang, Y., *Nat. Mater.* **2002**, *1*, 123-128.

140. Song, Z.; Zhan, H.; Zhou, Y., *Angew. Chem. Int. Ed.* **2010**, *49*, 8444-8448.

141. Song, Z.; Xu, T.; Gordin, M. L.; Jiang, Y.; Bae, I.; Xiao, Q.; Zhan, H.; Liu, J.; Wang, D., *Nano Lett.* **2012**, *12*, 2205-2211.

142. Genorio, B.; Pirnat, K.; Cerc-Korosec, R.; Dominko, R.; Gaberscek, M., *Angew. Chem. Int. Ed.* **2010**, *49*, 7222-7224.

143. Senoh, H.; Yao, M.; Sakaebe, H.; Yasuda, K.; Siroma, Z., *Electrochim. Acta* **2011**, *56*, 10145-10150.

144. Geng, J.; Bonnet, J.; Renault, S.; Dolhem, F.; Poizot, P., *Energy Environ. Sci.* **2010**, *3*, 1929-1933.

145. Han, X.; Qing, G.; Sun, J.; Sun, T., *Angew. Chem. Int. Ed.* **2012**, *51*, 5147-5151.

146. Hanyu, Y.; Honma, I., *Sci. Rep.* **2012**, *2*, 453.

147. Walker, W.; Grugeon, S.; Mentre, O.; Laruelle, S.; Tarascon, J.; Wudl, F., *J. Am. Chem. Soc.* **2010**, *132*, 6517-6523.

148. Nokami, T.; Matsuo, T.; Inatomi, Y.; Hojo. N.; Tsukagoshi, T.; Yoshizawa, H.; Shimizu, A.; Kuramoto, H.; Komae, K.; Tsuyama, H.; Yoshida, J., *J. Am. Chem. Soc.* **2012**, *134*, 19694-19700.

149. Kassam, A.; Burnell, D. J.; Dahn, J. R., *Electrochem. Solid-State Lett.* **2011**, *14*, A22-A23.

150. Pirnat, K.; Dominko, R.; Cerc-Korosec, R.; Mali, G.; Genorio, B.; Gaberscek, M., *J. Power Sources* **2012**, *199*, 308-314.

151. Xu, W.; Read, A.; Koech, P. K.; He, D.; Wang, C.; Xiao, J.; Padmaperuma, A. B.; Graff, G. L.; Liu, J.; Zhang, J., *J. Mater. Chem.* **2012**, *22*, 4032-4039.

152. Liu, H.; Li, J.; Lao, C.; Huang, C.; Li, Y.; Wang, Z.; Zhu, D., *Nanotechnology* **2007**, *18*, 495704.

153. Hirai, K.; Ichitsubo, T.; Uda, T.; Miyazaki, A.; Yagi, S.; Matsubara, E., *Acta Mater.* **2008**, *56*, 1539-1545.

154. Magasinski, A.; Dixon, P.; Hertzberg, B.; Kvit, A.; Ayala, J.; Yushin G., *Nat. Mater.* **2010**, *9*, 353-358.

155. Palomares, V.; Serras, P.; Villaluenga, I.; Hueso, K. B.; Carretero-González, J.; Rojo, T., *Energy Environ. Sci.* **2012**, *5*, 5884-5901.

156. Park, Y.; Shin, D.; Woo, S. H.; Choi, N. S.; Shin, K. H.; Oh, S. M.; Lee, K. T.; Hong, S. Y., *Adv. Mater.* **2012**, *24*, 3562-3567.

157. Abouimrane, A.; Weng, W.; Eltayeb, H.; Cui, Y.; Niklas, J.; Poluektov, O.; Amine, K., *Energy Environ. Sci.* **2012**, *5*, 9632-9638.

158. Okuyama, K.; Lenggoro, I. W., *Chem. Eng. Sci.* **2003**, *58*, 537-547.

159. Xu, B.; Yue, S.; Sui, Z.; Zhang, X.; Hou, S.; Cao, G.; Yang, Y., *Energy Environ. Sci.* **2011**, *4*, 2826-2830.

160. Luo, J.; Zhao, X.; Wu, J.; Jang, H. D.; Kung, H. H.; Huang, J., *J. Phys. Chem. Lett.* **2012**, *3*, 1824-1829.

161. Wen, Y.; Zhu, Y.; Langrock, A.; Manivannan, A.; Ehrman, S. H.; Wang, C., *Small* **2013**, *9*, 2810-2816.

162. Wang, Y.; Chou, S.; Liu, H.; Dou, S., *Carbon* **2013**, *57*, 202-208.

163. Liu, Y.; Xu, Y.; Zhu, Y.; Culver, J. N.; Lundgren, C. A.; Xu, K.; Wang, C., *ACS Nano* **2013**, *7*, 3627-3634.

164. Xin, S.; Yin, Y. X.; Guo, Y. G.; Wan, L. J., *Adv. Mater.* **2014**, *26*, 1261-1265.

165. Billaud, J.; Singh, G.; Armstrong, A. R.; Gonzalo, E.; Roddatis, V.; Armand, M.; Rojo, T.; Bruce, P. G., *Energy Environ. Sci.* **2014**, *7*, 1387-1391.

166. Komaba, S.; Murata, W.; Ishikawa, T.; Yabuuchi, N.; Ozeki, T.; Nakayama, T.; Ogata, A.; Gotoh, K.; Fujiwara, K., *Adv. Funct. Mater.* **2011**, *21*, 3859-3867.

167. Lotfabad, E. M.; Ding, J.; Cui, K.; Kohandehghan, A.; Kalisvaart, W. P.; Hazelton, M.; Mitlin, D., *ACS Nano* **2014**, *8*, 7115-7129.

168. Zhu, H.; Jia, Z.; Chen, Y.; Weadock, N.; Wan, J.; Vaaland, O.; Han, X.; Li, T.; Hu, L., *Nano Lett.* **2013**, *13*, 3093-3100.

169. Darwiche, A.; Marino, C.; Sougrati, M. T.; Fraisse, B.; Stievano, L.; Monconduit, L., *J. Am. Chem. Soc.* **2012**, *134*, 20805-20811.

170. Qian, J.; Wu, X.; Cao, Y.; Ai, X.; Yang, H., *Angew. Chem. Int. Ed.* **2013**, *52*, 4633-4636.

171. Kim, Y.; Park, Y.; Choi, A.; Choi, N. S.; Kim, J.; Lee, J.; Ryu, J. H.; Oh, S. M.; Lee, K. T., *Adv. Mater.* **2013**, *25*, 3045-3049.

172. Hu, Z.; Wang, L.; Zhang, K.; Wang, J.; Cheng, F.; Tao, Z.; Chen, J., *Angew. Chem. Int. Ed.* **2014**, *53*, 12794-12798.

173. Luo, C.; Zhu, Y.; Xu, Y.; Liu, Y.; Gao, T.; Wang, J.; Wang, C., *J. Power Sources* **2014**, *250*, 372-378.

174. Xiang, J.; Chang, C.; Li, M.; Wu, S.; Yuan, L.; Sun, J., *Cryst. Growth Des.* **2008**, *8*, 280-282.

175. Liu, K.; Zheng, J.; Zhong, G.; Yang, Y., *J. Mater. Chem.* **2011**, *21*, 4125-4131.

176. Kim, H.; Seo, D.-H.; Yoon, G.; Goddard, W. A.; Lee, Y. S.; Yoon, W.-S.; Kang, K., *J. Phys. Chem. Lett.* **2014**, *5*, 3086-3092.

177. Luo, C.; Huang, R.; Kevorkyants, R.; Pavanello, M.; He, H.; Wang, C., *Nano Lett.* **2014**, *14*, 1596-1602.

178. Song, Z.; Qian, Y.; Liu, X.; Zhang, T.; Zhu, Y.; Yu, H.; Otani, M.; Zhou, H., *Energy Environ. Sci.* **2014**, *7*, 4077-4086.

Peer-reviewed Publication

1. **Chao Luo**, Y. Zhu, O. Borodin, T. Gao, Y. Xu, C. Lundgren, K. Xu, C. Wang, Activation of Oxygen-Stabilized Sulfur for Li and Na Batteries, *Adv. Funct. Mater.* Accepted.
2. **Chao Luo**, J. Wang, X. Fan, Y. Zhu, F. Han, L. Suo, C. Wang, Roll-to-Roll Fabrication of Organic Nanorod Electrodes for Sodium Ion Batteries, *Nano Energy* **2015**, *13*, 537-545.
3. **Chao Luo**, J. Wang, L. Suo, J. Mao, X. Fan, C. Wang, *In situ* Formed Carbon Bonded and Encapsulated Selenium Composites for Li–Se and Na–Se Batteries, *J. Mater. Chem. A* **2015**, *3*, 555-561.
4. **Chao Luo**, R. Huang, R. Kevorkyants, M. Pavanello, H. He, C. Wang, Self-Assembled Organic Nanowires for High Power Density Lithium Ion Batteries, *Nano Lett.* **2014**, *14*, 1596-1602.
5. **Chao Luo**, Y. Zhu, Y. Wen, J. Wang, C. Wang, Carbonized Polyacrylonitrile Stabilized SeS_x Cathodes for Long Cycle Life and High Power Density Lithium Ion Batteries, *Adv. Funct. Mater.* **2014**, *24*, 4082-4089.
6. **Chao Luo**, Y. Zhu, Y. Xu, Y. Liu, T. Gao, J. Wang, C. Wang, Graphene Oxide Wrapped Croconic Acid Disodium Salt for Sodium Ion Battery Electrodes, *J. Power Sources* **2014**, *250*, 372-378.
7. **Chao Luo**, Y. Xu, Y. Zhu, Y. Liu, S. Zheng, Y. Liu, A. Langrock, C. Wang, Selenium@Mesoporous Carbon Composite with Superior Lithium and Sodium Storage Capacity, *ACS Nano* **2013**, *9*, 8003-8010.
8. **Chao Luo**, Q. Zhou, W. Lei, J. Wang, B. Zhang, X. Wang, Supramolecular Assembly of A New Squaraine and β-Cyclodextrin for Detection of Thiol-Containing Amino Acids in Water, *Supramol. Chem.* **2011**, *23*, 657-662.

9. **Chao Luo**, Q. Zhou, G. Jiang, L. He, B. Zhang, X. Wang, The Synthesis and $^1O_2$ Photosensitization of Halogenated Asymmetric Aniline-Based Squaraines, *New J. Chem.* **2011**, *35*, 1128-1132.
10. **Chao Luo**, Q. Zhou, B. Zhang, X. Wang, A New Squaraine and Hg^{2+}-Based Chemosensor with Tunable Measuring Range for Thiol-Containing Amino Acids, *New J. Chem.* **2011**, *35*, 45-48.
11. X. Fan, J. Mao, Y. Zhu, **Chao Luo**, L. Suo, T. Gao, F. Han, S.-C. Liou, C. Wang, Superior Stable Self-Healing SnP_3 Anode for Sodium-Ion Batteries, *Adv. Energy, Mater.* **2015**, DOI: 10.1002/aenm.201500174.
12. J. Wang, **Chao Luo**, J. Mao, Y. Zhu, X. Fan, T. Gao, A. Mignerey, C. Wang, Solid-State Fabrication of SnS_2/C Nanospheres for High Performance Na-Ion Battery Anode, *ACS Appl. Mater. Interfaces* **2015**, *7*, 11476-11481.
13. J. Mao, **Chao Luo**, T. Gao, C. Wang, Scalable Synthesis of $Na_3V_2(PO_4)_3$/C Porous Hollow Spheres for Na-Ion Batteries Cathode, *J. Mater. Chem. A* **2015**, *3*, 10378-10385.
14. L. Suo, Y. Zhu, F. Han, T. Gao, **Chao Luo**, X. Fan, Y. Hu, C. Wang, Carbon Cage Encapsulating Nano-cluster Li_2S by Ionic Liquid Polymerization and Pyrolysis for High Performance Li-S Batteries, *Nano Energy* **2015**, *13*, 467-473.
15. Y. Zhu, Y. Wen, X. Fan, T. Gao, F. Han, **Chao Luo**, S. Liou, C. Wang, Red Phosphorus-Single-Walled Carbon Nanotube Composite as a Superior Anode for Sodium Ion Batteries, *ACS nano* **2015**, *9*, 3254-3264.
16. T. Gao, F. Han, Y. Zhu, L. Suo, **Chao Luo**, K. Xu and C. Wang, Hybrid Mg^{2+}/Li^+ Battery with Long Cycle Life and High Rate Capability, *Advanced Energy Materials* **2015**, DOI: 10.1002/aenm.201401507.

17. J. Wang, **Chao Luo**, T. Gao, A. Langrock, A. C. Mignerey, C. Wang, An Advanced MoS_2/Carbon Anode for High Performance Sodium-Ion Batteries *Small* **2015**, *11*, 473-481.
18. Y. Xu, Y. Zhu, F. Han, **Chao Luo**, C. Wang, 3D Si/C Fiber Paper Electrodes Fabricated by a Combined Electrospray/Electrospinning Technology for Li-Ion Batteries, *Adv. Energy Mater.* **2015**, 5, 1400753.
19. S. Zheng, F. Yi, Z. Li, Y. Zhu, Y. Xu, **Chao Luo**, J. Yang, C. Wang, Copper-Stabilized Sulfur-Microporous Carbon Cathodes for Li-S Batteries, *Adv. Funct. Mater.* **2014**, *24*, 4156-4163.
20. Y. Zhu, Y. Xu, Y. Liu, **Chao Luo** and C. Wang, Comparison of Electrochemical Performances of Olivine $NaFePO_4$ in Sodium-Ion Batteries and Olivine $LiFePO_4$ in Lithium-Ion Batteries, *Nanoscale* **2013**, *5*, 780-787.
21. L. He, **Chao Luo**, Y. Hou, C. Li, Q. Zhou, Y. Sun, W. Wang, B. Zhang, X. Wang, The Effects of Micellar Media on the Photocatalytic H_2 Production from Water, *Int. J. Hydrogen Energy* **2011**, *36*, 10593-10599.

Conference Presentation

1. **Chao Luo**, J. Wang, C. Wang, "In Situ Formed Sulfur/Carbon Composites for Advanced Li-Sulfur and Na-Sulfur Batteries" Oral presentation, 2014 AICHE Annual Meeting, Atlanta, GA.

2. **Chao Luo**, J. Wang, X. Fan, Y. Zhu, F. Han, L. Suo, C. Wang, "In Situ Precipitated Organic Nanorod Electrodes for Sodium Ion Batteries" Oral Presentation, 227th ECS Meeting, Chicago, IL.